HOT-WIRE CHEMICAL VAPOUR DEPOSITION OF NANOCRYSTALLINE SILICON AND SILICON NITRIDE: GROWTH MECHANISMS AND FILAMENT STABILITY

CLIVE JUSTIN OLIPHANT

A thesis submitted in fulfilment of the requirement for the degree of Philosophiae Doctor in the Department of Physics, University of the Western Cape

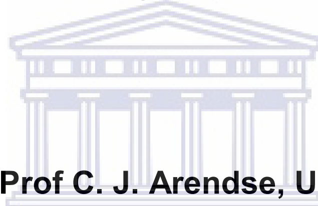

Supervisor : Prof C. J. Arendse, University of the Western Cape

Co-supervisors : Prof D. Knoesen, University of the Western Cape

Dr T. F. G. Muller, University of the Western Cape

October 2012

I dedicate this thesis to my wonderful fiancé Junique, who always believe in me, for your love, the hope and joy you instil in my life!

ACKNOWLEDGEMENTS

All praise to our Lord and Saviour Jesus Christ, through Whom and for Whom all things are created.

I am grateful to my supervisor Prof Christopher Arendse for your guidance, friendship and encouragement.

Prof Dirk Knoesen, for your help and teaching, especially for aiding me in understanding the patience and dexterity needed to prepare samples for microscopy.

Dr Theo Muller, I always look forward to our discussions ranging from science to social networking to deep spiritual matters.

My mentors at the National Metrology Institute of South Africa (NMISA), Mrs Loukie Adlem and Ms Sara Prins for your patience with me and for always keeping me grounded.

To the Solar Research Group previously at Utrecht University, who granted me the van der Weg scholarship and for welcoming me during my three months internship in the Netherlands. This was a significant turning point in my career as a scientist!

UNIVERSITY of the
WESTERN CAPE

I am thankful to Dr David Motaung, for assisting me with XRD, Raman, PL and FTIR measurements.

My colleagues at the NMISA, for your constant motivation and support in my career.

My fellow students and friends at the University of the Western Cape (UWC) and at the NMISA for always making me feel at home.

A special thanks to my wonderful family and friends in Cape Town and in Kimberley, especially my Mom and my sister, for your continuous love and care.

I am grateful for the financial assistance from the National Research Foundation and the NMISA.

Thank you!

DECLARATION

I declare that

"HOT-WIRE CHEMICAL VAPOUR DEPOSITION OF NANOCRYSTALLINE SILICON AND SILICON NITRIDE: GROWTH MECHANISMS AND FILAMENT STABILITY"

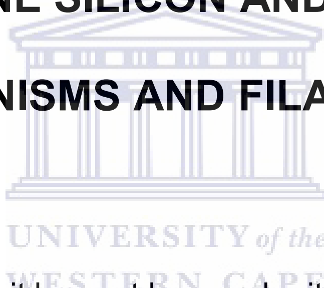

is my own work, that it has not been submitted for any degree or examination in any other university, and that all the sources I have used or quoted have been indicated and acknowledged by means of complete references.

Clive Justin Oliphant

Signature: …………………………… **October 2012**

KEYWORDS

HOT-WIRE CHEMICAL VAPOUR DEPOSITION OF NANOCRYSTALLINE SILICON AND SILICON NITRIDE: GROWTH MECHANISMS AND FILAMENT STABILITY

CLIVE JUSTIN OLIPHANT

UNIVERSITY of the
WESTERN CAPE

Hot-wire chemical vapour deposition

Nanocrystalline silicon

Silicon nitride

Electron backscatter diffraction

Filament degradation

Film growth kinetics

Elemental Composition

Optical properties

Time-of-flight secondary ion mass spectroscopy

ABSTRACT

"HOT-WIRE CHEMICAL VAPOUR DEPOSITION OF NANOCRYSTALLINE SILICON AND SILICON NITRIDE: GROWTH MECHANISMS AND FILAMENT STABILITY"

CLIVE JUSTIN OLIPHANT

Nanocrystalline silicon (nc-Si:H) is an interesting type of silicon with superior electrical properties that are more stable compared to amorphous silicon (a-Si:H). Silicon nitride (SiN_x) thin films are currently the dielectric widely applied in the microelectronics industry and are also effective antireflective and passivating layers for multicrystalline silicon solar cells. Research into the synthesis and characterization of nc-Si:H and SiN_x thin films is vital from a renewable energy aspect. In this thesis we investigated the film growth mechanisms and the filament stability during the hot-wire chemical vapour deposition (HWCVD) of nc-Si:H and SiN_x thin films.

During the HWCVD of nc-Si:H, electron backscatter diffraction (EBSD) revealed that the tantalum (Ta) filament aged to consists of a recrystallized Ta-core with Ta-rich silicides at the hotter centre regions and Si-rich Ta-silicides at the cooler ends nearer to the electrical contacts. The growth of nc-Si:H by HWCVD is controlled by surface reactions before and beyond the transition from a-Si:H to nc-Si:H. During the transition, the diffusion of hydrogen (H) within the film is proposed to be the reaction controlling step. The deposition pressure influenced the structural, mechanical and optical properties of nc-Si:H films mostly when the film thickness is below 250 nm. The film stress, optical band gap, refractive index and crystalline volume fraction approached similar values at longer deposition times irrespective of the deposition pressure.

UNIVERSITY of the
WESTERN CAPE

Filament degradation occurred during the HWCVD of SiN_x thin films from low total flow rate SiH_4 / ammonia (NH_3) / H_2 gas mixture. Similar to the HWCVD of nc-Si:H, the Ta-core recrystallized and silicides formed around the perimeter. However, Ta-nitrides formed within the filament bulk. The extent of nitride and silicide formation, porosity and cracks were all enhanced at the hotter centre regions, where filament failure eventually occurred. We also applied HWCVD to deposit transparent, low reflective and hydrogen containing SiN_x thin films at total gas flow rates less than 31 sccm with NH_3 flow rates as low as 3 sccm. Fluctuations within the SiN_x thin film growth rates were attributed to the depletion of growth species (Si, N, and H) from the ambient and their incorporation within the filament during its degradation.

CONTENTS

ACKNOWLEDGEMENTS .... **ii**

DECLARATION .... **v**

KEYWORDS .... **vi**

ABSTRACT .... **vii**

CONTENTS .... **ix**

1 INTRODUCTION **1**

1.1 SILICON AND ITS ALLOYS 2

1.2 HYDROGENATED NANOCRYSTALLINE SILICON 3

1.2.1 Structural properties 3

1.2.2 Optical properties 6

1.2.3 Electrical properties 9

1.2.4 Synthesis and growth mechanisms of nc-Si:H 11

1.3 SILICON NITRIDE 15

1.3.1 Structural and chemical properties 15

1.3.2 Optical properties 16

1.3.3 Electrical properties 18

1.3.4 Synthesis and growth mechanism of SiN_x 19

1.4 FILAMENT DEGRADATION 22

1.5 AIMS AND OUTLINE 25

UNIVERSITY of the
WESTERN CAPE

REFERENCES 27

2 EXPERIMENTAL TECHNIQUES **35**

2.1 HOT-WIRE CHEMICAL VAPOUR DEPOSITION SYSTEM 36

2.2 STRUCTURAL CHARACTERIZATION 37

2.2.1 X-ray diffraction...37

2.2.2 Electron backscatter diffraction 39

2.2.3 Raman spectroscopy 45

2.2.4 Atomic force microscopy 46

2.2.5 High-resolution transmission electron microscopy and electron energy loss spectroscopy 46

2.2.6 Scanning transmission electron microscopy..47

2.2.7 Fourier-transform infrared spectroscopy 48

2.3 COMPOSITION CHARACTERIZATION...50

2.3.1 X-ray photoelectron microscopy 50

2.3.2 Energy dispersive x-ray spectroscopy 52

2.3.3 Time-of-flight secondary ion mass spectroscopy 53

2.3.4 Elastic recoil detection...55

2.4 OPTICAL CHARACTERIZATION 57

2.5 MECHANICAL PROPERTIES...59

2.5.1 Film stress measurement...59

2.5.2 Vickers microhardness measurement..60

REFERENCES 61

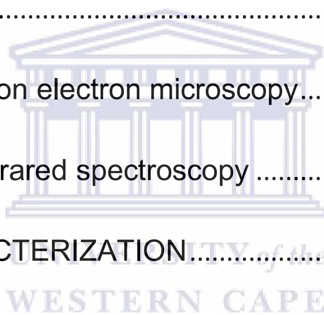
UNIVERSITY of the
WESTERN CAPE

3 STRUCTURAL EVOLUTION OF A TA-FILAMENT DURING HOT-WIRE CHEMICAL VAPOUR DEPOSITION OF SILICON INVESTIGATED BY ELECTRON BACKSCATTER DIFFRACTION 64

3.1 INTRODUCTION 65

3.2 EXPERIMENTAL DETAILS 66

3.3 RESULTS AND DISCUSSION 67

3.4 CONCLUSION 80

REFERENCES 81

4 GROWTH KINETICS OF nc-Si:H FABRICATED BY HWCVD 83

4.1 INTRODUCTION 84

4.2 EXPERIMENTAL DETAILS 85

4.3 RESULTS 86

4.4 DISCUSSION 94

4.5 CONCLUSION 96

REFERENCES 97

5 NANOSTRUCTURAL, MECHANICAL AND OPTICAL PROPERTIES OF nc-Si:H THIN FILMS DEPOSITED BY HWCVD AT HIGH PRESSURES 99

5.1 INTRODUCTION 100

5.2 EXPERIMENTAL DETAILS 101

5.3 RESULTS 104

5.4 DISCUSSION 115

5.5 CONCLUSION 121

REFERENCES 123

UNIVERSITY of the
WESTERN CAPE

6 **DEGRADATION OF A TANTALUM FILAMENT DURING THE HWCVD OF SILICON NITRIDE** **126**

6.1 INTRODUCTION 127

6.2 EXPERIMENTAL DETAILS 128

6.3 RESULTS 131

6.3 DISCUSSION 143

6.3 CONCLUSION 146

REFERENCES 148

7 **STRUCTURAL AND OPTICAL PROPERTIES OF SiN_x FABRICATED BY HOT-WIRE CVD** **150**

7.1 INTRODUCTION 151

7.2 EXPERIMENTAL DETAILS 152

7.3 RESULTS AND DISCUSSION 154

7.5 CONCLUSION 182

REFERENCES 183

SUMMARY **187**

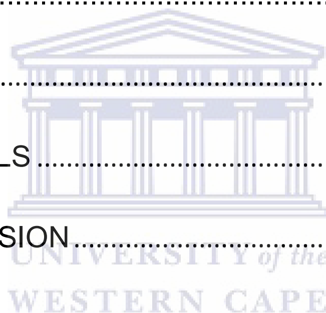
UNIVERSITY of the
WESTERN CAPE

CHAPTER 1

INTRODUCTION

ABSTRACT

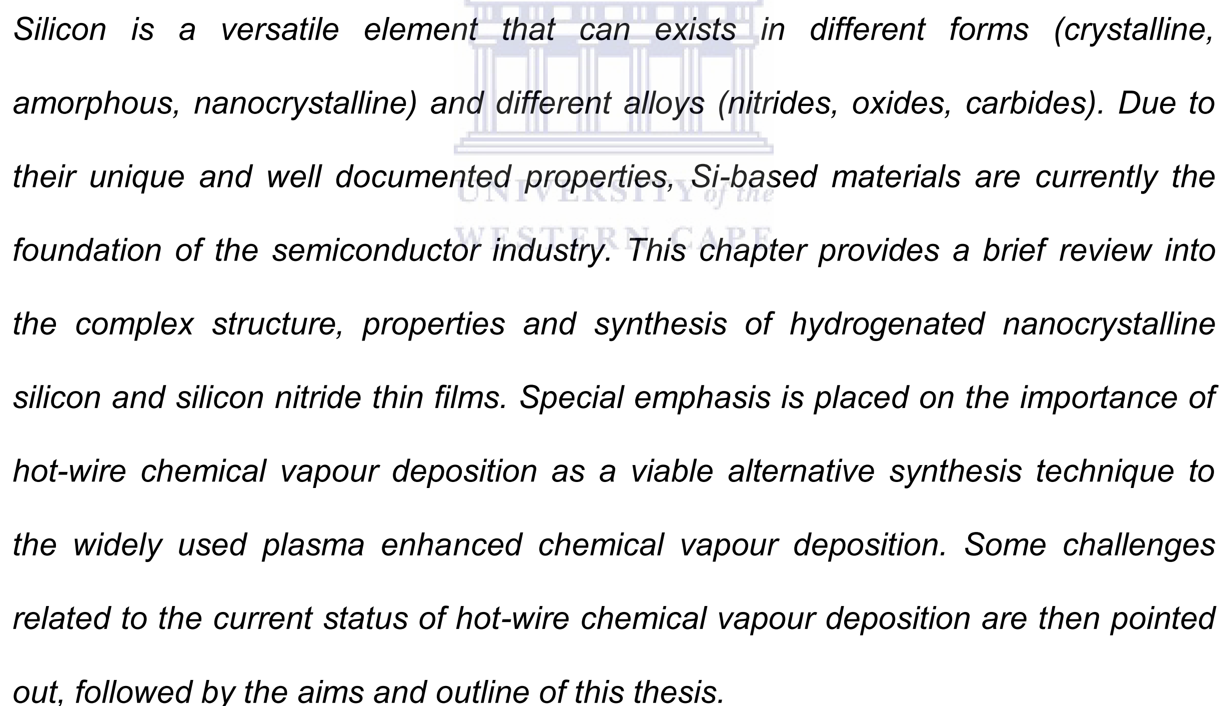

Silicon is a versatile element that can exists in different forms (crystalline, amorphous, nanocrystalline) and different alloys (nitrides, oxides, carbides). Due to their unique and well documented properties, Si-based materials are currently the foundation of the semiconductor industry. This chapter provides a brief review into the complex structure, properties and synthesis of hydrogenated nanocrystalline silicon and silicon nitride thin films. Special emphasis is placed on the importance of hot-wire chemical vapour deposition as a viable alternative synthesis technique to the widely used plasma enhanced chemical vapour deposition. Some challenges related to the current status of hot-wire chemical vapour deposition are then pointed out, followed by the aims and outline of this thesis.

UNIVERSITY of the
WESTERN CAPE

1.1 SILICON AND ITS ALLOYS

Silicon and its alloys, such as silicon nitride (SiN_x), silicon oxide (SiO_x), and silicon carbide (SiC_x), are main components in the current electronics industry. These materials enjoy applications in devices such as thin film transistors, solar cells and light emitting diodes. This wide application scope is related to the unique material properties (optical, electronic), chemical (doping, hydrogen content) and structure (amorphous, mixed phase, crystalline). Chemical vapour deposition (CVD) is a technique commonly used to fabricate thin films of Si and its alloys.

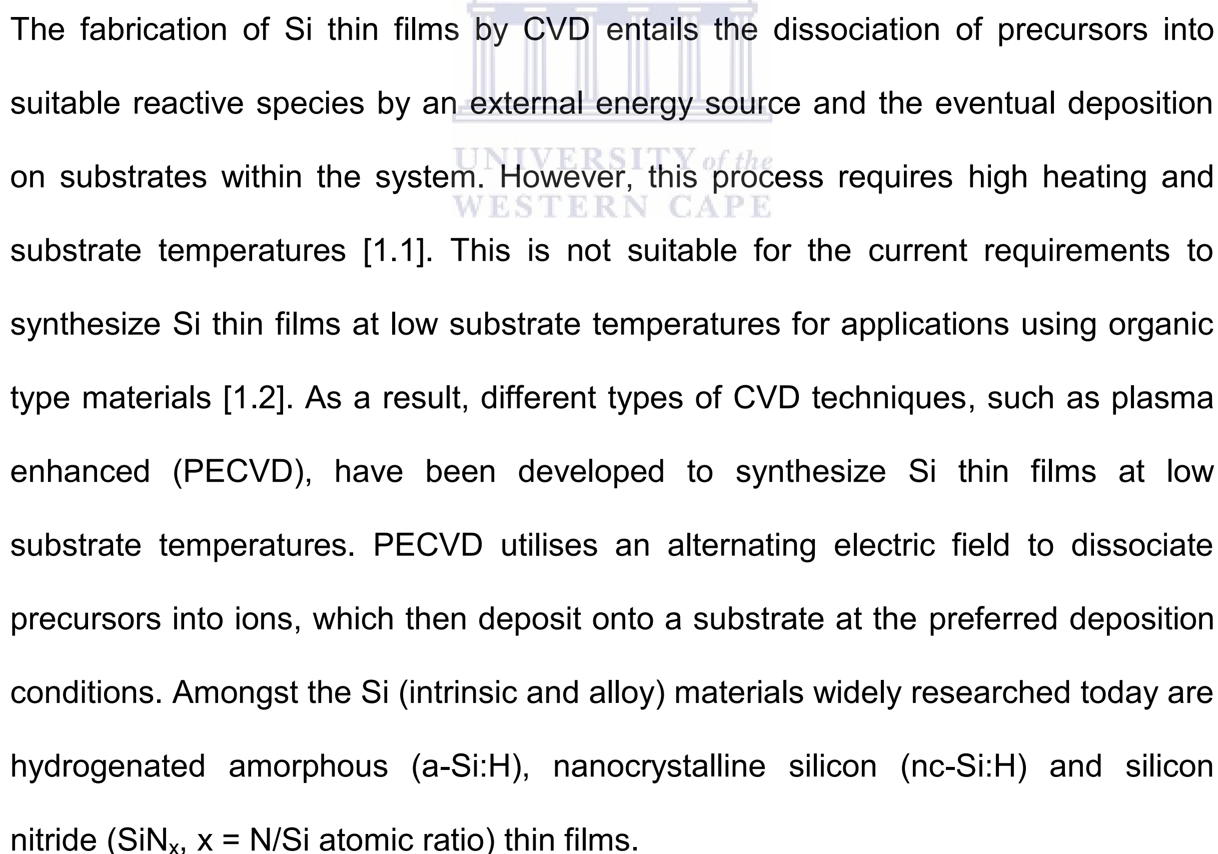

The fabrication of Si thin films by CVD entails the dissociation of precursors into suitable reactive species by an external energy source and the eventual deposition on substrates within the system. However, this process requires high heating and substrate temperatures [1.1]. This is not suitable for the current requirements to synthesize Si thin films at low substrate temperatures for applications using organic type materials [1.2]. As a result, different types of CVD techniques, such as plasma enhanced (PECVD), have been developed to synthesize Si thin films at low substrate temperatures. PECVD utilises an alternating electric field to dissociate precursors into ions, which then deposit onto a substrate at the preferred deposition conditions. Amongst the Si (intrinsic and alloy) materials widely researched today are hydrogenated amorphous (a-Si:H), nanocrystalline silicon (nc-Si:H) and silicon nitride (SiN_x, x = N/Si atomic ratio) thin films.

1.2 HYDROGENATED NANOCRYSTALLINE SILICON

1.2.1 Structural properties

Historically, hydrogenated nanocrystalline silicon (nc-Si:H) thin films progressed from the research of a-Si:H. Amorphous Si is characterised by a disordered atomic structure accompanied by Si-dangling bonds, which generate defect states within the band gap of a-Si. Hydrogen atoms assist in the passivation of the Si-dangling bonds, resulting in the decrease in the density of states within the band gap. Hydrogenated amorphous silicon (a-Si:H) films that possess a narrow distribution in both the Si-Si bond distance and the bonding angle are considered device quality [1.3].

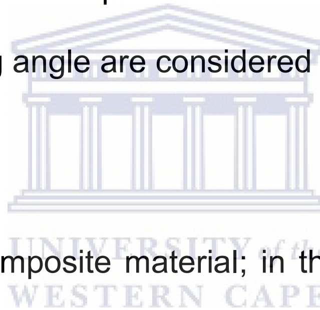
UNIVERSITY of the
WESTERN CAPE

Nanocrystalline silicon is a composite material; in that it consists of crystalline and amorphous regions. The crystalline regions are usually columnar in shape as shown by Figure 1.1 [1.4]. Originally, nc-Si:H was termed microcrystalline silicon (μc-Si:H) due to the size of the grains. However, the terminology developed as the research evolved and currently nomenclature such as protocrystalline, polymorphous and nanocrystalline silicon are used depending on the extent and growth stage of the crystallites, as illustrated in Figure 1.2 [1.5]. Nevertheless, μc-Si:H and nc-Si:H are terms used interchangeably in literature and in this thesis.

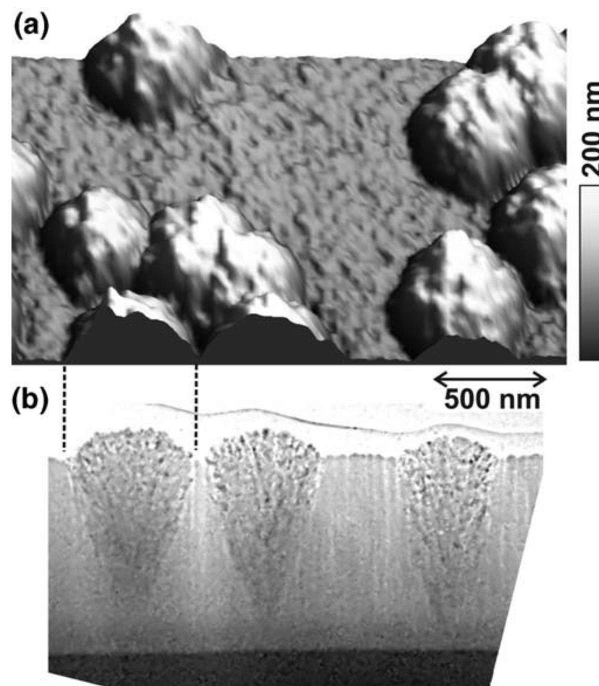

Figure 1.1: (a) Atomic force microscopy image of the nc-Si:H film surface and (b) corresponding transmission electron micrographs showing typical crystalline columns [1.4].

UNIVERSITY of the
WESTERN CAPE

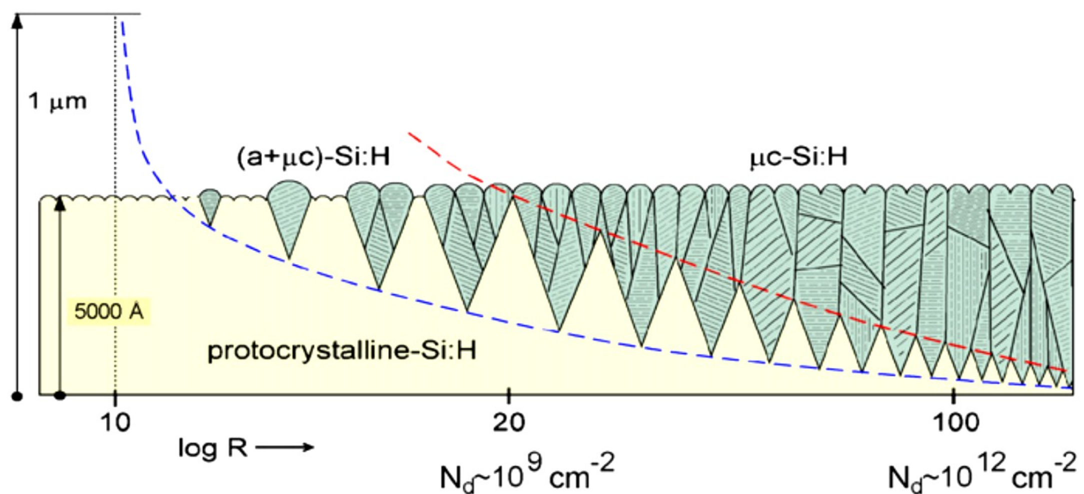

Figure 1.2: Schematic showing the evolution of the Si:H film structure as a function of hydrogen dilution (R= H_2/SiH_4) and film thickness. The corresponding nc-Si:H nuclei densities N_d are also indicated [1.5].

The extent of the crystallite phase, such as size and volume fraction, differentiates nc-Si:H from other classes of silicon (a-Si:H, c-Si, polycrystalline Si). Typically, nc-Si:H contains Si grains with sizes ranging from 20 nm to 100 nm [1.6, 1.7]. X-ray diffraction patterns generally reveal prominent (111), (220) and (311) lattice planes of the nanostructured Si crystals. However, preferential orientation in nc-Si:H has been reported [1.8 – 1.10], although it is not a requirement to achieve device quality material [1.11].

Besides the simultaneous presence of amorphous and crystalline Si regions, the existence of defects, such as microvoids, crystal twinning and grain boundaries, are important structural features of nc-Si:H thin films. In device quality nc-Si:H it is proposed that hydrogen atoms passivate dangling Si bonds at the grain boundaries [1.12]. The amorphous tissue around the crystallites can also act as a passivation 'layer' [1.13]. However, nc-Si:H films with interconnected porosity and defects experiences post-deposition oxidation within microvoids, Si dangling bonds and at grain boundaries [1.7, 1.13, 1.14], effectively degrading the optoelectronic properties.

UNIVERSITY of the
WESTERN CAPE

Surface features, such as the roughness and surface cavities, tend to enhance the optical absorption of nc-Si:H thin films due to diffuse light scattering at the surface [1.15]. In fact, Vallat-Sauvain *et al.* [1.16] found that the surface roughness increased abruptly at the a-Si:H / nc-Si:H transition. The presence of an amorphous Si incubation layer occurring during the initial growth stages of nc-Si:H at low hydrogen dilution values, was found to be detrimental to the carrier transport properties along the film growth direction [1.17].

The structural properties of nc-Si:H is diverse and complex. The properties of the different regions within this nanostructured composite are expected to be intimately linked. The interfaces between the differently ordered Si regions, the microvoids and the grain boundaries are important from an application development viewpoint. It is generally accepted that device quality nc-Si:H thin films reside in the narrow transition window from the a-Si:H to nc-Si:H phases [1.18 – 1.20].

1.2.2 Optical properties

Photons with energy greater than the optical band gap will be absorbed by the nc-Si:H thin film. The optical absorption occurs in both amorphous and crystalline regions. Figure 1.3 compares the absorption coefficient (α) of a-Si:H, nc-Si:H (μc-Si:H) and c-Si [1.21]. Amorphous silicon has a direct band gap, which makes it more efficient at absorbing photons than crystalline silicon. The absorption in nc-Si:H mainly follows the trend of c-Si. However, superior α-values are reached in nc-Si:H compared to a-Si:H and c-Si at photon energies < 1.8 eV. A possible explanation for the enhanced absorption may be light scattering by the rough surface of nc-Si:H and also additional absorption by the a-Si:H tissue [1.15]. Vepřek *et al.* [1.22] suggested that the enhanced optical absorption in nc-Si:H can be attributed to an improved coupling of the electromagnetic field of the incident light to the charge-density fluctuations at the grain boundaries of the quasi-isolated crystallites. The fluctuating charge-density originates from the movement of atomic bond charge caused by bond dilation at the grain boundaries [1.22].

UNIVERSITY of the
WESTERN CAPE

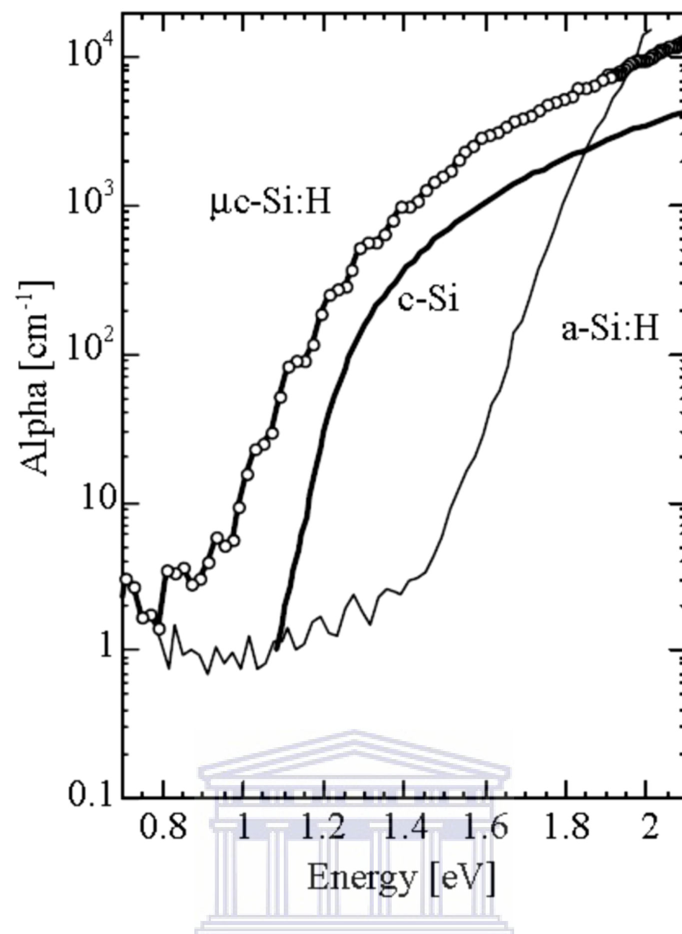

Figure 1.3: Optical absorption coefficient of an nc-Si:H layer in comparison with amorphous and crystalline silicon [1.21].

UNIVERSITY of the
WESTERN CAPE

Another interesting feature in the optical properties of nc-Si:H thin films is the apparent widening of the optical band gap with a decreasing crystallite size [1.23, 1.24]. This mechanism is known as the quantum confinement effect (QCE) and was also observed in nanocrystalline porous silicon [1.25]. The QCE expand the application scope of nc-Si:H to include light emitting materials [1.23].

In contrast to a-Si:H[1.26], the relationship between the bonded hydrogen content and optical band gap is not clear in nc-Si:H films [1.24, 1.27]. However, the most important function of hydrogen in the case of nc-Si:H is the passivation of dangling Si bonds at grain boundaries and also to some extent in the a-Si network [1.12]. The trend in Figure 1.4 shows that for nc-Si:H the total hydrogen (bonded and non-bonded) is less than that typically observed in a-Si:H, while a maximum value is reached at the transition from a-Si:H to nc-Si:H [1.28].

The presence of microvoids results in the dilation of Si-Si bonds, which is expected to reduce the film refractive index and blue shift the absorption edge [1.26, 1.27]. Moreover, post-oxidation is enhanced in nc-Si:H films with interconnected microvoids [1.12] and can subsequently reduce the red spectral response of a solar cell [1.7, 1.29]. The incorporation of oxygen into nc-Si:H can be reduced by optimising the material to consist of a dense a-Si:H network with a minimal interconnected void fraction [1.13]. Torres *et al.* [1.7] suggested a purifying technique based on lowering the reactor outgassing rate and a metallic-alloy gas purifier that reduces the oxygen contact to the sub parts-per-billion in the precursor gases.

UNIVERSITY of the
WESTERN CAPE

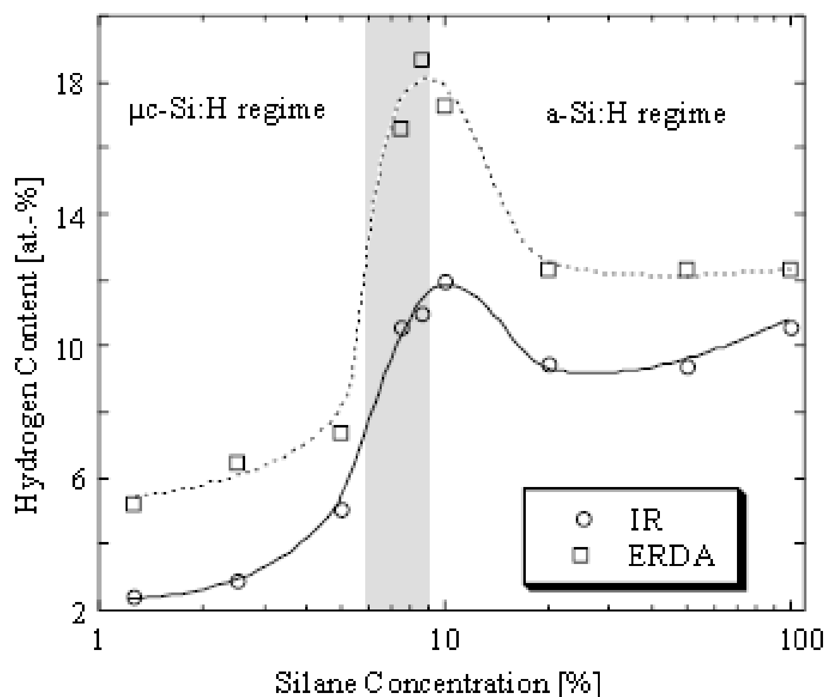

Figure 1.4: Hydrogen content of Si:H films at various H_2-dilution as determined by infrared spectroscopy (IR) and elastic recoil detection analysis (ERD) [1.28].

UNIVERSITY of the
WESTERN CAPE

1.2.3 Electrical properties

For a-Si:H based solar cells the suppression of light-induced degradation, called the Staebler-Wronski effect [1.30], is the most important factor to improve the efficiency. The inclusion of grains within the amorphous network is believed to minimize the light-induced degradation in the case of nc-Si:H thin films [1.31, 1.32]. Enhancing the crystallite size and volume fraction can however result in an increasing void and defect concentration within a-Si:H regions, and consequently a nc-Si:H thin film that is more prone to oxidation [1.13, 1.33]. The oxidation subsequently induces n-type behaviour by pushing the Fermi-level closer to the conduction band thereby increasing the dark current [1.7].

Nevertheless, nc-Si:H thin films deposited by HWCVD typically shows higher open circuit voltages (V_{OC}) than their PECVD counterparts [1.18]. The superior V_{OC} in the case of HWCVD is attributed to the higher fraction of ordered a-Si:H tissue (at the transition from a-Si:H to nc-Si:H) that leads to excellent grain boundary passivation [1.18].

The transport and recombination of the photogenerated charge carriers are suggested to be strongly influenced by the defect structure [1.34 - 1.38]. Currently, the exact location of the defects, whether being in the crystallite, grain boundary, amorphous, or the regions between columns (see Figure 1.1), is not known.

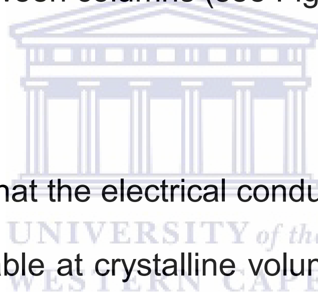
UNIVERSITY of the
WESTERN CAPE

Masuda *et al.* [1.37] reported that the electrical conductivity along the growth and the lateral directions was comparable at crystalline volume fractions of < 20 %. With an increase in the crystalline volume fraction, the conductivity along the growth direction was superior compared to the lateral direction. Additionally, the conductivity along the lateral direction decreased as the crystalline volume fraction increased, whereas the conductivity in the growth direction remained almost constant [1.37]. Based on transmission electron microscopy analysis, it was concluded that the differences in electrical conductivities can be attributed to the extent of the columnar crystalline regions within the films [1.37].

Unlike a-Si:H, the complex composite structure of nc-Si:H makes it difficult to accurately pinpoint the exact influence of each region on the charge carrier transport, recombination and consequently device performance [see Ref. 1.35 and references cited therein]. However, passivation of the dangling bonds by hydrogen, intermediate crystallite size / fraction and a densely packed, well-ordered a-Si:H network contribute to device quality nc-Si:H suitable for application in solar cells.

1.2.4 Synthesis and growth mechanisms of nc-Si:H

It is clear that the structure and the optoelectronic properties of nc-Si:H thin films are intricately linked. However, the growth process of nc-Si:H is currently not yet fully understood, which makes it difficult to controllably synthesize device quality material. As a result, intensive research is pursued in optimizing the nc-Si:H synthesis parameters with the aim of producing material close to the a-Si:H / nc-Si:H transition point with minimal defects and a reduced interconnected void fraction.

Additionally, fabricating device quality nc-Si:H thin films at high growth rates is important from an industrial viewpoint. PECVD is a well-established technique for fabricating a-Si:H thin films and has also received extensive applications in nc-Si:H synthesis. In fact, the current proposed growth processes of nc-Si:H has been formulated mostly from studies based on material deposited by PECVD [1.39].

UNIVERSITY of the WESTERN CAPE

In general, three major growth mechanisms have been suggested namely the etching by atomic hydrogen ($H^{\bullet}$) [1.40], chemical annealing [1.41] and surface diffusion [1.42]. Briefly, etching of Si, especially weakly bonded Si by $H^{\bullet}$ has been proposed based on the observations of a decreasing film thickness and enhancing crystallinity as more H_2 gas is introduced relative to SiH_4. Chemical annealing was proposed to explain the crystallisation of a-Si layers when exposed to $H^{\bullet}$. The thickness of the layers did not decrease, in which case etching by atomic hydrogen is excluded. The chemical annealing mechanism states that the $H^{\bullet}$ penetrates the subsurface where it annihilates strained bonds, thereby facilitating crystallisation. Surface diffusion occurs when the surface is covered by hydrogen and also when $H^{\bullet}$ combine and releases heat, i.e. local annealing. Subsequently, the recombination and hydrogen coverage promote the diffusion Si-containing species on the surface until it finds an energetically favoured site, ultimately favouring ordering/nucleation of crystallites. As diverse as these models may be, it is clear that the presence of atomic hydrogen during the deposition appears to be instrumental for the growth of nc-Si:H.

UNIVERSITY of the
WESTERN CAPE

In 1979, Weismann *et al.* [1.43] reported on the deposition of a-Si:H by another type of CVD technique, which used a restively heated filament to supply energy to dissociate the precursor gases. This technique has gone by many names, including hot-filament CVD [1.44], catalytic CVD [1.45], evaporative surface decomposition (ESD) [1.46] and hot-wire chemical vapour deposition (HWCVD) [1.47]. The term HWCVD is the most commonly used and will be used in this thesis.

Regardless of its relatively short history, the HWCVD method has been rapidly developed into a technique that can produce nc-Si:H thin films with film properties comparable to PECVD [1.18]. Moreover, the absence of plasma and the high efficiency at dissociating precursor gases contributes to the capability of HWCVD to fabricate nc-Si:H thin films with no damage caused by ion bombardment or dust formation as is the case for PECVD [1.12, 1.48].

Depositing device quality nc-Si:H thin films at high growth rates is currently a main focus in literature [1.18]. Higher growth rates, while maintaining suitable material properties, can be achieved by systematically studying the influence of each deposition parameter on the structural and optoelectronic properties. Improving the efficiency of dissociating the precursor gases can lead to an increase in film growth rate. In HWCVD this is achieved by increasing the filament temperature and the filament area. However, filament temperatures > 2000 °C lead to substantial substrate heating, which lead to defective materials as the incorporation of H into the film is reduced [1.18] and possible metal contamination by evaporating filament material [1.49]. Nevertheless, the heated filament plays an important role in the HWCVD process. In most cases transition metals such as W and Ta are employed as filaments [1.50 and references therein] due to their high melting temperatures, favourable mechanical properties and low vapour pressures. The filament's prime purpose is to dissociate the precursor gases (usually SiH_4 and H_2) into suitable radicals available for film growth.

UNIVERSITY of the WESTERN CAPE

Specifically, the SiH_4 and H_2 gases are efficiently dissociated into $H^•$ and Si radicals [1.51]. The subsequent gas phase reactions between radicals *en route* to the substrate have a critical impact on the material quality and depend on the deposition pressure and the substrate to filament distance (d_{f-s}).

The formation of SiH_3 via the hydrogen abstraction by $H^•$ from SiH_4 and the insertion reaction of Si into SiH_4 to form $HSiSiH3^•$ are proposed to be the most important gas phase reactions [1.52, 1.53]. Minimal secondary reactions occur at low deposition pressures and short d_{s-f} leading to the deposition of disordered material due to the high sticking probability of the Si radical [1.54]. On the other hand, multiple gas phase reactions occur at high deposition pressures and long d_{s-f}, which can result in the formation of higher silanes and subsequently defective, porous material [1.18]. Investigating intermediate deposition pressures and d_{s-f} are therefore a vital step in depositing device quality nc-Si:H thin films.

UNIVERSITY of the
WESTERN CAPE

The interconnection between the deposition parameters and the system geometry of each deposition chamber means that the optimum synthesis conditions will be unique for each HWCVD system. Key parameters then to consider for HWCVD of device quality nc-Si:H thin films include the deposition pressure, low substrate temperatures, a tantalum filament temperature of ~ 1600 °C and the hydrogen dilution value.

1.3 SILICON NITRIDE

1.3.1 Structural and chemical properties

Silicon nitride can exist in amorphous and crystalline forms. During the past 40 years, silicon nitride has been developed and industrialised into materials with thermal shock resistance, hardness, wear resistance and high temperature stability [1.56]. On the other hand, hydrogenated amorphous silicon nitride (SiN_x, where x is the N/Si ratio) is a wide band gap dielectric that is currently studied and applied extensively in the microelectronics industry.

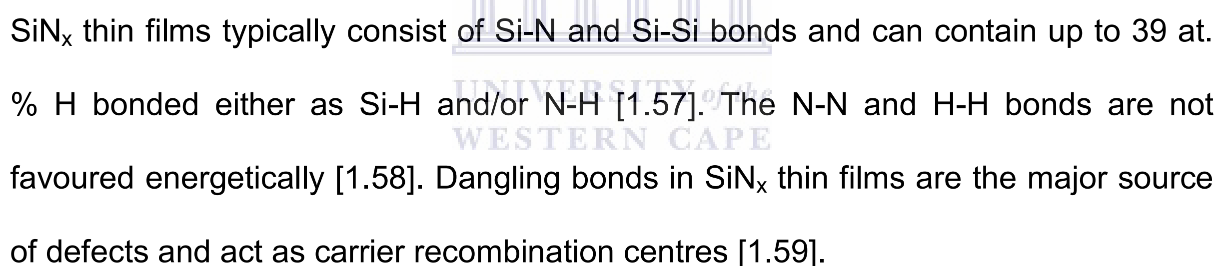

SiN_x thin films typically consist of Si-N and Si-Si bonds and can contain up to 39 at. % H bonded either as Si-H and/or N-H [1.57]. The N-N and H-H bonds are not favoured energetically [1.58]. Dangling bonds in SiN_x thin films are the major source of defects and act as carrier recombination centres [1.59].

SiN_x films have been applied widely as passivation layers on crystalline solar cells. Passivation is achieved during the firing-up step (necessary for forming the contacts) during which $H^{\bullet}$ is released from SiN_x and partly diffuses into the surface and bulk, passivating defects and grain boundaries in the crystalline Si solar cell [1.60]. The mass density of a SiN_x thin film influences its passivation capability. In general, dense SiN_x layers are effective at passivation [1.60]. However, too dense SiN_x thin films can hamper the diffusion of atomic hydrogen through the film [1.61].

Regardless, devices based on porous SiN_x films capped on both sides by a-Si:H synthesized by HWCVD also showed promising dielectric properties [1.62].

Typically, N-rich ($x \geq 1.33$) SiN_x films with root-mean-square (rms) roughness values of < 1 nm are suggested to be suitable for TFTs and anti-reflective coatings (ARC) on solar cells [1.60, 1.63]. However, Si-rich ($x \leq 1.33$) or sub-stoichiometric SiN_x thin films can contain quantum dots of Si (crystalline or amorphous), which is believed to enable this class of SiN_x as strong candidates for light emitting Si-based materials [1.64]. N-rich SiN_x layers tend to be denser and more thermally stable than their Si-rich counterparts [1.60, 1.65]. Lelièvre *et al.* [1.65] proposed that the more “opened”, less stable structure of Si-rich SiN_x films enhances the diffusion of H-radicals towards the SiN_x/Si interface during the deposition, resulting in effective surface bulk passivation. Whether Si- or N-rich, SiN_x thin films are versatile materials that can enhance the optoelectronic properties of solar cells or thin film transistors.

UNIVERSITY of the
WESTERN CAPE

1.3.2 Optical properties

The optical properties of SiN_x can be varied depending on its chemical composition, especially the N/Si ratio [1.60, 1.66, 1.67]. The incorporation of N within SiN_x results in a widened optical band gap from typical a-Si values (~ 1.8 eV) to close to the Si_3N_4 value of 5 eV and a reduction in the refractive index [1.68]. Typically, a refractive index of ~ 2 is characteristic of SiN_x close to stoichiometry [1.69], with higher numbers generally associated to an increasing Si-content.

The increasing optical band gap (decrease in Si-content) results in an improved transmission within the visible range. Moreover, the refractive index of ~ 1.9 is intermediate to that of air (1) and a Si-wafer (3.42), which means that N-rich SiN_x can be used as an antireflective and transparent coating on Si-based solar cells. The absorption is minimal as indicated by extinction coefficients which are < 0.1 in device quality N-rich SiN_x [1.60].

Light-emission from Si-rich SiN_x across the visible wavelength range has inspired numerous studies [1.64, 1.70 – 1.72]. Theories on the exact mechanism behind the luminescence however are still controversial. Two main theories have been prevalent; namely the quantum confinement effect from embedded Si quantum dots (see Figure 1.5) [1.64] and band tail luminescence [1.72]. Regardless, the added photoluminescence ability of a Si-rich SiN_x can aid in down converting high energy photons and luminescing closer to the band gap energy of the underlying solar cell.

UNIVERSITY of the
WESTERN CAPE

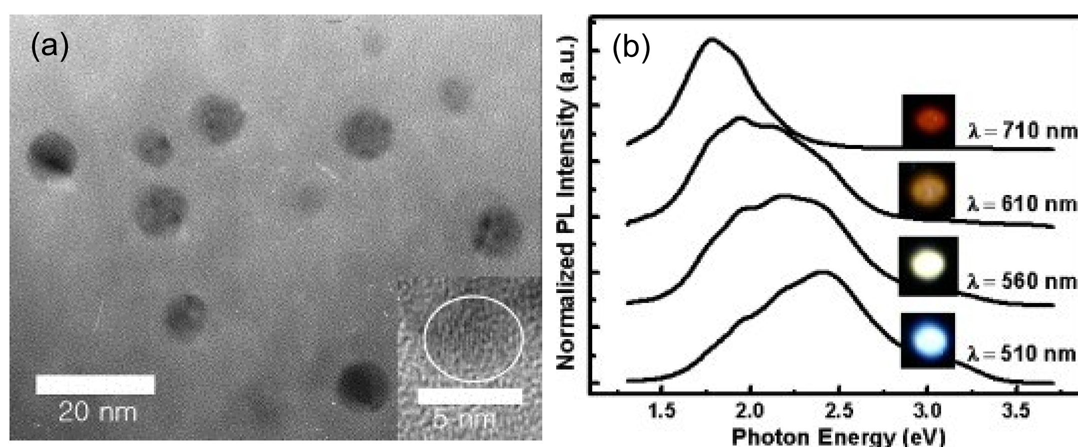

Figure 1.5: (a) High-resolution transmission electron image of Si nanocrystals embedded in SiN_x (inset magnified image of nanocrystals) and (b) photoluminescence spectra and pictures (insets) of SiN_x films with different size Si nanocrystals [1.70].

1.3.3 Electrical properties

SiN_x is one of the most widely used dielectrics in modern electronic technologies. Houweling *et al.* [1.63] reported on capacitance-voltage (C-V) measurements of N-rich SiN_x films with N/Si > 1.33 grown by HWCVD. It was found that the static dielectric constant ε amounted to ~ 6.3 and appeared to be independent of the composition. Additionally, trapped and fixed charges reached a maximum at N/Si ~ 1.33 and have values one order of magnitude lower for chemical compositions on either side of N/Si ~ 1.33. The HWCVD SiN_x films are suitable for gate dielectrics, since the breakdown field is ≥ 2 MV/cm [1.73].

Currently, there is an increasing demand for high quality liquid crystal displays (LCD) at low cost and that can be deposited on glass or plastic materials. Alpium *et al.* [1.69] successfully applied HWCVD to synthesize SiN_x layers at substrate temperatures of 100 and 250 °C with breakdown fields > 10 $MVcm^{-1}$ and electrical conductivity of ~ 10^{-14} $\Omega^{-1}cm^{-1}$. These low temperature HWCVD SiN_x films have properties superior to SiN_x deposited by electron cyclotron resonance assisted sputter deposition at a substrate temperature of 350 °C [1.74].

UNIVERSITY of the
WESTERN CAPE

Whereas most studies have focussed on investigating N-rich SiN_x, investigations into sub-stoichiometric SiN_x (x < 1.33) showed that these films also possess properties suitable for optoelectronic technologies [1.65, 1.68, 1.75, 1.76]. Giorgis *et al.* [1.76] reported that by varying the NH_3 flow rate relative to SiH_4 it is possible to obtain SiN_x films with properties such as spin densities (indicative of dangling bonds) of ~ 10^{17} cm^{-3}, band gap values at $\alpha = 10^4$ cm^{-1} (E_{04}) ranging from 1.90 eV – 3.25 eV and

dark- and photoconductivity similar to those of device quality amorphous silicon carbide.

1.3.4 Synthesis and growth mechanism of SiN_x

Important deposition parameters necessary for high growth rate of device quality SiN_x thin films include the deposition pressure, filament temperature, SiH_4 / NH_3 flow ratio and the substrate temperature. Similar to the case of nc-Si:H, the optimized HWCVD synthesis conditions for SiN_x may be unique for each deposition chamber.

Reports on research into the PECVD of SiN_x films first appeared in the 1970's [1.77]. Almost two decades later, Matsumura [1.78] reported the first HWCVD of SiN_x in 1989. Since then, the HWCVD technique has developed into a method that offers device quality SiN_x thin films at superior growth rates and with no ion bombardment as is the case for the industrial workhorse, PECVD.

UNIVERSITY of the
WESTERN CAPE

In the case of PECVD of SiN_x thin films, it was found that the plasma power plays a major role during the deposition. In general, the deposition rate enhances with an increasing plasma power until a critical power is reached, after which the rate decreases with an enhancing power [1.79]. This phenomenon was attributed to a simultaneous deposition-and-etching mechanism.

During PECVD, feed gas molecules (usually SiH_4 and NH_3) are dissociated into SiH_x and NH_x precursors with atomic hydrogen and ions. Consequently, below the critical power, the deposition of SiN_x by PECVD is determined by the adsorption and reactions between precursors at the substrate. However, etching becomes more pronounced above the critical power. It is also believed that etching gradually deteriorates the film thickness uniformity as the plasma power enhances [1.79].

There are however important advantages that HWCVD have over PECVD of SiN_x. The gas utilization during HWCVD is superior compared to PECVD and is important for rapid growth rates. Ansari *et al.* [1.80] used gas phase diagnostics to investigate the NH_3 and SiH_4 gas utilization with and without H_2 at a W-filament temperature of 2000 °C. The study showed that the gas utilization rates for NH_3 and SiH_4 increase with a decreasing total gas flow rate and the addition of H_2 to the gas mixture. Atomic hydrogen, which increases with the addition of H_2, was proposed to re-activate the W-filament surface poisoned by SiH_4. Furthermore, the addition of H_2 to the usual SiH_4 / NH_3 gas mixture over a heated filament (~ 2000 °C) is believed to lead to a higher concentration of $H^{\bullet}$ during the deposition, which then improves the quality of SiN_x films [1.81, 1.82].

UNIVERSITY of the
WESTERN CAPE

Umemoto *et al.* [1.83, 1.84] used laser and mass spectrometry to perform detailed analysis of the deposition chemistry related to the HWCVD of SiN_x from SiH_4 / NH_3 feedstock gases. It was found that NH_2 and atomic hydrogen species are produced by the dissociation of NH_3 by a heated W-filament [1.84]. However, the addition of SiH_4 to the gas mixture drastically decreased the number of N-containing radicals

[1.83]. In contrast to PECVD [1.85], no aminosilanes were detected in the HWCVD gas phase during the deposition of SiN_x [1.83]. Ansari *et al.* [1.80] postulated that the silicidation of the W-filament surface during exposure to SiH_4 reduced its NH_3 dissociation efficiency. This finding can also explains the necessity to use high NH_3 flow rates in SiH_4 / NH_3 based depositions [1.69] in order to increase the major SiN_x growth species NH_2 and SiH_3 [1.83]. Moreover, the addition of H_2 to the typical SiH_4 / NH_3 mixture enhanced the incorporation of N into SiN_x thin films [1.82] thereby allowing reduced NH_3 flow rates.

Some properties of SiN_x films deposited by HWCVD and PECVD are compared in Table 1.1 [1.60, 1.86]. Other than offering superior growth rates, HWCVD SiN_x films also tend to show reduced H-contents and film stress. The lower H-content in HWCVD SiN_x films has been attributed to a higher H density which is utilized more in NH_3 dissociation rather than being incorporated into the film [1.87]. The resultant lower H-content can also explain the more dense, low stress SiN_x deposited by HWCVD.

UNIVERSITY of the WESTERN CAPE

Table 1.1: Typical properties of SiN_x thin films prepared by HWCVD and PECVD.

Property	PECVD	HWCVD
Deposition rate (nm/min)	30 - 100	5 – 438
H content (%)	10 - 20	3 – 10
Stress (MPa)	400	50 – 400
Refractive index	1.9 – 2.0	1.9 – 2.0
Breakdown field (MV/min)	5 - 10	5 – 10

1.4 FILAMENT DEGRADATION

UNIVERSITY of the WESTERN CAPE

HWCVD is a promising technique for the large-scale fabrication of device quality nc-Si:H and SiN_x thin films. The optoelectronic properties of these films depend on their structure and chemical composition. The structure and chemical composition in turn are determined by the synthesis parameters. The filament plays a crucial role in the HWCVD process. Specifically, the filament surface, temperature, and operational lifetime influence the deposition stability and material properties. However, filament degradation is a major drawback in the HWCVD of nc-Si:H and SiN_x thin films. During the HWCVD of Si-based materials, the radicals generated by the dissociation of the precursor gases by the heated filament can diffuse into the filament and cause significant changes in its structure and even its failure [1.88]. As a result of filament degradation, the deposition process as a whole is influenced and consequently film properties [1.89].

By using secondary ion mass spectroscopy (SIMS) measurements, Bourée *et al.* [1.49] established that W impurities found in HWCVD nc-Si:H thin films originated from the evaporation of the filament during heating. Limiting the filament temperature to 1600 °C and its surface area to 5 cm^2 minimized the concentration of W within nc-Si:H thin films [1.49]. van der Werf *et al.* [1.90] reported that the formation of silicides on a W-filament surface reduced the catalytic capability of a W-filament for dissociating H_2 into atomic hydrogen. Monitoring *in situ* the power dissipation by heated W- and Ta-filaments; it was also found that more electrical power is used by the latter when exposed to a H_2 atmosphere, which was interpreted as an indication that Ta-filaments generate more atomic hydrogen than W [1.90].

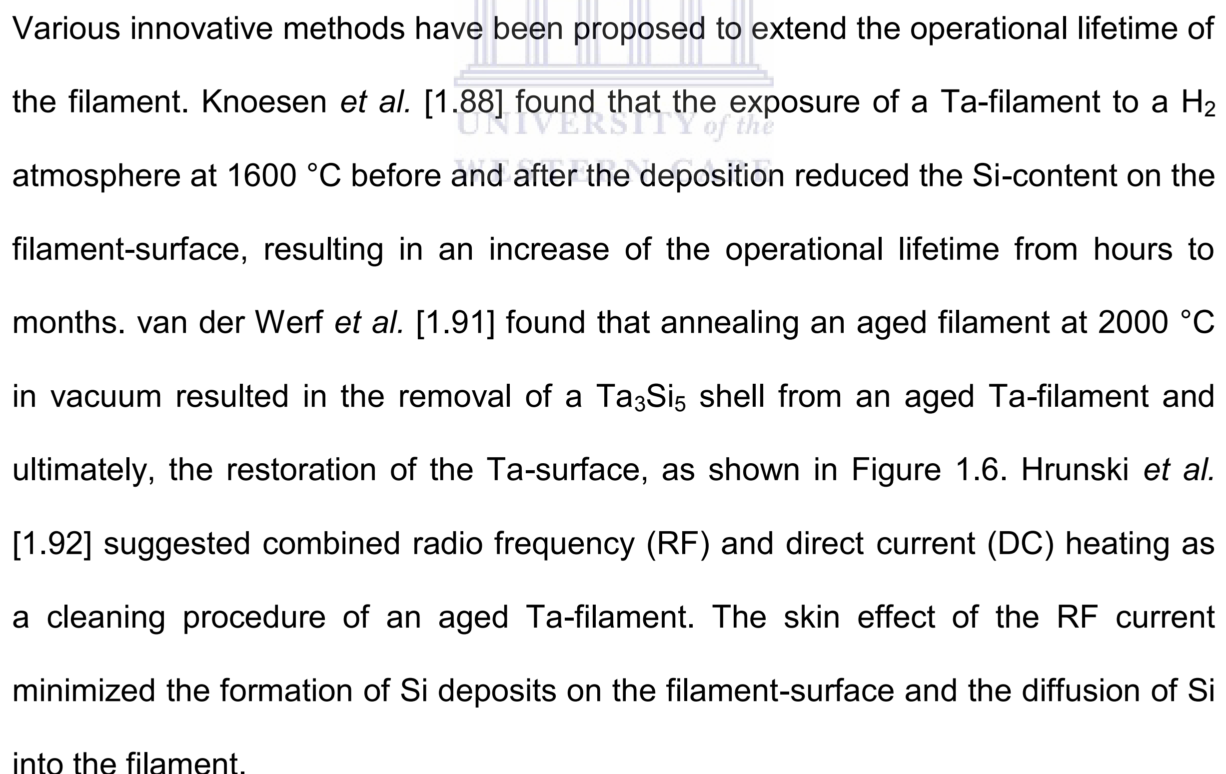

Various innovative methods have been proposed to extend the operational lifetime of the filament. Knoesen *et al.* [1.88] found that the exposure of a Ta-filament to a H_2 atmosphere at 1600 °C before and after the deposition reduced the Si-content on the filament-surface, resulting in an increase of the operational lifetime from hours to months. van der Werf *et al.* [1.91] found that annealing an aged filament at 2000 °C in vacuum resulted in the removal of a Ta_3Si_5 shell from an aged Ta-filament and ultimately, the restoration of the Ta-surface, as shown in Figure 1.6. Hrunski *et al.* [1.92] suggested combined radio frequency (RF) and direct current (DC) heating as a cleaning procedure of an aged Ta-filament. The skin effect of the RF current minimized the formation of Si deposits on the filament-surface and the diffusion of Si into the filament.

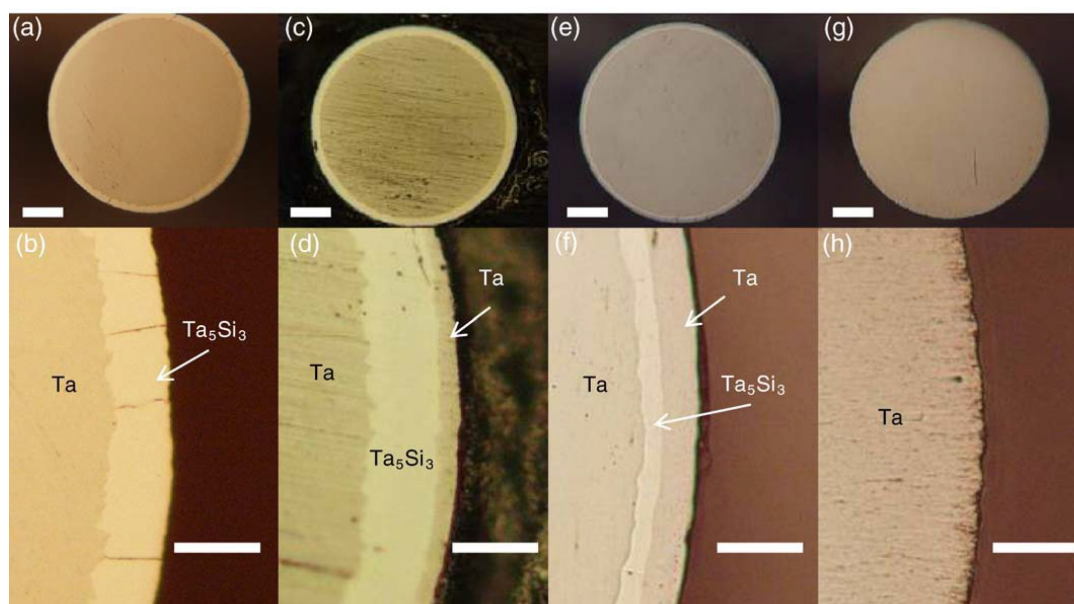

Figure 1.6: Top row shows optical micrographs of the cross-sections (scale bar 100 μm) with bottom row the outer regions at a higher magnification (the scale bar is 30 μm) of four Ta-filaments with similar deposition history annealed for different durations of (a, b) ~10 min (c, d) ~1 h (e, f) and (g, h) ~4 h [1.91].

UNIVERSITY of the
WESTERN CAPE

Despite the obvious influence of the dissociation processes at the filament-surface during the HWCVD of nc-Si:H and SiN_x films, investigations into the filament degradation mechanism at high H_2 dilutions and in a SiH_4 / NH_3 / H_2 mixture are scarce compared to that conducted at a-Si:H and SiN_x (SiH_4 / NH_3) deposition conditions [1.88, 1.92 - 1.97]. Nevertheless, accurately characterising the structural evolution of the filament is a vital step in obtaining a stable deposition regime.

1.5 AIMS AND OUTLINE

It is clear that an investigation into the thin film growth mechanisms and the filament degradation during the HWCVD of nc-Si:H and SiN_x are important from a scientific and industrial viewpoint. Therefore, the objectives of this thesis are: 1) to investigate the growth process of nc-Si:H thin films synthesized by HWCVD, 2) to investigate the growth process of SiN_x thin films synthesized by HWCVD, and 3) to study the stability of the filaments used for the HWCVD of nc-Si:H and SiN_x thin films with the aim of obtaining new insights into the filament degradation mechanism.

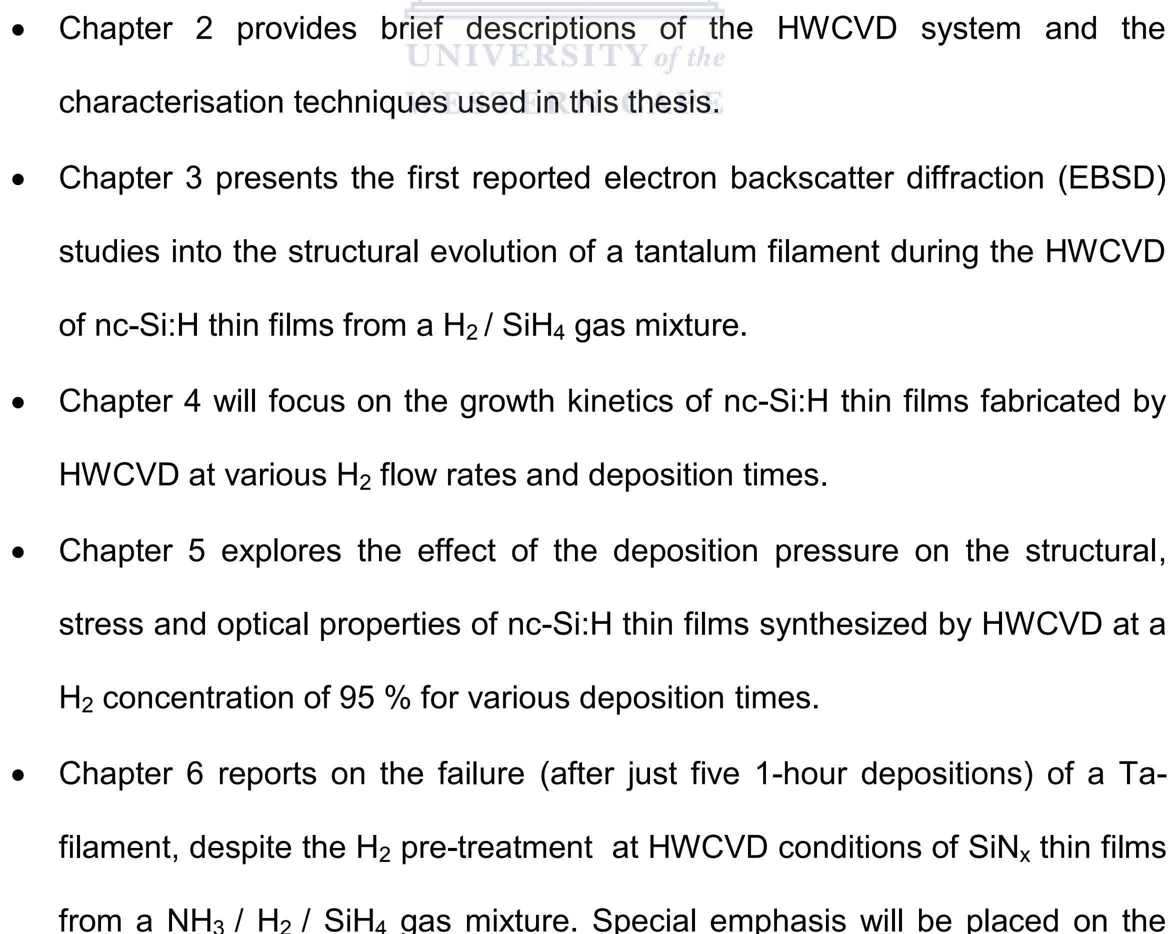

The outline of the thesis is as follows:

- Chapter 2 provides brief descriptions of the HWCVD system and the characterisation techniques used in this thesis.
- Chapter 3 presents the first reported electron backscatter diffraction (EBSD) studies into the structural evolution of a tantalum filament during the HWCVD of nc-Si:H thin films from a H_2 / SiH_4 gas mixture.
- Chapter 4 will focus on the growth kinetics of nc-Si:H thin films fabricated by HWCVD at various H_2 flow rates and deposition times.
- Chapter 5 explores the effect of the deposition pressure on the structural, stress and optical properties of nc-Si:H thin films synthesized by HWCVD at a H_2 concentration of 95 % for various deposition times.
- Chapter 6 reports on the failure (after just five 1-hour depositions) of a Ta-filament, despite the H_2 pre-treatment at HWCVD conditions of SiN_x thin films from a NH_3 / H_2 / SiH_4 gas mixture. Special emphasis will be placed on the

EBSD and time-of-flight secondary ion mass spectroscopy (TOF-SIMS) analysis of the aged filament.

- Chapter 7 presents the investigations into the synthesis and characterisation of SiN_x thin films fabricated by HWCVD at total SiH_4 / H_2 / NH_3 flow rates of 31 - 33 sccm for different NH_3 flow rates.
- Finally, a Summary of the investigations carried out in this thesis will be given.

REFERENCES

1.1 A. C. Jones, M. L. Hitchman (editors) (2008), **Chemical Vapour Deposition: Precursors, Processes and Applications**, Royal Society of Chemistry.

1.2 W. Huang, X. Wang, M. sheng, L. Xu, F. Stubhan, L. Luo, T. Feng, X. Wang, F. Zhang, S. Zou (2003) Mat. Sci. Eng. **B98**:248

1.3 A. McEvoy, T. Markvart, L. Castaner (2011), **Practical Handbook of Photovoltaics: Fundamentals and Applications**, Academic Press. Waltham, USA.

1.4 T. Mates, P. C. P. Bronsveld, A. Fejfar, B. Rezek, J. Kočka, J. K. Rath, R. E. I. Schropp (2006) J. Non-Cryst. Solids **352**:1011.

1.5 C.R. Wronski, B. Von Roedern, A. Kołodziej (2008) Vacuum **82**:1145.

1.6 R. E. I. Schropp, Miro Zeman (1998), **Amorphous and Microcrystalline Silicon Solar Cells: Modelling, Materials, and Device Technology**, Kluwer Academic Publishers, Norwell.

1.7 P. Torres, J. Meier, R. Flückiger, U. Kroll, J. A. Anna Selvan, A. Shah, S. D. Littelwood, I. E. Kelly, P. Giannoulès (1996) Appl. Phys. Lett. **69**:1373.

1.8 E. Vallat-Suavain, U. Kroll, J. Meier, A. Shah, J. Pohl (2000) J. Appl. Phys. **84**:3137.

1.9 T. Toyama, H Okamoto (2006) Solar Energy **8**0:658.

1.10 T. Sugano, T. Kitagawa, Y. Sobaji, T. Toyama, H. Okamoto (2005) J. Appl. Phys. **97**:094910.

1.11 S. Schicho, F. Köhler, R. Carius, A. Gordijn (2012) Sol. Energ. Mat. Sol. C. **98**:391.

UNIVERSITY of the WESTERN CAPE

1.12 A. V. Shah, J. Meier, E. Vallat-Suavain, N. Wyrsch, U. Kroll, C. Droz, U. Graf (2003) Sol. Energ. Mat. Sol. C. **78**:469.

1.13 A. C. Bronnenberg, A. H. M. Smets, M. Creatore, M. C. M. van de Sanden (2011) J. Non-Cryst. Solids **357**:884.

1.14 J. Kočka, H. Stuchíková, M. Ledinsky, J. Stuchlík, T. Mates, A. Fejfar (2009) Sol. Energ. Mat. Sol. C. **93**:1444.

1.15 A. Poruba, A. Fejfar, Z. Remeš, J. Špringer, M. Vaněček, J. Kočka, J. Meier, P. Torres, A. Shah (2000) J. Appl. Phys. **88**:148.

1.16 E. Vallat-Suavain, U. Kroll, J. Meier, N. Wyrsch, A. Shah (2000) J. Non-Cryst. Solids **266-269**:125.

1.17 C. Niikura, R. Brenot, J. Guillet, J. E. Bourée, J. P. Kleider, R. Brüggemann, C. Longeaud (2001) Sol. Energ. Mat. Sol. C. **66**:421.

1.18 S. Klein, F. Finger, R. Carius, M. Stutzmann (2005) J. Appl. Phys. **98**:024905.

1.19 M. Goerlitzer, P. Torres, N. Beck, N. Wyrsch, H. Keppner, J. Pohl, A. Shah (1998) J. Non-Cryst. Solids **227–230**: 996.

1.20 J. Meier, E. Vallat-Sauvain, S. Dubail, U. Kroll, J. Dubail, S. Golay, L. Feitknecht, P. Torres, S. Fay, D. Fischer, A. Shah (2001) Sol. Energ. Mat. Sol. C. **66**:73.

1.21 N. Beck, P. Torres, J. Fric, Z. Remes, A. Poruba, H.A. Stuchlikova, A. Fejfar, N. Wyrsch, M. Vanecek, J. Kocka, A. Shah (1997) Proc. Mater. Res. Soc. Symp. **452**:761.

1.22 S. Vepřek F. A. Sarott, Z. Iqbal (1987) Phys. Rev. B **36**:3344.

1.23 J. H. Shim, N. H. Cho (2006) Materials Science Forum **510-511**:958.

UNIVERSITY of the
WESTERN CAPE

1.24 C. J. Arendse, G. F. Malgas, T. F. G. Muller, D. Knoesen, C. J. Oliphant, D. E. Motaung, S. Halindintwali, B. W. Mwakikunga (2009) Nanoscale Res. Lett. **4**:307.

1.25 N. Koshida, A. Kojima, T. Migita, Y. Nakajima (2002) Mat. Sci. Eng. C **19**:285.

1.26 K.F. Feenstra, R.E.I. Schropp, W.F. van der Weg (1999) J. Appl. Phys. **85**:6843.

1.27 N. A. Bakr, A. M. Funde, V. S. Waman, M. M. Kamble, R. R. Hawaldar, D. P. Amalnerkar, V. G. Sathe, S. W. Gosavi, S. R. Jadkar (2011) J. Phys. Chem. Solids **72**:685.

1.28 U. Kroll, J. Meier, A. Shah, S. Mikhailov, J. Weber, J. Appl. Phys. (1996) **80**:4971.

1.29 M. Kondo, T. Matsui, Y. Nasuno, H. Sonobe, S. Shimizu (2006) Thin Solid Films **501**:243.

1.30 D. L. Staebler, C. R. Wronksi (1977) Appl. Phys. Lett. **31**:292.

1.31 M. Fonrodona, D. Soler, J. Escarré, F. Villar, J. Bertomeu, J. Andreu, A. Saboundji, N. Coulon, T. Mohammed-Brahim (2006) Thin Solid Films **501**:303.

1.32 S. Halindintwali, D. Knoesen, R. Swanepoel, B. A. Julies, C. Arendse, T. Muller, C. C. Theron, A. Gordjin, P. C. P. Bronsveld, J. K. Rath, R. E. I. Schropp (2007) Thin Solid Films **515**:8040.

1.33 S. Klein, T. Repmann, T. Brammer (2004) Solar Energy **77**:893.

1.34 K. Lips, P. Kanschat, W. Fuhs (2003) Sol. Energ. Mat. Sol. C. **78**:513.

1.35 O. Astakhov, R. Carius, F. Finger, Y. Petrusenko, V. Borysenko, D. Barankov (2009) Phys. Rev. B. **79**:104205.

UNIVERSITY of the WESTERN CAPE

1.36 J. Puigdollers, C. Voz, A. Orpella, I. Martín, D. Soler, M. Fonrodona, J. Bertomeu, J. Andreu, R. Alcubilla (2002) J. Non-Cryst. Solids **299-302**:400.

1.37 A. Masuda, R. Iduka, A. Heya, C. Niikura, H. Matsumura (1998) J. Non-Cryst. Solids **227-230**:987.

1.38 M. Kondo, S. Yamasaki, A. Matsuda (2000) J. Non-Cryst. Solids **266-229**:544.

1.39 A. Matsuda (1999) Thin Solid Films **337**:1

1.40 C.C. Tsai, G.B. Anderson, R. Thompson, B. Wacker (1989) J. Non-Cryst. Solids **114**:151.

1.41 K. Nakamura, K. Yoshida, S. Takeoka, I. Shimizu, Jpn. J. Appl. Phys. 34 (1995) 442.

1.42 A. Matsuda (1983) J. Non-Cryst. Solids **59 / 60**:767.

1.43 H. Wiesmann, A. K. Ghosh, T. McMahon, M. Strongin (1979) J. Appl. Phys. **50**:3752.

1.44 S. V. Desphande, J. L. Dupuie, E. Gulari (1996) Adv. Mater. Opt. Electron. **6**:135.

UNIVERSITY of the
WESTERN CAPE

1.45 H. Matsumura (1998) Jpn. J. Appl. Phys. **37**:3175.

1.46 J. Doyle, R. Robertson, G. H. Lin, M. Z. He, A. Gallagher (1988) J. Appl. Phys. **64**:3216.

1.47 A. Mahan, J. Carapella, B. Nelson, R. Crandall, I. Balberg (1991) J. Appl. Phys. **69**:6728.

1.48 A. Gordjin, L. Hodakova, J. K. Rath, R. E. I. Schropp (2006) J. Non-Cryst. Solids **352**:1868.

1.49 J. E. Bourée, J. Guillet, C. Grattepain, J. Chaumont (2003) Thin Solid Films **430**:110.

1.50 R. E. I. Schropp (2004) Thin Solid Films **451-452**:455.

1.51 J. Doyle, R. Robertson, G. H. Lin, M. Z. He, A. Gallagher (1988) J. Appl. Phys. **64**:3216.

1.52 A. Gallagher (2001) Thin Solid Films **395**:25.

1.53 Y. Nozaki, M. Kitazoe, K. Horri, H. Umemoto, A. Masuda, H. Matsumura (2001) Thin Solid Films **395**:47.

1.54 J. Perrin, O. Leroy, M. C. Bordage (1996) Contrib. Plasma Phys. **36**:3.

1.55 S. Halindintwali, D. Knoesen, R. Swanepoel, B. A. Julies, C. Arendse, T. Muller, C. C. Theron, A. Gordjin, P. C. P. Bronsveld, J. K. Rath, R. E. I. Schropp (2009) S. Afr. J. Sci. **105**:290.

1.56 J. R. Davis (1997), Heat resistant Materials, ASM International.

1.57 F. H. P. M. Habraken, A. E. T. Kuiper (1994) *Mater. Sci. Eng.* **R12**:123

1.58 E. Bustarret, M. Bensouda, M. C. Habrard, J. C. Bruyère, S. Poulin, S. C. Gujrathi (1988) *Phys. Rev. B* **38**:8171.

1.59 J. Robertson, M. J. Powell (1984) Appl. Phys. Lett. **44**:415.

1.60 V. Verlaan, C. H. M. van der Werf, Z. S. Houweling, I. G. Romijn, A. W. Weeber, H. F. W. Dekkers, H. D. Goldbach, R. E. I. Schropp (2007) Prog. Photovolt: Res. Appl. **15**:563.

1.61 I. G. Romijn, W. J. Soppe, H. C. Rieffe, W. C. Sinke, W. Weeber (2005) Presented at 15t Workshop on Crystalline Silicon Solar Cells and Modules: Materials Processes, Vail Colorado, USA.

1.62 B. Stannowski, J. K. Rath, R. E. I. Schropp (2001) Thin Solid Films **395**:339.

1.63 Z. S. Houweling, V. Verlaan, R. Bakker, C. H. M. van der Werf, U. Mai, R. E. I. Schropp (2007) MRS Proc. **989**:412.

1.64 N. Park, C. Choi, T. Seong, S. Park (2001) Phys. Rev. Lett. **86**:1355.

WESTERN CAPE

1.65 J. F. Lelièvre, E. Fourmond, A. Kaminski, O. Palais, D. Ballutaud, M. Lemiti (2009) Sol. Energ. Mat. Sol. C. **93**:1281.

1.66 B. Swatowska, T. Stapinski (2008) Vacuum **82**:942.

1.67 J. J. Mei, H. Chen, W. Z. Shen, H. F. Dekkers (2006) J. Appl. Phys. **100**:073516.

1.68 S. Jung, D. Gong, J. Yi (2011) Sol. Energ. Mat. Sol. C. **95**:546.

1.69 P. Alpium, L. M. Gonçalves, E. S. Marins, T. M. R. Viseu, S. Ferdov, J. E. Bourée (2009) Thin Solid Films **517**:3503.

1.70 K. Lee, T, Kim, J. Hwang, S. Jang, K. Jeong, M. Han, S. Won, J. Sok, K. Park, W. Hong (2009) Scripta Mater. **60**:703.

1.71 A. K. Panchal, C. S. Solanki (2009) Thin Solid Films **517**:3488.

1.72 J. Kistner, X. Chen, Y. Weng, H. P. Strunk, M. B. Schubert, J. H. Werner (2011) J. Appl. Phys. **110**:023520.

1.73 A. Sazonov, D. Stryahilev, A. Nathan, L. D. Bogomolova (2002) J. Non-Cryst. Sol. **299-302**:1360.

1.74 K. Deenamma Vargheese, G. Mohan Rao (2001) J. Vac. Sci. Technol., Part A **19**:2122.

1.75 H. Mäckel, R. Lüdemann (2002) J. Appl. Phys. **92**:2602.

1.76 F. Giorgis, P. Rava, R. Galloni, R. Rizzoli, C. Summonte, G. Crovini, F. Demichelis, C. F. Pirri, E. Tresso, V. Rigato (1996) J. Non-Cryst. Sol. **198-200**:596.

1.77 F. H. P. M. Habraken, A. E. T. Kuiper (1994) *Mater. Sci. Eng.* **R12**:123

1.78 H. Matsumura (1989) *Jp. J. Appl. Phys.* **28**:2136.

1.79 Y. Kuo (editor) (2004), **Thin Film Transistors: Amorphous silicon thin film transistors**, Kluwer Academic Publishers, Massachusetts.

UNIVERSITY of the WESTERN CAPE

1.80 S. G. Ansari, H. Umemoto, T. Morimoto, K. Yoneyama, A. Izumi, A. Masuda, H. Matsumara (2006) Thin Solid Films **501**:31.

1.81 F. Liu, S. Ward, L. Gedvilas, B. Keyes, B. To, Q. Wang, E. Sanchez S. Wang (2004) J. App. Phys. **96**:2973.

1.82 A. H. Mahan, A. C. Dillon, L. M. Gedvilas, D. L. Williamson, J. D. Perkins (2003) J. Appl. Phys. **94**:2360.

1.83 H. Umemoto, T. Morimoto, M. Yamawaki, Y. Masuda, A. Masuda, H. Matsumura (2003) Thin Solid Films **430**:24.

1.84 H. Umemoto, Y. Kashiwagi, K. Ohdaira, H. Kobayashi, K. Yasui (2011) Thin Solid Films **519**:4429.

1.85 D. L. Smith, A. S. Alimona, C. C. Chen, S. E. Ready, B. Wacker (1990) J. Electrochem. Soc. **137**:614.

1.86 A. Masuda, H. Umemoto, H. Matsumara (2006) Thin Solid Films **501**:149.

1.87 A. C. Dillon, L. Gedvillas, D. L. Williamson, J. Thiesen, J. D. Perkins, A. H. Mahan (2001) MRS Symp. Proc. **664**:A72.

1.88 D Knoesen, C Arendse, S Halindintwali, T Muller (2008) Thin Solid Films **516**:814.

1.89 S. Lien, M. Tseng, C. Chao, K. Weng, H. H. Yu, D. Wuu (2009) Thin Solid Films **517**:4720.

1.90 C. H. M. van der Werf, P. A. T. T. van Veenendaal, M.K. van Veen, A. J. Hardeman, M. Y. S. Rusche, J. K. Rath, R. E. I. Schropp (2003) Thin Solid Films **430**:46.

1.91 C. H. M. van der Werf, H. Li, V. Verlaan, C. J. Oliphant, R. Bakker, Z. S. Houweling, R. E. I. Schropp (2009) Thin Solid Films **517**:3431.

UNIVERSITY of the WESTERN CAPE

1.92 D. Hrunski, M. Scheib, M. Mertz, B. Schroeder (2009) Thin Solid Films **517**:3370.

1.93 C. E. Sveen, Y. Shi (2011) Thin Solid Films **519**:4447.

1.94 N. Kniffler, A. Pflueger, D. Scheller, B. Schroeder (2009) Thin Solid Films **517**:3424.

1.95 V Verlaan, CHM van der Werf, CJ Oliphant, R Bakker, ZS Houweling, REI Schropp (2009) Thin Solid Films **517**:3435

1.96 D. Hrunski, B. Schroeder, M. Scheib, R. M. Merz, W. Bock, C. Wagner (2008) Thin Solid Films **516**:818.

1.97 R Weissenbacher, R Haubner, K Aigner, B Lux (2002) Diamond and Related Materials **11**:191.

UNIVERSITY of the
WESTERN CAPE

CHAPTER 2

EXPERIMENTAL TECHNIQUES

ABSTRACT

Investigations into the synthesis and characterisation of hydrogenated nanocrystalline silicon (nc-Si:H) and silicon nitride (SiN_x) thin films are vital stages in the development and fabrication of devices based on these materials. This chapter will provide a brief description of the hot-wire chemical vapour deposition (HWCVD) chamber used for the synthesis of the nc-Si:H and SiN_x thin films investigated in this thesis. The characterization techniques that have been employed in this thesis to investigate the filament stability and the structure-property relationships of nanocrystalline silicon and silicon nitride will be briefly discussed. Particular emphasis will be placed on electron backscatter diffraction, x-ray diffraction and x-ray photoelectron spectroscopy. Each technique will be briefly introduced based on its relevance to this thesis, followed by a theoretical background and experimental set-up. More details of the measurement conditions and procedure are given in the subsequent chapters.

UNIVERSITY of the
WESTERN CAPE

2.1 HOT-WIRE CHEMICAL VAPOUR DEPOSITION SYSTEM

The MVSYSTEMS HWCVD system is specifically designed for the fabrication of high quality semiconductors and devices. The chamber can reach typical base pressures in the order of 10^{-9} mbar. Figure 2.1 shows a schematic of the HWCVD system [2.1].

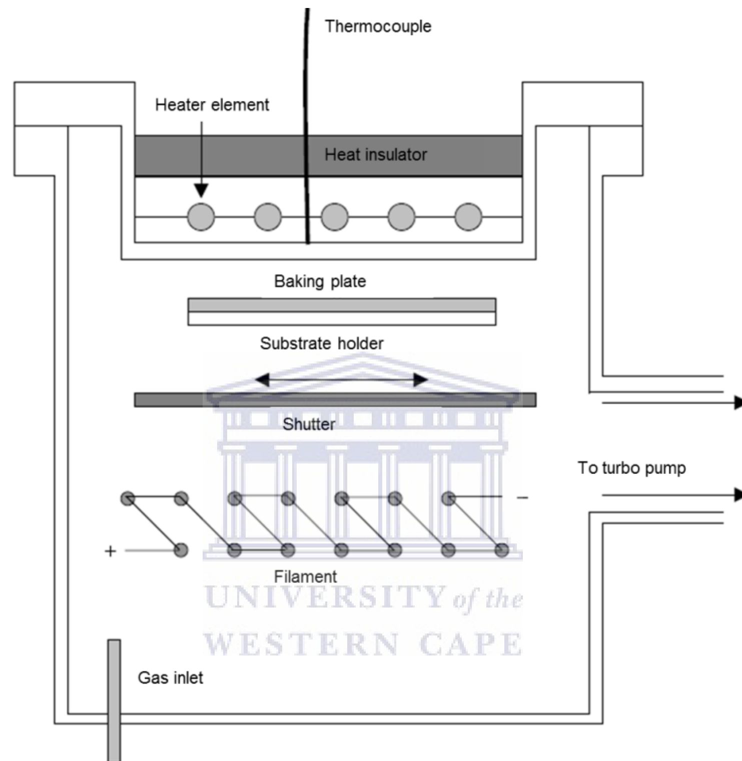

UNIVERSITY of the
WESTERN CAPE

Figure 2.1: Schematic showing the cross-sectional view of the HWCVD chamber.

Ammonia, hydrogen and silane gases can be dosed separately or as a mixture via a gas inlet. The gas flow rates are controlled by mass flow controllers. An automatic pressure controller allows for the regulation of the deposition pressure within the system by electronically adjusting a butterfly valve.

A tantalum (Ta)-filament (diameter ~ 250 μm, length 1 m) is heated by an AC current and the filament temperature is measured by an optical pyrometer. The substrate temperature is determined by the substrate heater and filament temperature [2.1]. The substrate stage can be extracted from the high vacuum chamber and removed from the HWCVD system via a load-lock, typically at 10^{-3} mbar.

Mounted on the substrate stage are monocrystalline silicon (100) and Corning 7059 glass substrates (25 mm X 25 mm). The substrates are prepared for deposition using a standard cleaning method consisting of: 5 minutes sonication in acetone, then methanol and then rinse in distilled water. The c-Si substrates were then further dipped for one minute in a 5 % HF solution.

2.2 STRUCTURAL CHARACTERIZATION

2.2.1 X-ray diffraction

The wavelength of x-rays is in the order of 10^{-10} m (Å), which matches that of the interatomic spacing of crystals. As a result, x-rays experience diffraction at certain incident angles. During most of the last 100 years x-ray diffraction (XRD) has been developed into a technique used for the identification and quantification of crystal structure, chemical analysis, stress measurement and particle size [2.2].

The well-known Bragg law defines the requirements for the diffraction of x-rays from by a crystal and is written as:

$$\lambda = 2d \sin \theta_B \qquad (2.1)$$

where λ is the x-ray wavelength, d the interatomic spacing and θ_B the diffraction angle.

The diffraction peaks measured during XRD are explained by the Bragg law. However, the width of the peaks increases as the size of the crystalline particles decreases; this effect becomes measureable below a crystallite size of 100 nm. The Scherrer equation [2.2] is then used to estimate the particle size from the measurement of the widths of the corresponding diffraction peaks and is expressed as:

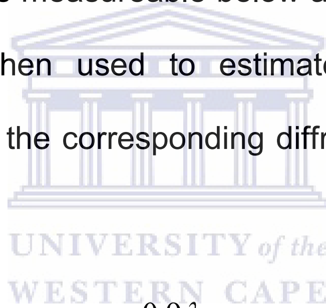

$$d_{XRD} = \frac{0.9\lambda}{B \cos \theta_B} \qquad (2.2)$$

where d_{XRD} is the size of the particles and B the width of the peak (in radians) taken from the full width at half maximum (FWHM). The particle size is not the only contributor to the peak width. In most cases, the strain/stress within the sample and instrumental broadening are also contributors to the broadening of the diffraction pattern of nanostructured materials. Separating the structure related broadening (size and strain) from the instrumental broadening is important to perform reliable XRD analysis.

XRD has provided valuable insights into the characterisation of nc-Si:H and SiN_x thin films. The type of information that is generally extracted from XRD is the determination of the crystalline volume fraction [2.3], particle size [2.4] and stress measurement [2.5]. XRD also provided insights into degradation studies of the filaments that were used during the HWCVD of nc-Si:H [2.6].

XRD patterns were collected in reflection geometry with a step size of 0.02°, using a PANalytical XPert diffractometer operating at 45 kV and 40 mA. Copper K_α radiation with a wavelength of 1.5406 Å was used as the x-ray source. The XRD patterns were indexed using the 2011/2012 database maintained by the International Centre for Diffraction Data (ICDD) [2.7]. A NIST SRM 660 LaB_6 reference material was used as a standard to determine the instrumental broadening and polycrystalline Si to determine the peak positions.

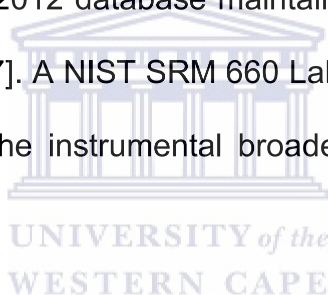
UNIVERSITY of the
WESTERN CAPE

2.2.2 Electron backscatter diffraction

The determination of a material's crystallographic information is vital to obtain an understanding of its structure-property relationships. As an add-on package to a scanning electron microscope (SEM), electron backscatter diffraction (EBSD) has been developed into a robust, accurate and fast characterisation technique that determines and quantifies crystallographic information [2.8]. It is possible to analyse thousands of orientations per hour, thereby allowing excellent statistical distributions.

Combined with measuring the elemental composition of the material, this allows for the analysis of the material's microstructure, elemental composition and crystallographic information, all within the SEM.

An EBSD pattern is obtained in a SEM by irradiating a tilted sample with a stationary electron beam. Figure 2.2 shows a diagram of the experimental arrangement to obtain an EBSD pattern within a SEM [2.9, 2.10]. The mechanism of EBSD pattern formation can either be described by the channelling or diffraction of electrons [2.8]. Nevertheless, in both mechanisms two flat cones of electrons emanate from a particular atomic plane. The cones interact with the phosphor screen on the EBSD detector, creating two lines separated by an angle equal to $2\theta_B$, where θ_B is the angle corresponding to diffraction.

UNIVERSITY of the
WESTERN CAPE

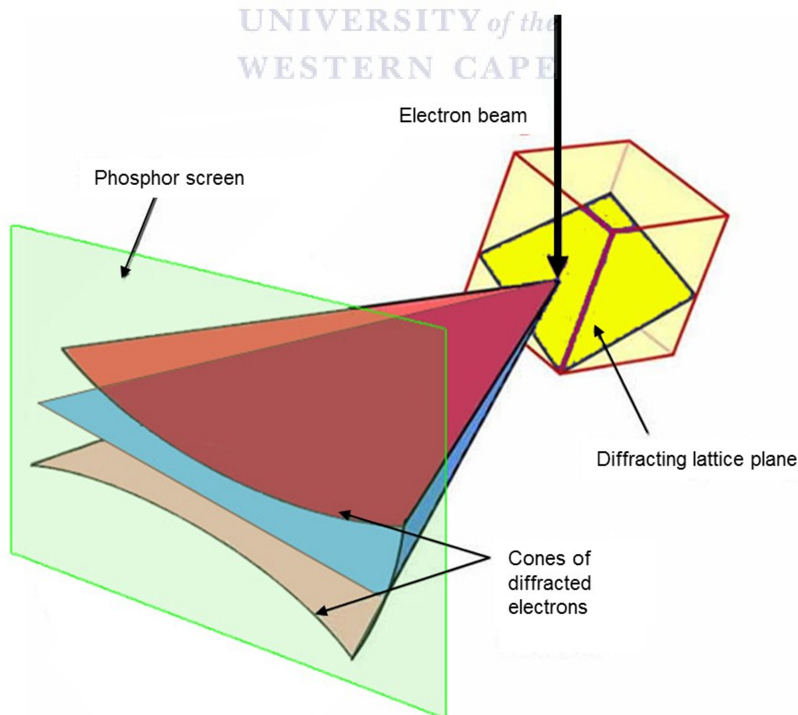

Figure 2.2: Formation of an EBSD pattern from the diffracted incident electron beam in a SEM adapted from [2.10].

The lines formed on the phosphor screen are known as Kikuchi lines. There are multiple regions where the Kikuchi lines intersect; the intersections correspond to zone axes within the crystal. In effect, the EBSD pattern is an angular map of the crystals within the sample. Figure 2.3 presents the relationship between the sample crystal structure and the detected EBSD pattern. Phase identification and crystallographic orientation are therefore possible from EBSD analysis.

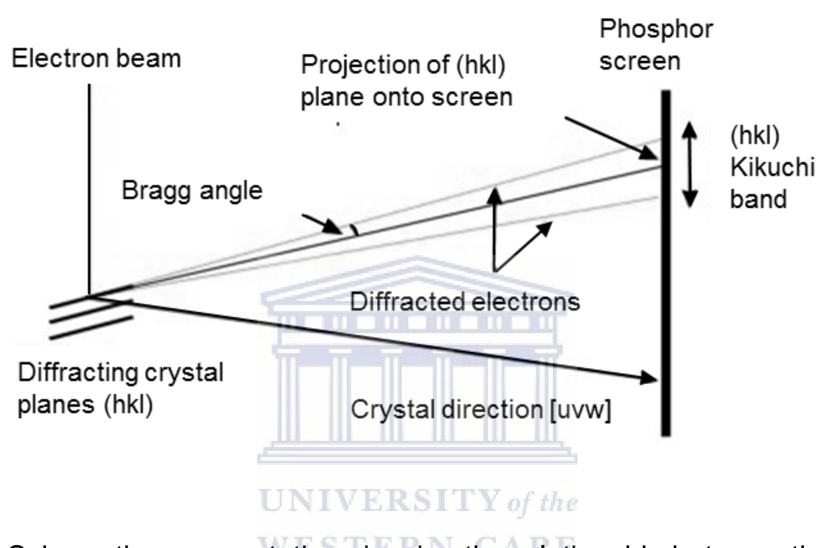

UNIVERSITY of the
WESTERN CAPE

Figure 2.3: Schematic representation showing the relationship between the EBSD pattern and the sample crystal structure adapted from [2.10].

However, the calculations necessary to determine the crystallographic information from the EBSD patterns are exhaustive. To simplify the calculation, the detected EBSD pattern is converted to a point. Specifically, the line composing the EBSD pattern is represented in image space by the formula for a straight line $y = mx + b$ which can be graphically plotted for each point (x, y) in the CCD image.

Instead of using (x, y) points to represent the line, the line in the image is converted to a point in the so-called Hough space represented by coordinates (ρ, θ) by:

$$\rho = x\cos\theta + y\sin\theta \tag{2.3}$$

with ρ being the distance to the line from the origin (0, 0) and θ the angle between ρ and the x-axis, as illustrated in Figure 2.4 [2.9, 2.10]. Effectively, the line on the CCD camera can be represented by a bright point in Hough space, which can be used to calculate the positions of the measured Kikuchi lines. Subsequently, by employing the system geometrical calibration, the angles between the planes producing the Kikuchi lines can be determined and compared to a set of pre-loaded patterns to assign the relevant Miller indices and determine the crystal orientation. This automated EBSD indexing and orientation process is summarized in Figure 2.5 [2.10].

UNIVERSITY of the
WESTERN CAPE

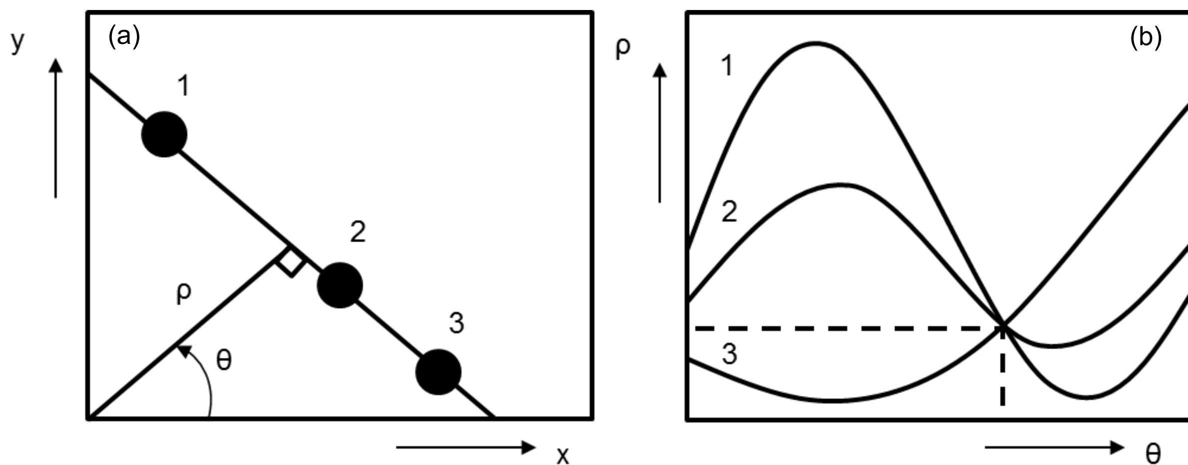

Figure 2.4: Transformation of (a) a line into (b) Hough space [2.9, 2.10].

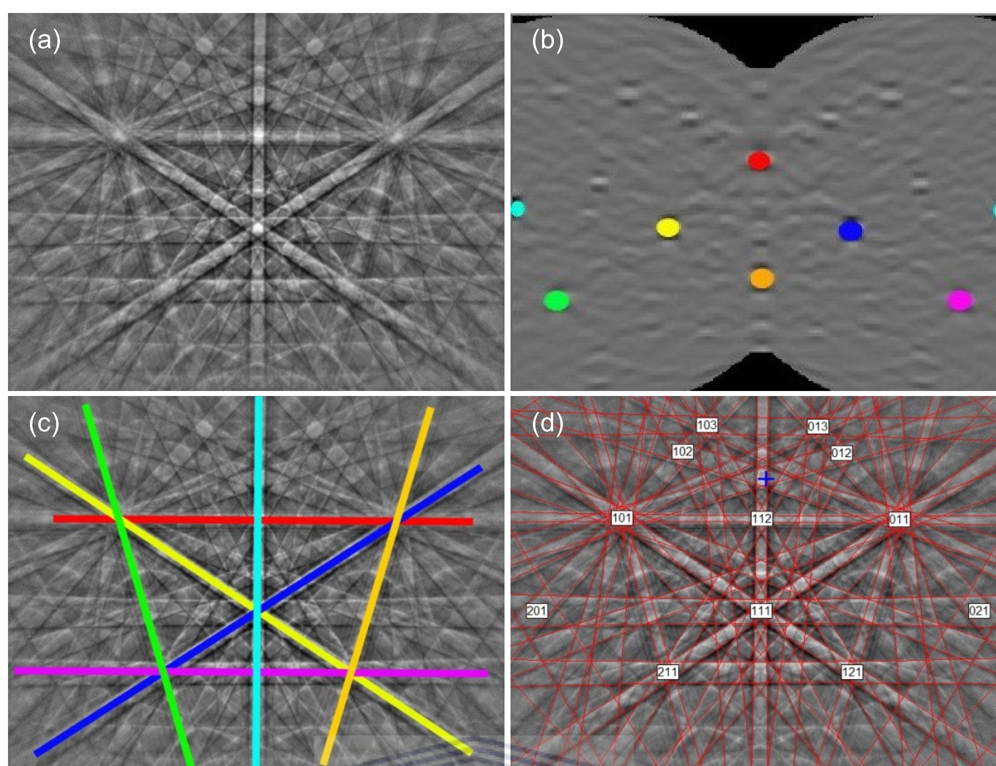

Figure 2.5: Process of finding the Kikuchi bands in the EBSD pattern using the Hough transformation taken from [2.10]: (a) Si diffraction pattern at 20 kV, (b) Hough transformation and colour coded identification of the pattern in (a), (c) peaks found in the Hough transform overlaid onto the original EBSD pattern and (d) indexed Si diffraction pattern.

EBSD is a surface technique, in that the pattern originates from the first 10 – 100 nm of the sample surface [2.8]. The electron beam profile within the sample has a narrower energy distribution when the sample is tilted. Specifically, the backscattered electrons that have lost a small fraction of their energy contribute to the EBSD pattern [2.8]. These electrons originate from the surface in close proximity to the incident electron beam, which means that EBSD has a spatial resolution directly related to the incident electron beam size.

The spatial resolution also depends on the material type and the electron beam acceleration voltage. The beam spread (interaction volume) is larger in low atomic number, less dense materials; this effect is enhanced as the acceleration voltage increases. As a result, the area from where the backscatter electrons originate enlarges, decreasing the resolution of EBSD for low atomic number materials at high beam energy. Nonetheless, EBSD resolutions of 30 nm in aluminium and 10 nm in brass were obtained at an acceleration voltage of 20 kV in a field-emission gun (FEG) SEM [2.11]. Isabell *et al.* [2.12] reported on EBSD resolutions in Ni of 100 and 50 nm at 20 and 10 kV, respectively.

UNIVERSITY of the
WESTERN CAPE

EBSD analysis was performed in a Zeiss LEO 1525 FEGSEM at 25 kV with the sample tilted 70° relative to the incident electron beam. The OXFORD INCA Crystal software was used to solve the characteristic EBSD patterns emanating from the sample. However, as extensive as the phase list is in the OXFORD INCA Crystal software is, there is a lack of tantalum silicides and nitrides. Fortunately, the software allows for the addition of new phases to the list. The information required for the addition of new phases is the space group number, unit cell parameters, atomic position of the elements and the atom occupancy, which are available in the ICDD database [2.7]. XRD was employed to validate the EBSD analysis performed on the aged Ta filaments used in this thesis.

2.2.3 Raman spectroscopy

The Raman effect occurs when photons in an intense laser beam are scattered inelastically by vibrating molecules. Subsequently, the photon undergoes a frequency shift equal to the frequency of a phonon that was either created (Stokes scattering) or annihilated (anti-Stokes) during the photon-molecule interaction.

The phonon density of states of nc-Si:H and SiN_x are reflected by the Raman spectrum. Within the wavenumber range of 100 to 1500 cm^{-1} the detected bands consists of the transverse optic (TO) mode of crystalline silicon centred at 520 cm^{-1}. Also present are the amorphous silicon modes consisting of the transverse acoustic (TA) at 150 cm^{-1}, longitudinal acoustic (LA) at 330 cm^{-1}, the longitudinal optic at 445 cm^{-1} and the TO at 480 cm^{-1}. As a result, Raman spectroscopy is a versatile analysis technique and has been used to analyse the short-range ordering of hydrogenated nanocrystalline and amorphous silicon thin films [2.13]. Raman spectroscopy can also be employed to identify Si-N bands, which occurs at 826 cm^{-1} and 730 cm^{-1} [2.14, 2.15].

Raman spectra were recorded in backscattering geometry with a spectral resolution of 0.4 cm^{-1}, using a Jobin-Yvon HR800 micro-Raman spectrometer operated at an excitation wavelength of 514.5 nm. Monocrystalline silicon was used to calibrate the spectrometer. The power of the Raman laser was kept below 5 mW to avoid laser induced crystallisation.

UNIVERSITY of the WESTERN CAPE

2.2.4 Atomic force microscopy

Atomic force microscopy (AFM) was used to measure the 3D surface morphologies of the SiN_x and nc-Si:H thin films. Topography 3D images of the films were collected using a Veeco NanoScope IV Multi-Mode AFM in tapping mode in air at room temperature with a tip size of ≈ 10 nm. Root mean square (RMS) values were then determined from the AFM software.

2.2.5 High-resolution transmission electron microscopy and electron energy loss spectroscopy

The need for the characterisation of materials at atomic resolution has increased with the advent of nanoscience within the last few decades. High-resolution transmission electron microscopy (HRTEM) involves the atomically resolved imaging and analysis of a thin sample using a high energy electron beam (100 to 300 keV).

UNIVERSITY of the
WESTERN CAPE

The high-resolution within an HRTEM is achieved based on the wave nature of electrons and corrections within the electron column to minimise lens aberrations. Consequently, HRTEM is a powerful technique that provides ultra-high resolution studies probing the defects, crystallography and elemental composition of well-prepared samples.

One of the advanced techniques accompanying modern HRTEM's is electron energy loss spectroscopy (EELS). During EELS a sample is irradiated with a high energy electron beam. The electrons that underwent inelastic scattering (loss of energy) with the atoms composing the sample contain information of the chemical composition and band structure of the sample.

HRTEM and EELS studies were performed in a JEOL ARM 200F TEM in scanning transmission electron microscopy mode at 200 kV. The Gatan Quantum GIF energy filter was used to acquire the EELS element maps at a collection angle of 41.7 mrad. Electron diffraction was performed in a FEI Tecnai F20 TEM at an acceleration voltage of 200 kV.

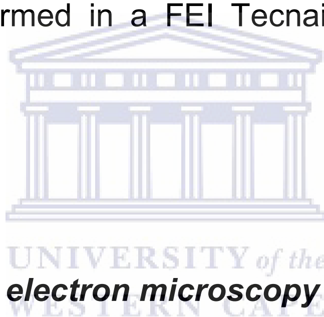

2.2.6 Scanning transmission electron microscopy

High-resolution analysis of thin film analysis within a SEM is limited to the interaction volume of the incident electron beam. However, the origin of the detected electrons may be decreased by reducing the thickness of the film. By placing an electron detector below the sample it becomes possible to perform scanning transmission electron microscopy (STEM) within the SEM by measuring the transmitted electrons. The internal structure of the thin films can then be analysed to obtain information relating to the porosity, crystallinity and phase contrast at high resolution within a FEGSEM.

A FEI Helios NanoLab 650 dual beam focus ion beam scanning electron microscope (FIBSEM) was used to prepare and image cross-sections of the films. The STEM analysis was performed in the Helios at an acceleration voltage of 30 kV.

2.2.7 Fourier-transform infrared spectroscopy

Fourier transformed infrared (FTIR) spectroscopy was used to determine and quantify the asymmetrical bonding configurations of SiN_x thin films on c-Si substrates. Table 2.1 summarises the generally accepted vibrational modes and corresponding absorption bands of typically observed in SiN_x and Si:H thin films [2.16, 2.17]. According to the Brodsky-Cardona-Cuomo (BCC) correction proposed by Brodsky *et al.* [2.18], the relationship between the transmission spectrum and the absorption coefficient α(ω) in the case where the refractive index of the Si:H film and the substrate are equal is given by:

UNIVERSITY of the WESTERN CAPE

$$T(\omega) = \frac{4T_0 e^{-\alpha_{BCC} d}}{[(1+T_0)^2 - (1-T_0)^2 e^{-2\alpha_{BCC} d}} \tag{2.4}$$

where d is the thickness of the SiN layer, T_0 the baseline transmission when α(ω) = 0; T_0 = 0.54 for crystalline Si. Maley [2.19] proposed correcting the BCC correction itself to eliminate the effect of coherent reflections in the Si:H films by:

$$\alpha_{TRUE} = \frac{\alpha_{BCC}}{1.72 - 12\omega d} \text{; for } \omega d \le 0.06 \quad \text{or} \quad \alpha_{TRUE} = \alpha_{BCC} \text{; for } \omega d > 0.06 \tag{2.5}$$

Table 2.1: Generally accepted assignments of Si-H, Si-N and N-H vibrational modes to absorption bands [2.16, 2.17].

Wavenumber (cm^{-1})	Vibrational mode
630	$Si\text{-}H_x$ rocking
845, 890	$(Si\text{-}H_2)_n$ bending
850	Si-N stretching
880	$Si\text{-}H_2$ bending
1200	N-H bending
2000	Si-H (isolated) stretching
2100	Si-H stretching
2070-2100	Si-H (on voids), $Si\text{-}H_2$, $(Si\text{-}H)_n$ stretching
2130	$Si\text{-}H_2$ stretching
3300	N-H stretching

UNIVERSITY of the
WESTERN CAPE

The integrated absorption at a specific bond X-Y is a measure of the amount of that specific bonding configuration. The bond density [X-Y] is determined by:

$$[X-Y] = A_{X-Y} \int \frac{\alpha(\omega)}{\omega} = A_{X-Y} I_{X-Y} \qquad (2.6)$$

where $A_{X\text{-}Y}$ is the FTIR proportionality factor and $I_{X\text{-}Y}$ the integrated absorption.

The bonding configuration of the SiN_x and nc-Si:H thin films were investigated using a Perkin Elmer fast-Fourier transformed infrared (FTIR) spectrometer at a spectral resolution of 1 cm^{-1}. A background spectrum was subtracted from a bare area of a c-Si (100) substrate.

2.3 COMPOSITION CHARACTERIZATION

2.3.1 X-ray photoelectron microscopy

X-ray photoelectron spectroscopy (XPS) is extensively used to interrogate the chemical composition of surfaces. Surface analysis using XPS involves irradiating a material with monochromatic soft X-rays, usually Al K_α (1486.7 eV) [2.20]. The X-rays interact with the surface atoms resulting in the emission of electrons via the photoelectron effect. The emitted photoelectrons have kinetic energies given by:

$$KE = h\nu - BE - \sigma_S \tag{2.7}$$

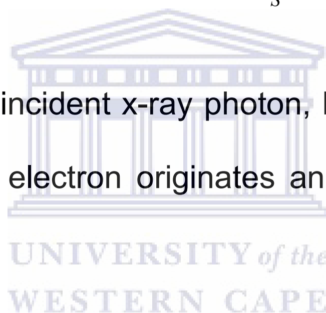

where hv is the energy of the incident x-ray photon, BE is the binding energy of the atomic orbital from which the electron originates and σ_S is the spectrometer work function.

The binding energy corresponds to the energy difference between initial and final states after the photoelectron has left the atom and is characteristic to each atom. Elemental quantification is performed using the area and height of the specific energy peaks.

Methods involving peak area sensitivity factors are typically more accurate and generally used. The number of atoms n of the element per cm^3 of the sample for homogenous sample is given by [2.20]:

$$n = {}^{I}\!\!\diagup_{f\sigma\theta y\lambda AT} \tag{2.8}$$

where I is the number of photoelectrons per second in a specific spectra peak, f is the x-ray flux in photons/cm^2/s, σ is the photoelectron cross-section for the specific atomic orbital in cm^2, θ is an angular efficiency factor of the detector based on the instrumental arrangement, y is the efficiency of the photoelectric process for the formation of the photoelectrons in the sample, A the area of the sample from which the photoelectrons are detected, λ is the electron mean free path of the photoelectrons in the sample and T is the electron detection efficiency for the electrons emitted from the sample. The denominator in equation (2.8) is known as the atomic sensitivity factor S. Reference values for S are dependent on the XPS system geometry and are pre-loaded on most modern systems.

UNIVERSITY of the
WESTERN CAPE

Accordingly, XPS analysis offers qualitative and quantitative chemical composition analysis of the surface. In some XPS systems, elemental depth profiling is possible. During automated depth profiling, argon ions are used to sputter a surface by removing atomic layers. XPS is then performed on the surface after each sputtering cycle, thereby providing the elemental composition within the sample.

XPS was performed in wide and narrow energy band scan modes on a PHI Quanta 2000 spectrometer using monochromatic $Al_{K\alpha}$ X-rays. Elemental concentration sputtering depth profiles were obtained via sputtering using Ar ions in the narrow scan mode.

2.3.2 Energy dispersive x-ray spectroscopy

Energy dispersive x-ray spectroscopy (EDS) has been developed into a quantitative technique widely used during electron microscopy. The EDS procedure consists of the generation, detection and quantification of a characteristic x-ray emitted from the sample. During the SEM analysis, electrons within the incident beam remove some of the sample's electrons that occupy different energy levels. The removal of one of the electrons from the energy shell results in an unstable atomic energy state. An electron from a neighbouring energy level fills the empty level which results in the emission of an x-ray with a characteristic energy. The emitted characteristic x-ray then allows for the identification of an element.

In practice only elements with an atomic number $Z > 4$ can be detected. Furthermore, the energy resolution of the EDS detector is currently between 125 to 135 eV, which results in the overlapping of some elements x-ray energy lines (e.g. Si and Ta/W). Also, as the generation of the x-rays occur throughout the interaction volume, quantifying the elemental concentration requires correction for matrix effects.

Briefly, the atomic number (Z), x-ray absorption (A) and fluorescence (F), collectively known as the ZAF correction factors, is widely used to determine the total matrix correction [2.8]. Modern EDS software packages come pre-loaded with standards (calculated from first-principles or fitted standards) that allows for the so-called “standardless quantification” of elemental composition from EDS.

EDS analysis was performed in a Zeiss LEO 1525 FEGSEM. The peak positions in the EDS spectra and beam stability were determined with a pure element standard using the OXFORD INCA EDS software.

2.3.3 Time-of-flight secondary ion mass spectroscopy

UNIVERSITY of the WESTERN CAPE

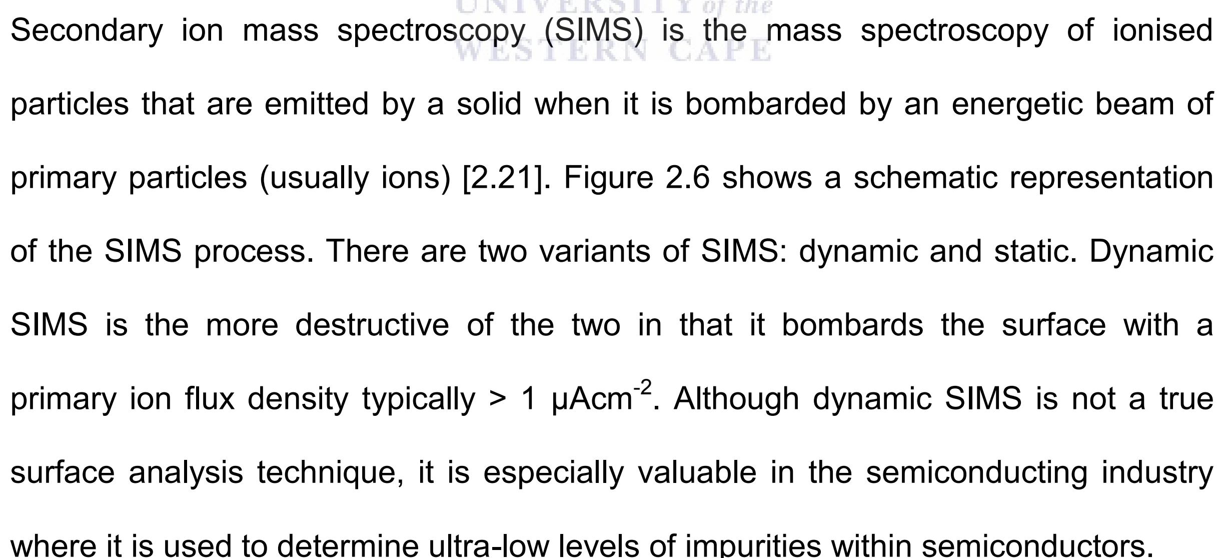

Secondary ion mass spectroscopy (SIMS) is the mass spectroscopy of ionised particles that are emitted by a solid when it is bombarded by an energetic beam of primary particles (usually ions) [2.21]. Figure 2.6 shows a schematic representation of the SIMS process. There are two variants of SIMS: dynamic and static. Dynamic SIMS is the more destructive of the two in that it bombards the surface with a primary ion flux density typically > 1 μAcm^{-2}. Although dynamic SIMS is not a true surface analysis technique, it is especially valuable in the semiconducting industry where it is used to determine ultra-low levels of impurities within semiconductors.

Static SIMS on the other hand involves bombarding the surface with a low particle flux density (< 1 nA cm^{-2}). The secondary ions emitted during static SIMS originate from the topmost atomic layer as most of the surface is only expected to be bombarded once by an incident particle during the analysis, i.e. the surface is essentially *static*.

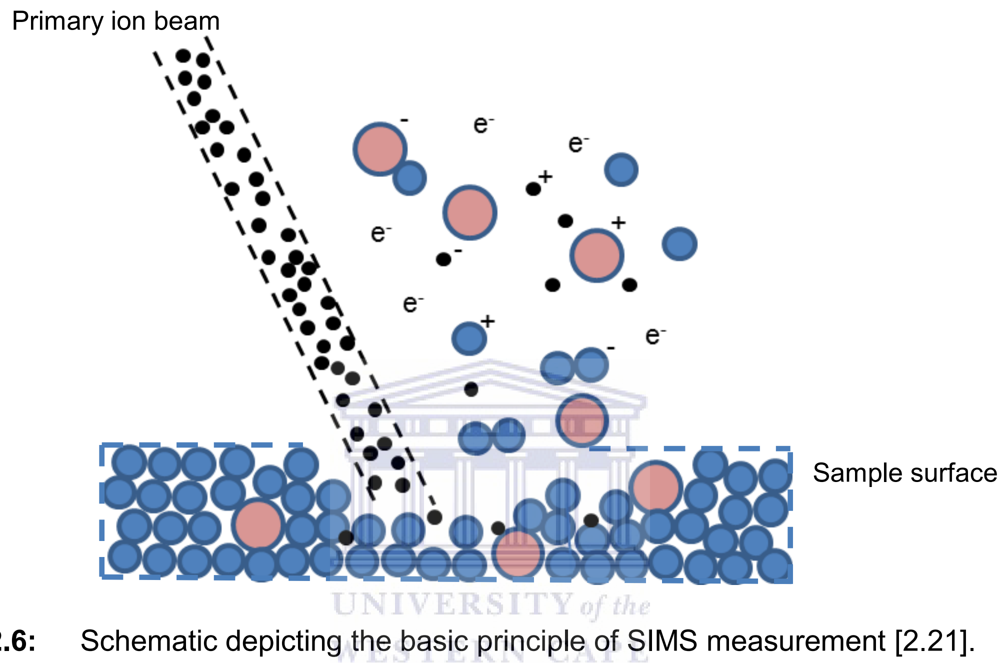

Figure 2.6: Schematic depicting the basic principle of SIMS measurement [2.21].

UNIVERSITY of the
WESTERN CAPE

A time-of-flight (TOF) instrument is one of the widely used mass analysers. However, TOF-SIMS suffers from sample matrix effects and is time consuming in depth profiling a surface on the micron level. Despite these drawbacks, TOF-SIMS has a superior sensitivity and unrivalled mass resolution capabilities in analysing the emitted secondary ions.

TOF-SIMS was performed on the aged filament (SiN_x deposition conditions) using an ionTOF ToF-SIMS[5] system. Elemental maps of the aged filaments were accumulated after sputtering the surface with oxygen ions.

2.3.4 Elastic recoil detection

Elastic recoil detection (ERD) is a technique used to determine the composition of light elements [2.22, 2.23]. Similar to Rutherford backscatter diffraction (RBS), ERD is based on the elastic collision between energetic ions and atoms within the sample. The difference is that during ERD the elements to be analysed are recoiled in a forward direction because of their inferior mass relative to the incident ion. Consider the following situation: a beam of projectiles with mass M_1, atomic number Z_1 at energy E_0 is incident upon a sample. The recoiled atom of mass M_2, atomic number Z_2, is scattered with energy E_2 at an angle Φ. This scenario is depicted in a schematic of the experiment in the laboratory reference frame shown in Figure 2.7.

UNIVERSITY of the
WESTERN CAPE

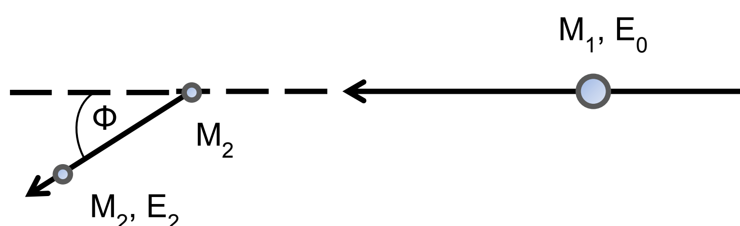

Figure 2.7: Schematic depicting the elastic collision between a projectile of mass M_1 at energy E_0, and the target mass M_2, which is initially at rest. After the collision, the target mass is scattered with an energy E_2 at a scattering angle Φ.

The energy of the recoiled atom can be related to the projectile energy by the kinematic factor, K, by [2.22, 2.23]:

$$E_2 = KE_0 \tag{2.9}$$

where;

$$K = \frac{4M_1 M_2}{\left(M_1 + M_2\right)} \cos^2 \Phi \tag{2.10}$$

From equation (2.10) it is clear that the kinematic factor K depends on the scattering angle Φ, the projectile mass M_1 and recoiled mass M_2. The recoiled mass can therefore be determined if the ratio E_2/E_0, the projectile mass and the scattering angle are known.

UNIVERSITY of the
WESTERN CAPE

The probability with which the elastic collision occurs is another important factor. The chance that one particle from the projectile beam ejects a recoil atom in such a way that it is recoiled in the direction of the detector is described by the Rutherford differential cross section, which is governed by columbic scattering.

The differential cross-section is given by [2.22, 2.23]:

$$\frac{d\sigma}{d\Omega} = \left(\frac{Z_1 Z_2 e^2 \left(1 + {M_1}/{M_2}\right)}{2E_0} \right)^2 \frac{1}{\cos^3 \Phi} \tag{2.11}$$

where Ω is the finite solid angle spanned by the detector, and e is the electron charge.

For a constant concentration of target atoms, the yield/number of detected particles is related to the number of target atoms/cm^2 by [2.22, 2.23]:

$$Y = Q\Omega N_S \int_0^{E_0} \frac{d\sigma}{d\Omega}(E,\Phi)\left(\frac{dE}{dx}\right)^{-1} dE \tag{2.12}$$

By employing a Mylar foil (15 μm thick) in-front of the detector all elements except for H are effectively prevented from reaching the detector. The total hydrogen content in the SiN_x films was then determined using ERD analysis at the Materials Research Group at iThemba Labs in Faure, South Africa. ERD was performed using 3 MeV He^{2+} ions generated by a Van de Graaff generator. A Kapton reference material (coated with ~ 1 Å Pt) was used for energy and geometry calibration.

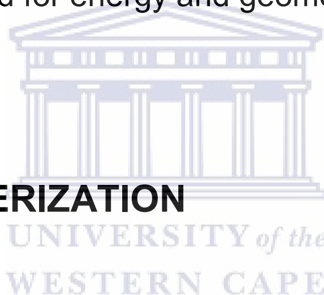

2.4 OPTICAL CHARACTERIZATION

The optical properties of the nc-Si:H and the SiN_x thin films were determined from reflection and transmission measurements in the range 1.4 – 6.2 eV. The optical constants (refractive index, thickness, absorption coefficient and extinction coefficient) were extracted from UV-VIS reflection and transmission spectra by employing the Bruggeman Effective Medium Approximation (BEMA) [2.24] using the Scout program [2.25].

The absorption coefficient at different photon energies E, α (E) was calculated from the imaginary part of the complex refractive index $\boldsymbol{n} = n + ik$ by:

$$\alpha(E) = \frac{4\pi k(E)}{\lambda} \qquad (2.13)$$

where λ is the wavelength of the incident radiation and k the extinction coefficient. The optical band gap E_g can be estimated from the real part of the refractive index n(E) and α(E) by the following relation:

$$[\alpha(E)n(E)E]^{1/(1+p+q)} = B_g(E - E_g) \qquad (2.14)$$

where B_g is a constant. The parameters p and q describe the density of states (DOS) distribution of the band edges. If the DOS distribution is taken to be parabolic in both the valence and conduction band, i.e. p = q = ½, then equation (13) describes the Tauc plot [2.26]. The Tauc band gap E_{TAUC} is then determined by extrapolating $[\alpha(E)n(E)E]^{1/2}$ versus E to α(E) = 0 for α(E) ≥ 10^3 cm^{-1}. Figure 2.8 shows Tauc plots of typical SiN_x samples with different-contents.

UNIVERSITY of the
WESTERN CAPE

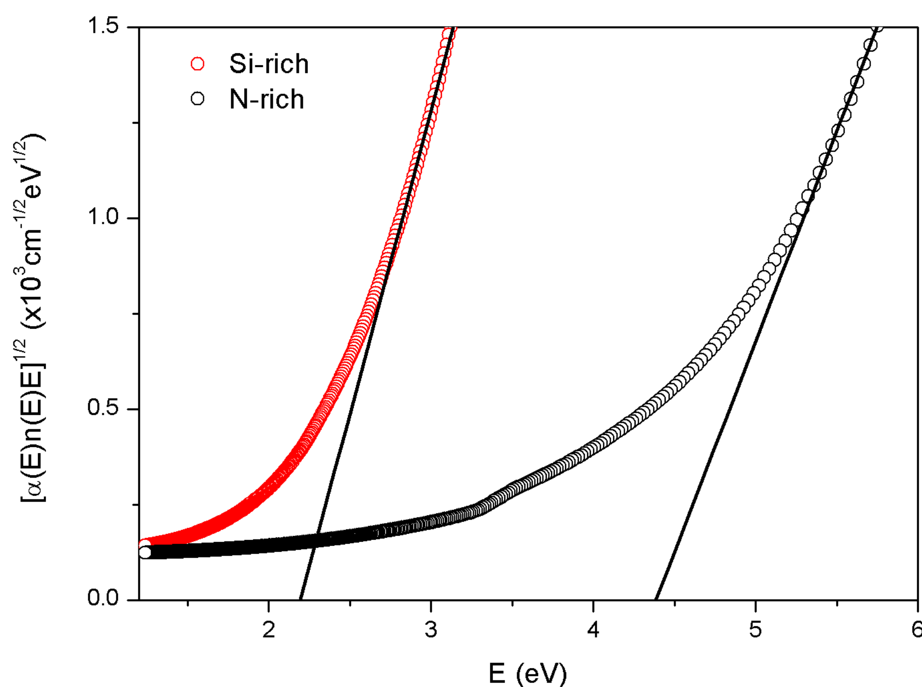

Figure 2.8: Examples of estimating the optical band gap from the Tauc plot for typically silicon-rich and nitrogen rich SiN_x samples.

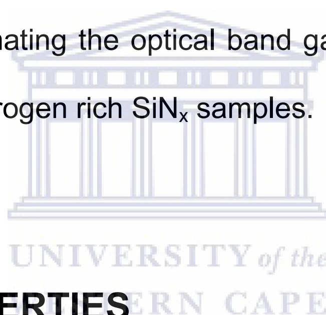
UNIVERSITY of the WESTERN CAPE

2.5 MECHANICAL PROPERTIES

2.5.1 Film Stress measurement

The total film stress (σ_{TOTAL}) is assessed from curvature measurements on Corning substrates with and without a thin film by using Stoney's equation [2.27]:

$$\sigma_{TOTAL} = \frac{1}{6}\left(\frac{1}{R_1} - \frac{1}{R_0}\right)\frac{E_S}{1-\upsilon_S}\frac{t_S^2}{t_F} \qquad (2.15)$$

where: R_1 and R_0 is the radius of curvature the Corning substrate after and before the deposition, respectively, E_S the Young's modulus and v_S the Poisson's ratio of the Corning substrate, t_S and t_f the thickness of the substrate and film, respectively.

Curvature measurements were performed along 10 line scans (horizontally and vertically) spaced ~ 2mm on the Corning substrate (film side-up) using the Taylor profilometer at the National Metrology Institute of South Africa (NMISA). The total film stress is the sum of the intrinsic film stress (σ_i) and thermal stress (σ_T) components. The thermal stress is determined by:

$$\sigma_T = \frac{E_f}{1-\nu_f}\left(a_S - a_f\right)\left(\Delta T\right) \qquad (2.16)$$

where E_f, v_f and α_f correspond to the film Young's modulus, Poisson ratio and thermal expansion coefficient, respectively and ΔT is the difference between the substrate and room temperature.

2.5.2 Vickers microhardness measurement

UNIVERSITY of the
WESTERN CAPE

Microhardness test encompasses the routine determination of hardness from indentations made by diamond tips with loads that do not exceed 1 kg [2.28]. Specifically, the hardness is measured by determining the dimensions of the resulting indentation with a microscope and using conversion tables in accordance to international standards. Vickers microhardness measurements were carried out using a FM-700 Microhardness Tester. Indentations were performed at loads in the range 0.05 to 0.1 kg and a dwell time of 10 s.

REFERENCES

2.1 C.J. Arendse (1999), **Thermal Stability and Defect Structure of Hot-wire Deposited Amorphous Silicon**, PhD thesis, University of the Western Cape, Bellville, South Africa.

2.2 H.P. Klug & L.E. Alexander (1974), **X-Ray Diffraction Procedures for Polycrystalline and Amorphous Materials** (2nd edition), Wiley-Interscience Publication, New York.

2.3 A. H. Mahan, A. C. Dillon, L. M. Gedvilas, D. L. Williamson, J. D. Perkins (2003) J. Appl. Phys. **94**:2360.

2.4 C. J. Oliphant, C. J. Arendse, D. Knoesen, T. F. G. Muller, S. Prins, G. Malgas (2011) Thin Solid Films **519**:4437.

2.5 M. Härting, S. Woodford, D. Knoesen, R. Bucher, D. T. Britton (2003) Thin Solid Films **430**:153.

2.6 C. J. Oliphant, C. J. Arendse, S. N. Prins, D. Knoesen, G. Malgas (2012) Journal of Materials Science 47: 2405.

2.7 International Centre For Diffraction Data (2011) PDF-4^{+} (Version 4.1102) [software], Pennsylvania {www.icdd.com}.

2.8 J. Goldstein, D. Newbury, D. Joy, C. Lyman, P. Echlin, E. Lifshin, L. Sawyer & J. Michael (2003), **Scanning Electron Microscopy and X-ray Microanalysis** (3rd edition), Kluwer Academic / Plenum Publishers, New York.

2.9 A. J. Schwartz, M. Kumar, B. L. Adams & D. P. Field (eds.) (2009), **Electron Backscatter Diffraction in Materials Science** (2nd edition) Kluwer Academic / Plenum Publishers, New York.

UNIVERSITY of the WESTERN CAPE

2.10 Oxford Instruments, Electron Backscatter Diffraction Analysis-Educational Website, last accessed on 15 August 2012, {www.ebsd.com}.

2.11 F. J. Humphreys, Y. Huang, I. Brough, C. Harris (1999) Journal of Microscopy **195**:212.

2.12 T. C. Isabell, V. P. Dravid (1997) Ultramicroscopy **67**:59.

2.13 A. H. Mahan, R. Biswas, L. M. Gedvilas, D. L. Williamson, B. C. Pan (2004) J. Appl. Phys. **96**:3818.

2.14 L. V. Mercaldo, E. M. Esposito, P. D. Veneri, G. Fameli, S. Mirabella, G. Nicotra (2010) Appl. Phys. Lett. **97**:153112.

2.15 J. Bandet, B. Despax, M. Caumont (1999) J. Appl. Phys. **85**:7899.

2.16 E. Bustarret, M. Bensouda, M. C. Habrard, J. C. Bruyère, S. Poulin, S. C. Gujrathi (1988) Phys. Rev. B **38**:8171.

2.17 R. A. Street (1991) **Hydrogenated Amorphous Silicon**, Cambridge University Press, New York.

2.18 M. H. Brodsky, M. Cardona, J. J. Cuomo (1977) Phys. Rev. B **16**:3556.

2.19 N. Maley (1992) Phys. Rev. B **46**:2078.

2.20 J. F. Moulder, W. F. Stickle, P. E. Sobol & K. D. Bomben (1995), **Handbook of X-ray Photoelectron Spectroscopy**, Physical Electronics, Inc., Minnesota.

2.21 J. Vickerman (ed.) (1997), **Surface Analysis**, John Wiley and Sons, Sussex.

2.22 L. C. Feldman & J. W. Mayer (1986), **Fundamentals of Surface and Thin Film Analysis**, North-Holland Publ., Amsterdam.

2.23 J. R. Tesmer, M. Nastasi, J. C. Barbour, C. J. Maggiore & J. W. Mayer (1995), **Handbook of Modern Ion Beam Materials Analysis**, Pittsburgh, Pennsylvania.

UNIVERSITY of the WESTERN CAPE

2.24 D.A.G. Bruggeman (1935) Ann. Phys. **24**:636.

2.25 W. Theiss, W. Theiss Hard-and Software-Scout Product, last accessed on 15 August 2012 {www.mtheiss.com}.

2.26 J. Tauc (1972), **Optical Properties of Solids**, F. Abeles (ed.), North-Holland Publ., Amsterdam.

2.27 G. G. Stoney (1909) Proc. R. Soc. Lond. A **82**:172.

2.28 Harry Chandler (ed.) (1999), **Hardness Testing** (2nd edition), ASM International, Ohio.

CHAPTER 3

STRUCTURAL EVOLUTION OF A Ta-FILAMENT DURING HOT-WIRE CHEMICAL VAPOUR DEPOSITION OF SILICON INVESTIGATED BY ELECTRON BACKSCATTER DIFFRACTION

ABSTRACT

We report on the application of electron backscatter diffraction to investigate the structural changes of a tantalum filament operated at typical hot-wire chemical vapour deposition conditions for the synthesis of hydrogenated nanocrystalline silicon. Various tantalum-silicides, identified by electron backscatter diffraction, form preferentially along the length of the filament. The filament has a recrystallized Ta inner core and a $TaSi_2$ *layer encapsulated with a Si layer at the cooler ends. The α-*Ta_5Si_3*, metastable* Ta_5Si_3 *and* Ta_2Si *phases formed in addition to recrystallized Ta and* $TaSi_2$ *at the centre regions. Cracks and porosity were prevalent throughout the length of the filament. Hardness measurements revealed that the recrystallized Ta core adds durability, whereas the silicides were harder but less tough. The microstructural evolution of the aged tantalum filament can be ascribed to the thermal gradient along the filament length, recrystallization of Ta and the variation of silicon content within the filament.*

UNIVERSITY of the WESTERN CAPE

3.1 INTRODUCTION

The hot-wire chemical vapour deposition (HWCVD) technique has shown promise as a viable route for the synthesis of device quality silicon thin films at high growth rates without reducing the film quality [3.1]. However, one of the main concerns facing HWCVD is filament ageing, i.e. the reaction between the heated metallic filament (usually Ta or W) and the process gas mixture, which results in the formation of various silicides, cracks along the filament length, and in some cases solid Si deposition [3.2-3.5]. These structural changes lead to unstable deposition conditions and a reduced filament operational lifetime.

Despite the remarkable progress in minimizing the influences of filament ageing on its operational lifetime via pre- and post-deposition treatments with hydrogen [3.4] and in vacuum [3.5], and RF and DC heating [3.2], there still exists a need to further interrogate the filament ageing process, especially at hydrogenated nanocrystalline silicon (nc-Si:H) deposition conditions. To date, the techniques used to characterize filament ageing have been limited to mostly x-ray diffraction (XRD), scanning electron microscopy (SEM), optical microscopy and in-situ resistance/temperature curves. However, in the case of characterization of tantalum-silicides by energy dispersive x-ray spectroscopy (EDS); there is an overlap of the $Ta_{M\alpha}$ and $Si_{K\alpha}$ peaks, which poses a risk of an incorrect determination of the elemental composition. In this contribution we will show how electron backscatter diffraction (EBSD) can be used to overcome the current limitations of EDS of tantalum and its silicides due to its inherent ability to discern between the crystallography of different phases. XRD and SEM analysis will be used to validate the EBSD results.

UNIVERSITY of the
WESTERN CAPE

3.2 EXPERIMENTAL DETAILS

A Ta-filament with a diameter of ~ 250 μm and length ~ 1 m was used to synthesize nc-Si:H thin films at a temperature of 1600 °C using an MVSystems HWCVD reactor described elsewhere [3.6]. Prior to and after each deposition run, a standard 30 sccm H_2 gas treatment process was performed for 5 minutes [3.4]. The deposition pressure, substrate temperature, silane flow rate and hydrogen flow rate were fixed to 60 μbar, 200 °C, 1.5 sccm and 27.5 sccm, respectively. After failure/ burnout, which occurred after 15 one-hour deposition runs, the Ta-filament was carefully removed from the HWCVD reactor in order to limit any mechanical disturbances. Multiple regions were cut off along the length of the filament. Representative cross-sections of the aged Ta-filaments were metallographically prepared from the centre and cooler end (electrical contact) regions using fine grinding discs, polishing and then final polishing by means of ~ 40 nm colloidal silica suspension.

UNIVERSITY of the
WESTERN CAPE

The microstructure of the cross-sections were analysed using a LEO 1525 field-emission gun scanning electron microscope (FEGSEM). Backscatter and forward scatter electron images were accumulated to distinguish the phases present. EBSD analysis was performed at 25 kV with the sample tilted to 70° relative to the incident electron beam. The OXFORD INCA Crystal software was used to solve the characteristic Kikuchi patterns emanating from the sample, thereby allowing for the identification of the different phases present. The filament was also crushed along different sections for XRD studies. XRD patterns were collected in reflection geometry at 2θ-values ranging from 10 – 90° with a step size of 0.02°, using a PANalytical XPert diffractometer operating at 45 kV and 40 mA. Copper K_α radiation

with a wavelength of 1.5406 Å was used as the X-ray source. The XRD patterns were indexed using the database maintained by the International Centre for Diffraction Data (ICDD) [3.7]. Vickers hardness measurements were carried out using a FM-700 Microhardness Tester. Indentations were performed at a load of 0.1 kg and a dwell time of 10 s.

3.3 RESULTS AND DISCUSSION

Figure 3.1 shows a forescatter image of the cross-section of the pure Ta-filament prior to the deposition. The different regions of contrast are a result of the orientation of the Ta grains with respect to the electron beam, illustrated by the corresponding EBSD grain orientation map in Figure 3.1b. The dark region in Figure 3.1b corresponds to the resin where no diffraction by Ta occurred.

UNIVERSITY of the
WESTERN CAPE

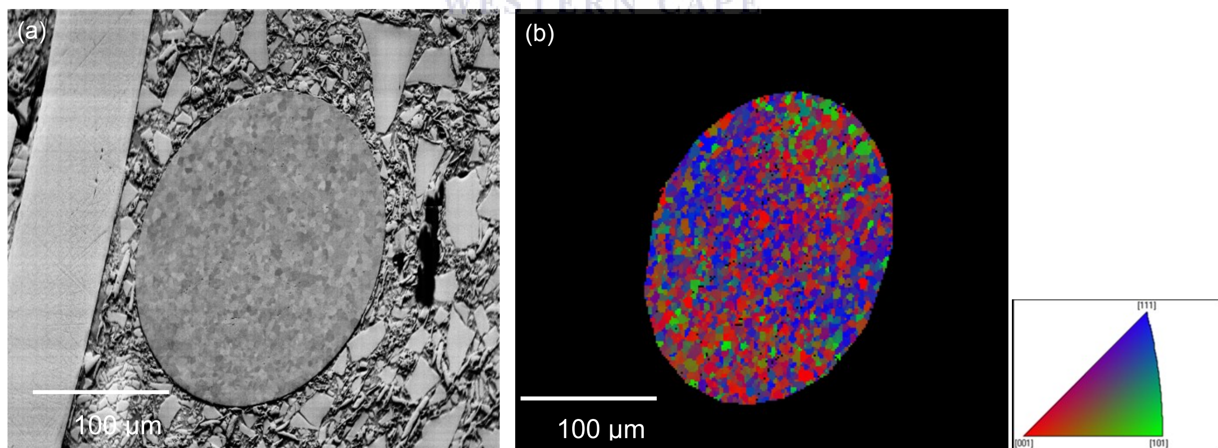

Figure 3.1: (a) Forescatter micrograph of the pure Ta-filament and (b) its corresponding EBSD grain map with orientation key.

Figure 3.2 shows a secondary electron micrograph of the aged filament-surface. A surface layer composed of pure Si is present, as concluded by EDS analysis with the absence of the $Ta_{L\alpha}$ peaks. Figure 3.3 shows a backscatter electron micrograph of the cross-section of the aged filament sampled from the ends. The filament diameter increased by ~ 100 μm and its morphology changed drastically with a 200 μm-thick silicide layer, encapsulating a predominately Ta inner core of diameter ~ 180 μm. Cracks appear within the silicide layer that extends throughout the length of the filament and it contains a porous structure (~50 μm thick) at its outer perimeter. It should also be noted that severe crack formation is absent from the inner core of the filament.

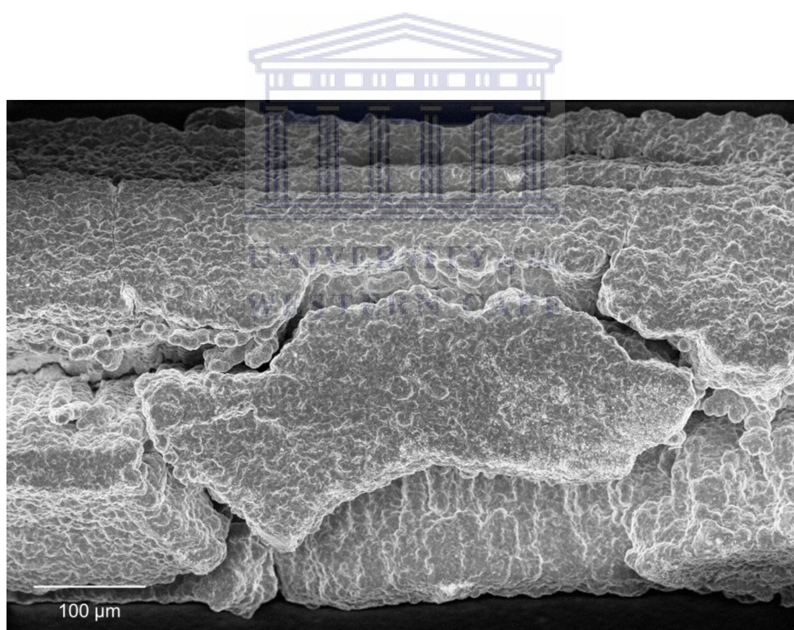

Figure 3.2: Secondary electron micrograph of the filament-surface sampled from the ends.

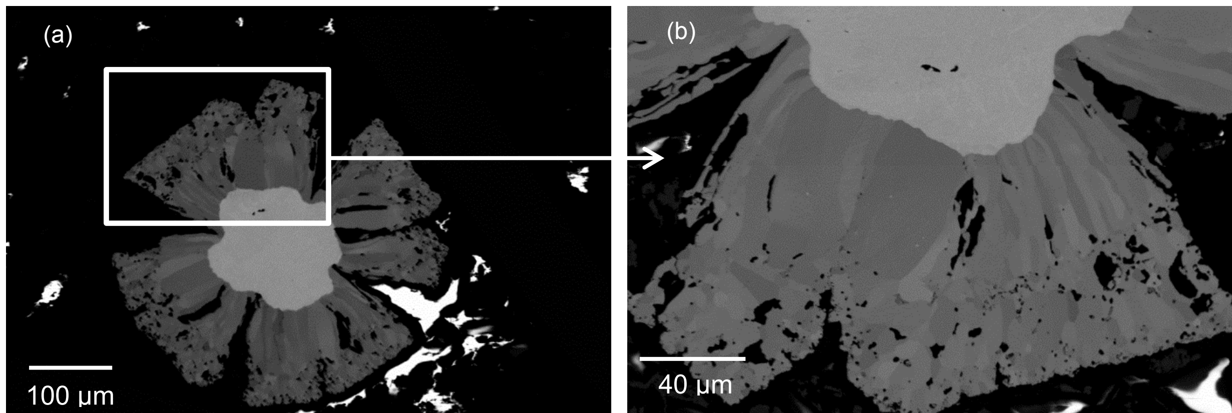

Figure 3.3: (a) Backscatter electron micrograph of the filament cross-section sampled from the ends and (b) higher magnification micrograph.

UNIVERSITY of the
WESTERN CAPE

Figure 3.3b reveals that regions of contrast exist within the silicide layer, which increases in length moving from the outer perimeter radially inwardly. EDS analysis of Si and Ta is difficult considering the overlap of the $Si_{K\alpha}$ and $Ta_{M\alpha}$ peaks, given the difference in their characteristic X-ray energy of only 30.2 eV, which is less than the detector resolution of 138 eV. Therefore it is not possible to conclude from our current EDS system if the contrast in the backscatter micrograph is caused by differences in elemental composition.

EBSD phase maps of the aged filament's cross-section sampled from the ends are presented in Figure 3.4. The phase maps show that a $TaSi_2$ layer encapsulates a Ta inner core. EBSD also reveals that there is an outer Si shell enclosing the filament. The average grain size of the $TaSi_2$ phase increases inwardly from the perimeter as shown in Figure 3.5. These grains are also orientated differently (inset) with respect to the electron beam, which causes the contrast differences within the silicide layer observed in Figure 3.3b.

On the other hand, EBSD reveals that there appears to be a preferential orientation developing radially inward. Figure 3.6 discloses that the inner core is composed of recrystallized Ta grains. This is most likely the origin of the enhancement of the grain size and preferential orientation of the $TaSi_2$ phase radially inward. EBSD therefore compensates for the limited analysis capabilities of EDS for tantalum-silicides, due to its ability to discern the crystallographic structure of the aged filament.

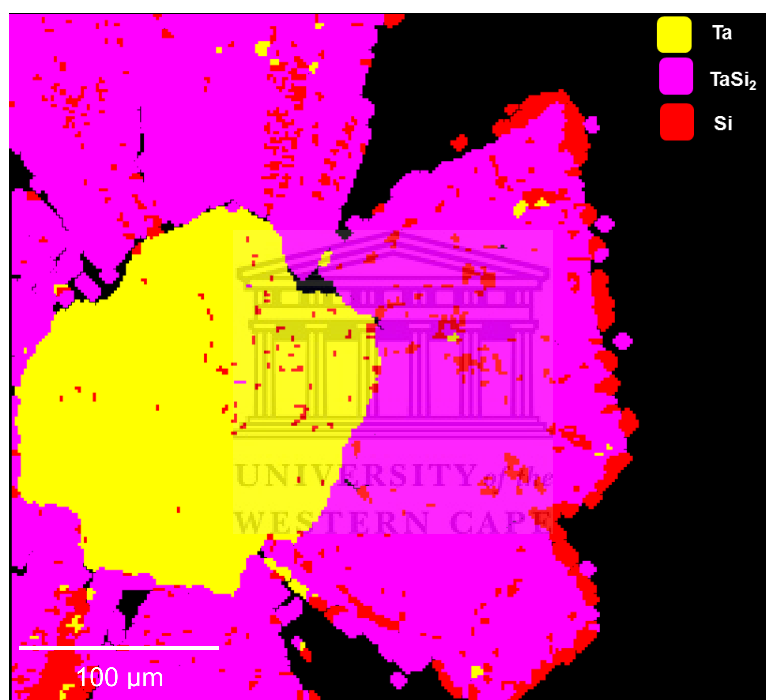

Figure 3.4: EBSD phase map of the filament cross-section sampled from the ends.

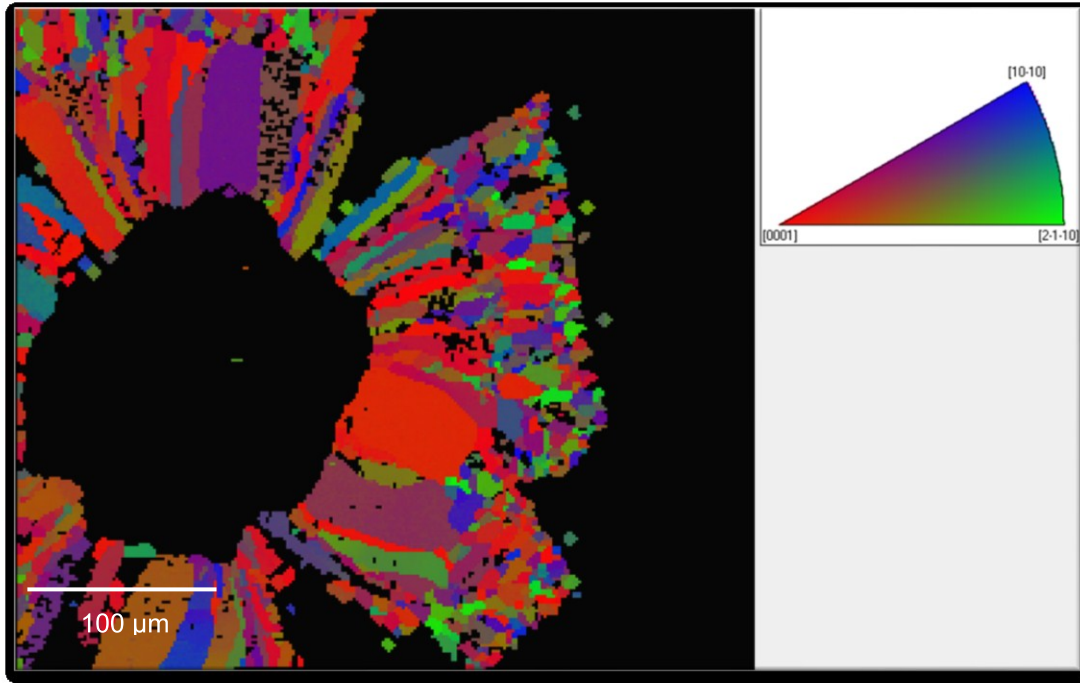

Figure 3.5: $TaSi_2$ grain map with orientation key.

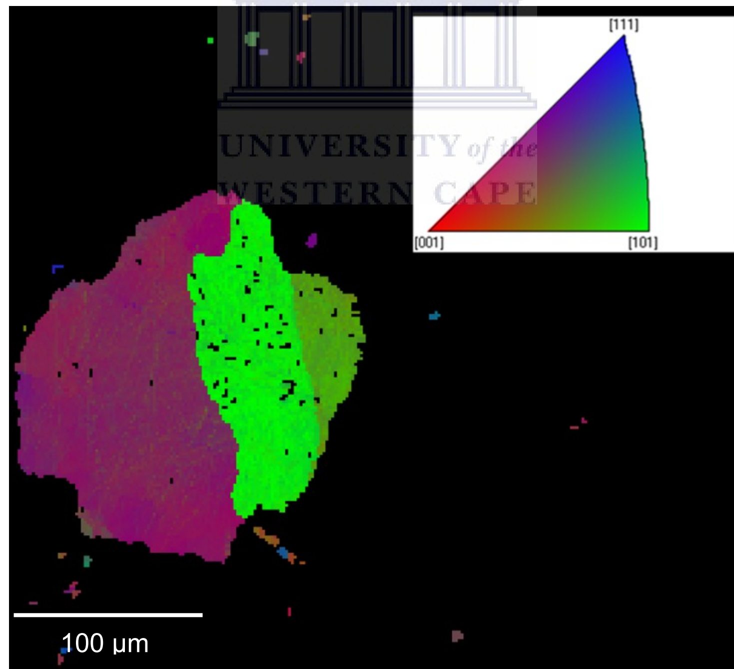

Figure 3.6: Ta grain orientation map from the end regions with orientation key.

UNIVERSITY of the
WESTERN CAPE

Figure 3.7 presents secondary electron micrographs of the filament-surface sampled from the centre regions. Noticeable is the porous and cracked structure of the aged filament. Figure 3.8 shows a backscatter electron micrograph of the aged filament's cross-section sampled from the centre region. The filament diameter increased by ~ 50 μm, a minor increase compared to the cooler ends. Cracks and a ~ 60 μm-thick porous structure are present, similar to the end regions. However, the porosity is enhanced and there appears to be 5 regions of different contrast as shown in Figure 3.8b. The diameter of the aged filament increased by ~ 33% and ~ 17% at the ends and the centre regions, respectively. This is attributed to the inferior Si evaporation rate at the cooler ends compared to the hotter centre region, thereby resulting in more Si incorporation and consequently thicker silicide layers at the ends. Again, due to the inability of EDS to discern between Ta and Si, it is impossible to accurately identify the regions of contrast observed by SEM of the aged filaments.

UNIVERSITY of the
WESTERN CAPE

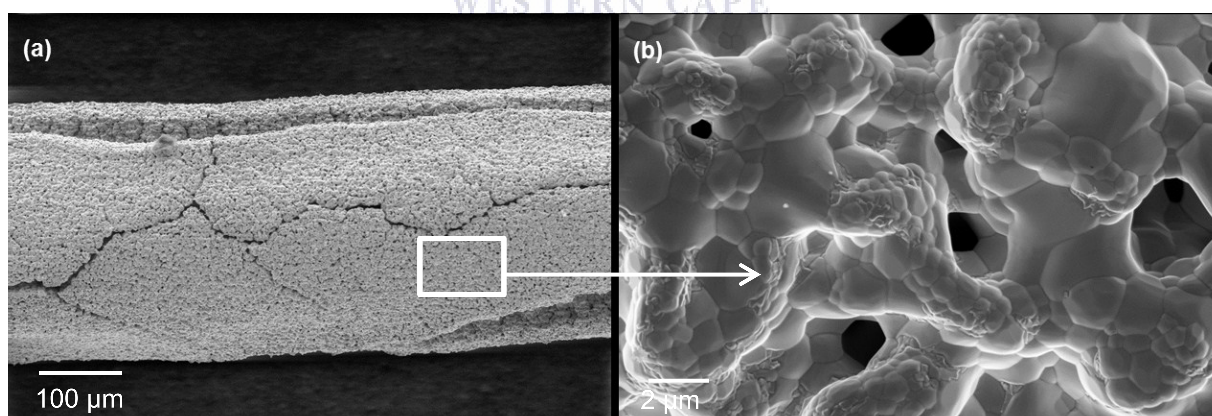

Figure 3.7: (a) Secondary electron micrograph of the filament-surface sampled from the centre regions and (b) higher magnification micrograph.

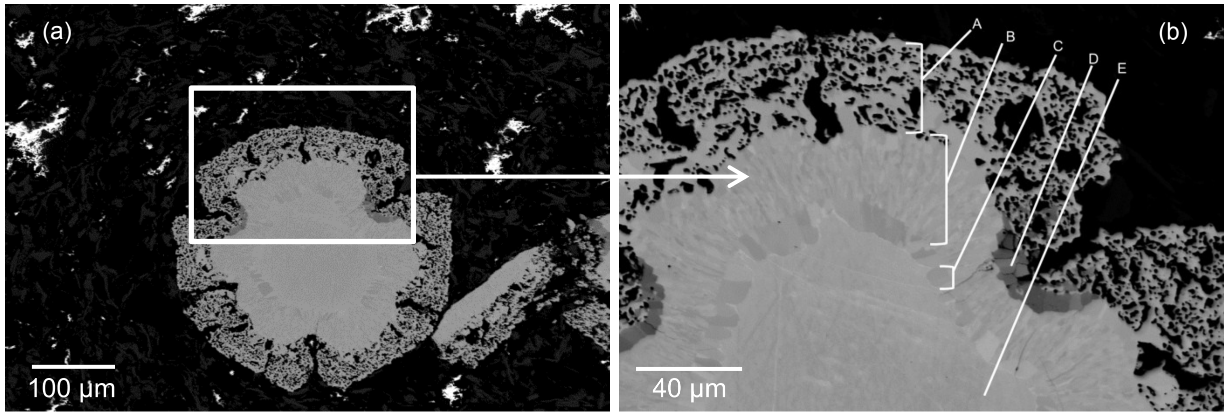

Figure 3.8: (a) Backscatter electron micrograph of the filament cross-section sampled from the centre region and (b) higher magnification micrograph revealing the different regions of contrast and structure

UNIVERSITY of the
WESTERN CAPE

An EBSD phase map of the aged filament's cross-section sampled from the centre region is shown in Figure 3.9. Complementary to the backscatter images (Figure 3.8), the $TaSi_2$, Ta_5Si_3, αTa_5Si_3, Ta_2Si and Ta phases are identified and their crystallographic information is summarized in Table 1 [3.8]. It must be noted that previous microscopy studies revealed the existence of silicide layers [3.5], but were unable to accurately identify the phases. However, EBSD identifies and isolates the location of these silicides that have eluded investigations thus far. The reduction of the Si constituent within the silicides from the perimeter radially inward does however confirm earlier reports [3.4].

In contrast to the end regions, the grain size and preferential orientation at the centre region do not enhance radially inward as illustrated in Figure 3.10, despite the fact that the Ta core is recrystallized as depicted in Figure 3.11. We ascribe this behaviour to the superior Si diffusion rate within the filament, due to the higher temperature at the centre. Consequently, silicidation occurs faster than the recrystallization/growth of Ta grains. Nevertheless, the concentration of Si available for silicidation is superior at the ends compared to the centre regions; the reason being the presence of Ta rich silicides at the latter. It is the inferior temperature and/or Si rich silicides at the end regions that hamper the in-diffusion of Si, consequently resulting in an inferior silicidation rate compared to the Ta recrystallization/ growth rate thereby providing increasing Ta grain sizes for silicidation radially inward.

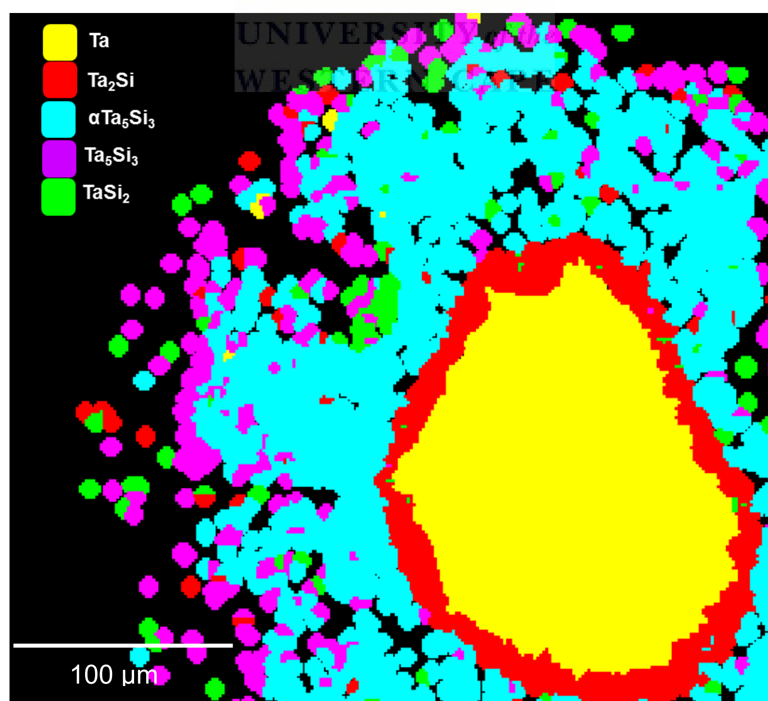

Figure 3.9: EBSD phase map of the filament cross-section shown in Figure 3.8.

Table 3.1: Ta-Si crystal structure data

Phase	Space group	Prototype
Ta	$Im\bar{3}m$	W
Ta_2Si	I4/m	Al_2Cu
α-Ta_5Si_3	I4/mcm	Cr_5B_3
Ta_5Si_3 (metastable)	P63/mcm	Mn_5Si_3
$TaSi_2$	P6222	$CrSi_2$
Si	Fd3m	C (diamond)

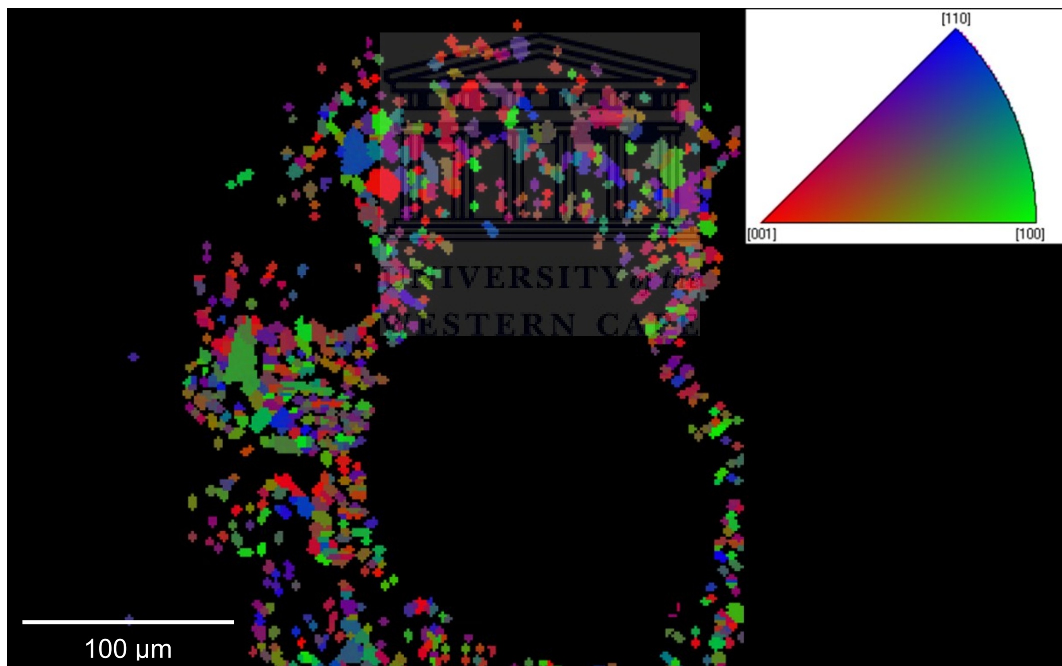

Figure 3.10: Grain orientation map of the α-Ta_5Si_3 phase.

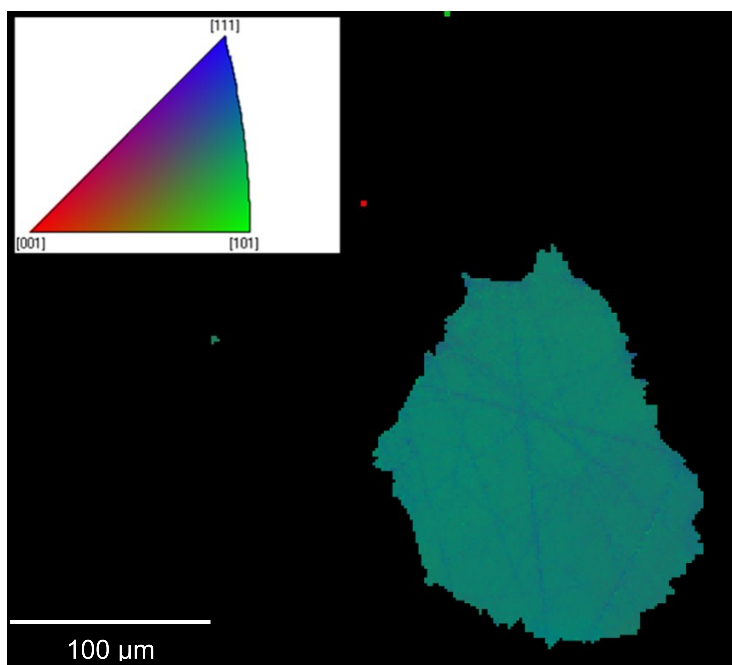

Figure 3.11: Grain orientation map of the Ta inner core at the centre regions of the filament.

UNIVERSITY of the
WESTERN CAPE

Figure 3.12 compares the XRD patterns recorded on the pure Ta-filament and the crushed ageing Ta-filaments. The XRD results complement the SEM and EBSD results by disclosing that the pure Ta-filament transforms into various silicides, depending on the region of the filament itself. At the ends Ta, Si and $TaSi_2$ were detected, while more Ta-rich phases exist at the filament centre. Moreover, the intensities of the $Ta_{(200)}$ and $Ta_{(211)}$ peaks decreased giving way to a preferential $Ta_{(110)}$ and $Ta_{(220)}$ (~ 2θ = 38.5° and 82.4°, respectively) orientation, confirming the EBSD observation of the recrystallization of Ta. van der Werf et al. [3.5] reported in their XRD analysis on the formation of the Ta_5Si_3 phase with no observations of Ta peaks, despite SEM clearly showing a Ta-inner core with multiple silicide layers. We believe that to properly exploit XRD phase analysis it must be performed on crushed aged filaments.

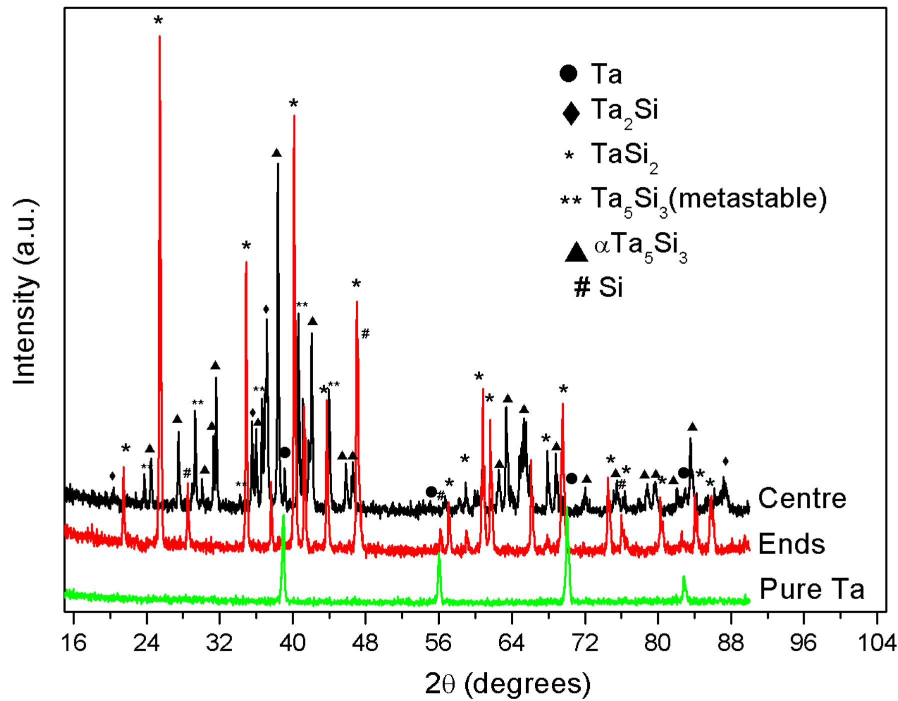

Figure 3.12: XRD patterns of the pure Ta-filament and the crushed aged Ta-filaments.

UNIVERSITY of the
WESTERN CAPE

Vickers hardness measurements were performed on the cross-sections of the filament. The calculated hardness values are based on the average of three measurements and a standard deviation of ~ 15 %; the values are reported in Table 2. We believe that the difference in our hardness value for the metastable Ta_5Si_3 phase may be related to its porous structure. The hardness of the Ta phase enhanced from 1.079 GPa (pure) to 2.354 GPa (aged) in both the centre and ends regions. Additionally, Figure 3.13 shows that no noticeable cracks emanated from the indentations on the Ta core, in contrast to the multiple cracks observed from the indentations on the silicides. This indicates that the Ta core is tougher than the silicides [3.9]. The presence of the recrystallized Ta therefore adds durability during synthesis at operational temperatures where sagging is usually observed.

However, it may be detrimental to the filament lifetime when the filament temperature is ramped-up to operational conditions or as the filament is cooled down to room temperature due to the different mechanical strengths and ductility of Ta and its silicides.

Table 3.2: Hardness values of the filament compared to literature (where available).

Phase	Hardness (GPa)	Literature (GPa)
Ta (pure filament)	1.079	0.9 [3.10]
Ta (recrystallized)	2.354	1.96 [3.10]
Ta_2Si	10.290	-
α-Ta_5Si_3	16.200	11.77 [3.11]
Ta_5Si_3 (metastable)	1.961	11.77-14.71 [3.10]
$TaSi_2$	9.268	9.2 [3.12]

UNIVERSITY of the
WESTERN CAPE

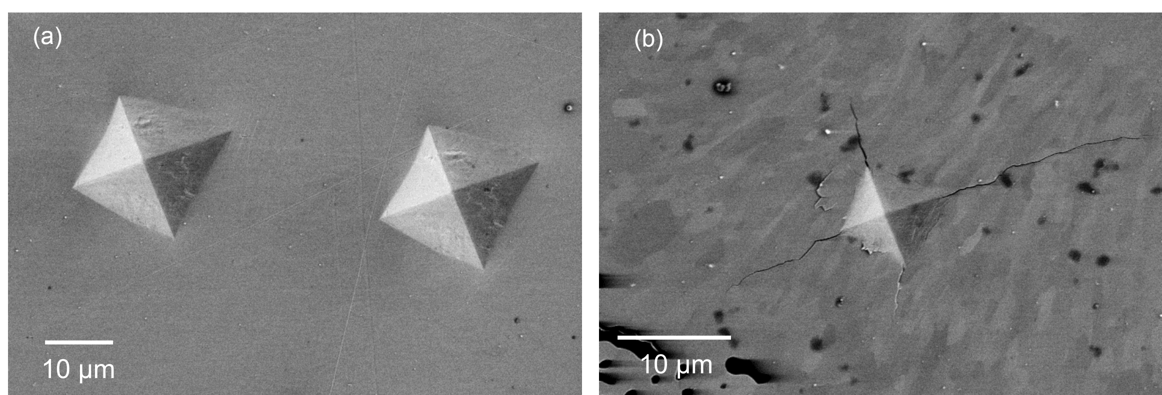

Figure 3. 13: Vickers hardness indentations in (a) the Ta core and (b) α-Ta_5Si_3 from the centre regions.

The EBSD, SEM, EDS and XRD results indicate that the microstructural properties of the Ta filament vary throughout its length, which in turn determined its mechanical properties, ultimately influencing its operational lifetime and stability during deposition. These findings highlight the complex reactions occurring at the filament surface where dissociation, diffusion, desorption and adsorption of the SiH_4/H_2 gas mixture and recrystallization of Ta are all possible. Furthermore, these complex reactions may be directly linked to the presence of a thermal gradient along the filament length [3.4]. The operational lifetime of the filament under investigation amounted to about 15 hours and it appears that the persistence of the Ta core may be related to an increase in the difficulty for Si to diffuse through the silicides layers to react with the Ta.

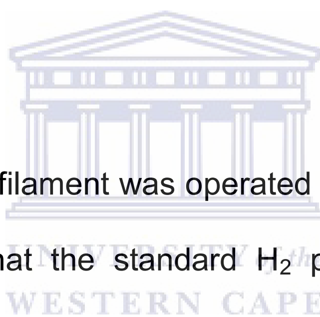

It may be pointed out that this filament was operated at 1600 °C in a H_2 rich ambient for nc-Si:H deposition and that the standard H_2 pre- and post-treatments were performed [3.4]. Moreover, a heated Ta filament acts as an efficient source for the production of atomic hydrogen [3.13]. There may therefore be a possibility that hydrogen damage [3.14], i.e. porosity and cracks could also be caused by overexposing the filament to an atomic hydrogen/H_2 rich ambient as proposed in literature to increase the filament lifetime [3.4].

3.4 CONCLUSION

Various microbeam analysis-based investigations disclosed that a Ta-filament transforms into 4 different silicides encapsulated by a solid Si layer during the deposition of nc-Si:H thin films by HWCVD. SEM and XRD analysis; and EBSD concurred on the formation of the $TaSi_2$ and Si phases around a Ta core at the filament ends, while the Ta_2Si, $TaSi_2$, α-Ta_5Si_3 and the metastable Ta_5Si_3 phases formed at the filament centre. The hardness measurements showed that the recrystallized Ta core is softer but tougher than its silicide layers. The microstructural evolution and degradation of the ageing filament were explained in terms of a thermal gradient along the length of the filament, variation of silicon content within the filament and differences in mechanical properties between Ta and its silicides.

UNIVERSITY of the
WESTERN CAPE

REFERENCES

3.1 A. H. Mahan, J. Carapella, B. P. Nelson, R. S. Crandall, I. Balberg (1991) J. Appl. Phys. **69**:6728.

3.2 D. Hrunski, B. Schroeder, M. Scheib, R. M. Merz, W. Bock, C. Wagner (2008) Thin Solid Films **516**:818.

3.3 D. Hrunski, M. Scheib, M. Merz, B. Schroeder (2009) Thin Solid Films **517**:3370.

3.4 D. Knoesen, C. Arendse, S. Halindintwali, T. Muller (2008) Thin Solid Films **516**:814.

3.5 C. H. M. van der Werf, H. Li, V. Verlaan, C. J. Oliphant, R. Bakker, Z. S. Houweling, REI Schropp (2009) Thin Solid Films **571**:3431.

3.6 C. J. Arendse, D. Knoesen, D. T. Britton (2006) Thin Solid Films **501**:92.

3.7 ICDD card numbers: Ta (04-008-3222), Ta_2Si (04-004-7298), $TaSi_2$ (04-004-7273), αTa_5Si_3 (04-004-7245), metastableTa_5Si_3 (04-004-7297) and Si (04-012-7888).

3.8 T. B. Massalski (1990), **Binary Alloy Phase Diagrams**, 2nd edition, vol. 3, ASM International.

3.9 A. G. Evans and E. A. Charles (1978) Journal of the American Ceramic Society, **59**:371.

3.10 F. Cardarelli (2008), **Materials Handbook: A Concise Desktop Reference**, 2nd edition, Springer-Verlag.

3.11 K. H. Stern (editor) (1996), **Metallurgical and Ceramic Protective Coatings**, Chapman and Hall, UK.

3.12 C. Hu, L. He, F. Li, Ling Wu, J. Wang, M. Li, Y. Bao, and Y. Zhou (2010), International Journal of Applied Ceramic Technology **7**:697.

3.13 C. H. M. van der Werf, P. A. T. T. van Veenendaal, M. K. van Veen, A. J. Hardeman, M. Y. S. Rusche, J. K. Rath, R. E. I. Schropp (2003) Thin Solid Films **430**:46.

3.14 A. K. Das (1997), **Metallurgy of Failure Analysis**, McGraw-Hill.

CHAPTER 4

GROWTH KINETICS OF nc-Si:H FABRICATED BY HWCVD

ABSTRACT

We report on the growth kinetics of hydrogenated nanocrystalline silicon, with specific focus on the effects of the deposition time and hydrogen dilution on the nano-structural properties. The increase in the crystallite size, attributed to the agglomeration of smaller nano-crystallites, is accompanied by a reduction in the compressive strain within the crystalline region and an improved ordering and reduction in the tensile stress in the amorphous network. These changes are intimately related to the absorption characteristics of the material. Surface diffusion determines the growth in the amorphous regime, whereas competing reactions between silicon etching by atomic hydrogen and precursor deposition govern the film growth at the high-dilution regime. The diffusion of hydrogen within the film controls the growth during the transition from amorphous to nanocrystalline silicon.

UNIVERSITY of the
WESTERN CAPE

4.1 INTRODUCTION

Hydrogenated amorphous silicon (a-Si:H) is an important material in modern electronic devices such as solar cells and thin film transistors. Currently, the focus has shifted towards hydrogenated nanocrystalline silicon (nc-Si:H) as a possible replacement for a-Si:H, due to its unique properties, e.g. tailored optical band gap [4.1] and superior resistance to photo-induced degradation [4.2]. The growth process and structure-property relationship of nc-Si:H dates back to 1989 [4.3] and has been the centre of numerous studies, as they would assist in the enhancement of growth rates and film properties. A need also exist for developing the synthesis of device quality nc-Si:H at low substrate temperatures as it would promote the use of flexible substrates.

This contribution presents an investigation into the effects of hydrogen (H)-dilution and deposition time on the evolution of the nano-structural properties and the absorption characteristics of nc-Si:H synthesized by hot-wire chemical vapour deposition (HWCVD) at a substrate temperature of 200 °C. Subsequently, growth mechanisms are deduced from the observations for each H-dilution regime.

UNIVERSITY of the
WESTERN CAPE

4.2 EXPERIMENTAL DETAILS

The thin films were simultaneously deposited on single-side polished (100) crystalline silicon and Corning 7059 glass substrates using an ultra-high vacuum HWCVD system [4.4] from various gas mixtures of SiH_4 and H_2. The H-dilution ratio, defined as $R = \frac{\Phi_{H_2}}{(\Phi_{H_2} + \Phi_{SiH_4})}$, where Φ denotes the gas flow rate, was varied from 80 – 95 %. At each R-value, varying the deposition time from 10 – 60 minutes enabled control over the film thickness. During all depositions, the filament temperature, deposition pressure, substrate temperature and total gas flow rate were fixed at 1600 °C, 60 μbar, 200 °C and 30 sccm, respectively.

UNIVERSITY of the
WESTERN CAPE

The structural properties were investigated using a Jobin-Yvon HR800 micro-Raman spectrometer in backscattering geometry at room temperature in the region 100 – 1000 cm^{-1}, using an excitation wavelength of 514.5 nm. X-ray diffraction (XRD) was performed using a PANalytical Xpert diffractometer at 2θ-values ranging from 5 – 90°, with a step size of 0.02°. Copper $K_{\alpha 1}$ radiation with a wavelength of 1.5406 Å was used as the x-ray source. A FEI Helios focus ion beam scanning transmission electron microscopy (STEM) was used to prepare and image cross-sections of the films. The film-thickness was determined using a Veeco profilometer. Ultraviolet-visible (UV-VIS) spectra were measured in transmission mode from 200 – 900 nm using a Perkin-Elmer LAMDA 7505 UV/VIS spectrophotometer. The absorption spectra were calculated using the method proposed by Swanepoel [4.5].

4.3 RESULTS

Figure 4.1 (a) and (b) present the XRD patterns, highlighting the variations in the film crystallinity as a function of deposition time and H-dilution. After the first 10 minutes of deposition, the emergence of the Si (111) diffraction peak occurs at a H-dilution of 95%. After 60 minutes, the Si (111) diffraction peak is visible at R-values $\geq$ 83%. In all cases the peaks are shifted to higher 2θ values, i.e. decrease interplanar spacing (compression). This suggests that the crystalline evolution, and hence the growth process, of nc-Si:H is dependent not only on the H-dilution, but also on the deposition time. The enhancement of the Si (111) peak intensities and the reduction of its full width at half maximum (FWHM) with increasing H-dilution and deposition time indicate an increased crystalline volume fraction and a growth in the Si nano-crystallite size, respectively. The presence of lattice strain, nano-sized crystallites and instrumental effects are commonly the main contributors to the peak broadening in an XRD spectrum [4.6] and has generally been overlooked, especially for nc-Si:H [4.7]. For accurate quantitative analysis; polycrystalline silicon and a NIST SRM 660 LaB_6 reference samples were used to obtain the corrected 2θ-peak position and the instrumental broadening, respectively. The crystallite size d_{XRD} of the Si (111)-peak was then calculated from the Scherrer formula:

$$d_{XRD} = \frac{0.9\lambda}{B_{structure} \cos\theta} \tag{4.1}$$

where $B_{structure}$ is the structural broadening calculated from the measured FWHM of the raw spectrum and that of the LaB_6 reference by:

$$B_{structure} = B_{measured} - B_{reference} \tag{4.2}$$

The contribution of the lattice strain ε to the peak broadening was calculated from:

$$B_{strain} = 4\varepsilon \tan\theta \tag{4.3}$$

where $B^2_{strain} = B^2_{measured} - B^2_{reference}$ [4.6].

Figure 4.1c shows the crystallite size-strain analysis of the Si (111) peak at different hydrogen dilutions and deposition times. It is evident that the growth in crystallite size is associated with a reduction in the compressive strain of the Si crystallites.

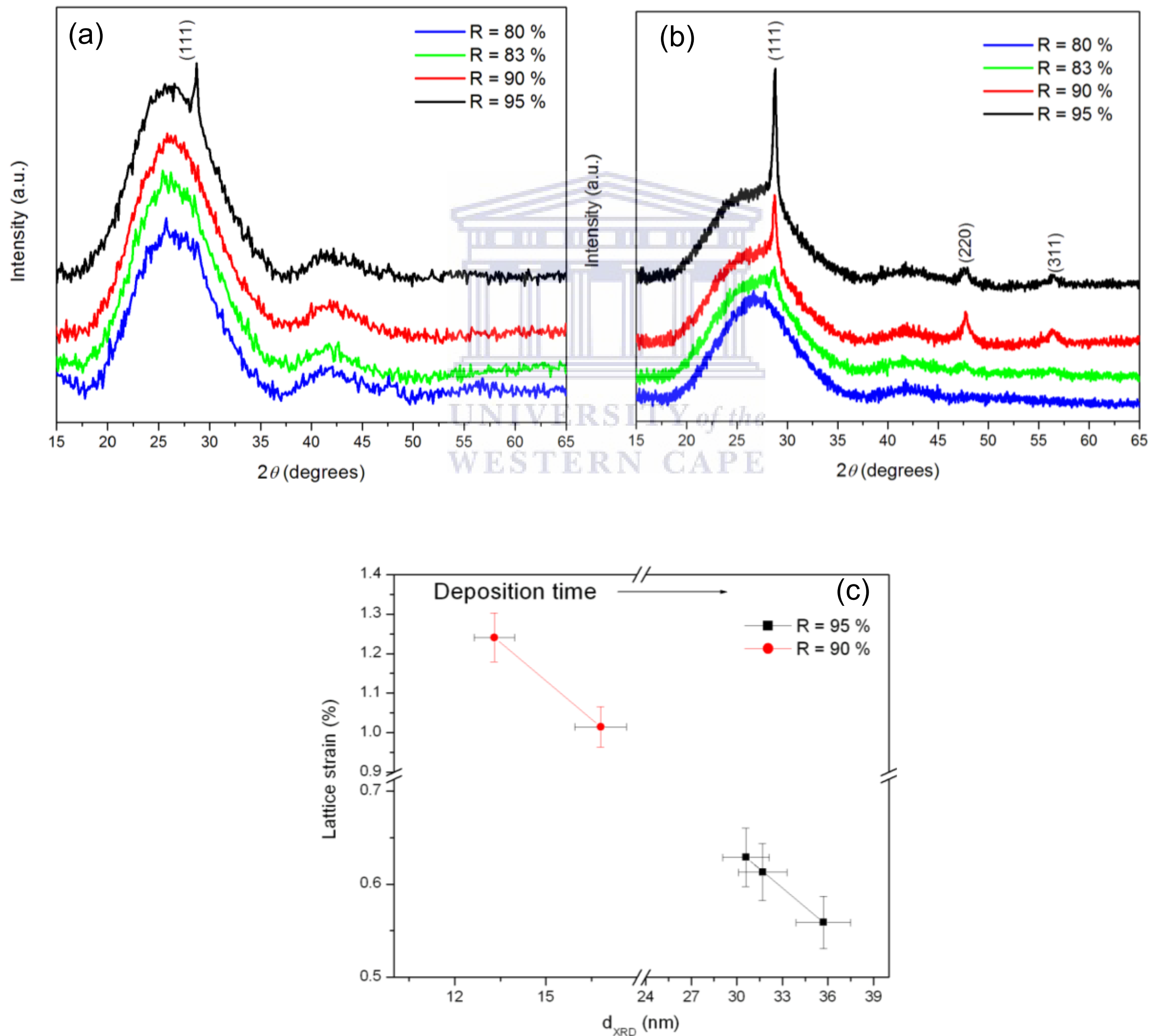

Figure 4.1: XRD spectra of the samples deposited at different H-dilutions for (a) 10 minutes and (b) 60 minutes. (c) Size-strain analyses of samples deposited at different H-dilutions and deposition times.

Figure 4.2 presents STEM images of the film cross-section of the nc-Si:H thin film deposited at 90%. Noticeable is the characteristic conical growth of crystalline regions indicating an enhancement in the crystallinity as the film become thicker. The STEM images also reveal the presence of twinned crystals. Figure 4.3 shows a series of secondary electron images; each image is taken at intervals of 4 nm "slices" into the film. The voids are prevalent along the boundary between the amorphous and crystalline regions.

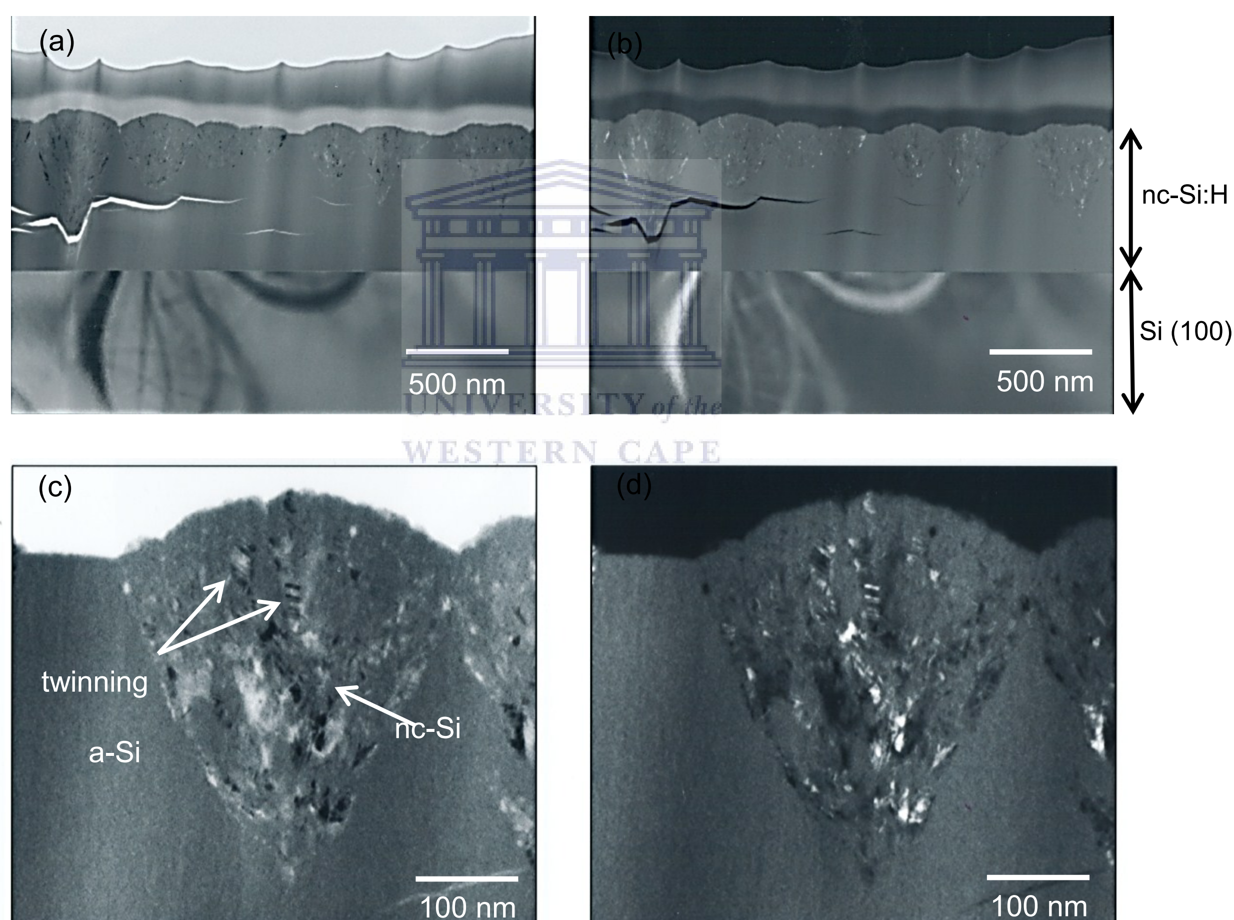

UNIVERSITY of the
WESTERN CAPE

Figure 4.2: STEM images in (a) bright field and (b) dark field modes. (c) and (d) are higher magnification images.

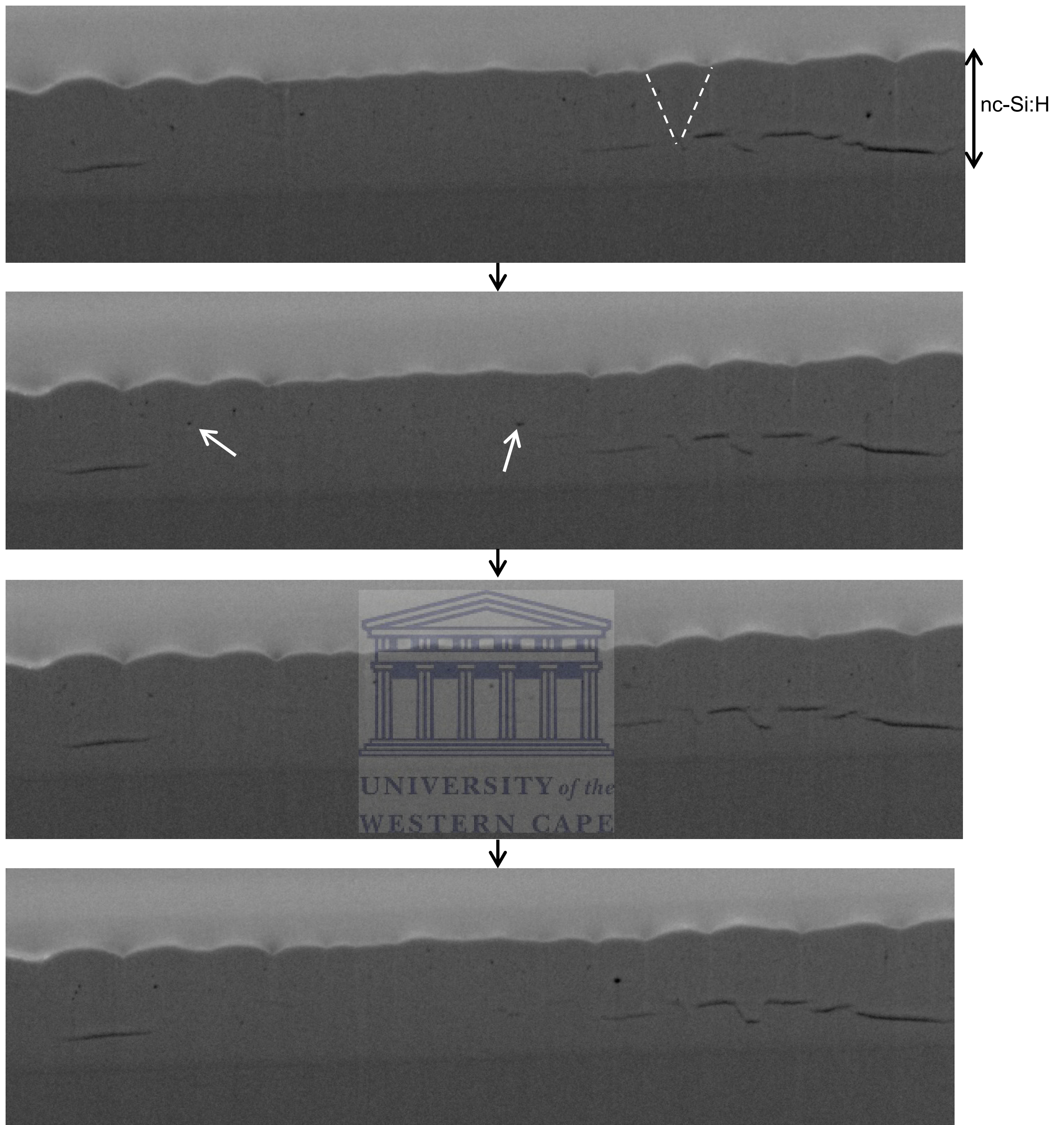

UNIVERSITY of the
WESTERN CAPE

Figure 4.3: Series of secondary electron micrographs of the nc-Si:H film (R = 90%) taken at each interval consisting of 4 nm slices into the sample showing the locations of voids.

Figure 4.4 (a) and (b) compares the Raman spectra of the thin films deposited for 10 and 60 minutes at various H-dilutions. The spectra display the following main features: (i) a sharp peak centred around 516 cm^{-1}, associated with the transverse optic (TO) mode of the nc-Si phase; (ii) the broad shoulder centred around 480 cm^{-1}, due to the TO-mode of the amorphous silicon (a-Si) phase; and (iii) a smaller shoulder around 505 cm^{-1}, corresponding to the distribution of crystalline grain boundaries in the sample. The appearance of the nc-Si TO-peak at R ≥ 83 % signals the nucleation of smaller Si nano-crystallites within the a-Si matrix after 10 minutes of deposition, which is undetectable with XRD. It should be noted that Raman spectroscopy is more sensitive to short-range order than XRD.

UNIVERSITY of the
WESTERN CAPE

The crystalline volume fraction (*fc*) was estimated from the integrated areas of the afore-mentioned deconvoluted Gaussian peaks (505 cm^{-1} and 480 cm^{-1}) and a Lorentz peak (516 cm^{-1}):

$$f_c = \frac{A_{505} + A_{516}}{A_{505} + A_{516} + A_{480}} \tag{4.4}$$

The crystallite size is empirically determined from the shift of the nc-Si TO-peak relative to the bulk c-Si peak at 520 cm^{-1} [4.8]. Caution should be exercised when using this relation, since the shift in the 520 cm^{-1} peak can also be associated with changes in the stress; and therefore the values should not be taken as absolute [4.9].

Figure 4.4 (c) and (d) show that the crystalline volume fraction increased and saturates after 20 minutes, while the crystallite size varied slightly (~ 1 nm) with increasing H-dilution and deposition time, which is contrary to previous studies [4.10]. Therefore, an increase in H-dilution and deposition time induces an enhanced nucleation rate of silicon nano-crystals. The peak position of the a-Si TO-peak shifts to higher wavenumbers with an increase in H-dilution and time, which is indicative of an enhancing compressive strain within the a-Si network [4.11].

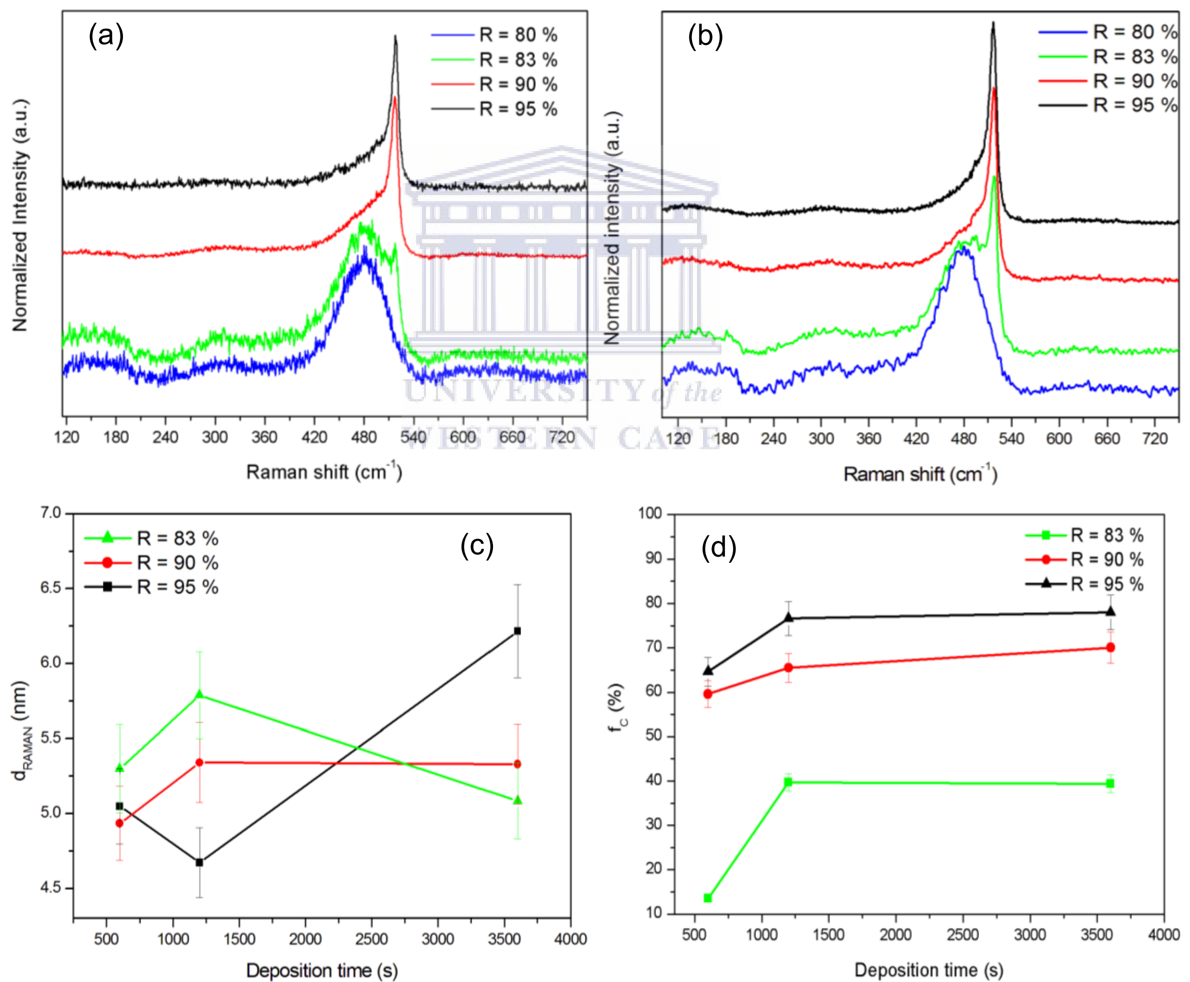

Figure 4.4: Raman spectra of the samples deposited at different H-dilutions for (a) 10 minutes and (b) 60 minutes. (c) Average crystallite size and (d) crystalline volume fraction of the samples as a function of H-dilution and deposition time.

The main factors that influence the absorption characteristics of nc-Si:H includes the quantum confinement effect due to the nano-crystallite size [4.1], film stress [4.12], hydrogen concentration and distribution, and microvoids [4.13]. Presented in Figure 4.5 is the spectral absorption dependence of the samples deposited for 60 minutes as a function of H-dilution. A systematic reduction in the absorption coefficient is evident with increasing H-dilution, which is attributed to the indirect transitions, characteristic of nc-Si:H with a large crystalline volume fraction.

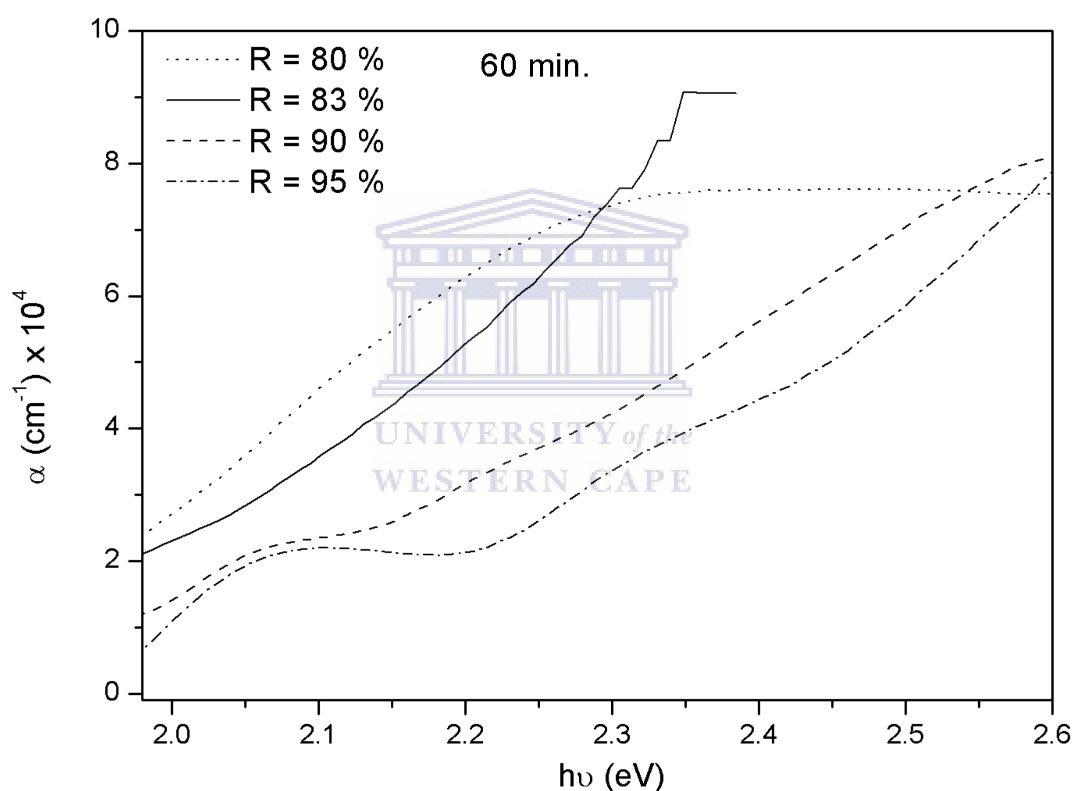

Figure 4.5: Absorption coefficient spectra of the samples deposited for 60 minutes.

The XRD and Raman results reveal that the structural order of both the a-Si and nc-Si regions within the films varies with H-dilutions and deposition time, i.e. there may be different growth mechanisms at work depending on the deposition regime. Since the growth of nc-Si:H are governed by reactions at the substrate, plotting the film thickness (d_f) as a function of time at different H-dilutions can reveal if the growth process is surface controlled or diffusion controlled. Figure 4.6 shows the film thickness as a function of deposition time at various H-dilutions. A linear growth rate occurs at R = 80 and 95 %, which suggests that the reactions at the surface of the thin film controls film growth within this regime. Conversely, when the film undergoes transformation from a-Si:H to nc-Si:H (R = 83 – 90%) the growth follows a parabolic law, suggesting a diffusion-based growth.

UNIVERSITY of the
WESTERN CAPE

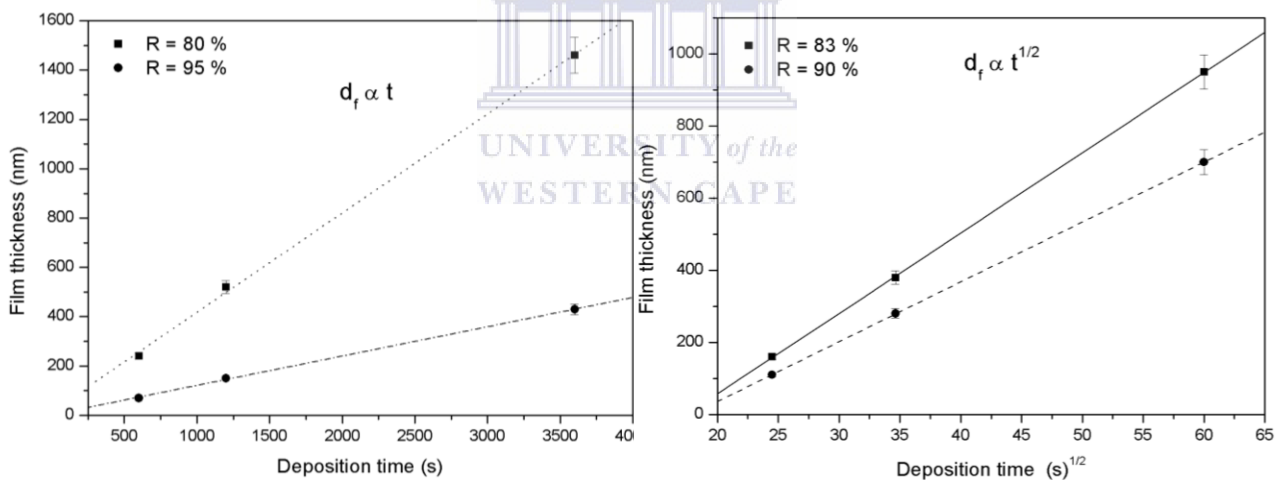

Figure 4.6: Growth kinetics of the a-Si:H and nc-Si:H thin films at different H-dilutions.

4.4 DISCUSSION

The increase of crystallite size observed in XRD can be attributed to the agglomeration of smaller nano-crystallites into larger crystallites, accompanied by the removal of strained Si-H bonds from the grain boundaries, and the nucleation of smaller crystallites, not necessarily detectable by XRD. This results in the growth of the crystallite size and an increase in the crystalline volume fraction with increasing deposition time or film thickness, also reported by Wronski *et al.* [4.14].

The shift in 2θ values to higher values compared to monocrystalline silicon indicates a decrease in the interplanar distance which may indicate compression. The size-strain analysis suggests that larger Si crystallites (> 12 nm) are under compressive stress, attributed to the surrounding a-Si network that is initially under tensile stress. The combined effects of these two types of stresses then determine the total film stress [4.12]. Therefore the reduction in compressive strain in the Si nano-crystallites can be associated with an improvement in the ordering and a reduction in the tensile stress in the surrounding a-Si network. Tensile stress in nc-Si:H originates from the removal of H from grain boundaries, coalescence of crystallites and the presence of microvoids [4.13], which are characteristic for these films [4.1].

UNIVERSITY of the
WESTERN CAPE

Three schools of thought have been receiving the most attention to date for a possible growth mechanism, i.e. the atomic hydrogen ($H^{\bullet}$)-etching model [4.15], the surface diffusion [4.16] and the chemical annealing model [4.17]. The $H^{\bullet}$-etching model entails the selective etching of the a-Si phase by $H^{\bullet}$, while the surface reaction models suggest an increased mobility of Si-containing radicals on an H-terminated surface until it finds energetically favourable sites to grow. The chemical annealing

model claims that exothermic recombination of $H^{\bullet}$ to from molecular hydrogen (H_2) and the insertion of H into strained bonds serves as energy for the rearrangement of the Si-network or crystal nucleation.

Yang *et al.* [4.18] performed *in situ* spectroscopic ellipsometry to analyse the microstructure of an a-Si:H / microcrystalline silicon (µc-Si:H) interface. They found that $H^{\bullet}$ penetrates the surface of the a-Si:H layer and increases its H-content. Subsequently, a µc-Si:H layer nucleates on top of a high H-content a-Si:H layer. The µc-Si:H layer then grows at the expense of the underlying high H-content a-Si:H layer. Reduced levels of H-coverage on the surface and the low substrate temperature suggests that the surface diffusion of Si-species may determine the growth at R = 80 %. Increasing the H-dilution ratio to 83 – 90% implies an increase in the $H^{\bullet}$ concentration, subsequently leading to the diffusion of $H^{\bullet}$ into the a-Si:H network where reconstruction and ordering occurs. This leads to the in-diffusion of $H^{\bullet}$ as being the governing factor in film growth at these conditions. At 95 %, extreme levels of $H^{\bullet}$-etching exists. In conjunction with a superior flux of $H^{\bullet}$, competing rates of $H^{\bullet}$-etching and Si deposition at the surface becomes the dominating step for film growth at this regime of deposition.

UNIVERSITY of the
WESTERN CAPE

The origin of voids in the nc-Si:H thin film is tentatively attributed to the $H^{\bullet}$-assisted reconstruction by etching and chemical annealing of the film during growth, as also suggested by Luysburg *et al.* [4.19]. The exact origin and evolution of the microvoids and twins will be determined in future studies.

4.5 CONCLUSION

The growth process of nc-Si:H during HWCVD was interpreted in detail as a function of deposition time and H-dilution. The increase in the Si crystallite size was attributed to the agglomeration of smaller nano-crystallites into larger crystallites, accompanied by the removal of strained Si-H bonds from the grain boundaries, and the nucleation of smaller crystallites, undetectable by XRD. The growth in crystallite size is associated with a reduction in compressive strain in the Si nano-crystallites and is due to an improved ordering and a reduction in the tensile stress in the surrounding a-Si network. The reduction in the absorption coefficient with increasing H-dilution is ascribed to the indirect transitions, characteristic of nc-Si:H with a large crystalline volume fraction. At R = 80 % the film growth was determined by surface diffusion of growth species, while at R = 95 % the growth was due to competing $H^{\bullet}$-etching effects and Si deposition. The growth-controlling step at the transition regime was determined to be the diffusion of $H^{\bullet}$ within the film.

UNIVERSITY of the WESTERN CAPE

REFERENCES

4.1 J. Son, J. Shim, N. Cho (2010) Curr. Appl. Physics **10**:S365.

4.2 V. Shah, J. Meier, E. Vallat-Sauvain, N. Wyrsch, U. Kroll, C. Droz, U. Graf (2003) Sol. Energy Mater. Sol. Cells **78**:469.

4.3 R. W. Collins, B. Yang (1989) J. Vac. Sci. Technol. B **7**:1155.

4.4 C. J. Arendse (1999), **Thermal Stability and Defect Structure of Hot-wire Deposited Amorphous Silicon**, PhD thesis, University of the Western Cape, Bellville, South Africa.

4.5 R. Swanepoel (1983) J. Phys. E. Sci. Instrum. **16**:1214.

4.6 H. P. Klug & L.E. Alexander (1974), **X-Ray Diffraction Procedures for Polycrystalline and Amorphous Materials**, 2nd edition, Wiley-Interscience Publication, New York.

4.7 B. P. Swain (2009) S. Afr. J. Sci. **105**:77.

4.8 Y. He, C. Yin, G. Cheng, L. Wang, X. Liu, G.Y. Hu (1994) J. Appl. Phys. **75**:797.

4.9 Th. Englert, G. Abstreiteret (1980) Solid-State Electron. **23**:31.

4.10 P. Gogoi, P. Agarwal (2009) Sol. Energy Mater. Sol. Cells **93**:199.

4.11 I. de Wolf (1996) Semicond. Sci. Technol. **11**:139.

4.12 M. Ali (2007) J. Luminescence **126**:614.

4.13 K. F. Feenstra, R. E. I. Schropp, W. F. van der Weg (1999) J. Appl. Phys. **85**:6843.

4.14 C. R. Wronski, B. Von Roedern, A. Kołodziej (2008) Vacuum **82**:1145.

4.15 C. C. Tsai, G.B. Anderson, R. Thompson, B. Wacker (1989) J. Non-Cryst. Solids **114**:151.

4.16 A. Matsuda (1983) J. Non-Cryst. Solids **59-60**:767.

UNIVERSITY of the WESTERN CAPE

4.17 K. Nakamura, K. Yoshida, S. Takeoka, I. Shimizu (1995) Jpn. J. Appl. Phys. **34**:442.

4.18 Y. H. Yang, M. Katiyar, G. F. Feng, N. Maley, J. R. Abelson (1994) Appl. Phys. Lett. **65**:1769.

4.19 M. Luysberg, P. Hapke, R. Carius, F. Finger (1997) Philos. Mag. A **75**:31.

UNIVERSITY of the
WESTERN CAPE

CHAPTER 5

NANOSTRUCTURAL, MECHANICAL AND OPTICAL PROPERTIES OF nc-Si:H THIN FILMS DEPOSITED BY HWCVD AT HIGH PRESSURES

ABSTRACT

This contribution reports on the correlation between the nanostructural, mechanical and optical properties of hydrogenated nanocrystalline silicon thin films deposited by hot-wire chemical vapour deposition at high process pressures. Raman spectroscopy reveals that the films are mixed phased containing both crystalline and amorphous silicon. Atomic force microscopy, infrared spectroscopy and scanning electron microscopy disclose that the films are composed of voids and particulate regions with dimensions similar to that of the crystallite size, as calculated from x-ray diffraction. The particulate regions coalesce and enlarge at longer deposition times, accompanied by a reduction in the size of the void regions. Throughout the progression of the film growth; the presence of the voids, the stress, and crystallite size and volume fraction govern the optical band gap and the refractive index. The substrate effects on the nanocrystalline silicon thin films, prevalent especially at film thicknesses below 150 nm, are also highlighted.

UNIVERSITY of the
WESTERN CAPE

5.1 INTRODUCTION

Hydrogenated nanocrystalline silicon (nc-Si:H) has received much research interest due to its potential applications in thin film transistors (TFTs) [5.1] and solar cells [5.2]. A number of deposition techniques have been applied to deposit nc-Si:H thin films, including plasma-enhanced chemical vapour deposition (PECVD) [5.3] and hot-wire chemical vapour deposition (HWCVD) [5.4]. The HWCVD technique has been identified as a viable alternative to the industrially developed PECVD, due to its superior growth rates [5.5], relatively simple scale-up [5.6] and absence of ion bombardment during the synthesis. The ability to synthesize nc-Si:H at low substrate temperatures (< 200 °C) also opens the possibility of integration of nc-Si:H with polymeric materials [5.7].

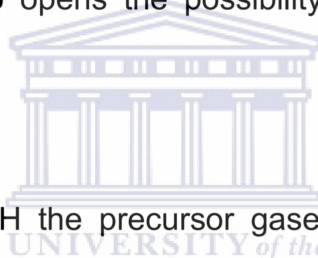
UNIVERSITY of the
WESTERN CAPE

During the HWCVD of nc-Si:H the precursor gases are dissociated at a heated filament, which leads to the generation of different radical species. Subsequently, these reactive species undergo secondary gas-phase reactions that eventually, at the desired deposition conditions, adsorb onto a substrate to grow into nc-Si:H thin films. The interconnection between the deposition parameters; such as the chamber geometry, filament temperature, gas composition, deposition pressure, filament-to-substrate distance and substrate temperature; plays a critical role in determining the eventual film properties [5.8]. Consequently, there exists an optimized deposition regime unique to each HWCVD reactor. The pursuit in understanding the growth of nc-Si:H films based on the deposition conditions, is thus on-going.

Compared to the numerous studies on the role of hydrogen dilution during the HWCVD of nc-Si:H, there have been limited investigations into the influence of the deposition pressure (P_{DEP}) on the material's nanostructural and optical properties, especially at high deposition pressures (≥ 60 µbar) and low substrate temperatures. Nevertheless, valuable insights into the growth of nc-Si:H were gained through these studies, for example the transition from amorphous silicon to microcrystalline silicon at a certain deposition range without H-dilution [5.9], variation in crystalline volume fraction [5.10] and film growth rate. The structural properties of nc-Si:H has an important impact on its optical properties and eventual device characteristics. In this contribution, we present our findings on the influence of the deposition time and pressure on the nanostructural, mechanical and optical properties of nc-Si:H thin films deposited by HWCVD from a silane and hydrogen gas mixture.

5.2 EXPERIMENTAL DETAILS

5.2.1 Thin film deposition

The nc-Si:H thin films were deposited by the HWCVD process simultaneously on Corning 7059 glass and <100> c-Si wafers at a fixed substrate temperature of 200 °C. A detailed description of the HWCVD system is provided elsewhere [5.11, 5.12]. A constant mixture of 1.5 sccm silane (SiH_4) and 28.5 sccm hydrogen (H_2) were used as precursor gases. The tantalum filament (length 1 m and Ø 300 µm) was heated to a temperature of 1600 °C and prepared in accordance with the suggestions proposed by Knoesen *et al.* [5.11]. The deposition pressure was varied

at 60, 80 and 100 µbar. For each deposition pressure, the deposition time was also varied at 10, 20 and 60 minutes.

5.2.2 Characterization

The thickness and the stress of the nc-Si:H films were determined by a Taylor stylus profilometer. The film stress (σ) was assessed from changes in the curvature of the bare Corning 7059 substrate and that of one with a thin film on it, using Stoney's equation [5.13]. The fixed contribution of the thermal stress, i.e. the mismatch between the thermal expansion of the film and the substrate, was determined from the information for crystalline silicon and the linear expansion coefficients for microcrystalline silicon reported by Takimoto *et al*. [5.14]. The thermal stress amounted to 0.1 GPa and was subtracted from the film stress, as estimated from the deflection measurements.

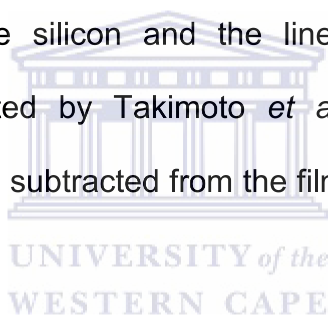
UNIVERSITY of the
WESTERN CAPE

Raman spectra were recorded in backscattering geometry in the region 100 – 800 cm^{-1} with a spectral resolution of 0.4 cm^{-1}, using a Jobin-Yvon HR800 micro-Raman spectrometer operated at an excitation wavelength of 514.5 nm. The power of the Raman laser was kept below 5 mW to avoid laser induced crystallisation. The Raman spectra were deconvoluted in the range 400 – 540 cm^{-1} into a sharp peak centred at ~ 517 cm^{-1} (c-Si transverse optical mode), broad band at ~ 480 cm^{-1} (amorphous Si transverse optical mode) and ~ 505 cm^{-1} (grain boundary contribution). The crystalline volume fraction, $f_c = {A_{505} + A_{517}}\big/{A_{505} + A_{517} + A_{480}}$, was estimated from the integrated areas of the aforementioned peaks [5.15]. The

crystallite size (d_{Raman}) was empirically calculated from $d_{Raman} = 2\pi\sqrt{2cm^{-1}/\Delta\omega}$, where Δω is the peak shift of the 517 cm^{-1} peak relative to the crystalline silicon (c-Si) peak [5.16]. X-ray diffraction (XRD) patterns were obtained in reflection geometry at 2θ-values ranging from 10° to 90° with a step size of 0.02° using a PANalytical Xpert diffractometer operated at 45kV and 40 mA. Cu K_α line (λ = 1.54056 Å) was the X-ray source. Polycrystalline silicon and a NIST SRM 660 LaB_6 reference sample were used to obtain the corrected 2θ-peak position and the instrumental broadening, respectively. The average volume-weighted domain size was estimated from the Scherrer formula, $d_{XRD} = \frac{0.9\lambda}{B_{STRUCTURE}\cos\theta}$, where $B_{STRUCTURE}$ is the structural broadening calculated from the measured FWHM of the raw spectrum and that of the LaB_6 reference. The lattice strain / distortion ε was calculated from $B_{STRAIN} = 4\varepsilon\tan\theta$ where $B_{STRAIN}^2 = B_{MEASURED}^2 - B_{REFERENCE}^2$ [5.17].

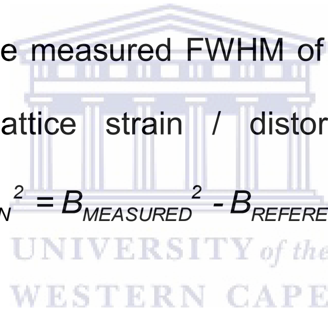
UNIVERSITY of the
WESTERN CAPE

Three dimensional (3D) topography images of at least three random areas of the nc-Si:H thin films were collected using a Veeco NanoScope IV Multi-Mode atomic force microscope (AFM) in tapping mode with a tip diameter of ~ 10 nm. Cross-sectional scanning electron microscopy (SEM) micrographs were recorded using a LEO 1525 field emission gun SEM operated at an accelerating voltage of 5 kV. Fourier transform infrared (FTIR) absorption spectra were collected in transmission geometry from 400 to 4000 cm^{-1} at a step size of 1 cm^{-1} using a Perkin-Elmer Spectrum 100 FTIR spectrophotometer. Optical transmission spectra were measured using a CARY 1E UV/VIS spectrophotometer in the range 200 – 900 nm with a spectral resolution of 1 nm. The refractive index and absorption coefficients were calculated by employing the effective medium approximation model [5.18].

5.3 RESULTS

5.3.1 Nanostructural properties

Raman spectroscopy is the established technique used to identify and quantify the mixed-phase, nanostructural properties of nc-Si:H. Fig. 5.1a shows a typical Raman spectrum for nc-Si:H deposited at 80 μbar; similar spectra were observed for 60 and 100 μbar. The mixed-phase is apparent by the presence of the characteristic nc-Si peak at ~ 517 cm^{-1} and the a-Si TO-peak at 480 cm^{-1}.

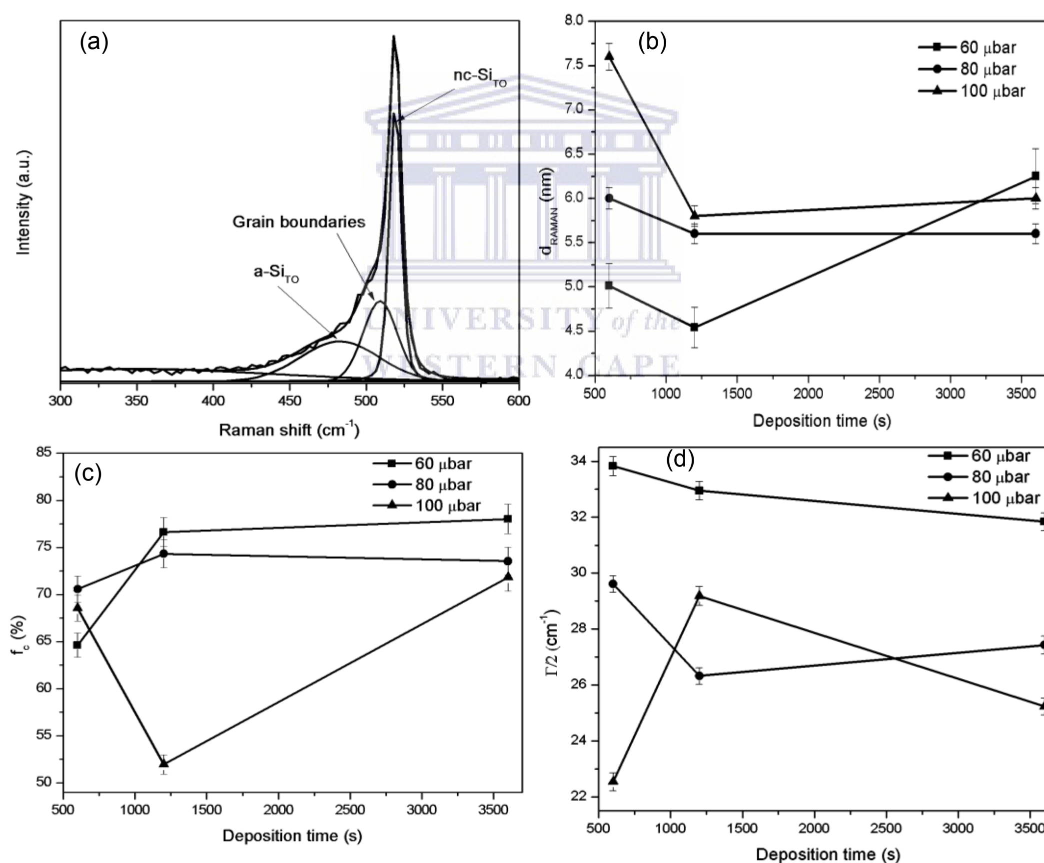

Figure 5.1: (a) Typical deconvoluted Raman spectrum at P_{DEP} = 80 μbar, deposition pressure and time effects on (b) the crystallite size, (c) crystalline volume fraction and (d) HWHM of the a-Si TO peak.

Contrary to the results reported by Bakr *et al*. [5.19], the crystallite size increases with an increasing deposition pressure and decreases with longer deposition times (see Fig. 5.1b) at P_{DEP} ≥ 80 µbar. The value of the crystalline volume fraction and its variation with deposition time were similar from 60 to 80 µbar during the first 60 min of deposition. On the other hand, f_C decreases from 10 to 20 min at a deposition pressure of 100 µbar and interestingly increases to converge to a similar crystalline volume fraction compared to lower deposition pressures at 60 min.

The enhancement in the crystallinity of the sample occurs simultaneously with a decrease in the half-width-at-half-maximum ($\Gamma/2$) of the a-Si TO-peak, i.e. an enhanced short range ordering within the a-Si network [5.20]. The films deposited at pressures ≥ 80 µbar displayed superior ordering within the a-Si network relative to a deposition pressure of 60 µbar. Raman spectroscopy therefore reveals that there is a direct relationship between the variation of the crystalline volume fraction and the structural order within the a-Si network.

UNIVERSITY of the
WESTERN CAPE

Raman spectroscopy provides information pertaining to the short range ordering (SRO) of the film [5.20]. Due to the superior penetration depth of x-rays, XRD was therefore used as a complementary technique to Raman spectroscopy to probe the medium range ordering (MRO) of the nc-Si:H thin films. Presented in Fig. 2 are XRD patterns (vertically offset for clarity) of the nc-Si:H thin films at 80 and 100 µbar. After 60 min the XRD patterns displayed three orientations consisting of a dominating <111> orientation and relatively weaker intensities in the <220> and <311> orientations superimposed on a broad peak at ~ 2θ = 26°, ascribed to the Corning glass substrate.

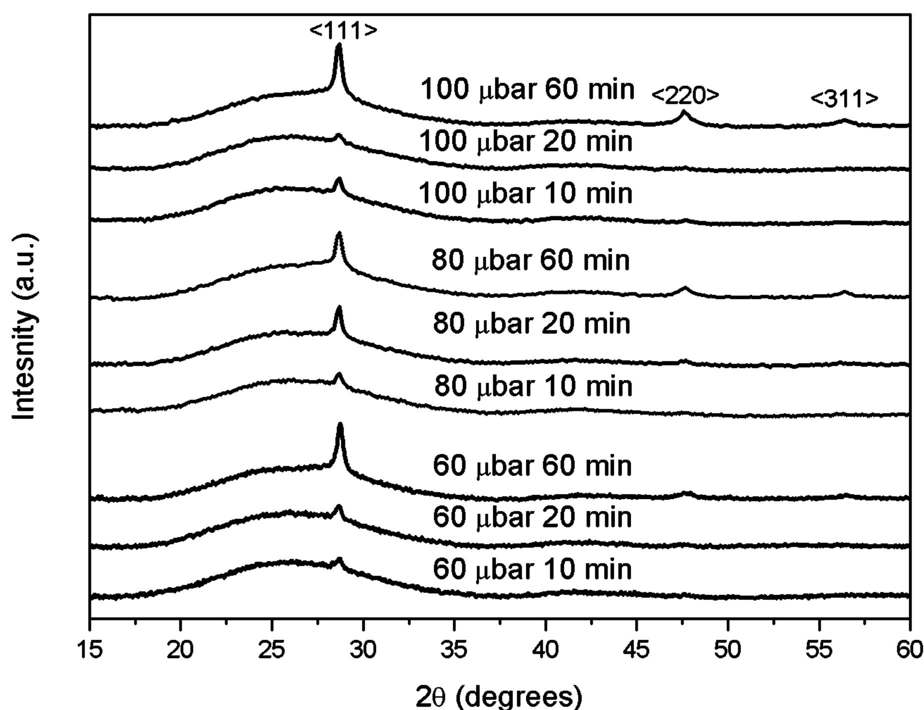

Figure 5.2: XRD patterns of the nc-Si:H films as a function of deposition time at 80 and 100 μbar.

UNIVERSITY of the
WESTERN CAPE

The peak intensities enhance with longer deposition times for pressures ≤ 80 μbar indicating an increase in the crystallinity within the films. However, at 100 μbar the crystallinity initially decreases from 10 to 20 min and then increases until 60 min as deduced from the XRD peak intensities, similar to the behaviour of f_C determined from Raman spectroscopy. Table 5.1 summarizes the average crystallite size and lattice strain analysis determined from the XRD patterns. The XRD results show that the crystallite size of Si <111> orientated crystallites increases and their corresponding lattice strain decreases with longer deposition time and increasing deposition pressure. These values are interpreted as upper bounds of a crystallite size distribution [5.21] and will therefore be greater than that determined from Raman spectroscopy.

Table 5.1: Average crystallite size and lattice strain at 60, 80 and 100 μbar for different deposition times.

Deposition time (min)	P_{DEP} (μbar)	d_{XRD} (nm)	ε (%)
	60		
10		29.8	0.63
20		31.5	0.58
60		36.0	0.55
	80		
10		30.4	0.63
20		43.2	0.49
60		51.2	0.43
	100		
10		35.7	0.56
20		45.2	0.46
60		63.1	0.37

UNIVERSITY of the
WESTERN CAPE

FTIR spectroscopy is the established technique used to probe the Si-H bonding configuration and to calculate the total bonded hydrogen (H) content in nc-Si:H and related materials. Figure 5.3 shows a typical FTIR absorption spectrum for the nc-Si:H film deposited at 80 μbar for 60 min. Three Si-H_x absorption regions can be distinguished: 600 – 750 cm^{-1} due to Si-H_x wagging, 850 – 880 cm^{-1} corresponding to Si-H_2 bending, and 1900 – 2150 cm^{-1} due to Si-H_x stretching [5.22].

The Si-H_x stretching bands can be further subdivided into two peaks at ~ 2000 cm^{-1} assigned to the Si-H groups in the a-Si tissue, and at ~ 2100 cm^{-1} attributed to the Si-H or SiH_2 on crystalline surfaces and / or voids [5.22, 5.23].

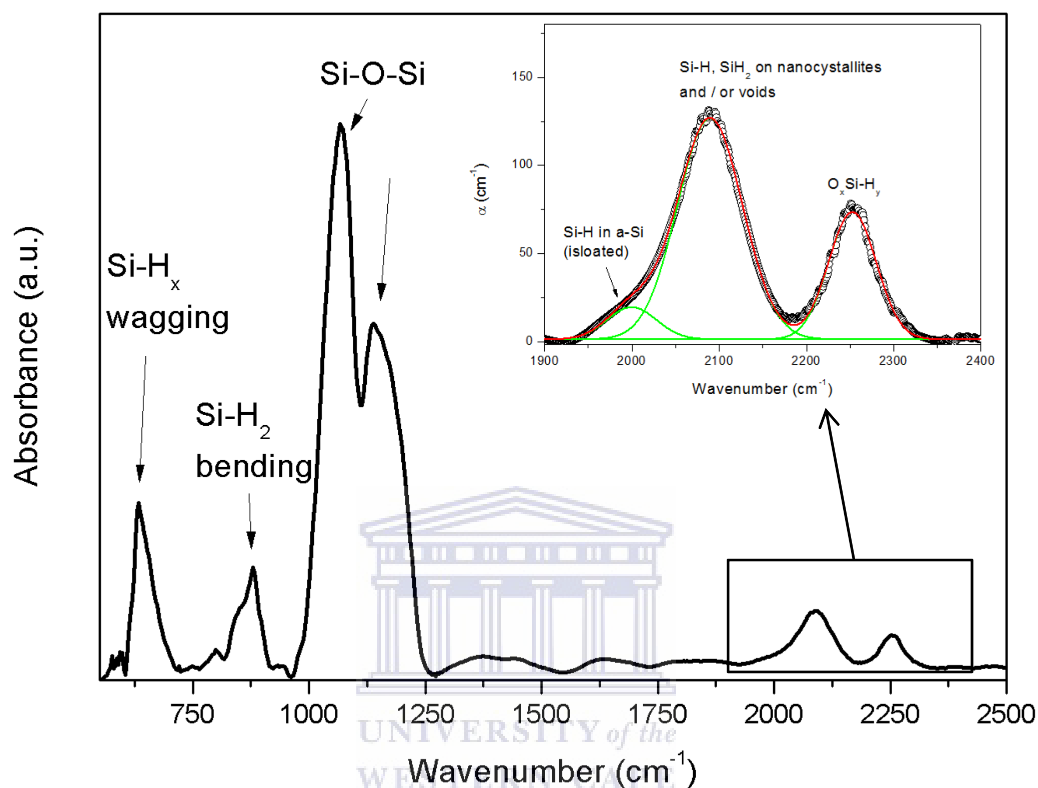

UNIVERSITY of the
WESTERN CAPE

Figure 5.3: Typical FTIR spectrum of a nc-Si:H film deposited at 80 µbar for 60 min. The inset shows the deconvolution of the peaks within the Si-H_x stretching modes.

The bands at 920 - 1250 cm^{-1} are allocated to the asymmetric Si-O-Si stretching vibration [5.24], while the 2250 cm^{-1} band is associated to the O_xSi-H_y vibration [5.25]. The oxygen-related vibrations are present in all the deposition pressure ranges investigated in this study; indicating that the nc-Si:H films are oxidized. Figure 5.4 shows an XPS elemental depth profile; disclosing that the O-content is mostly on the film surface and decreases to less than 5 at.% within the film bulk.

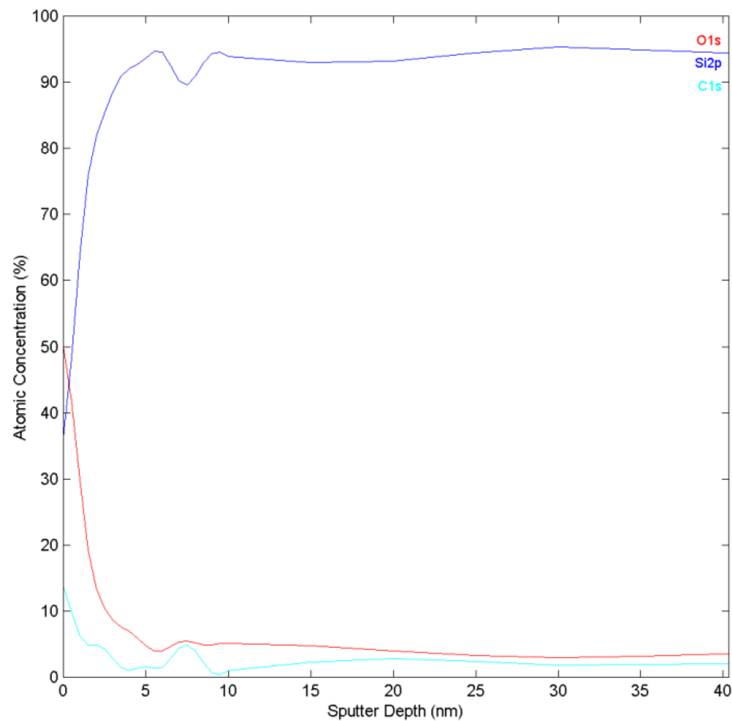

Figure 5.4: XPS depth profile showing the atomic concentrations of Si, O and C within the nc-Si:H films deposited at 80 µbar for 60 min.

UNIVERSITY of the
WESTERN CAPE

The total bonded H-content was estimated from the integrated absorption of the 640 cm^{-1} band using procedures proposed by Brodsky *et al.* [5.26] and Maley [5.27]. To quantify the fraction of H bonded on the surface of the nano-crystallites and / or voids relative to that bonded in the a-Si tissue, we define a structure factor R_S as [5.28]: $R_S = \frac{I_{2100}}{I_{2100} + I_{2000}}$, where *I* denotes the integrated intensity of each decomposed peak. Figure 5.5 shows the plots of the total bonded H and the R_S values as a function of deposition time at different pressures. At the first 10 min, the H concentration is superior in nc-Si:H deposited at 60 and 80 µbar amounting to 2.8 at.% and 4.0 at.%, respectively compared to the film deposited at 100 µbar.

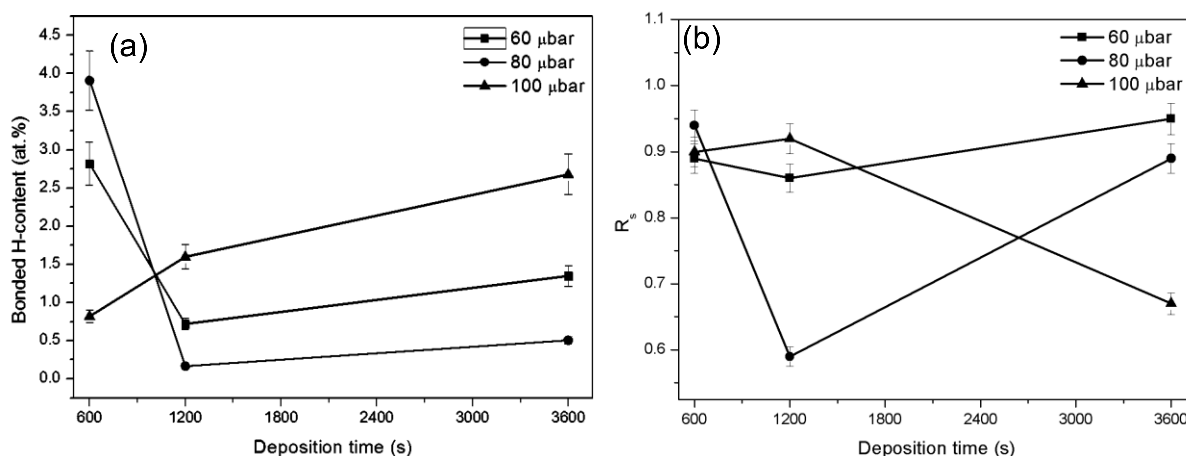

Figure 5.5: (a) Total bonded H and (b) structure factor as a function of deposition time and pressure.

Regardless of the different H-contents, more than 90 % of the H was bonded to the nanocrystalline surface and / or voids at 10 min across all the deposition pressures. Subsequently at 20 min the H-content drastically decreased for P_{DEP} ≤ 80 µbar, whereas it increased during the same time at 100 µbar. At 60 minutes the H-content enhances across all deposition pressures.

The percentage of H bonded to the nano-crystallites and / or voids decreased at 20 min for P_{DEP} ≤ 80 µbar reaching values of ~ 85 % and ~ 60 % at 60 µbar and 80 µbar, respectively. Afterwards, the R_S value recovers to values ranging between 88 to 90 % at 60 min. In contrast, at 100 µbar the H bonded to the nano-crystallites surface and / or voids enhanced slightly at 20 min to ~ 95 %, subsequently decreasing afterwards to ~ 66 % at 60 min.

UNIVERSITY of the
WESTERN CAPE

5.3.2 Film Stress

Fig. 5.6 shows the film stress for nc-Si:H thin films as a function of deposition time and pressure. At 10 min, the films exhibit tensile stress that decreased in magnitude at 20 min, and even switched over to compressive stress at pressures ≤ 80 μbar. Subsequently, the film stress becomes tensile ultimately reaching similar values at 60 min. The magnitude of film stress compares well with that typically reported for microcrystalline silicon thin films deposited by PECVD [5.29].

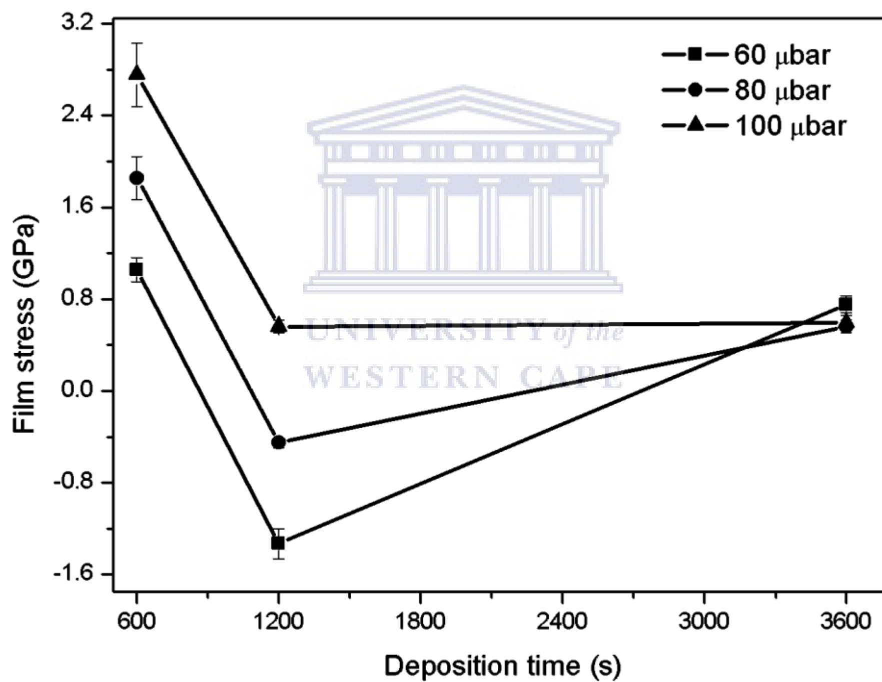

Figure 5.6: Film stress as a function of deposition time and pressure.

5.3.3 Morphology

Fig. 5.7 presents 3D AFM surface topography of nc-Si:H thin films at 80 µbar showing that significant microstructural changes occur with varying deposition time. The film surface consists of particles with a diameter range of ~ 36 nm (standard deviation 14 nm) at 10 min that coalesce to form larger clusters with sizes ranging from ~ 65 nm (standard deviation 25 nm) at 60 min, roughly corresponding to the crystallite size determined from XRD (see Table 1).

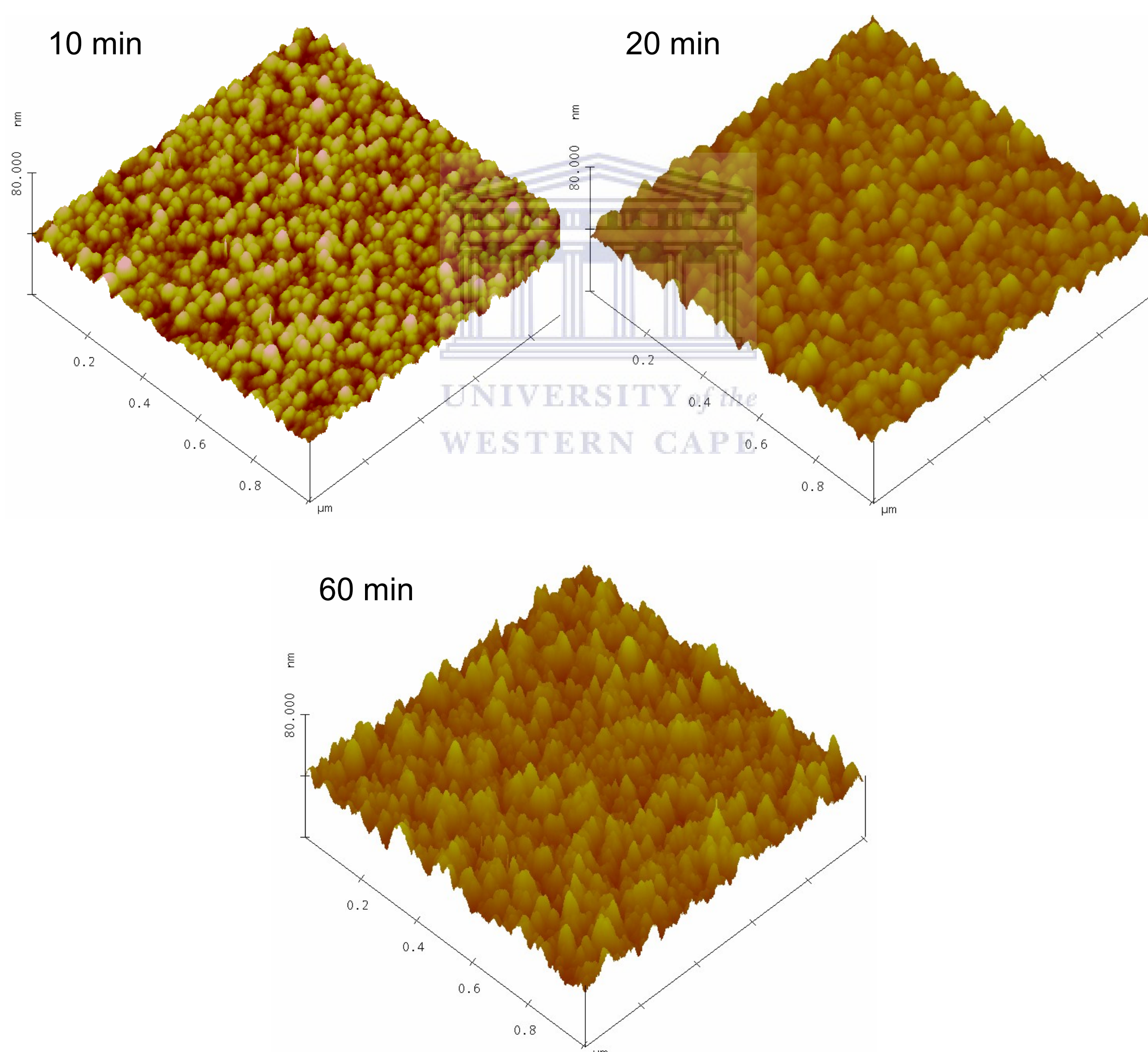

UNIVERSITY of the
WESTERN CAPE

Figure 5.7: 3D AFM topography images of films deposited at 80 µbar as a function of deposition time (scan size: 1µm by 1 µm).

Fig. 5.8 shows SEM micrographs of the film cross-sections as a function of deposition time at 80 μbar and 100 μbar. During the first 20 min, the film displays a porous, columnar structure with boundaries between particulate areas extending from the substrate to the film surface as indicated by the arrows in Figure 5.8a. However, at 60 minutes a reduction in the width of the boundary regions occurred with an increase in the particulate size. The difference in the average particulate size and shape was enhanced at 100 μbar.

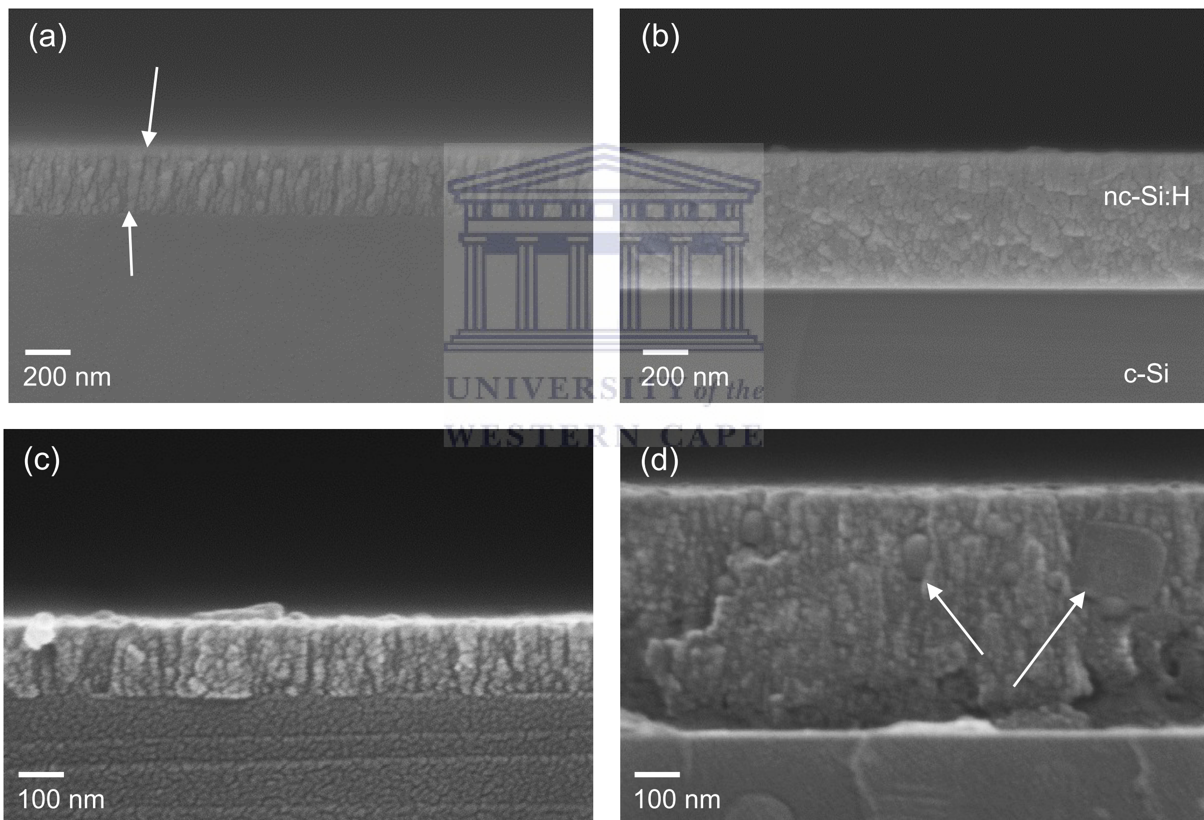

UNIVERSITY of the
WESTERN CAPE

Figure 5.8: SEM micrographs of the film deposited at: 80 μbar for (a) 20 min, (b) 60 min and at 100 μbar for (c) 20 min and (d) 60 min.

5.3.4 Optical Properties

Fig. 5.9 presents the variation in the optical band gap E_{04}, expressed as the energy where the absorption coefficient = 10^4 cm^{-1}, as a function of f_c. The band gap increases monotonically with the crystalline volume fraction, similar to the results reported by Waman *et al.* [5.9]. Table 5.2 compares the static refractive index n_0 in relation to the film stress at different deposition pressures and time. During the first 20 min a reduction in the magnitude of the tensile stress results in an increase in the refractive index at pressures ≤ 80 μbar. Since n_0 is related to film density, this implies that the film becomes denser. Afterwards, the compressive stress reduces and finally switches over to tensile stress again, which enhances until 60 min accompanied by a decrease in n_0. At 100 μbar the film tensile stress reduces in magnitude which leads to a decrease in n_0 until 60 min.

UNIVERSITY of the
WESTERN CAPE

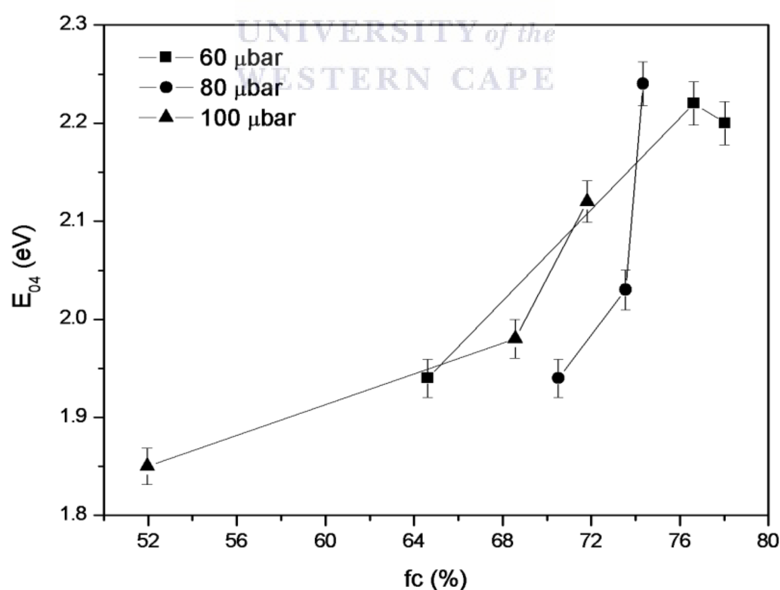

Figure 5.9: Variation of the optical band gap with the crystalline volume fraction at various deposition pressures.

Table 5.2: Variation in the static refractive index versus the film stress

Dep. Time (min)	$\sigma_{60\mu bar}$ (GPa)	$n_{60\mu bar}$	$\sigma_{80\mu bar}$ (GPa)	$n_{80\mu bar}$	$\sigma_{100\mu bar}$ (GPa)	$n_{100\mu bar}$
10	1.06	2.88	1.86	3.13	2.76	3.13
20	-1.33	3.30	-0.450	3.16	0.560	2.96
60	0.750	2.86	0.560	2.88	0.601	2.81

5.4 DISCUSSION

Relating the HWCVD conditions to the nanostructural, morphological, mechanical and optical properties of the nc-Si:H is complex due to the simultaneous presence of nc-Si, grain boundaries, voids, a-Si, different S-H bonding configurations and oxygen within the films.

UNIVERSITY of the WESTERN CAPE

Initially, all the nc-Si:H films are under tensile stress. The magnitude of the tensile stress decreases with an increasing deposition pressure at 10 min. Due to the complex composite nature of nc-Si:H, the high values of the tensile stress (from 1 to 3 GPa) can be attributed to various sources. In general, tensile stresses within thin films occur during growth when the neighbouring regions of 'islands' (crystallites or amorphous) coalesce [5.30, 5.31]. Specifically, two neighbouring crystallites elastically deform in order to replace the two grain free surfaces with a single grain boundary [5.31]. This can be visualized as a 'zipping' process between the grains, which can also result in the formation of voids. Tensile strain values then exists

between the crystallites, resulting in tensile stress. During the coalescence event, the resulting maximum stress is dependent on the crystallite sizes d (σ_{max} α 1/d), implying that a stress of several GPa is possible when d < 10 nm [5.31]. Oxidation of the film after the deposition is a major concern for nc-Si:H films. XPS revealed that the surfaces (~ 2 – 10 nm) of the nc-Si:H films are oxidized. The interatomic distances of Si-O (1.65 Å) is shorter compared to that of Si-Si (2.35 Å) [5.32]. However, this does not cause significant compression stresses due to the inferior oxide thickness compared to the bulk. Extrinsic thermal stress can also cause large values of tensile stress within the film [5.30]. During the first 10 min, the different expansion coefficients between the very thin nc-Si:H films and substrate play a critical role on the film structure. The relatively thin nc-Si:H films are not able to cover the substrate and still maintain its structural integrity. Consequently, this results in the films being stretched on the substrate, causing voids and large values of tensile stress below deposition times of 20 min. The origin behind the superior tensile value for the film deposited at 100 μbar for 10 min is attributed to a higher void fraction. The higher void fraction is expected considering the high R_S value and the reduced bonded H-content within the films at 100 μbar during the first 10 min. The large tensile stress values observed at 10 min are attributed to the small grain sizes of d_{RAMAN} < 10 nm, the enhanced presence of voids and thermal stress.

In all pressures regimes, the d_{RAMAN} size decreases at 20 min. At the same time, the tensile stress within the film decreases, even becoming compressive at P_{DEP} ≤ 80 μbar. The reducing tensile stress results in a contraction of the crystallite dimensions, causing a reduction in the average crystallite sizes. The enhancing crystalline volume fraction and the increasing SRO (judged from the HWHM of a-Si

UNIVERSITY of the
WESTERN CAPE

TO peak) at 20 min for P_{DEP} ≤ 80 μbar indicates that smaller grains may have nucleated, which can also explain the observed reduction of the average crystallite size estimated by the Raman analysis.

The FTIR analysis revealed that the bonded H content in the a-Si network becomes enhanced compared to that bonded on nano-crystallite surface and / or voids at 20 min for P_{DEP} ≤ 80 μbar. Combined with the expanding larger crystallites as seen from the XRD analysis (see Table 5.1), this leads to a densification of the a-Si tissue, eventually counteracting the tension caused by coalescence and growth of the crystallites. The ordering within the a-Si network improves as shown by the reduction in the HWHM of the Raman a-Si TO peak (see Figure 5.1). The appearance of the compressive stress in the nc-Si:H thin films is therefore attributed to the densification of the a-Si tissue and the subsequent ordering within the a-Si network, which results in a more coordinated, continued bulk film structure as shown by the XRD and SEM analysis. Considering that the H-content decreased significantly at 20 min for P_{DEP} ≤ 80 μbar, another possibility for the generation of compressive stress within the nc-Si:H films can be based on a recent *in situ* XRD study performed by Sharma *et al.* [5.33] on the crystallization kinetics of a-Si:H films. It was found that in highly disordered a-Si:H films, the collapse of nano-voids occurs subsequent to the out-diffusion of H leading to a more compact structure [5.33]. In our case, the growing crystallites can also exert pressure on the void rich a-Si network, aiding in the collapsing of the voids within the a-Si tissue.

UNIVERSITY of the
WESTERN CAPE

At 100 µbar the a-Si network experienced a reduction in its SRO and a slight increase in H-content at 20 min. However, most of the H (~ 95 %) was found to be bonded to the surface of the crystallites and / or voids, indicating a more defective a-Si tissue. Moreover, considering that the H-content increased slightly at 20 min for 100 µbar, this would minimize the collapse of nano-voids [5.33]. As a result, the a-Si was not as dense compared to lower pressures and the nc-Si:H deposited at 100 µbar for 20 min did not show compressive stress, despite the reducing film tensile stress compared to 10 min.

After 60 min of deposition, the film stress became tensile again. Floro *et al.* [5.31] observed a similar trend in a-Si film stress as a function of time, i.e. tensile, then compression and then tensile again. Using high-resolution transmission electron microscopy, they found that nanovoid tracks developed in the thickening a-Si films, which was proposed to be the cause of the final tensile stress. Smith *et al.* [5.34] applied non-equilibrium molecular dynamics to study the relationship between the structure and growth of thin films and found that voids are formed due to surface roughness and shadowing effects. Specifically, atoms depositing at the top regions of protruding surface features experience attraction towards each other, leading to the creation of outgrowths with voids underneath. Based on the AFM analysis and on the findings of Floro *et al.* [5.31] and Smith *et al.* [5.34]; the tensile stresses at 60 min are attributed to shadowing effects and subsequent void formation caused by the roughening nc-Si:H surfaces.

UNIVERSITY of the
WESTERN CAPE

Further insights into the thin film growth process can be deduced from studying the relationship between the film thickness (*d*) and the root-mean-square roughness (*δ*) calculated from the AFM images [5.35, 5.36]. According to fractal analysis, the film thickness scales with the roughness via the relation $\delta \sim d^{\beta}$, where β is the dynamic scaling exponent. Fig. 5.10 presents the variation of *δ* as a function of *d* at various deposition pressures. At $P_{DEP} \leq 80$ μbar, linear fits reveal that $\beta \approx 0.4 \pm 0.05$, indicative of random deposition [5.35], which is the cause of the relatively inferior medium range ordering at these conditions. The random deposition based surface reactions are therefore responsible for the linear growth mechanism observed for nc-Si:H deposited at 60 μbar in Chapter 4. Moreover, the random deposition processes at $P_{DEP} \leq 80$ μbar favours the shadowing effect during the deposition, which can lead to the generation of voids and consequently tensile stress at longer deposition times.

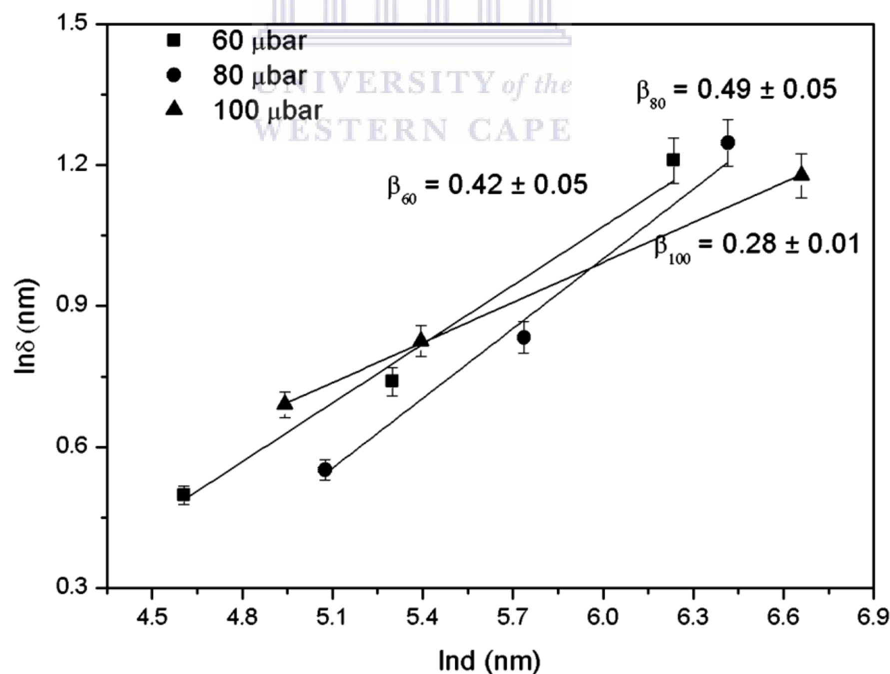

Figure 5.10: Variation in δ and film thickness at different P_{DEP}. Root-mean-square roughness is within 5 % standard deviation.

UNIVERSITY of the WESTERN CAPE

However, at 100 μbar β ~ 0.28 ± 0.01, which points to finite diffusion, i.e. radicals that arrive at the growth surface will diffuse around until they settle at energetically favoured sites. The decrease in β with an increase in deposition pressure is contrary to the results reported by Gu *et al.* [5.36]. We attribute this to the higher deposition pressures used in this study. A higher concentration of atomic hydrogen is expected to be prevalent at higher deposition pressures, which covers the growing surface more efficiently, thereby promoting surface diffusion [5.37], and is more favourable for medium range ordering and reduced lattice strain. Moreover, the creation of hydrogen containing radicals due to enhanced secondary reactions is favoured at elevated pressures [5.8, 5.38]. These radicals have a lower sticking coefficient than Si (prevalent at lower deposition pressures) which will contribute to a lower β value [5.39].

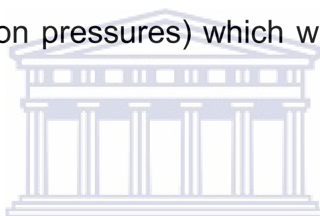

UNIVERSITY of the
WESTERN CAPE

The observed widening of the optical band gap with a growth in the crystalline volume fraction was also observed by Waman *et al.* [5.9], who ascribed it to the presence of tensile stress, i.e. increased Si-Si bonding distances. However, our results show that the optical band gap increased despite the presence of compressive stress at 20 minutes. Given the fact that the average crystallite size as probed by Raman spectroscopy decreased at 20 min while the crystallite volume fraction increased, opens up the possibility of the nucleation of smaller, undetectable crystallites. The presence of these nano-sized crystallites results in the widening of the optical band gap due to the quantum confinement effect [5.3, 5.28].

The static refractive index is an indication of the film density. At 20 min the film density increased due to the decreasing tensile stress (compression). However, as the films become more roughened, voids can form due to shadowing effects, ultimately inducing tensile stress and an optically less dense material at 60 min.

The deposition pressure influenced the film structure, mechanical and optical properties at film thickness below 250 nm. Interestingly, at 60 min the films displayed almost similar crystalline volume fractions, film stress, optical band gap and static refractive indexes for the entire deposition pressure range of 60 – 100 μbar. It was found the crystallization enhances as the thickness of nc-Si:H films increases [5.40]. The similar structural, optical and mechanical properties of nc-Si:H films at 60 min are attributed to a similar crystallinity present at certain thicknesses for a fixed H_2-dilution.

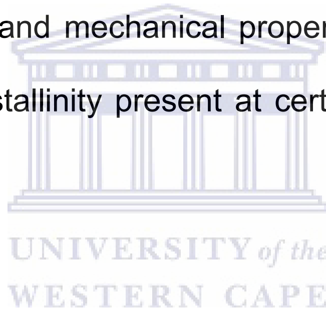
UNIVERSITY of the
WESTERN CAPE

5.5 CONCLUSION

The correlation between the nanostructural, mechanical and optical properties of hot-wire deposited nc-Si:H thin films were investigated as a function of deposition pressure and time. The growth in the crystallite size and the reduction of the lattice strain with increasing deposition pressure are ascribed to the increased atomic hydrogen concentration. The films are composed of voids and particulate regions with dimensions similar to that of the crystallite size, as calculated from x-ray diffraction. At 10 min, all the films were under tensile stress arising from coalescence of grains and the presence of crystallites with sizes < 10 nm.

The expanding crystallites led to a densification of the a-Si network, which counteracted the tensile stress created by the expanded crystallites, leading to a reduction in tensile stress, even compressive stress at $P_{DEP} \leq 80$ µbar at 20 min. A combination of roughening and shadowing effects at 60 min resulted in the formation of voids and ultimately tensile stress. The changes in the static refractive index were correlated with the film stress. The general widening of the optical band gap with a growth in the crystalline volume fraction has been ascribed to the nucleation of smaller nano-crystallites via the quantum confinement effect. After 60 min of deposition, all results indicate that the nanostructural, mechanical and optical properties are less dependent on the deposition pressure.

UNIVERSITY of the
WESTERN CAPE

REFERENCES

5.1 I. Cheng, S. Allen, S. Wagner (2004) J. Non-Cryst. Solids **338-340**:720.

5.2 G. Yue, L. Sivec, B. Yan, J. Yang, S. Guha (2010) Mater. Res. Soc. Symp. Proc. 1245.

5.3 J. H. Shim, S. Im, N. H. Cho (2004) Appl. Surf. Sci. **234**:268.

5.4 H. Li, R. H. Franken, R. L. Stolk, C. H. M. van der Werf, J. K. Rath, R. E. I. Schropp (2008) J. Non-Cryst. Solids **354**:2087.

5.5 P. Gogoi, H. S. Jha, P. Agarwal (2011) Thin Solid Films **519**:4506.

5.6 A. Ledermann, U. Weber, C. Mukherjee, B. Schroeder (2001) Thin Solid Films **395**:61.

5.7 F. Villar, J. Escarré, A. Antony, M. Stella, F. Rojas, J. M. Asensi, J. Bertomeu, J. Andreu (2008) Thin Solid Films **516**:584.

5.8 S. Klein, F. Finger, R. Carius, M. Stutzmann (2005) J. Appl. Phys. **98**:024905.

5.9 V.S. Waman, A.M. Funde, M. M. Kamble, M. R. Pramod, R. R. Hawaldar, D. P. Amalnerkar, V. G. Sathe, S. W. Gosavi, S. R. Jadkar (2011) J. Nanotechnol. **2011**:1.

5.10 S. Halindintwali, D. Knoesen, R. Swanepoel, B. A. Julies, C. Arendse, T. Muller, C. C. Theron, A. Gordijn, P. C. P. Bronsveld, J. K. Rath, R. E. I. Schropp (2007) Thin Solid Films **515**:8040.

5.11 D. Knoesen, C. Arendse, S. Halindintwali, T. Muller (2008) Thin Solid Films **516**:822.

5.12 C. J. Arendse, D. T. Britton, D. Knoesen (2006) Thin Solid Films **501**:92.

5.13 G. Stoney (1909) Proc. R. Soc. London, Ser. A **82**:172.

UNIVERSITY of the WESTERN CAPE

5.14 K. Takimoto, A. Fukuta, Y. Yamamoto, N. Yoshida, T. Itoh, S. Nonomura (2002) J. Non-Cryst. Solids **299-302**:314.

5.15 M. Wakagi, T. Kaneko, K. Ogata, A. Nakano (1993) Mater. Res. Sot. Symp. Proc. **283**:555.

5.16 Y. He, C. Yin, G. Cheng, L. Wang, X. Liu, G. Y. Hu (1994) J. Appl. Phys. **75**:797.

5.17 H.P. Klug & L.E. Alexander (1974), **X-Ray Diffraction Procedures for Polycrystalline and Amorphous Materials**, 2nd edition, Wiley-Interscience Publication, New York.

5.18 T. F. G. Muller, C. J. Arendse, S. Halindintwali, D. Knoesen, R. E. I. Schropp (2011) Thin Solid Films **519**:4462.

5.19 N. A. Bakr, A. M. Funde, V. S. Waman, M. M. Kamble, R. R. Hawaldar, D. P. Amalnerkar, V. G. Sathe, S. W. Gosavi, S. R. Jadkar (2011) J. Phys. Chem. Solids **72**:685.

5.20 A. H. Mahan, R. Biswas, L. M. Gedvilas, D. L. Williamson, B. C. Pan (2004) J. Appl. Phys. **96**:3818.

5.21 J. L. Langford, D. Louër, P. Scardi (2000) J. Appl. Crystallogr. **33**:964.

5.22 R. A. Street (1991) **Hydrogenated Amorphous Silicon**, Cambridge University Press, New York.

5.23 D. Han, K. Wang, JM Owens, L. Gedvillas, B. Nelson, H. Habuchi, M. Tanaka (2003) J. Appl. Phys. **93**:3776.

5.24 C. T. Kirk (1988) Phys. Rev. B **38**:1255.

5.25 A. C. Bronnenberg, A. H. M. Smets, M. Creatore, M. C. M. van de Sanden (2011) J. Non-Cryst. Solids **357**:884.

5.26 M. H. Brodsky, M. Cardona, J. J. Cuomo (1977) Phys. Rev. B **16**:3556.

UNIVERSITY of the
WESTERN CAPE

5.27 N. Maley (1992) Phys. Rev. B **46**:2078.

5.28 C. J. Arendse, G. F. Malgas, T. F. G. Muller, D. Knoesen, C. J. Oliphant, D. E. Motaung, S. Halindintwali, B. W. Mwakikunga (2009) Nanoscale. Res. Lett. **4**:307.

5.29 K. Christova, S. Alexandrova, A. Abramov, E. Valcheva, B. Ranguelov, C. Longeaud, S. Reynolds, P. R. i Cobarrocas (2010) J. Phys.: Conf. Ser. **253**:012056.

5.30 C. V. Thompson, R. Carel (1996) J. Mech. Phys. Solids **44**:657.

5.31 J. A. Floro, P. G. Kotula, S. C. Seel, D. J. Srolovitz (2003) Phys. Rev. Lett. **91**:096101.

5.32 A. McEvoy, T. Markvart, L. Castaner (2011), **Practical Handbook of Photovoltaics: Fundamentals and Applications**, Academic Press. Waltham, USA.

5.33 K. Sharma, M. A. Verheijen, M. C. M. van de Sanden, M. Creatore (2012) J. Appl. Phys. **111**:033508.

5.34 R. W. Smith, D. J. Srolovitz (1996) J. Appl. Phys. **79**:1448.

5.35 P. Meakin (1998), **Fractals, Scaling, Growth far from Equilibrium**, Cambridge University Press, Cambridge.

5.36 J. Gu, Y. Zhou, M. Zhu, F. Liu, J. Liu (2005 J. Cryst. Growth. **285**:491.

5.37 A. Matsuda (1983) J. Non-Cryst. Solids **59/60**:767.

5.38 K. F. Feenstra, R. E. I. Schropp, W. F. van der Weg (1999) J. Appl. Phys. **85**:6843.

5.39 J. Perrin, O. Leroy, M. C. Bordage (1996) Contrib. Plasma Phys. **36**:3.

5.40 C. R. Wronski, B. von Roedern, A. Kołodziej (2008) Vacuum **82**:1145.

UNIVERSITY of the
WESTERN CAPE

CHAPTER 6

DEGRADATION OF A TANTALUM FILAMENT DURING THE HWCVD OF SILICON NITRIDE

ABSTRACT

A tantalum filament experienced degradation during the hot-wire chemical vapour deposition of silicon nitride. Novel electron backscatter diffraction measurements revealed that Ta and some of its nitrides (Ta_2N and TaN) and silicides (Ta_2Si, Ta_3Si, and α-Ta_5Si_3) formed at the hotter centre filament regions. The deposition of β-Si_3N_4 and the growth of the metastable Ta_5Si_3, α-Ta_5Si_3, Ta_3Si, Ta_2Si, Ta_2N, and TaN, phases within and around a Ta core occurred at the cooler filament ends. The filament has a recrystallized Ta inner core with nanosized Ta grains at the cooler ends. Time-of-flight secondary ion mass spectroscopy disclosed the presence of H, N and Si containing ions within the aged filament bulk. Hardness measurements revealed that the Ta core experienced significant hardening, whereas the silicides and nitrides were harder but more brittle. The microstructural evolution of the aged Ta-filament can be ascribed to the thermal gradient along the filament length, distribution and concentration of Si, N and H containing areas within the filament and the recrystallizing Ta core. The filament failure at the centre region is ascribed to the combined effects of pore formation, crack growth and the different thermal expansion amongst the various phases, which are all enhanced at the hotter regions.

UNIVERSITY of the WESTERN CAPE

6.1 INTRODUCTION

The hot-wire chemical vapour deposition (HWCVD) technique has shown great potential as a viable alternative to plasma enhanced CVD (PECVD) for the mass production of silicon nitride [6.1, 6.2]. Control over the HWCVD conditions ensured a close to stoichiometric N/Si ratio and an enhanced mass density, which is important for applications as anti-reflective and passivation coatings for solar cells [6.3]. HWCVD has also shown the ability to synthesize SiN_x layers with embedded silicon quantum dots, which may be useful for applications in light emitting materials [6.4].

The most striking feature, however, of HWCVD is its superior SiN_x growth rates compared to PECVD [6.2] and the absence of ion bombardment during the deposition. These advantages of HWCVD are directly linked to the efficient dissociation process of the precursor gas mixtures (usually SiH_4 and NH_3) in the vicinity of a heated filament and also with the addition of H_2 gas [6.5].

UNIVERSITY of the
WESTERN CAPE

Despite the obvious advantage that the heated filament grants to HWCVD, few studies have been reported on the interaction of nitrogen-containing gases and the filament. Weissenbacher *et al.* [6.6] reported on the pre-nitridation of Ta-filaments as a means to prevent filament failure during the HWCVD of boron-carbon-nitrogen layers. They found that the exposure of a Ta-filament (heated to 2000 °C) to a N_2 ambient at 12 mbar resulted in the formation of a Ta_2N layer encapsulating a Ta inner core.

In contrast, Verlaan *et al.* [6.7] did not observe any Ta-nitride phases forming during the HWCVD of a-SiN_x:H layers at a filament temperature of 2300 °C and deposition pressures ranging from 0.2 - 0.8 mbar. Instead, they found a relatively unchanged Ta phase at the centre regions of the filament and the deposition of SiN_x layers at the filament ends near the cooler contacts.

In this study we used Ta-filaments heated to 1600 °C in a $NH_3/SiH_4/H_2$ ambient to synthesized a-SiN_x:H layers at very promising growth rates despite the relative low deposition pressure and precursor gas flow rates used (refer to Chapter 7). Regardless of these promising deposition conditions and the filament pre-treatment, as suggested by Knoesen *et al.* [6.8], the Ta-filament experienced failure at the end of the deposition after a total of five 1 hour depositions. The origins for the filament degradation are identified based on elemental, microstructural and mechanical properties of the aged filaments.

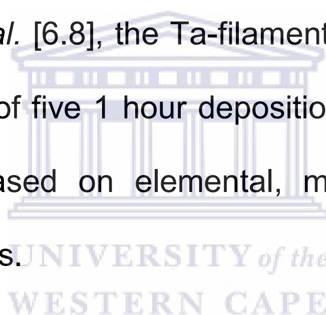
UNIVERSITY of the
WESTERN CAPE

6.2 EXPERIMENTAL DETAILS

A Ta-filament with a diameter of 244.8 ± 10.0 μm and length ~ 1 m, prepared according to a standard process [6.8], was used to synthesize SiN_x thin films at a filament temperature of 1600 °C using an MVSystems HWCVD reactor. The deposition pressure, substrate temperature, silane flow rate and hydrogen flow rate were fixed to 150 μbar, 240 °C, 2 sccm and 27 sccm, respectively. The only deposition variable was the NH_3 flow rate, which was changed from 1 to 3 sccm (in increments of 0.5 sccm). The same filament was used for all the SiN_x depositions and lasted for five 1 hour depositions.

The filament failure occurred at the centre regions as shown in figure 6.1, in contrast to that usually observed for nc-Si:H [6.9] and a-Si:H depositions [6.8] where the filament burns through at the areas close to the electrical contacts.

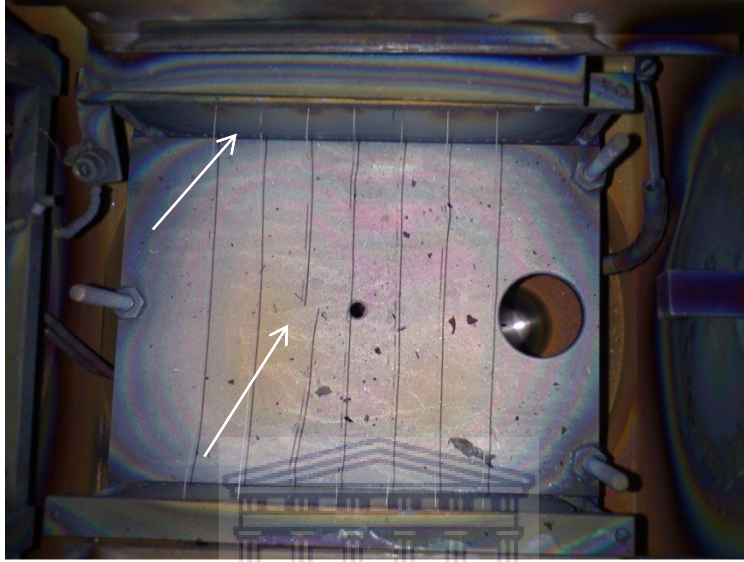

Figure 6.1: Photo showing the aged Ta-filament. The arrows indicate the cooler ends and the centre regions where failure occurred.

UNIVERSITY of the
WESTERN CAPE

The Ta-filament was subsequently carefully removed from the HWCVD reactor in order to limit any mechanical disturbances. Multiple regions were sampled along the length of the filament. Cross-sections of the aged Ta-filaments were metallographically prepared from the centre (hotter) and the ends (colder) regions using a series of coarse and fine grinding discs, polishing and then final polishing by means of ~ 40 nm colloidal silica suspension.

The microstructure of the cross-sections was analysed using optical microscopy and a LEO 1525 field-emission gun scanning electron microscope (FEGSEM). Backscatter and secondary electron images were accumulated to distinguish the phases present and the morphology of the filaments. Electron backscatter diffraction (EBSD) analysis was performed using the OXFORD INCA Crystal software. Energy dispersive x-ray spectroscopy (EDS) was performed using the OXFORD Energy software. EBSD and EDS analysis were performed at an acceleration voltage of 25 kV and 20 kV, respectively. The elemental composition of the filament was probed using an ionTOF ToF-SIMS5 time-of-flight secondary ion mass spectroscopy (TOF-SIMS). Elemental maps of the aged filaments were accumulated after sputtering the surface with oxygen ions.

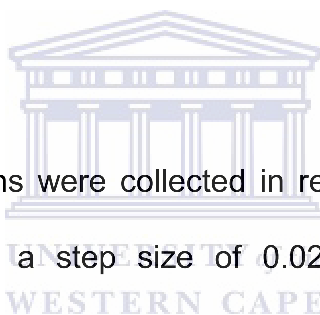

X-ray diffraction (XRD) patterns were collected in reflection geometry at 2θ-values ranging from 10 – 90° with a step size of 0.02°, using a PANalytical XPert diffractometer operated at 45 kV and 40 mA. Copper K_{α} radiation with a wavelength of 1.5406 Å was used as the X-ray source. The XRD patterns were indexed using the database maintained by the International Centre for Diffraction Data (ICDD) [6.10]. Vickers microhardness measurements were carried out using a FM-700 Microhardness Tester. Indentations were performed at a load of 0.05 kg and a dwell time of 10 s.

6.3 RESULTS

Figure 6.2 compares the filament surface in the as-delivered state (pure) and at the ends (contact regions) after exposing it to the $SiH_4/NH_3/H_2$ atmosphere at 1600 °C. A thick layer is visible on the filament surface after the deposition. Energy dispersive x-ray spectroscopy (EDS) revealed that this layer is composed of 48 at % Si and 52 at% N; i.e. the filament acts as a high temperature substrate for the deposition of non-stoichiometric silicon nitride. Verlaan *et al.* [6.8] also reported on the deposition of solid SiN_x layers at the cooler ends of the filament. The morphology of the silicon nitride layer varied along the filament's length, with some regions displaying the characteristic prism shaped β-Si_3N_4 [6.11].

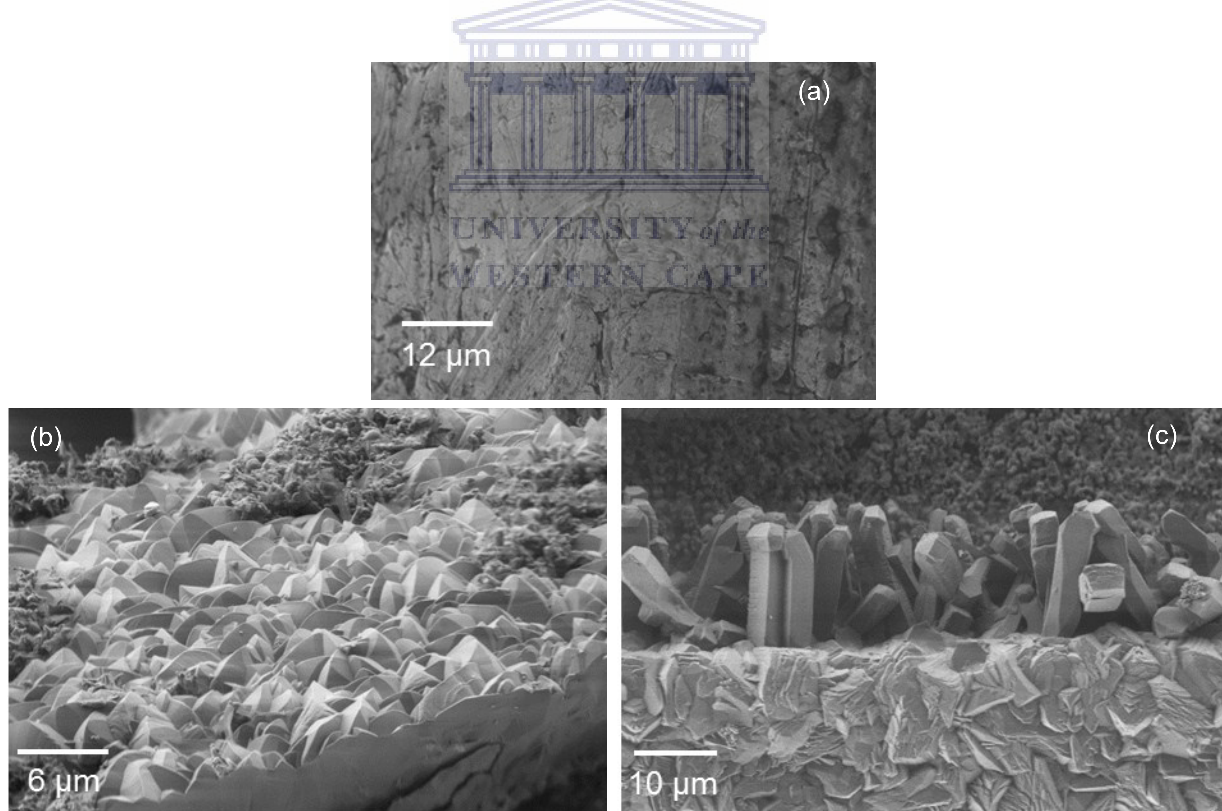

Figure 6.2: Secondary electron (SE) micrographs showing the surface of (a) pure and (b), (c) aged filament.

Figure 6.3 presents backscatter electron (BSE) micrographs revealing the internal structure of the pure and aged filament ends. The filament diameter increased to 341.01 ± 10.17 μm. Cracks are also visible extending from the filament surface into the bulk. The contrast in the backscatter signal is proportional to the atomic number; with low atomic number elements such as silicon and nitrogen appearing darker than heavier elements such as tantalum. However, the contrast in a BSE image is also influenced by the grain orientation (refer to Chapter 3). This is clearly illustrated in the pure filament cross-section where the orientations of the grains allow for the channelling of the incident electron beam, thereby resulting in contrast based on crystal orientation.

UNIVERSITY of the
WESTERN CAPE

The darker silicon nitride layer, with uniform thickness of 15.21 ± 2.18 μm, encapsulates the filament (see Figure 6.3c). Moving radially inward, a slightly brighter layer is visible with grains aligned radially inward, indicating a diffusion based growth. The core of the aged filament is comprised of areas with different contrasts. The identification of the regions with differing contrast is difficult based solely on BSE images and EDS. In fact, Figure 6.4 shows that the EDS analysis indicated similar atomic percentages for the dark and brighter regions within the filament bulk (~ 10 at% N, 18 at% Si and 72 at% Ta). Performing elemental analysis on the areas is also uncertain considering the overlap of $Ta_{M\alpha}$ and $Si_{K\alpha}$ peaks in EDS as shown in Figure 6.4b.

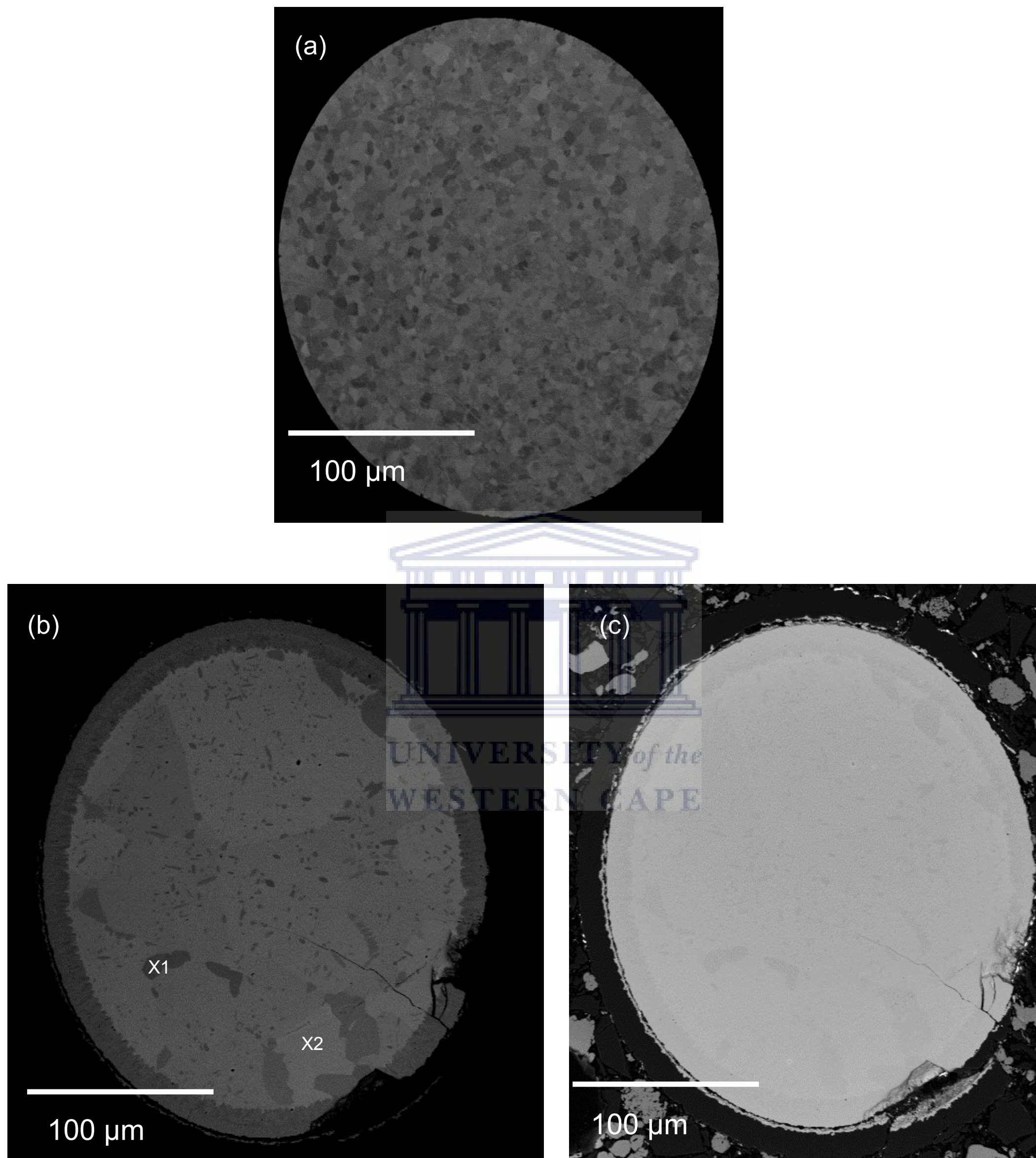

UNIVERSITY of the
WESTERN CAPE

Figure 6.3: BSE micrographs of (a) the pure Ta-filament and (b) aged filament. (c) SE micrograph of image (b) revealing an outer layer. X1 and X2 indicates the areas where EDS was performed.

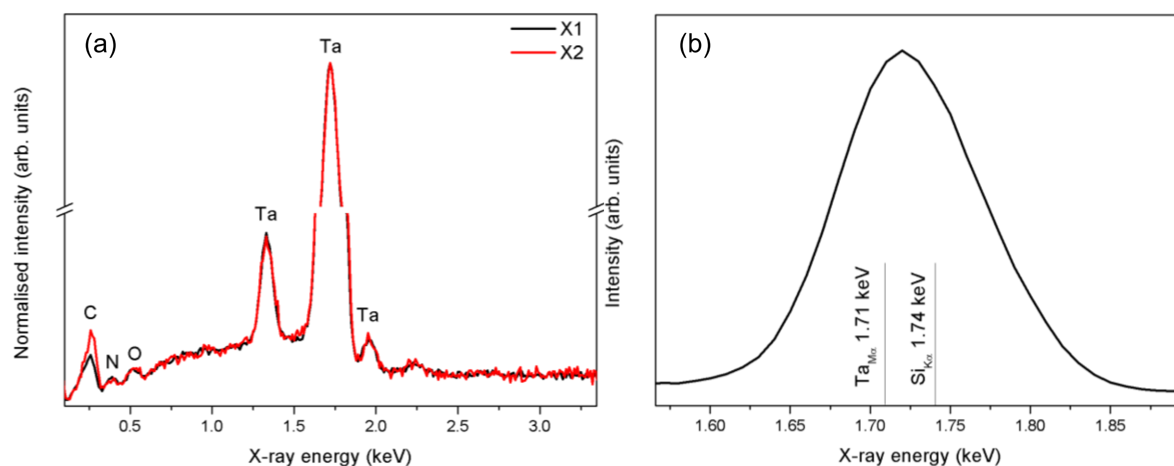

Figure 6.4: EDS spectra of (a) areas marked with X1 and X2 in Figure 6.3b and (b) illustrating the overlap in $Ta_{M\alpha}$ and $Si_{K\alpha}$ peaks.

UNIVERSITY of the
WESTERN CAPE

TOF-SIMS analysis was therefore performed to identify the elements present of the aged cross-section sampled from the ends. Figure 6.5 shows TOF-SIMS elemental maps revealing the locations of the N, Ta and Si containing ions. The TOF-SIMS results corroborates with the EDS analysis on the presence of a silicon nitride layer on the filament surface. In addition, TOF-SIMS revealed that SiH and Si are prominent within the silicon nitride layer. The layer below the silicon nitride layer and the filament bulk contained regions of TaN and TaO_2. Interestingly, there seems to be significant signals of H and TaH within the filament bulk. The areas rich in C corresponds the resin used to mount the sample.

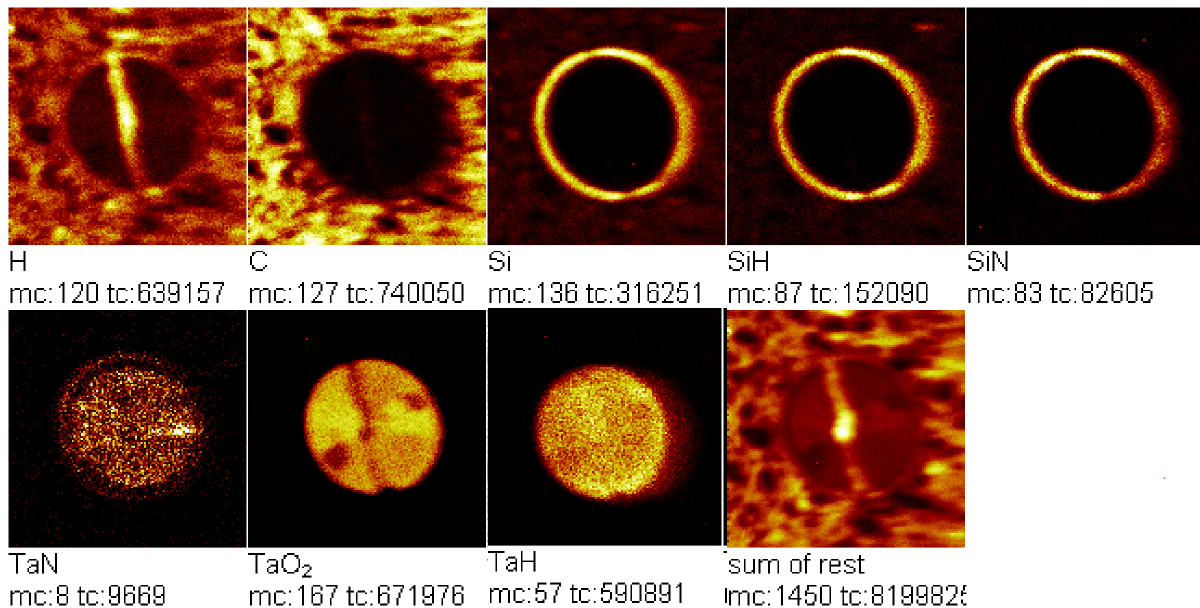

Figure 6.5: TOF-SIMS elemental maps of the aged Ta-filament sampled from the ends.

UNIVERSITY of the
WESTERN CAPE

The TOF-SIMS analysis provided a wealth of information pertaining to the elemental composition of the filament. However, the regions of contrast in the filament bulk remain obscure. EBSD was subsequently used to further scrutinize the microstructure of the aged filament at the ends. Figure 6.6 shows EBSD phase maps of the cross-section of the aged filament sampled from the ends. Six phases are identified in decreasing order of prominence namely: Ta, Ta_2N, Ta_2Si, α-Ta_5Si_3, TaN, Ta_5Si_3 (metastable), Ta_3Si and β-Si_3N_4. The Ta-silicides are present at the outer perimeters of the filament. However, it is not presently clear the reason why TOF-SIMS in both positive and negative modes did not detect Ta-silicides.

The outer silicon nitride layer did not show any Kikuchi patterns as it experienced considerable beam damage at an accelerating voltage of 25 kV. Lowering the accelerating voltage did not induce a detectable EBSD signal. As a result, it was not possible in the current system to perform EBSD of the outer silicon nitride layer.

The EBSD phase map shown in Figure 6.7 discloses that the dark areas of contrast in the filament bulk are predominantly Ta_2N regions. Moreover, porosity is prevalent throughout the filament bulk, occupying spaces at grain boundaries and within the grains. Figure 6.8 shows the Ta grain map, which discloses that the Ta_2N regions formed within Ta grains and especially at the Ta grain boundaries.

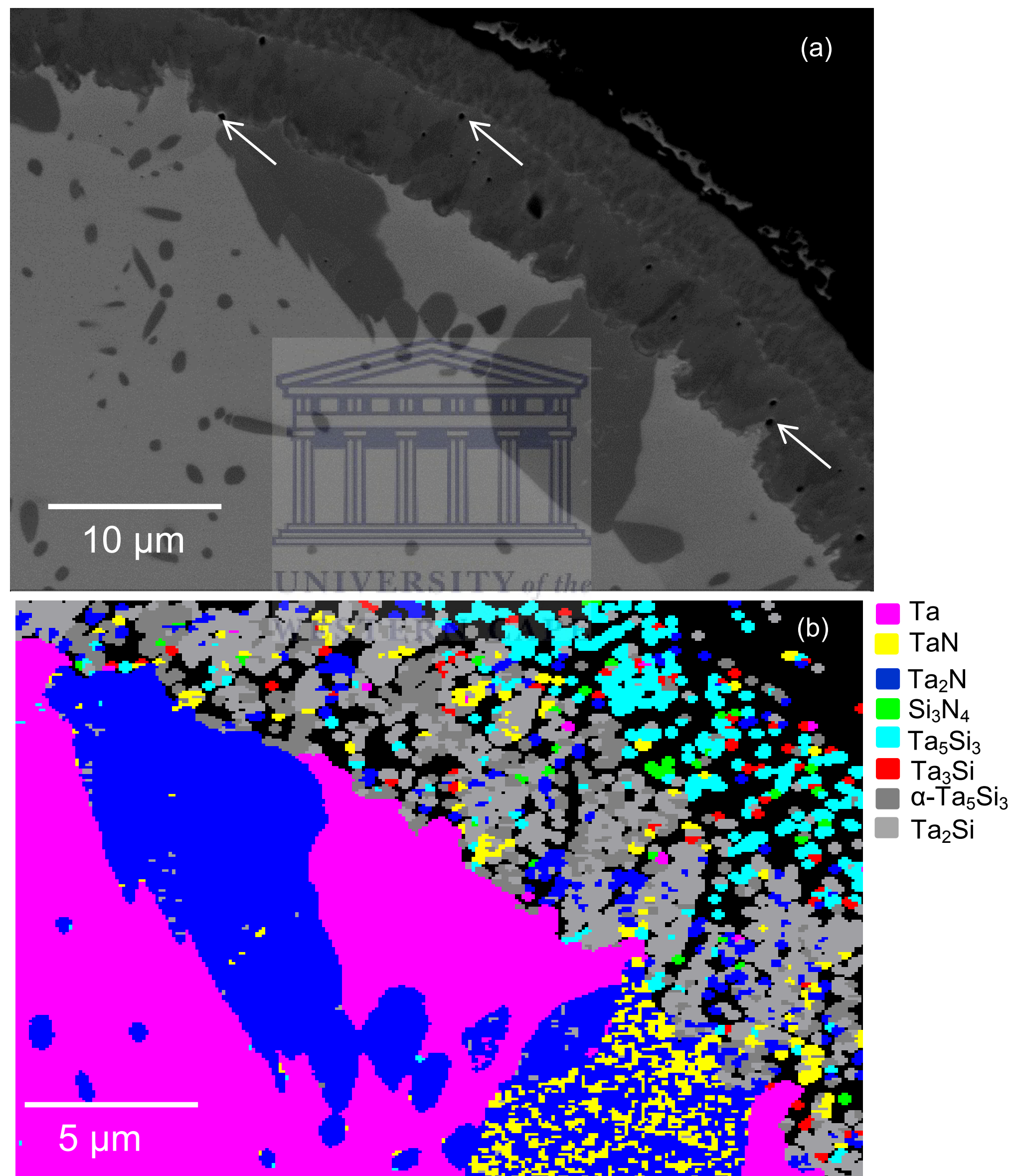

Figure 6.6: (a) BSE image of the filament edge and (b) corresponding EBSD phase map. The arrow shows the location of pores.

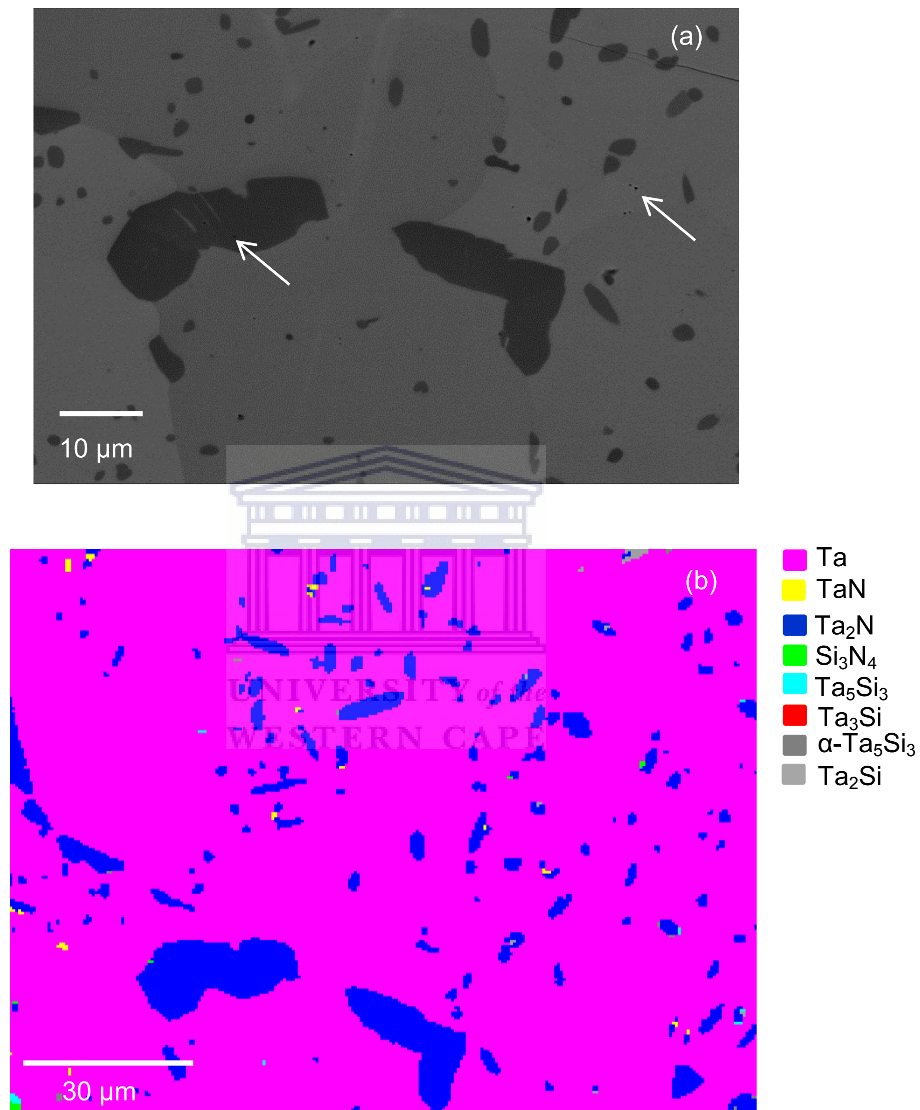

Figure 6.7: (a) BSE image with arrows showing the pores and (b) corresponding EBSD phase map of the aged filament core.

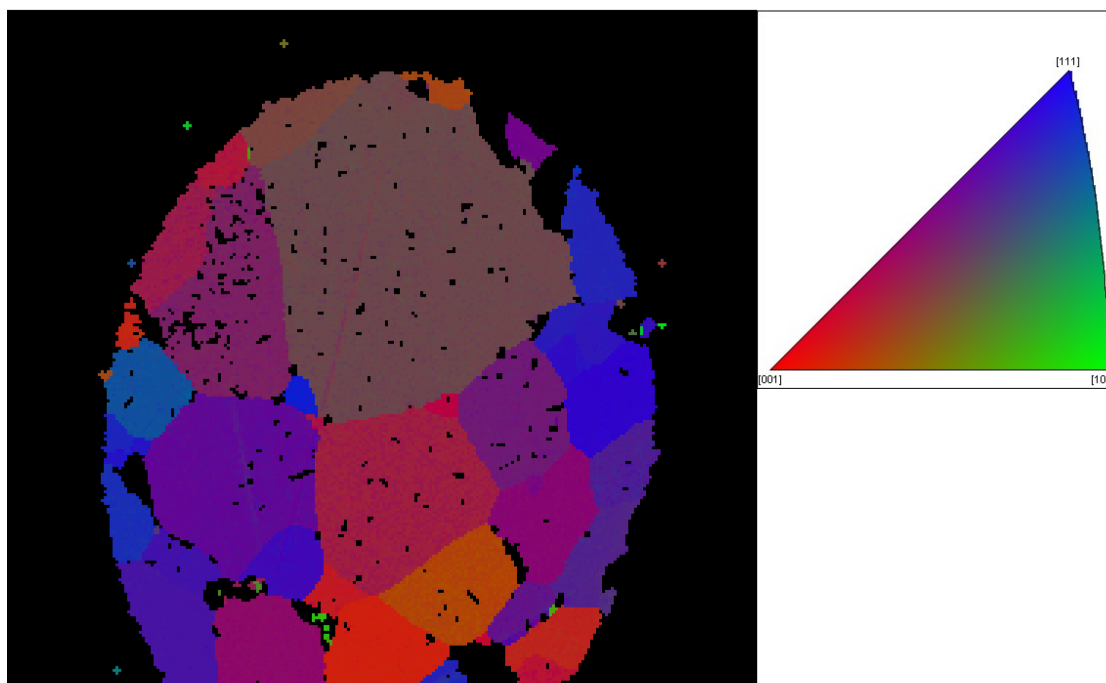

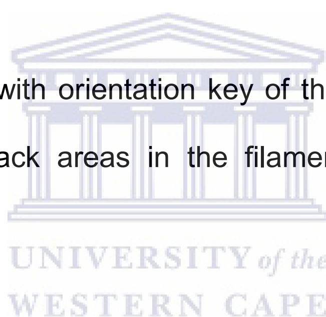
UNIVERSITY of the
WESTERN CAPE

Figure 6.8 EBSD grain map with orientation key of the aged Ta-filament sampled from the ends. The black areas in the filament bulk are regions where Ta_2N formed.

Figure 6.9 shows a SE image of the aged filament-surface from the centre regions. No detectable SiN_x deposition occurred and pores are prevalent at grain boundaries. Figure 6.10 presents a BSE image of the centre filament cross-section. In contrast to the end regions, the filament diameter increased slightly to 272.25 ± 3.39 μm and a thicker Ta-silicide layer, of thickness 27.35 ± 3.67 μm, is present. The cracks and pores are also more pronounced compared to the end regions. Figure 6.11 shows EBSD phase maps of the centre cross-sections revealing the presence of the Ta, TaN, Ta_2N, α-Ta_5Si_3, Ta_5Si_3, $TaSi_2$ and Ta_2Si phases. Moreover, the concentration of the Ta_2N phase is enhanced at the centre compared to the ends and extents from the outer regions of the filament into the bulk more effectively than at the ends.

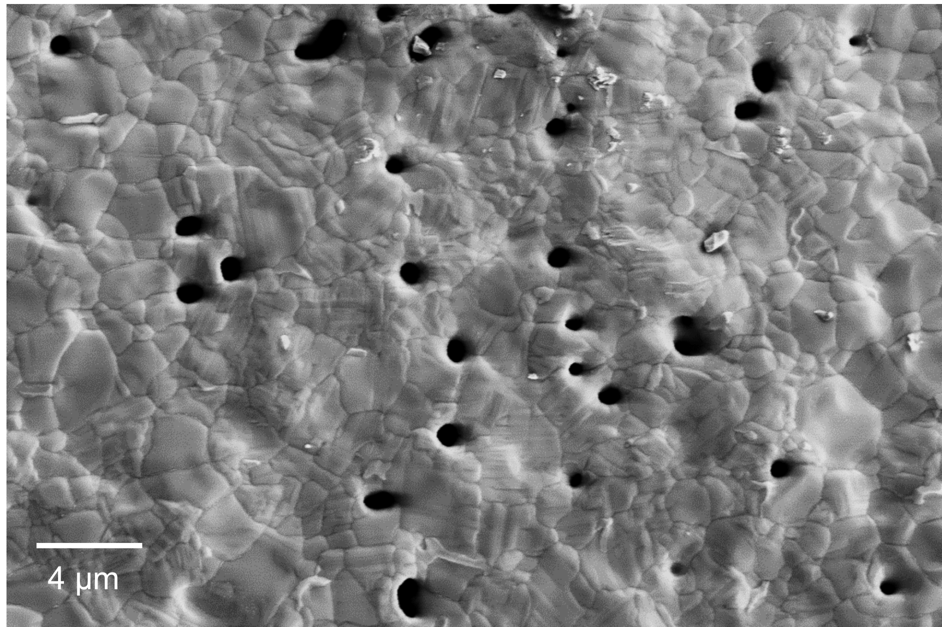

Figure 6.9: SE micrograph of the centre filament-surface.

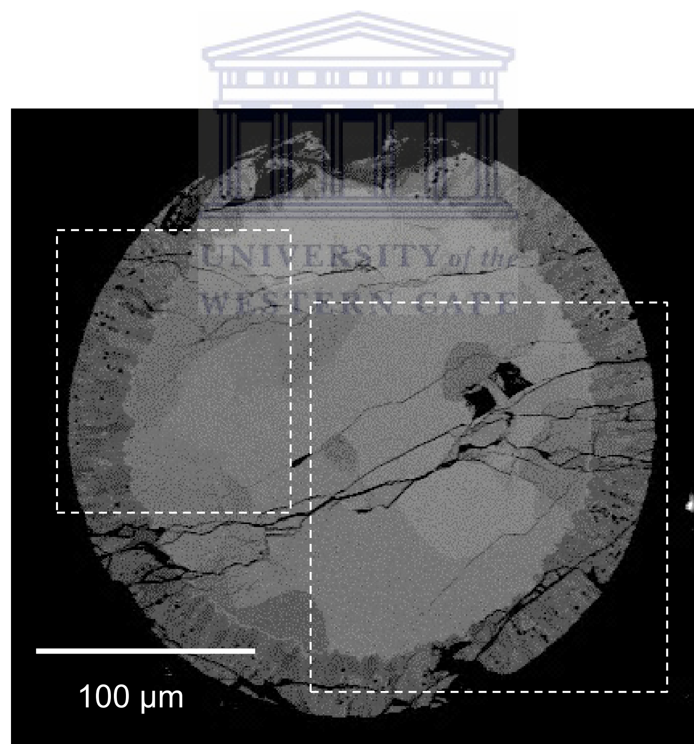

Figure 6.10: BSE micrograph of the filament sampled from the center regions. The areas marked by squares are regions were EBSD was performed.

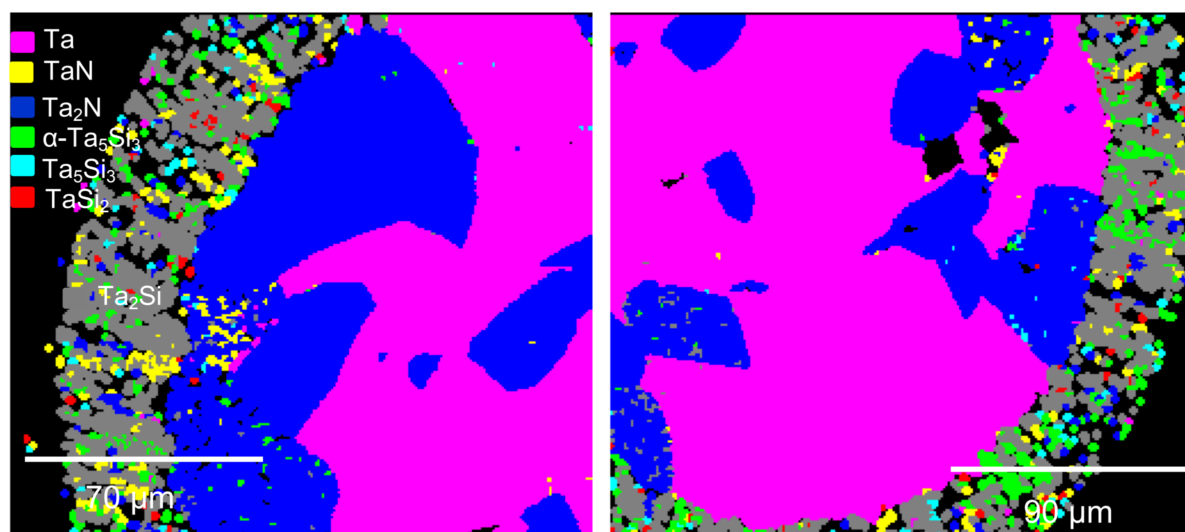

Figure 6.11 EBSD phase maps of the centre filament regions highlighted in Figure 6.10.

UNIVERSITY of the
WESTERN CAPE

Figure 6.12 presents optical micrographs of the aged filament sampled from the ends and from the centre. The pronounced presence of the Ta_2N and Ta-silicide phases in addition to the absence of the Si_3N_4 layer is noticeable for the centre regions. The centre regions also possessed larger pore sizes. Cracks appear to radiate from the pore regions and branches out upon entering Ta_2N regions. The presence of cracks indicates that the aged filament is brittle.

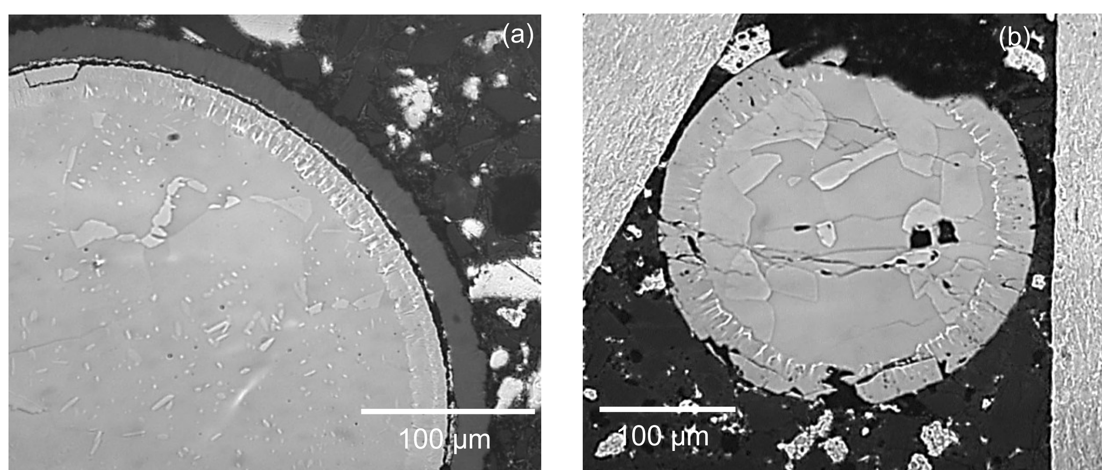

Figure 6.12: Optical micrographs of the aged filament sampled from the (a) ends and (b) centre regions. The arrows show the position of pores and cracks.

Presented in Figure 6.13 are XRD patterns of the pure and aged filaments. The XRD analysis corroborates the EBSD findings on the presence of Ta, Ta_2Si, Ta_3Si, α-Ta_5Si_3, Ta_5Si_3 (metastable), Ta_2N, TaN and β-Si_3N_4 phases at the ends. The same phases are present at the centre except for the β-Si_3N_4, Ta_3Si and the Ta_5Si_3 (metastable). XRD did not detect the $TaSi_2$ phase at the centre regions contrary to the EBSD analysis. A possible reason for this discrepancy is the relatively low concentration and crystallite size of the $TaSi_2$ phase, which will minimise its contribution to the XRD pattern. Interestingly, the Ta XRD peaks at the ends displayed broadening which indicate strained, nano sized grains of Ta. The grain size of the nano Ta grains calculated from the Debye equation (corrected for strain broadening) [6.12] amounted to ~ 6 nm.

UNIVERSITY of the
WESTERN CAPE

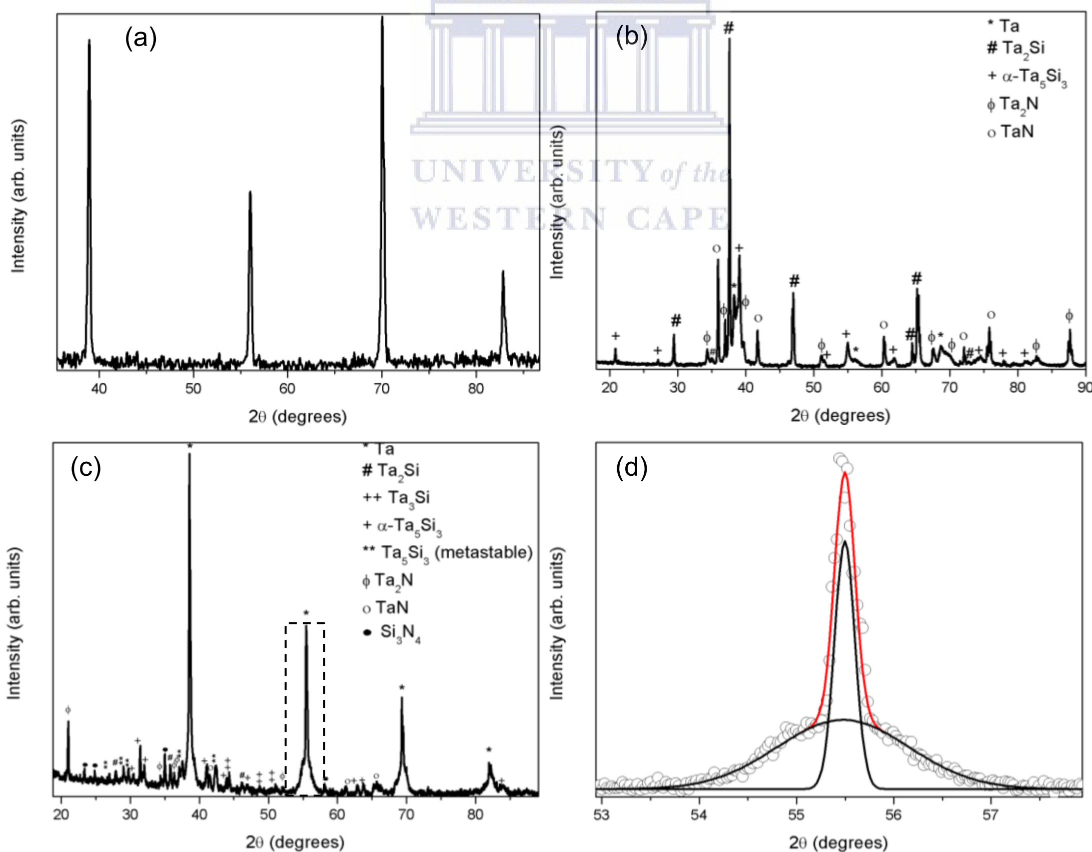

Figure 6.13: XRD patterns of (a) pure Ta, (b) centre, (c) ends and (d) Ta peak deconvolution of the highlighted region in (c).

Table 6.1 presents the microhardness values at different regions within the filament. The Ta phase experienced significant hardening during ageing to values of 7.493 GPa and 12.41 GPa at the ends and centre, respectively. However, the Ta_2N phase possessed a hardness almost half that of the reference value of 30 GPa. The hardness of the silicides and β-Si_3N_4 phases compared well with the values reported in literature.

Table 6.1: Hardness values of the filament compared to literature (where available).

Phase	Hardness at ends (GPa)	Hardness at centre (GPa)	Literature (GPa)
Ta (pure)	1.079		0.9 [6.13]
Ta (aged)	7.493	12.41	0.98-11.77 for 0-16 at% N [6.14]
Ta_2N	17.08	17.04	30 [6.15]
Ta_5Si_3 (metastable)	10.26	-	11.77 -14.71 [6.13]
α-Ta_5Si_3 +Ta_2Si	14.57	-	Ta_2Si-10.29 (This thesis) α-Ta_5Si_3-16.20 [6.16]
Ta_2Si		14.54	
β-Si_3N_4	15.85	-	17.20 [6.15]

UNIVERSITY of the WESTERN CAPE

6.3 DISCUSSION

A heated Ta-filament was exposed to a gas mixture of $SiH_4/NH_3/H_2$ and experienced degradation during the HWCVD of SiN_x. Weissenbacher *et al.* [6.6] reported on the interaction of NH_3 with heated Ta-filaments. They found that the Ta-filament surface transformed to Ta_2N encapsulating a Ta core. In contrast, Verlaan *et al.* [6.7] reported no Ta_2N phase formation and a relatively unchanged Ta-filament. A possible reason for the discrepancies may be related to the difference in deposition pressure, i.e. number of N molecules (12 mbar [6.6] versus 200 - 800 µbar [6.7]).

However, in this study we used a lower deposition pressure of 150 µbar, a reduced filament temperature of 1600 °C and inferior NH_3 flow rates of 1 – 3 sccm. Despite these lower deposition parameters, we observed the transformation of the pure Ta-filament to Ta-silicides, nitrides and even solid depositions of a Si_3N_4 layer at the cooler regions. The deviation from previous investigations may be related to less evaporation of Si and N containing radicals from the filament-surface at 1600 °C and the addition of H_2 gas to the precursor gas mixture used in this study. An increase in atomic hydrogen is expected at higher NH_3 flow rates, which further dissociates other precursor gases [6.5]. This enhancement in the dissociation rates of the precursor gases brings about superior numbers of N and Si containing radicals. The N and Si containing radicals diffuse into the heated Ta-filament to form various silicides and nitrides depending on the concentration of N and Si atoms [6.17].

The coexistence of Ta_2N and Ta within the filament bulk is justified based on the Ta-N phase diagram [6.17]. In addition, the diffusion lengths of H and N are expected to be larger than that of Si. N and H will therefore diffuse more effectively into the filament bulk. The diffusion paths are most likely along the Ta grain boundaries, which ultimately become preferred sites for Ta_2N formations. Silicon will accumulate at the filament edges as it will become more difficult for it to diffuse through the N and H containing Ta phase eventually resulting in the growth of Ta-silicides at the filament perimeter, similar to that reported for nc-Si:H thin film depositions [6.9]. The higher temperature at the filament centre leads to a higher concentration of Si, N and H containing radicals. Consequently, this result in a superior silicide thickness and higher concentrations of the Ta_2N phase compared to the ends regions.

Porosity was observed throughout the filament, particularly at the grain boundaries. The evaporation of Ta may not contribute considerably to the formation of pores since the filament temperature was ~ 1600 °C. Enhanced gas pressure within the filament itself is the more probable cause for the formation of the pores. Specifically, the accumulation of N, Si and H containing molecules can form gas (instead of Ta-silicides or nitrides) that results in the increase of pressure within some regions to such an extent that bubbles (pores) form. Verlaan *et al.* [6.7] also observed gas porosity in their filament study and ascribed it to the formation of N_2 gas. In our case, Si and H containing gases can also contribute to the formation of gas porosity. Moreover, the pores will tend to form at grain boundaries as these are the diffusion paths for Si, H and N.

UNIVERSITY of the
WESTERN CAPE

The hardness of the aged Ta was found to increase drastically to ~ 4X and ~6X that of the pure Ta at the filament ends and centre, respectively. There are several factors in this study that can induce hardening of Ta. Hardening in metals corresponds mainly to the minimisation or suppression of movement of dislocations in the crystal lattice [6.18]. There are three main routes for hardening metals namely: grain size reduction, solid solution hardening and strain (age) hardening [6.18]. Reducing the grain size inhibits the movement of dislocations as the orientation varies drastically from each grain to the next; this is known as the Hall-Petch relationship. However, this holds for grains down to ~ 10 nm; below this limit the grains slip more easily thereby weakening the metal [6.19]. Strain hardening occurs when the concentration of dislocations saturates by repeatedly deforming (e.g. hammering, rolling) a metal.

Strengthening by solid solution may be more appropriate in our case. The solid solution of N, H and Si within Ta grains may act as defects within the Ta crystal lattice that create strain fields that inhibits dislocation movement, ultimately improving the hardness of the material. The concentration and diffusion of Si, N and H containing radicals are enhanced at the hotter, centre regions, which induce a superior hardness in Ta compared to the end regions. In addition to the solid solution of N, Si and H in Ta, another contributor to minimising dislocation movements is the presence of a harder phase, i.e. the Ta_2N phase in our case.

The value of the Ta_2N phase is almost half that of the referenced value of 30 GPa [6.15]. This may be attributed to a less dense Ta_2N phase in our case, which is not unrealistic considering the presence of pores within the filament. Despite the increased hardness of the aged Ta-filament, the main concern is the observed brittle structure of the entire degraded filament.

The origin of the filament failure at the centre regions during the HWCVD of SiN_x thin films may be explained as follows. Gas porosity and embrittlement are enhanced at the hotter centre regions due to the increased incorporation of N, H and Si containing gases. Eventually the gas pressure within the pores reaches considerable magnitudes, initiating cracks that travel through the embrittled filament. Additionally, the different thermal expansion properties of the phases in the aged Ta-filament induce stress within the filament, which may also assists in crack formation/growth. Consequently, the enhancing pore size and different thermal properties of the aged filament induces failure at the centre regions.

WESTERN CAPE

6.3 CONCLUSION

The Ta-filament experienced significant structural changes during the HWCVD of SiN_x. The addition of H_2 to the precursor gas mixture enhanced the concentration of Si and N containing radicals, which diffused into the filament. SEM, XRD and EBSD concurred on the formation of a recrystallized Ta core and some of its nitrides (Ta_2N and TaN) and silicides (Ta_2Si, Ta_3Si, α-Ta_5Si_3) formed at the hotter centre filament regions while the deposition of β-Si_3N_4, and the growth of the metastable Ta_5Si_3, α-Ta_5Si_3, Ta_3Si, Ta_2Si, Ta_2N, TaN phases appeared at the cooler filament ends. The

hardness measurements showed that the aged Ta core experienced significant hardening due to the solid solution of N, Si and H in Ta. The filament failed at the hotter centre due to the enhanced rates of pore formation and different thermal expansion properties of the different phases constituting the aged filament.

REFERENCES

6.1 R. E. I. Schropp (2009) Thin Solid Films **517**:3415.

6.2 V. Verlaan, Z. S. Houweling, C. H. M. van der Werf, I. G. Romijn, A. W. Weeber, H. D. Goldbach , R. E. I. Schropp (2008) Thin Solid Films **516**:533.

6.3 V. Verlaan, Z. S. Houweling, C. H. M. van der Werf, I. G. Romijn, A. W. Weeber, H. F. W. Dekkers, H. D. Goldbach, R. E. I. Schropp (2007) Prog. Photovolt. Res. Appl. **15**:563.

6.4 A. K. Panchal, C. S. Solanki (2009) Journal of Crystal Growth **311**:2659.

6.5 A. H. Mahan, A. C. Dillon, L. M. Gedvilas, D. L. Williamson, J. D. Perkins (2003) J. Appl. Phys. **94**:2360.

6.6 R. Weissenbacher, R. Haubner, K. Aigner, B. Lux (2002) Diamond and Related Materials **11**:191.

6.7 V. Verlaan, C. H. M. van der Werf, C. J. Oliphant, R. Bakker, Z. S. Houweling, R. E. I. Schropp (2009) Thin Solid Films **517**:3435.

6.8 D. Knoesen, C. Arendse, S. Halindintwali, T. Muller (2008) Thin Solid Films **516**:814.

6.9 C. J. Oliphant, C. J. Arendse, S. N. Prins, G. F. Malgas, D. Knoesen (2012) J. Mater. Sci. **47**:2405.

6.10 ICDD card numbers: Ta (04-008-3222), Ta_3Si (04-005-5965), Ta_2Si (04-004-7298), α-Ta_5Si_3 (04-004-7245), metastableTa_5Si_3 (04-004-7297), Ta_2N (04-003-4166), TaN (04-015-1263), β-Si_3N_4 (04-013-1344).

6.11 O. R. Monteiro, Z. Wang, I. G. Brown (1996) J. Mater. Sci. **31**:6029.

6.12 H. P. Klug, L. E. Alexander (1974), **X-Ray Diffraction Procedures for Polycrystalline and Amorphous Materials**, 2nd edition, Wiley-Interscience Publication.

6.13 F. Cardarelli (2008), **Materials Handbook: A Concise Desktop Reference**, 2nd edition, Springer-Verlag.

6.14 T. E. Tietz, JW Wilson (1965), **Behaviour and Properties of Refractory Metals, Technology and Engineering**.

6.15 A. Cavaleiro, J. T. M. de Hosson (editors) (2006), **Nanostructured Coatings**, Springer Science+Business Media,

6.16 K. H. Stern (editor) (1996), **Metallurgical and Ceramic Protective Coatings**, Chapman and Hall UK.

6.17 T. B. Massalski (1990), **Binary Alloy Phase Diagrams**, 2nd edition, vol. 3, ASM International.

6.18 W. D. Callister, D. G. Rethwisch (2011), **Fundamentals of Materials Science and Engineering: An Integrated Approach**, John Wiley and Sons.

6.19 C. A. Schuh, T. G. Nieh (2003) Mat. Res. Soc. Symp. Proc. **740**:27.

UNIVERSITY of the
WESTERN CAPE

CHAPTER 7

STRUCTURAL AND OPTICAL PROPERTIES OF SiN_x FABRICATED BY HOT-WIRE CVD

ABSTRACT

Silicon nitride thin films were synthesized at promising growth rates from gas mixtures consisting of SiH_4, NH_3 and H_2 using hot-wire chemical vapour deposition. Initially, the samples are biphasic in that they consist of both Si-Si and Si-N regions. Increasing the NH_3 flow rate resulted in the increase of the N content and Si-N bonding at the expense of the Si and hydrogen content within the films. Energy dispersive x-ray spectroscopy (EDS) and x-ray photoelectron spectroscopy (XPS) gave similar atomic N/Si ratios. Raman spectroscopy revealed that the incorporation of N within the film reduces the ordering of the Si-Si regions. Transmission electron microscopy and electron energy loss spectroscopy discloses that samples are amorphous, dense and contain a nitrogen rich silicon oxynitride interface with the Si substrate. The film stress is compressive for Si- and H-rich silicon nitride films and changes to tensile stress as the N content increases. The optical properties (refractive index and optical band gap) were found to vary linearly with the N/Si ratio. A relationship between the HWCVD synthesis conditions, the film composition, stress, microstructure and optical properties is also discussed.

UNIVERSITY of the WESTERN CAPE

7.1 INTRODUCTION

Silicon nitride (SiN_x) is an important dielectric that enjoyed active research interest during the last few decades. SiN_x has been applied as surface and bulk passivation layers for solar cells [7.1], thin film transistors [7.2], antireflection coatings [7.3] and has shown promise as a light emitting material [7.4]. The wide application scope of SiN_x can be attributed to its refractive index, optical band gap, structural properties and molecular composition; all of which can be tuned by varying the deposition conditions [7.1, 7.5, 7.6].

Plasma enhanced chemical vapour deposition (PECVD) is the conventional synthesis technique for manufacturing SiN_x thin films. An alternative technique for the synthesis of SiN_x is hot-wire chemical vapour deposition (HWCVD). Compared to PECVD, samples synthesized by HWCVD experience no ion bombardment and can be deposited at higher deposition rates [7.7]. Despite the numerous studies on the synthesis of SiN_x from SiH_4 and NH_3 gas mixtures, reports on the effect of adding H_2 to the process gasses on the structure-property relationship of SiN_x thin films has received less attention [7.8 - 7.10]. The benefits of adding H_2 to the usual NH_3 / SiH_4 gas mixture include an enhanced incorporation of N into the thin film, NH_3 flow rates down to 5 sccm and film conformity on the substrate [7.8 - 7.10]. In most cases, the filament temperature during the HWCVD of SiN_x films were > 1700 °C [7.1 – 7.3, 7.5, 7.7 – 7.11], which can lead to filament metal impurities incorporated into the films [7.9, 7.12].

In this study, we employ HWCVD to deposit transparent, low reflection, dense amorphous SiN_x thin films from a SiH_4 / NH_3 / H_2 gas mixture at a substrate temperature of 240 °C and a filament temperature of ~ 1600 °C. The total gas flow rate ranged from 30 – 33 sccm with that of NH_3 varied from 1 to 3 sccm. In addition, we compare the N/Si compositional characterization of SiN_x thin films as probed by energy dispersive x-ray spectroscopy (EDS) and x-ray photoelectron spectroscopy (XPS).

7.2 EXPERIMENTAL DETAILS

7.2.1 Deposition conditions

UNIVERSITY of the
WESTERN CAPE

SiN_x thin films were deposited simultaneously on Corning 7059 and Si (100) substrates using a high vacuum MVSystems HWCVD system described elsewhere [7.13]. The deposition time, substrate temperature, deposition pressure, filament temperature, silane flow rate and hydrogen flow rate were fixed at 60 minutes, 240 °C, 150 µbar, 1600 °C, 2 sccm and 28 sccm, respectively. The NH_3 flow rate was varied from 1 – 3 sccm (in increments of 0.5 sccm).

7.2.2 Thin film characterization

The elemental composition of the SiN_x thin films were determined using XPS and EDS. XPS was performed in wide and narrow scan modes on a PHI Quanta 2000 spectrometer using monochromatic $Al_{K\alpha}$ X-rays. EDS analysis was performed at 6 kV using a pure Si standard as the quantification optimization element in an OXFORD

INCA EDS system in a Zeiss LEO 1525 field emission gun scanning electron microscope (FEGSEM). The bonding configuration of the SiN_x thin films were investigated using a Perkin Elmer Spectrum 100 fast-Fourier transformed infrared (FTIR). The spectra were collected in transmission geometry from 400 to 4000 cm^{-1} with a spectral resolution of 1 cm^{-1}. The FTIR spectra were corrected for coherent and incoherent reflections [7.14, 7.15]. The total hydrogen content in the film was determined using elastic recoil detection (ERD) analysis. The ERD analysis was conducted using a 3 MeV mono-energetic and collimated beam of $^{4}He^{+}$ ions accelerated by the van de Graaff accelerator at iThemba Labs, in Cape Town, South Africa. The recoiled atoms were detected at an angle of 30° with respect to the incident ion beam. A Kapton reference material (coated with ~ 1 Å Pt) was used for energy calibration. The total H content was calculated from the ERD spectra using the SIMNRA simulation software.

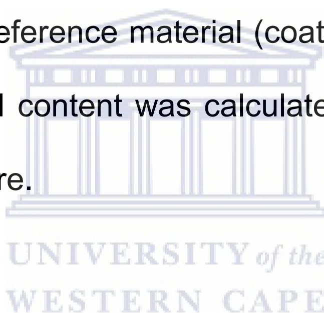
UNIVERSITY of the
WESTERN CAPE

Raman spectra were recorded in backscattering geometry in the region 100 – 1300 cm^{-1} with a spectral resolution of 0.4 cm^{-1}, using a Jobin-Yvon HR800 micro-Raman spectrometer operated at an excitation wavelength of 514.5 nm. The power of the Raman laser was kept below 5 mW to avoid laser induced crystallisation. Cross-sections of the SiN_x films were prepared by a FEI Helios NanoLab 650 Dual Beam focussed-ion beam SEM (FIBSEM). Subsequently, high-resolution transmission electron microscopy (HRTEM) was performed on the cross-sections using a JEOL ARM 200F TEM. Electron energy loss spectroscopy (EELS) was performed in scanning transmission electron microscopy (STEM) mode at a step size of 4 nm x 4 nm to acquire Si, N and O elemental maps. The Gatan Quantum GIF energy filter was used to perform the EELS maps at a collection angle of 41.7 mrad. Electron

diffraction was performed on a FEI Tecnai F20 FEGTEM at 200 kV. The film stress was estimated from curvature measurements determined on Corning (thermal expansion 4.6 μ / °C, Young's modulus 67.6 GPs and Poisson's ratio 0.28) substrates before and after deposition using a Taylor stylus profilometer. The total film stress was then determined using Stoney's equation [7.16]. However, the total film tress is equal to sum of the intrinsic stress and the thermal stress. The thermal stress was determined from the constants for a-Si in [7.17] (thermal expansion coefficient 1 μ / °C, Young's modulus 130 GPa and Poison's ratio 0.28).

Optical transmission and reflection spectra were measured using a CARY 1E UV/VIS spectrophotometer in the range 200 – 900 nm with a spectral resolution of 1 nm. The refractive index, absorption coefficients and optical thickness were calculated by employing the Bruggeman effective medium approximation (BEMA) model [7.18].

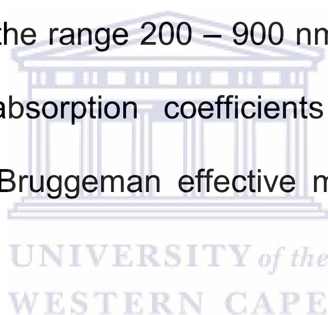
UNIVERSITY of the
WESTERN CAPE

7.3 RESULTS AND DISCUSSION

7.3.1 Film growth rate

Figure 7.1 shows the film growth rate as a function of NH_3 flow rate (Φ_{NH3}). The growth rate enhances with increasing Φ_{NH3} values. The growth rates are inferior relative to that reported for PECVD [7.17] and also for typical HWCVD [7.7]. However, the growth rates are still promising considering that we used a lower deposition pressure, filament temperature of 1600 °C and total gas flow rates lower by a factor of ~ 12 compared to that used in [7.7].

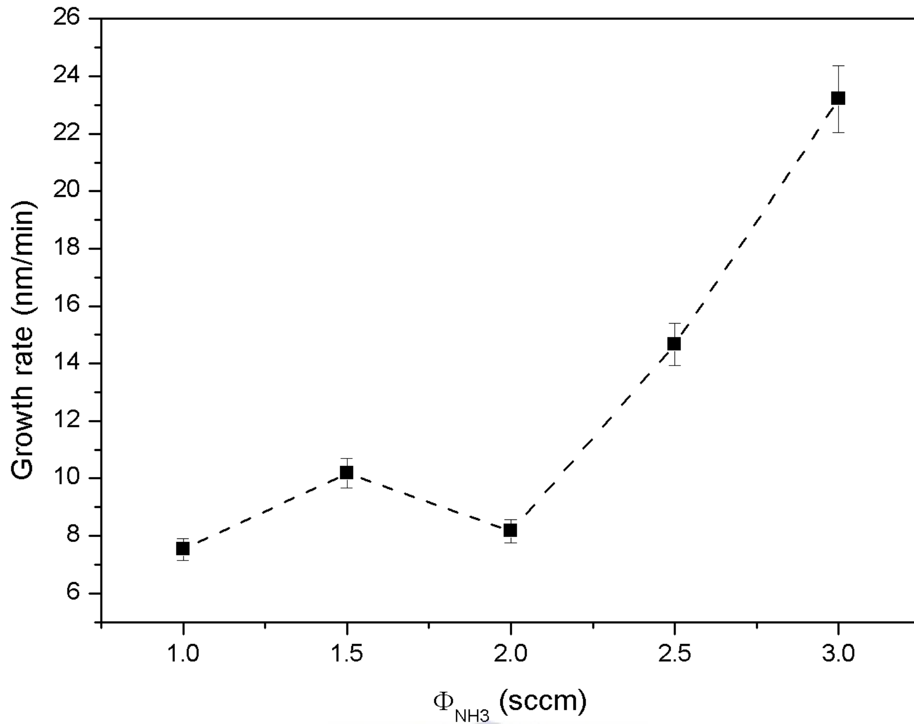

Figure 7.1: Film growth rate at various NH_3 flow rates.

UNIVERSITY of the
WESTERN CAPE

The HWCVD process of SiN_x is complex and can be divided into three stages, namely the dissociation of the NH_3, SiH_4 and H_2 gases at the filament, gas phase reactions and finally surface reactions at the substrate. During the gas dissociations at the heated Ta-filament; Si, N and H containing radicals are created, which can then proceed to the other two growth stages. However, the results in Chapter 6 revealed that the radicals diffuse within the Ta-filament consequently resulting in the formation of Ta-nitrides and -silicides. This depletion of growth species from the ambient can lead to inferior growth rates, especially in this study where the depositions were started with a pure Ta-filament surface.

The inferior concentrations of growth species, as a result of filament ageing, have also been observed in the HWCVD of diamond thin films [7.19]. The initial inferior growth rates at NH_3 flow rates ≤ 2 sccm can be ascribed in part by the depletion of Si and N containing radicals from the ambient and their subsequent incorporation into the filament. Afterwards, the silicide layer encapsulating the filament (refer to Chapter 6) becomes thicker, which reduces the diffusion of radicals within the filament, i.e. more radicals are now available for the deposition leading to the higher growth rates at higher NH_3 flow rates.

Gas phase reactions are also a contributing factor to the film growth rate. The probability for a gas molecule to be dissociated by the heated filament surface is inversely proportional to the pressure and directly proportional to the square root of the filament temperature [7.19, 7.20]. It is therefore possible that not all SiH_4 molecules are dissociated at our deposition conditions; given the deposition pressure of 150 µbar and low filament temperature of 1600 °C. However, the NH_3 partial pressure enhances with an increasing NH_3 gas flow rate. Coupled with the high H_2 concentration and the effectiveness of a heated filament to dissociate H_2 [7.21], a high concentration of atomic hydrogen is expected during the deposition. Atomic hydrogen is unstable and can dissociate those SiH_4 molecules that were not dissociated by the heated filament. Consequently an increase in growth rate occurs at higher NH_3 flow rates.

UNIVERSITY of the
WESTERN CAPE

7.3.2 Compositional properties

Figure 7.2 presents the ERD spectra of the thin films with the corresponding simulated fit. Figure 7.3 reveals that the hydrogen concentration decreases monotonically from ~ 16 to ~ 9 at. % with an increase in Φ_{NH3}.

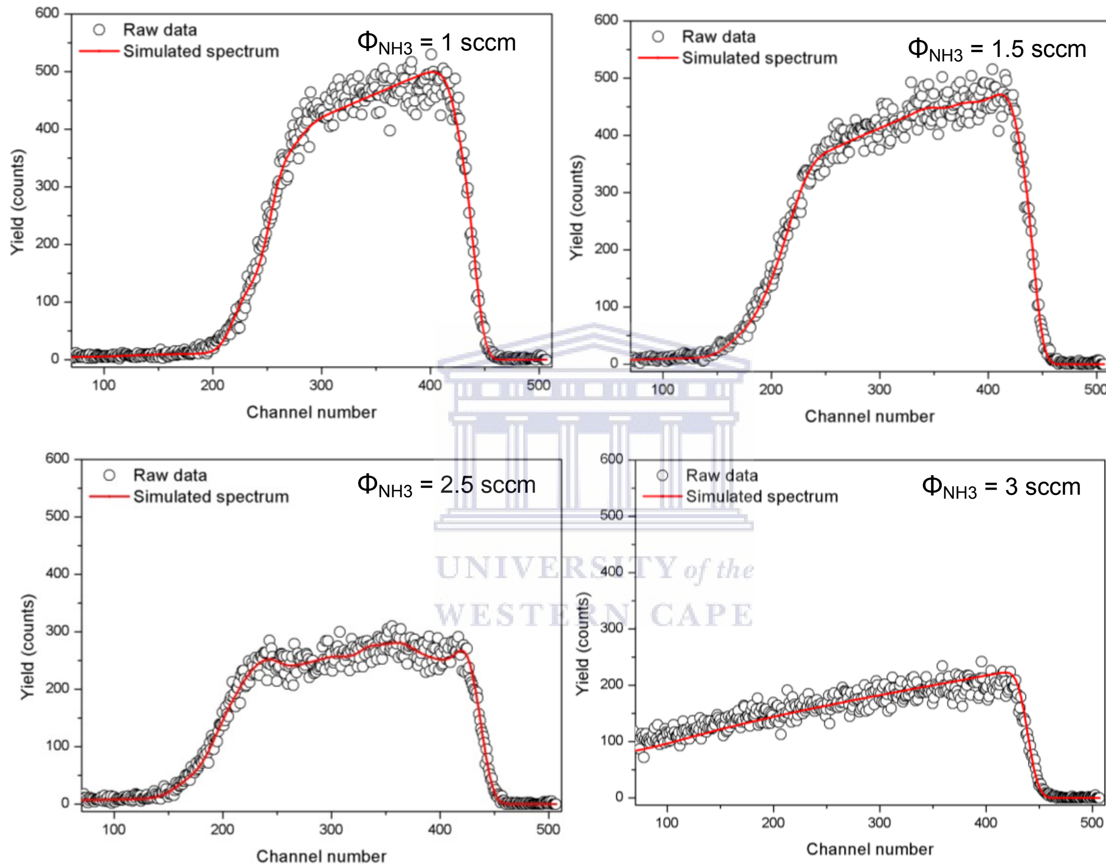

Figure 7.2: ERD spectra (with the SIMNRA simulated fit) for SiN_x thin films deposited at different NH_3 flow rates.

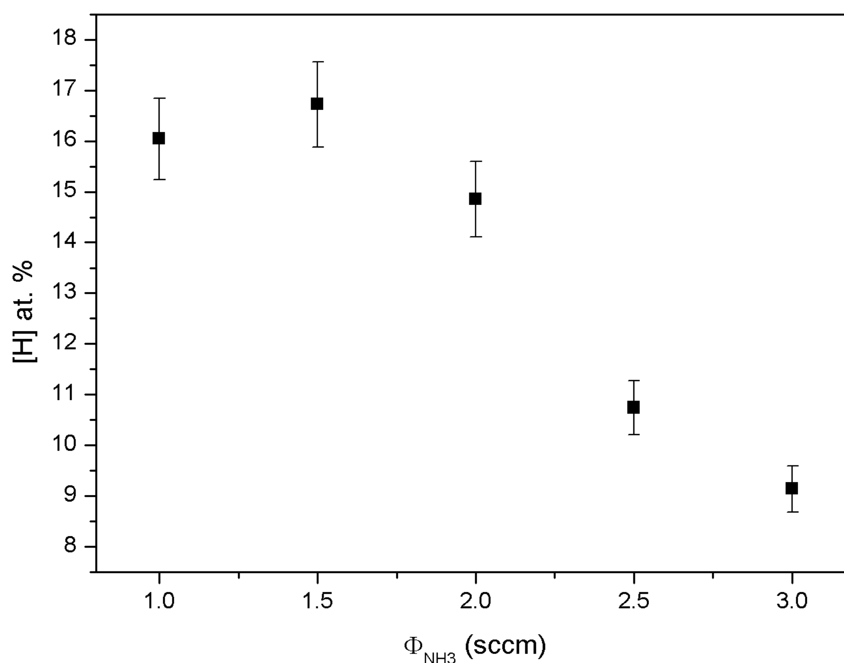

Figure 7.3: Total hydrogen content as a function of Φ_{NH3}.

UNIVERSITY of the
WESTERN CAPE

Figure 7.4 shows deconvoluted XPS spectra of the Si 2p orbital for SiN_x thin films deposited at various Φ_{NH3}. The spectra can be deconvoluted into three Gaussian peaks with centres at ~ 99.4 eV (Si-Si), 103 eV (Si-O) and 100.1 eV (Si-N). The presence of the Si-O peak indicates that the surface is oxidised. In addition, the simultaneous presence of Si-Si and Si-N reveal that the films are dual phase, i.e. the films are composed of a mixture of Si-Si and Si-N networks. Figure 7.5a presents the relationship between the Si-N area percentage (relative to Si-O and Si-Si) as a function of Φ_{NH3} flow rate. The concentration of the Si-N bonds grows linearly with increasing NH_3 flow rate at the expense of the Si-Si bonds, indicating an efficient use of the supply gases. This phenomenon has been observed before and was attributed to the gas phase dissociation of NH_3 by atomic hydrogen [7.8]. Figure 7.5b shows an XPS depth profile for the sample deposited at Φ_{NH3} = 3 sccm. The depth profile reveals that O and C are surface contaminates while homogenous atomic concentrations of N and Si constitute the bulk of the film.

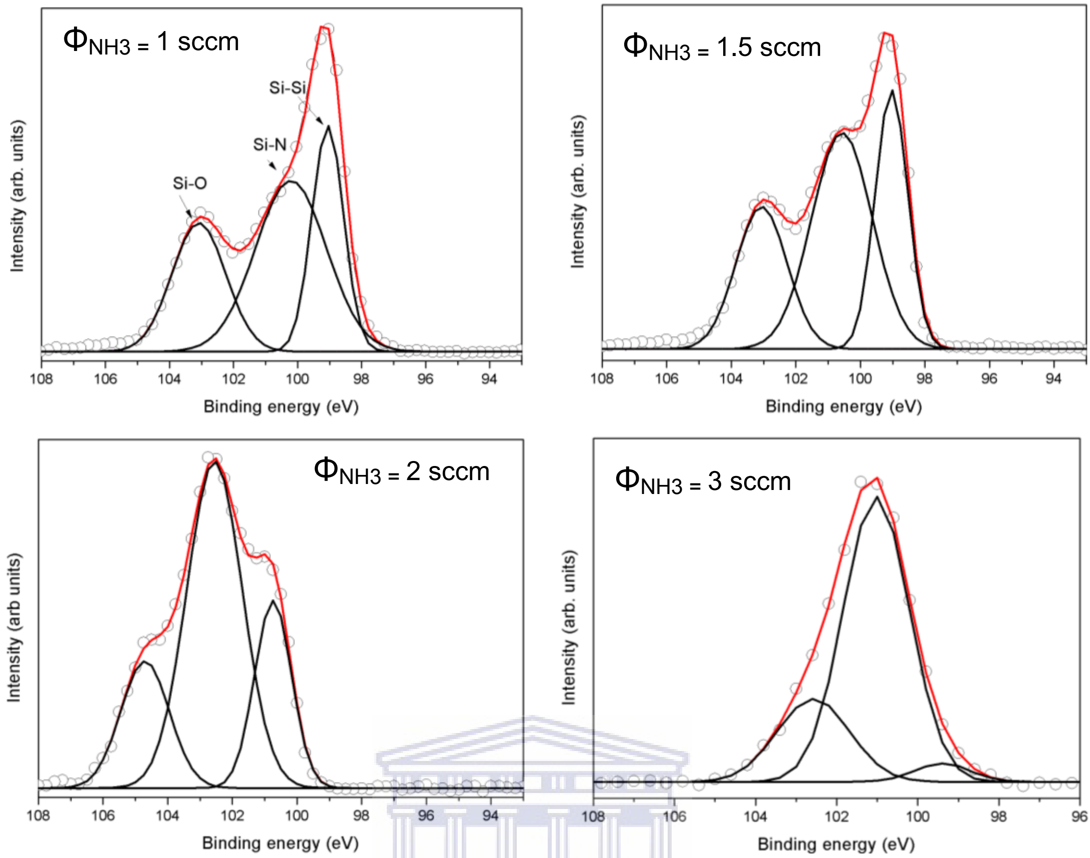

Figure 7.4: XPS spectra of Si 2p level for SiN_x films deposited at various Φ_{NH3}.

UNIVERSITY of the
WESTERN CAPE

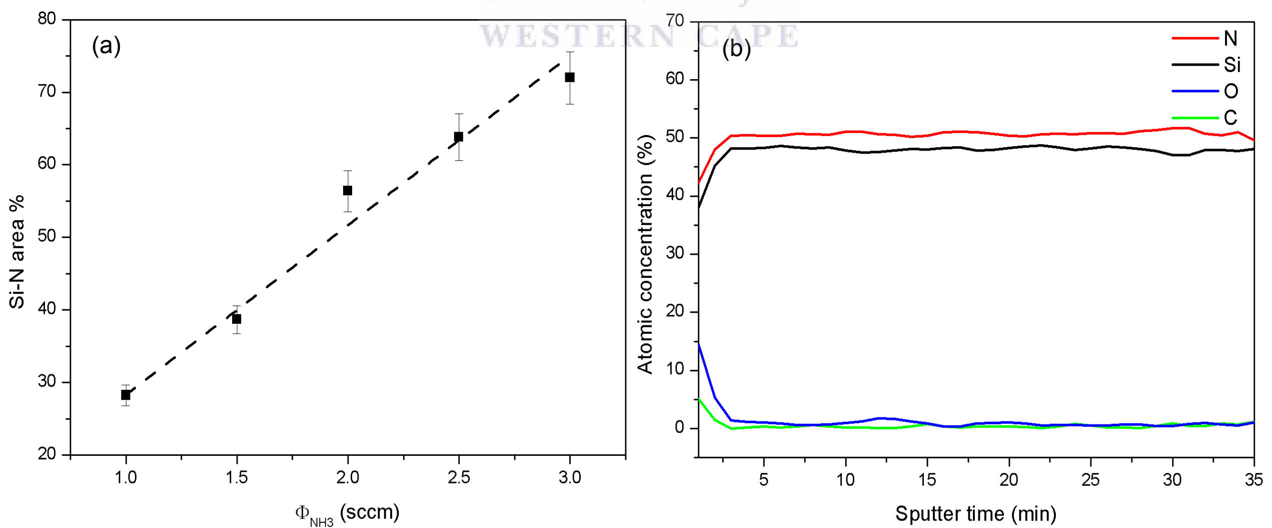

Figure 7.5: (a) Si-N area percentage (with linear fit) at various NH_3 flow rates and (b) XPS elemental depth profile of the sample deposited at Φ_{NH3} = 3 sccm.

The N/Si atomic ratio (x) is the most important factor that governs the electrical and optical properties of SiN_x. In general, the N/Si ratio is determined from Rutherford backscatter spectroscopy (RBS), heavy ion elastic recoil detection (ERD) [7.7], FTIR [7.8] or indirectly from the film refractive index [7.22]. However, the proportionality constants necessary for quantification from FTIR varies with film composition [7.23]; and the refractive index is influenced by the film density which, in turn, may also depend on the deposition technique [7.24]. Currently, scanning electron microscopes (SEM) are becoming increasingly accessible and coupled to a SEM in most cases is an energy dispersive x-ray spectroscopy (EDS) detector. EDS is used to identify and quantify elemental compositions of various elements with an atomic number larger than 4 (Be). Despite its immense development for determining elemental compositions of bulk materials, EDS on thin films within the SEM have received less attention. This can be attributed to the beam penetration depth, issues relating to the homogeneity of the thin film (which will influence the quantification) and relatively high inaccuracies for low atomic number elements such as C. Nevertheless, with the advent of more sensitive detectors and enhanced detection levels at low acceleration voltages, EDS may be used as an alternative option to determine the elemental composition of SiN_x thin films.

UNIVERSITY of the
WESTERN CAPE

Monte Carlo simulations [7.25] were performed in order to determine the expected beam penetration depth. The modelling conditions were: a spot size of 10 nm, accelerating voltage of 6 kV and a number of 1000 electrons. Figure 7.6 shows the Monte Carlo results for samples with different N-contents. The X-rays used by EDS for quantification originate from the total blue area. We therefore expect that the Si from the c-Si substrate will not interfere with the analysis. EDS was performed on

SiN_x deposited on glass to validate that the substrate does not interfere with the analysis. Figure 7.7 compares EDS spectra of the Corning substrate and typical SiN_x samples. No detectable B, Al and Ba are present in the EDS spectra of SiN_x samples, indicating that the substrate elemental contributions are excluded from the analysis. The O and C signals in the SiN_x EDS spectra originate from the surface contamination of the SiN_x thin films as shown by XPS (see Figure 7.5b).

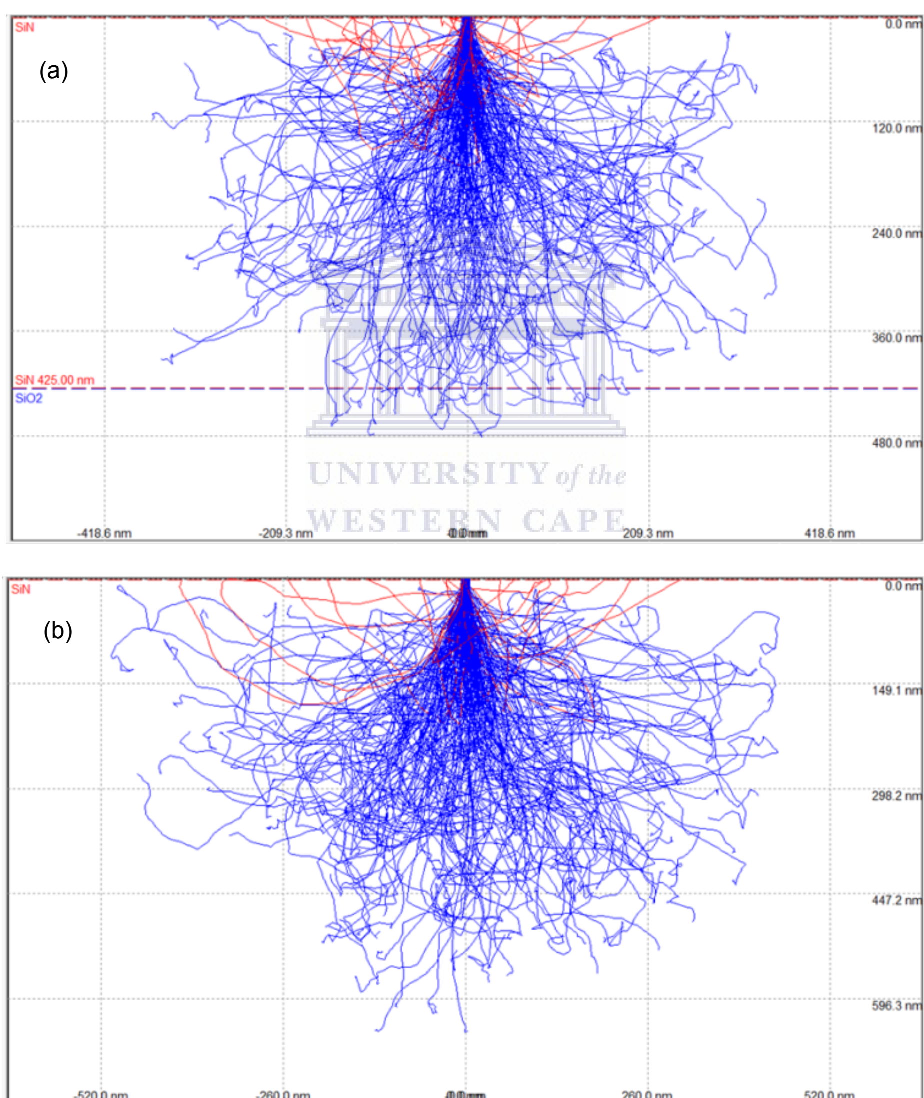

UNIVERSITY of the
WESTERN CAPE

Figure 7.6: Monte Carlo simulations of the expected SEM beam penetration depth and profile for SiN_x films with N-content of (a) 25 at. % and (b) 45 at. %.

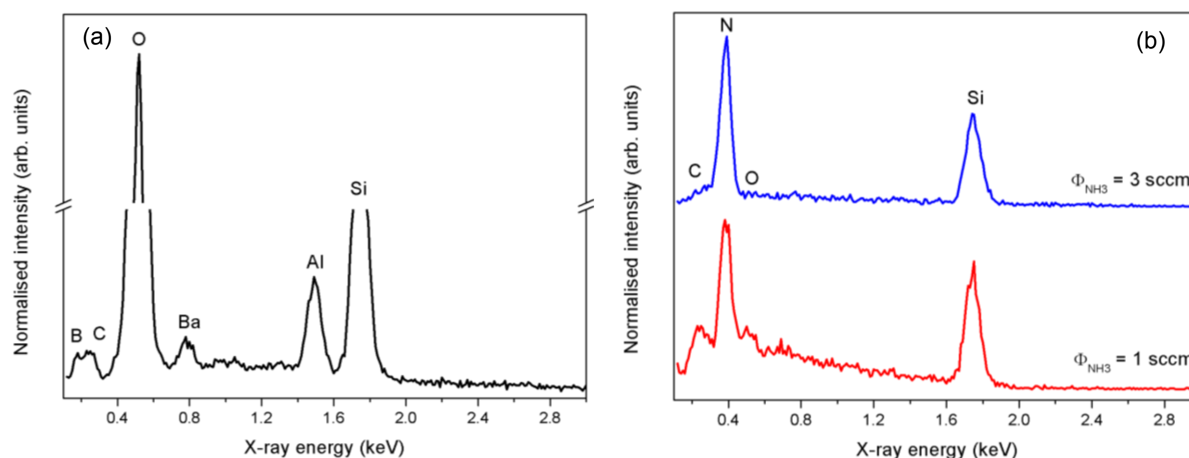

Figure 7.7: EDS spectra of (a) Corning substrate and (b) SiN_x films deposited at different NH_3 flow rates (vertically offset for clarity).

Presented in Table 7.1 is a comparison between the N and Si atomic percentages determined from XPS and EDS; showing the good correlation between these two independent techniques. The values are adjusted to include the H-content determined from ERD.

UNIVERSITY of the
WESTERN CAPE

Table 7.1: Comparison between XPS and EDS. The values are within 5 at. % standard deviation. The total hydrogen content [H] was determined from ERD.

Φ_{NH3} (sccm)	**N_{XPS} (at. %)**	**N_{EDS} (at. %)**	**Si_{XPS} (at. %)**	**Si_{EDS} (at. %)**	**[H] (at. %)**	x_{XPS}	x_{EDS}
1	15.66	18.65	68.30	65.31	16.04	0.23	0.29
1.5	20.90	22.33	62.38	60.95	16.72	0.34	0.37
2	30.72	31.02	54.43	54.13	14.85	0.56	0.57
2.5	42.31	45.45	46.95	43.81	10.74	0.90	1.03
3	47.01	49.27	43.85	41.59	9.14	1.07	1.18

FTIR is the preferred technique used to determine and quantify the bonding configurations of SiN_x thin films. Figure 7.8 shows a typical FTIR spectrum of a SiN_x sample revealing the presence of four peaks: the Si-N (stretching) mode near 850 cm^{-1}, N-H bending mode at 1200 cm^{-1}, the Si-H stretching mode near 2190 cm^{-1} and the N-H stretching mode around 3330 cm^{-1} [7.23].

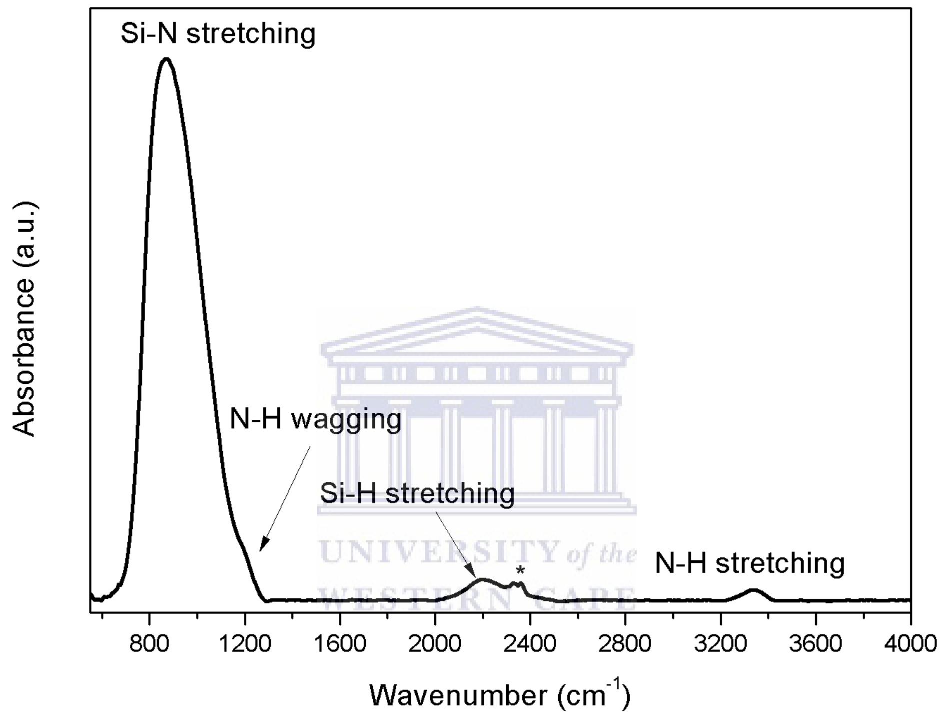

Figure 7.8: Typical FTIR spectrum of the sample deposited at 3 sccm NH_3. The peaks indicated by * correspond to fluctuations in the CO_2 concentrations within the spectrometer which were consequently not properly removed by the background.

The amounts of the Si-N, N-H and Si-H bonds can be obtained from the relevant infrared absorption bands by:

$$[X-Y]=A_{X-Y}\int\frac{\alpha(\omega)}{\omega} \tag{7.1}$$

where $\alpha(\omega)$ is the absorption coefficient at wavenumber ω and $A_{X\text{-}Y}$ is the proportionality coefficient. The proportionality coefficients proposed by Lanford and Rand [7.26] for the N-H and Si-H bond concentrations were used. For the [Si-N] the average value of 1.4 X 10^{19} cm^{-2} was chosen as proposed by Verlaan *et al.* [7.5]. Then, assuming the absence of H-H and N-N bonds in the thin films [7.5, 7.22, 7.27], the atom concentrations of H, N and Si can be determined by the following set of equations [7.27]:

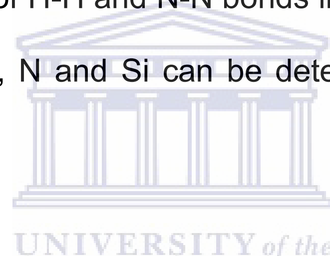

$$[H]=[Si-H]+[N-H] \tag{7.2}$$

$$[N]=\frac{[Si-N]+[N-H]}{3} \tag{7.3}$$

$$[Si]=\frac{[Si-N]+[Si-H]}{4}+\frac{[Si-Si]}{2} \tag{7.4}$$

The [Si-Si] bond density can be derived from equation (4) and [Si] = [N]/x as:

$$[Si-Si]=2\frac{[N]}{x}-\frac{[Si-N]+[N-H]}{2} \tag{7.5}$$

Figure 7.9 presents the FTIR atomic bonding densities of [H], [N], [Si] and [Si-Si]. A relatively higher concentrations of [Si-Si], [Si] and [H] exist at N/Si ≤ 0.30, which then decrease with an increasing N/Si ratio. Initially, the [N] atomic density is in inferior amounts, which then gradually increase with an increasing N/Si ratio. The values of the bonding densities are relatively inferior compared to that reported for SiN_x films deposited from SiH_4 and NH_3 mixtures [7.5, 7.28] (the studies used the same proportionality factors), which indicates an increase in defects as the NH_3 flow rate increases. The peak position of the Si-H bond is influenced by the composition of the SiN_x films [7.7] and more specifically, the different types of back bonding of the hydrogenated Si atom [7.22]. Figure 7.9b reveals that the peak position of S-H scales linearly with N/Si. The absence of NH_3 from the gas mixture in this study will result in the deposition of microcrystalline silicon instead of amorphous silicon as the high H_2 dilution in this study favours the crystallization of silicon [7.29]. The Si-H peak position at 2092 cm^{-1} (N/Si = 0) falls within the range expected for microcrystalline silicon [7.30] and is close to 2220 cm^{-1} for N/Si ≈ 1.33 corresponding to a-Si_3N_4 [7.1].

UNIVERSITY of the
WESTERN CAPE

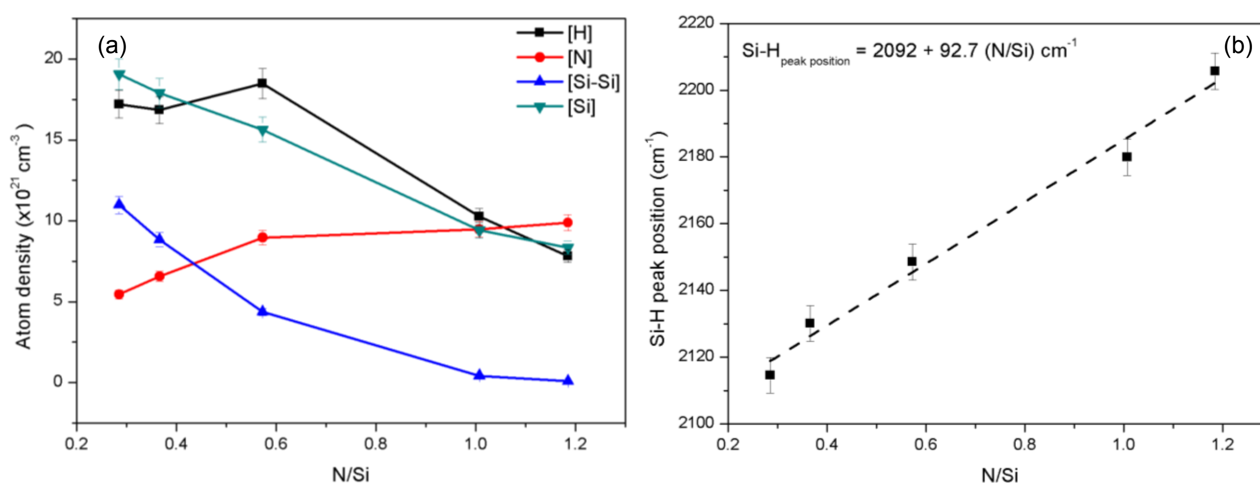

Figure 7.9: (a) FTIR bond densities and (b) variation of the Si-H peak position as a function of N/Si.

An increase in the NH_3 flow rate results in an enhancement in the incorporation of N into the film. The Si-N and Si-H bonds are more energetically favoured than Si-Si bonds [7.31]. Consequently, the Si-Si bonding decreases at the expense of the Si-N bonds as the N content within the film enhances. However, the number of Si-H bonds and H concentration decreased at higher NH_3 flow rates. Verlaan *et al.* [7.32] observed similar trends and attributed the decreasing S-H and H-concentration to cross-linking reactions within the film, i.e. the formation of Si-N and H_2 (released as gas [7.33]) bonds via the reactions of N-H with Si-H bonds.

7.3.4 Film microstructure

UNIVERSITY of the
WESTERN CAPE

The surface roughness of SiN_x thin films is an important parameter to be considered in thin film transistors and anti-reflective coatings for solar cells. Figure 7.10 shows representative 3D AFM images of SiN_x thin films with varying N-content. The root-mean-square (RMS) roughness values shown in Figure 7.11 reveals that the surface roughness decreases to a minimum value of ~ 0.15 nm, substantially lower than that reported for HWCVD of SiN_x using a SiH_4 and NH_3 mixture [7.34].

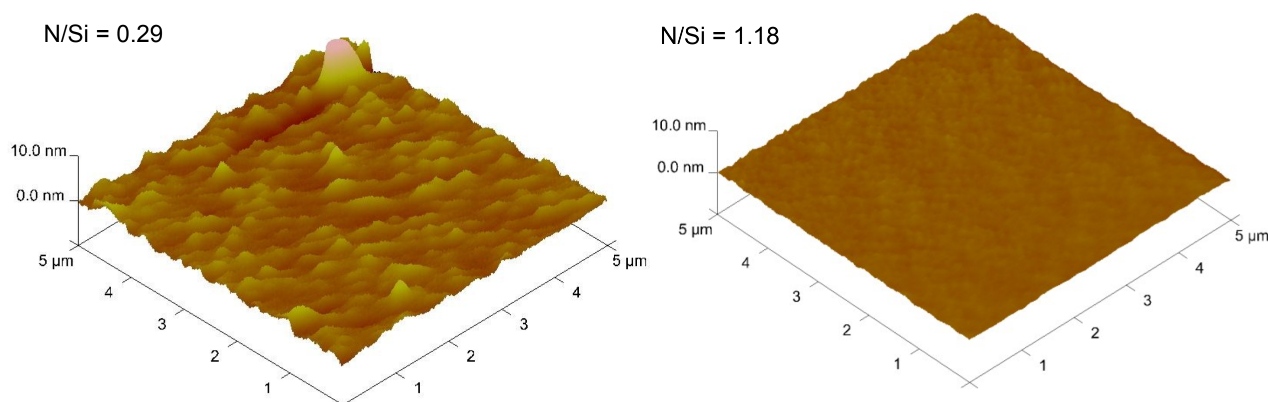

Figure 7.10: 3D AFM micrographs of the SiN_x films at different N/Si ratios.

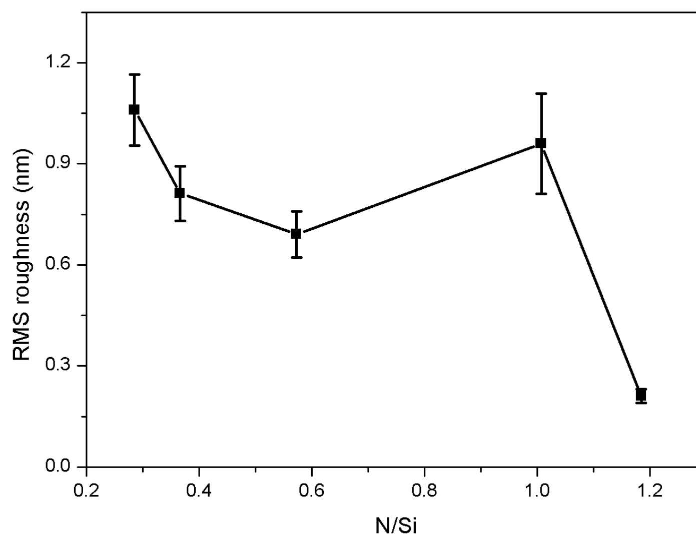

Figure 7.11: RMS roughness values at various N/Si ratios.

UNIVERSITY of the

The increasing NH_3 flow rate results in an increased atomic hydrogen concentration which improves the H-coverage on the growing surface. Consequently, the diffusion of radicals on the growing surface develops, which creates smoother surfaces as the NH_3 flow rate increases. The internal structure of the SiN_x thin films were further investigated by TEM and EELS. Figure 7.12 shows TEM micrographs of the SiN_x films at x = 0.29 and x = 1.18. The films are amorphous as indicated by electron diffraction patterns (insets in Figure 7.12) and are dense, which is suitable for device applications. The film thickness increased with an increasing NH_3 flow rate, confirming the UV-VIS and profilometer measurements. Figure 7.13 presents EELS elemental maps of Si, N and O. Despite the thickness of the cross-sections being less than at most half the inelastic electron mean free path at 200 kV, the EELS maps are qualitative in that it was not possible in the current TEM set-up to monitor the intensity and position of the zero-loss peak while acquiring the elemental maps. Nevertheless, valuable qualitative information about the Si, N and O profiles within the SiN_x can be extracted from EELS.

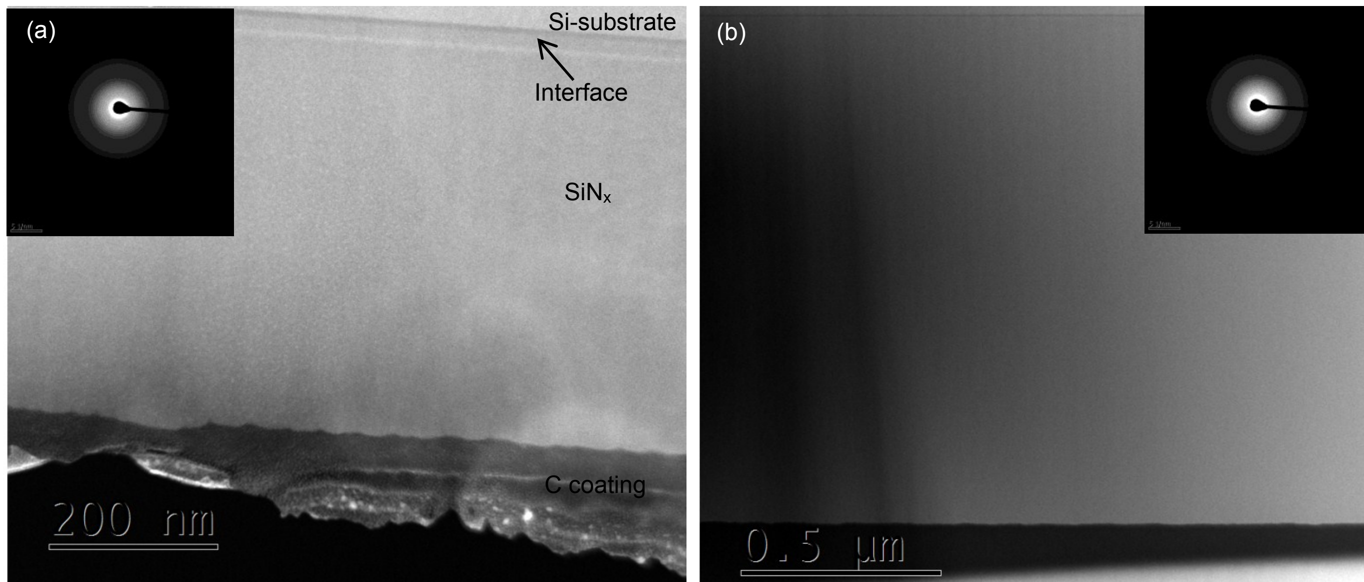

Figure 7.12: TEM micrographs of the SiN_x thin films at (a) N/Si = 0.29 and (b) 1.18. The insets show diffraction patterns in each case.

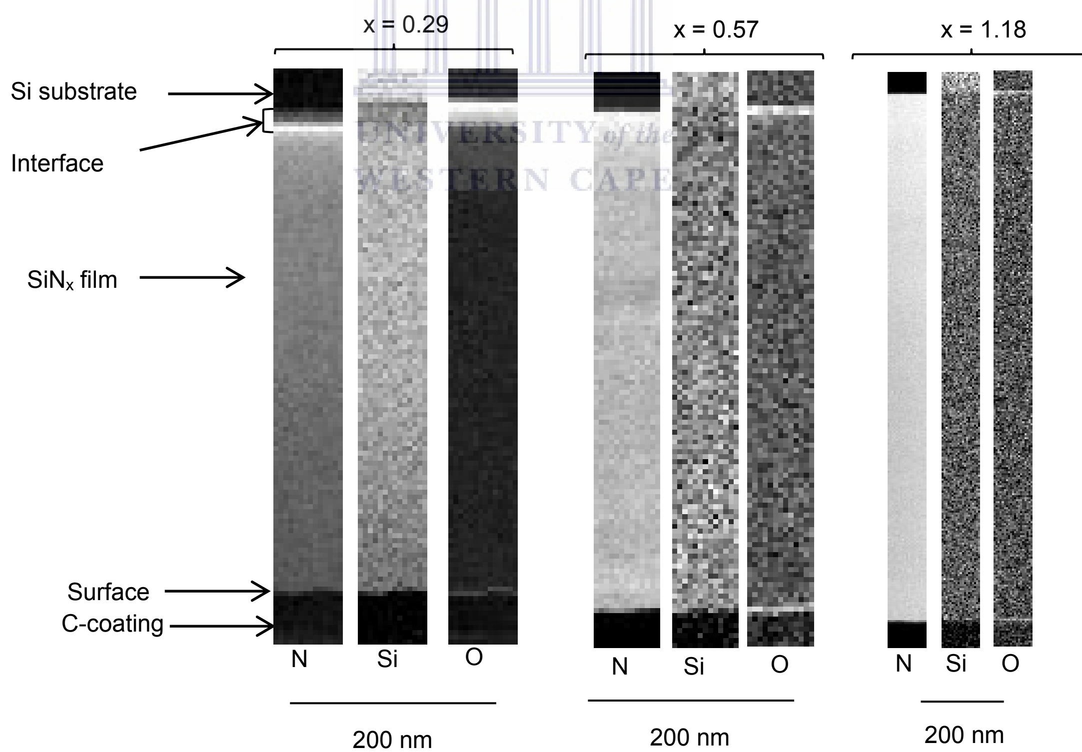

Figure 7.13: Normalized EELS elemental N, Si and O maps of the SiN_x thin films with different N/Si ratios.

The O-signal is intense at the SiN_x/c-Si substrate interface and at the SiN_x surface. The presence of an oxide between the SiN_x and the substrate indicates that the HF dip was not effective in removing the native oxide from the c-Si substrate. Confirming the XPS findings are surface oxide layers on the SiN_x films. However, oxidation subsequent to the FIB sample preparation also occurs and contributes to the O-signal throughout the SiN_x/c-Si cross-sections as revealed by the similar O-signal intensities at the C-coating, SiN_x film bulk and the c-Si substrate.

The intensity of the EELS N-signal is homogenous throughout the SiN_x films and enhances relative to the Si-signal with an increasing N/Si ratio indicating an enriching N-content within the films, supporting the XPS, EDS and FTIR analysis. Furthermore, there are regions within the N- and Si-signals which have different brightness indicating nanosized regions with Si- and/or N-rich areas. Interestingly, a nitrogen rich silicon oxide interface resides between the SiN_x and c-Si substrate. The thickness of the silicon oxynitride layer decreased from ~ 30 nm to 10 nm as the NH_3 flow rate increases from 1 to 3 sccm.

UNIVERSITY of the
WESTERN CAPE

XRD analysis confirmed the absence of crystallinity from the deposited SiN_x thin films, as shown in Figure 7.14. The broad peaks centred on 2θ values of ~ 26 ° and ~ 44 ° are attributed to the Corning substrate. Raman spectroscopy is a powerful tool for probing the structure of Si based thin films.

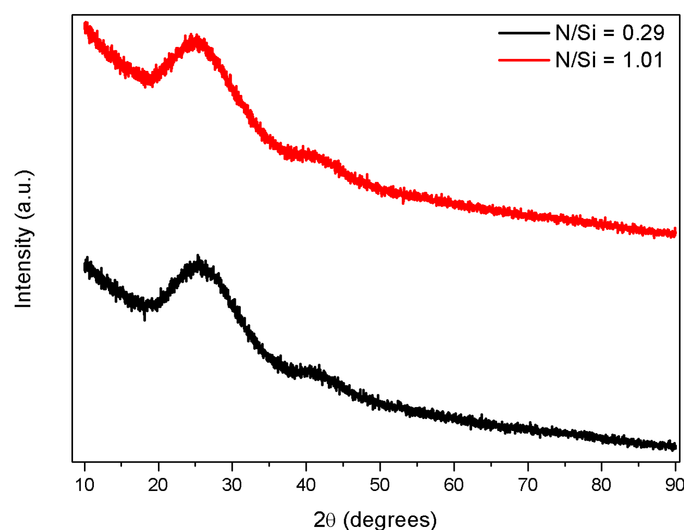

Figure 7.14: XRD patterns for SiN_x films with different N/Si ratios.

UNIVERSITY of the
WESTERN CAPE

Figure 7.15 presents the Raman spectra for samples with different N/Si ratios. The dual phase nature of the films is clear through the simultaneous presence of a-Si transverse optic (TO) peak at ~ 480 cm^{-1} with the 2nd order TO peak at ~ 930 cm^{-1} and SiN_x peaks at ~ 800 cm^{-1} [7.35, 7.36]. Samples with a higher N/Si ratio displayed more SiN_x peaks at 700 cm^{-1} and 1150 cm^{-1} [7.36]. The absence of a peak at ~ 515 cm^{-1} indicates that there is no detectable crystallinity [7.37] confirming the TEM and XRD analysis.

The 2TO peak of a-Si tends to be more enhanced relative to the TO peak in SiN_x compared to a typical a-Si:H thin film as illustrated by Figure 7.16. To further demonstrate this observation, the Raman spectra were deconvoluted into Gaussian peaks corresponding to a-Si and SiN_x as shown in Figure 7.17.

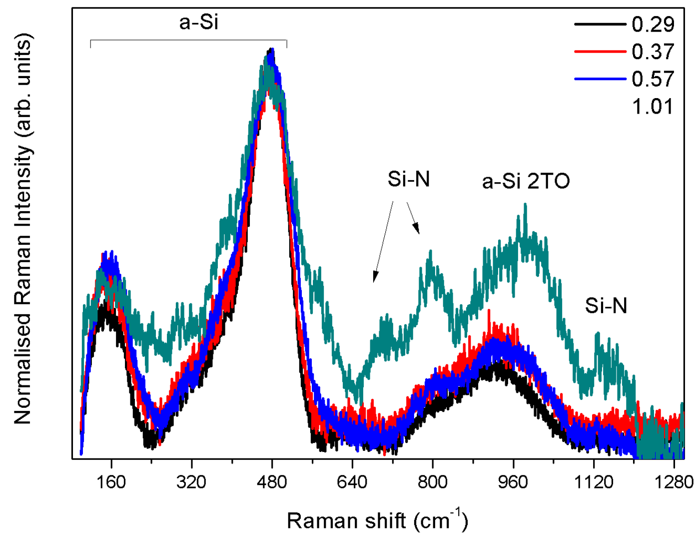

Figure 7.15: Raman spectra of the SiN_x samples with varying N/Si ratios.

UNIVERSITY of the
WESTERN CAPE

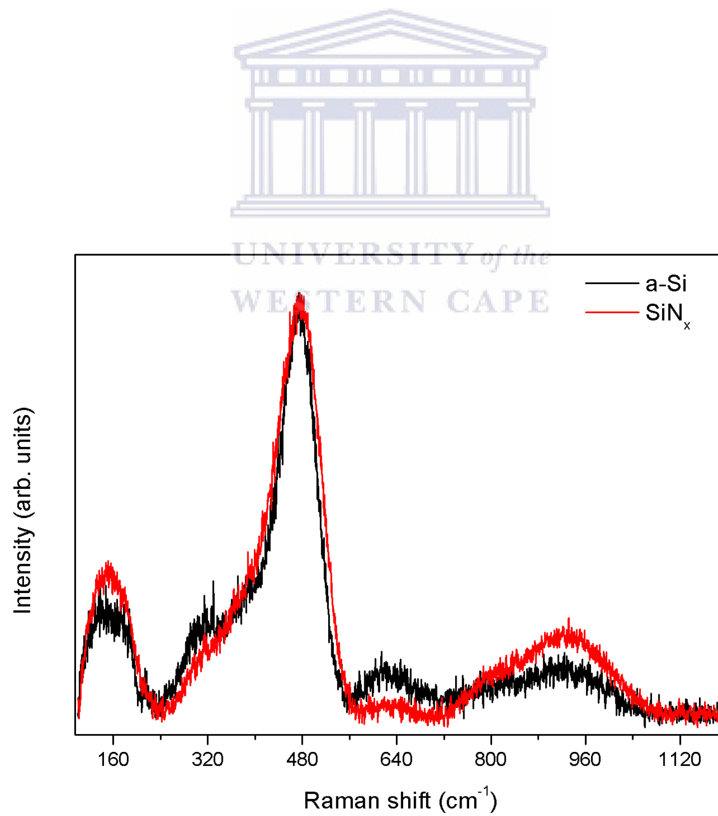

Figure 7.16: Comparison between typical Raman spectra of a-Si and SiN_x films.

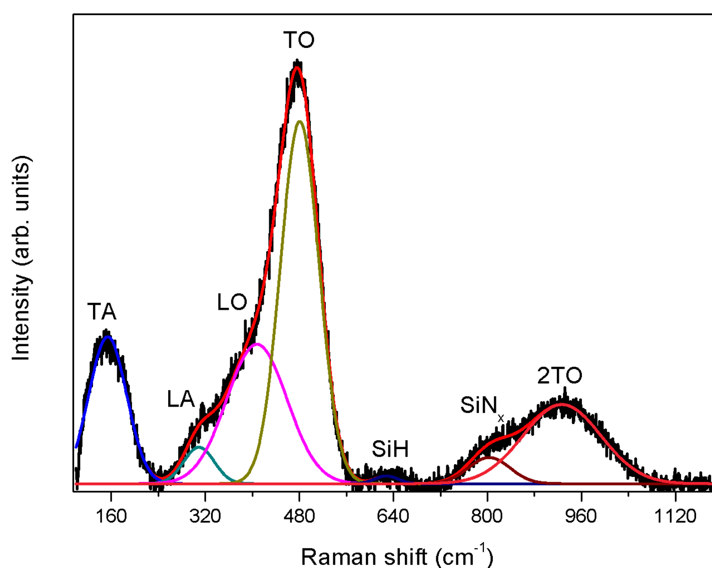

Figure 7.17: Deconvoluted Raman spectrum of a SiN_x sample. The a-Si peaks labeled TO, 2TO LO, LA and TA are present with peaks for SiN_x and SiH.

UNIVERSITY of the
WESTERN CAPE

Figure 7.18 shows the integrated intensity ratio of the SiN_x and a-Si TO peaks (I_{SiNx} / $I_{a\text{-}Si}$), revealing that it increases with an increasing N/Si ratio, which is indicative of an increasing fraction of SiN_x, corroborating the XPS and FTIR results. The full width at half maximum (FWHM) of the a-Si TO peak increases with an enhancing N/Si ratio, whereas the FWHM of the SiN_x peak increases until N/Si ~ 0.6 and then decreases at higher N values. This can be interpreted as the ordering within the a-Si network is relatively enhanced within Si-rich SiN_x films.

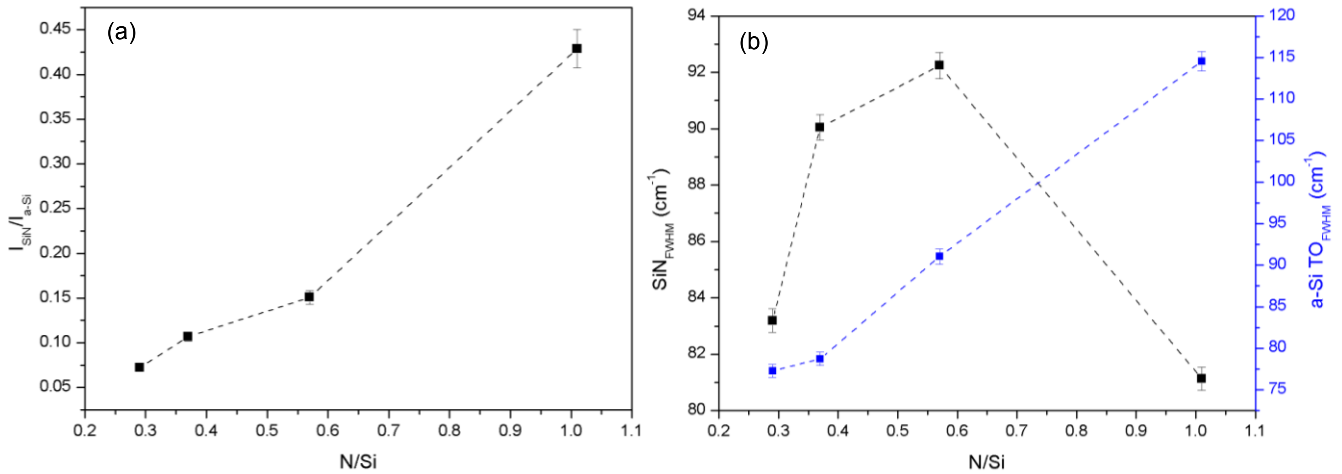

Figure 7.18: (a) Intensity ratio of the a-Si TO peak to the SiN_x peak and (b) variation of the FWHM of the SiN_x and a-Si TO peaks at different N/Si ratios.

UNIVERSITY of the
WESTERN CAPE

Figure 7.19 presents the integrated intensity ratio $\eta = I_{2T0} / I_{TO}$ of a-Si; disclosing that it increases monotonically with an increasing N/Si ratio. Initially, $\eta = 0.22$, below the value of 0.25 for a-Si and above that of bulk c-Si of 0.10 [7.38]. Subsequently, η transcends the value for a-Si reaching values of ~ 0.62 for samples with high N-content. Mercaldo *et al.* [7.35] observed a $\eta \sim 1$ and attributed it to size-dependent enhanced electron-phonon coupling in amorphous or crystalline nanostructures within a SiN_x thin film.

However, in this study it was not possible to directly analyse regions smaller than 4 nm using EELS. Additionally, the samples experienced damage after prolonged exposure to the 200 kV electron beam. Nevertheless, the nanoscale regions of brightness in the EELS Si-maps and the simultaneous presence of Si-Si and Si-N bonds suggest that amorphous nanosized Si-rich regions are present within the SiN_x thin films.

Moreover, the disorder increases within the Si-Si regions as more N is incorporated. The cross-section of the TO Raman peak is largely determined by the deformation potential involving short-range interaction between the Si-Si lattice displacement and electrons [7.39]. Adapting this to amorphous materials, the enhancing defects (corresponding to an increasing tensile stress) induces an enlarging displacement which reduces the TO scattering cross-section and eventually higher I_{2T0} / I_{TO} ratios.

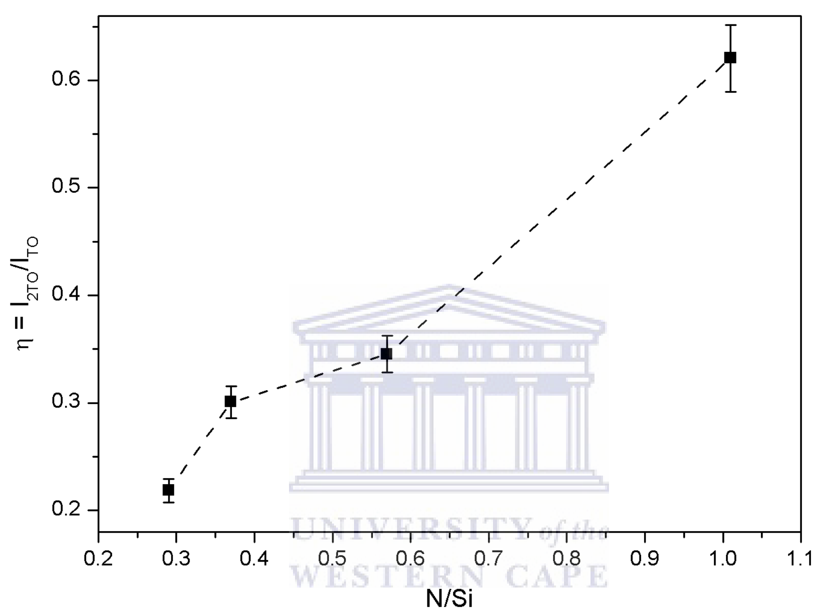

UNIVERSITY of the
WESTERN CAPE

Figure 7.19: Intensity ratio of second- to first-order of a-Si at various N/Si ratios.

Regardless of the high hydrogen dilution used in this study, no crystallization occurred as revealed by XRD, Raman spectroscopy and electron diffraction in the TEM analysis. This can be explained by the increased incorporation of nitrogen and the decrease of the H-content as the N/Si ratio increases, which create defects within the SiN_x thin films. Coupled with the low substrate temperature of 240 °C, this impedes crystallisation. The increasing number of defects results in the observed decreasing FTIR bonding densities and the observed disordering within the Si-Si regions as shown by Raman spectroscopy.

Wanka *et al.* [7.40] reported on the effective etching of a native oxide film on silicon by atomic hydrogen generated by a heated filament. In line with the findings by Wanka *et al.* [7.40] the reduction in the oxide thickness between the SiN_x/c-Si interface as the NH_3 flow rate increases is attributed to an enhancing etching by atomic hydrogen.

The presence of a nitrogen-rich interface between the SiN_x and the underlying c-Si substrate is attributed to the diffusion of N within the oxide layer. Crystalline silicon has a higher packing density of Si atoms compared to its amorphous state. The higher density of dangling Si bonds within the c-Si/film interface provides a superior number of N bonding sites compared to the a-SiN_x:H layer. The N atoms then passivate the dangling bonds within the oxide by forming energetically favoured Si-N bonds, resulting in a nitrogen-rich interface. Fukuda *et al.* [7.41] reported similar findings in their thermally oxynitridation studies of a Si (100) wafer. The decreasing N-rich interface thickness with an increasing NH_3 flow rate is due to the reduction in the native oxide thickness owing to the enhancing etching of atomic hydrogen. Coupled to a higher H density, the dangling bonds within the interface are passivated by hydrogen reducing the areas where N can bond, subsequently resulting in a decreasing N-rich interface. The presence of defects within the SiN_x thin films further manifest in the form of film stress. Figure 7.20 shows the film stress as a function of N/Si; revealing that the film is under compresive stress for $x < 0.4$ and then under tensile stress for $x > 0.55$. Hasegawa *et al.* [7.42] also observed a change in stress from compression to tensile at N/Si ~ 0.5 and attributed it to the rearangment in the Si-N network.

UNIVERSITY of the WESTERN CAPE

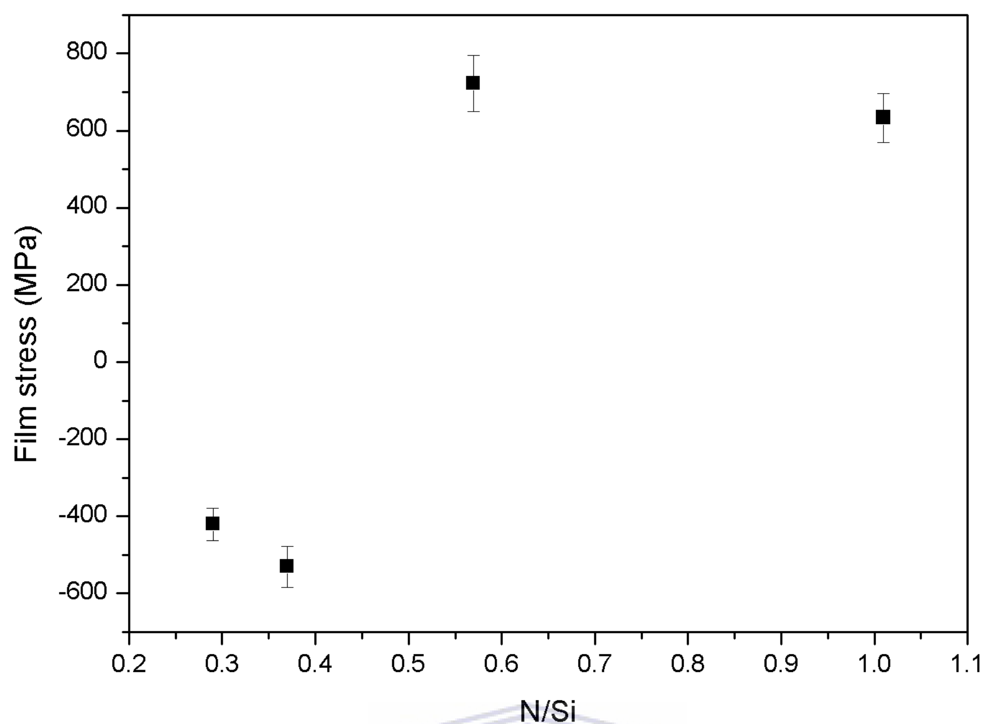

Figure 7.20: Intrinsic film stress at various N/Si ratios.

UNIVERSITY of the
WESTERN CAPE

Specifically, the distance between Si and N becomes shortened within the distorted bonding arrangment leading to a contraction of the films as the N content increases ultimately leading to tensile stress [7.42]. Additionally, the inreasing deposition rate as the NH_3 flow rate enhances results in a higher supply rate of radicals compared to the rate of Si, H and N incorporation wihin the SiN_x thin films consequently resulting in the deposition of a disordered, tensile network at N/Si > 0.55.

7.3.3 Optical Properties and Film stress

The understanding of the optical properties of SiN_x films is vital considering that they can be applied as anti-reflective coatings on solar cells. Figure 7.21 illustrates the evolution of the UV-VIS transmission and reflection spectra of the SiN_x thin films possesing different N/Si ratios. Figure 7.21a shows that the transmission is enhanced as the N content increases and the blue shift (higher photon energy) indicates an increasing optical band gap. Correspondingly, the reflection of the SiN_x thin films decreases as the N content increase.

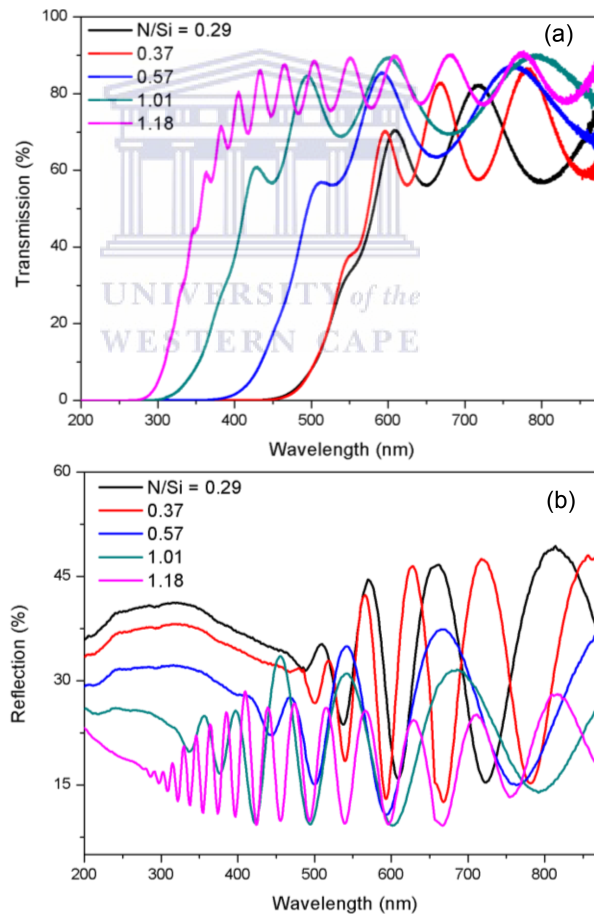

Figure 7.21: (a) Transmission and (b) reflection spectra of SiN_x thin films with different N/Si ratio.

The absorption coefficient, extinction coefficient and refractive index were then extracted from the reflection spectra by fitting the BEMA model in the SCOUT software [7.18], as illustrated in Figure 7.22.

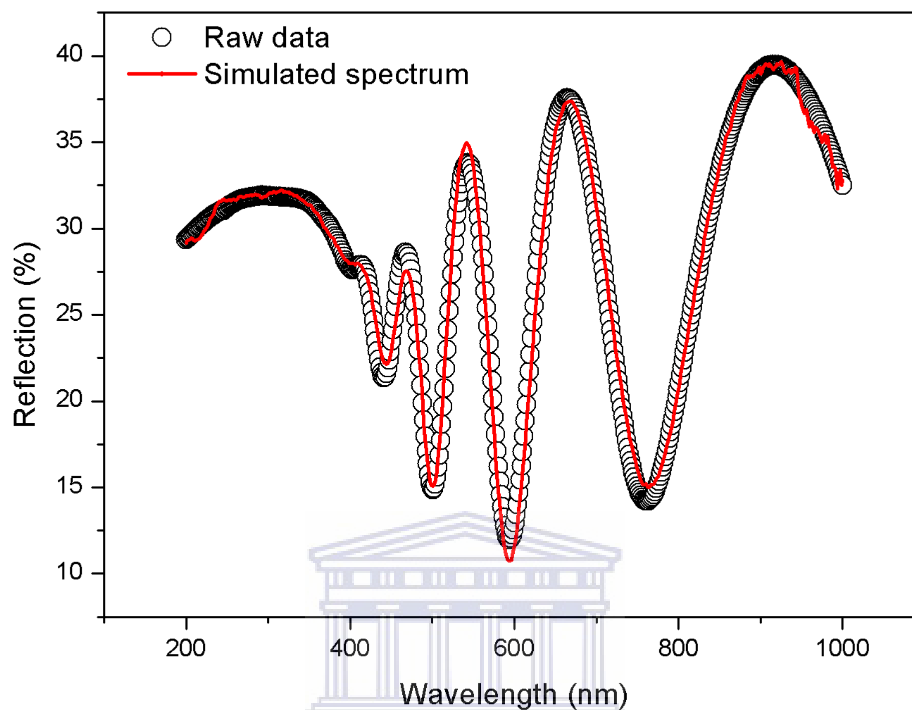

Figure 7.22: An example of a reflection spectrum and corresponding simulated fit.

UNIVERSITY of the
WESTERN CAPE

Figure 7.23 presents the dispersion in the absorption coefficient and refractive index at vaiours photon energies. The refractive index and absorption coeficient decrease with an enhancing N content within the films. This trend is consistent with the enhancing SiN phase as observed by XPS. Figure 7.24 shows the refractive index (n) at 632 nm and the extintion coeffifcient (k) at 400 nm of the SiN_x thin films as a function of N/Si.

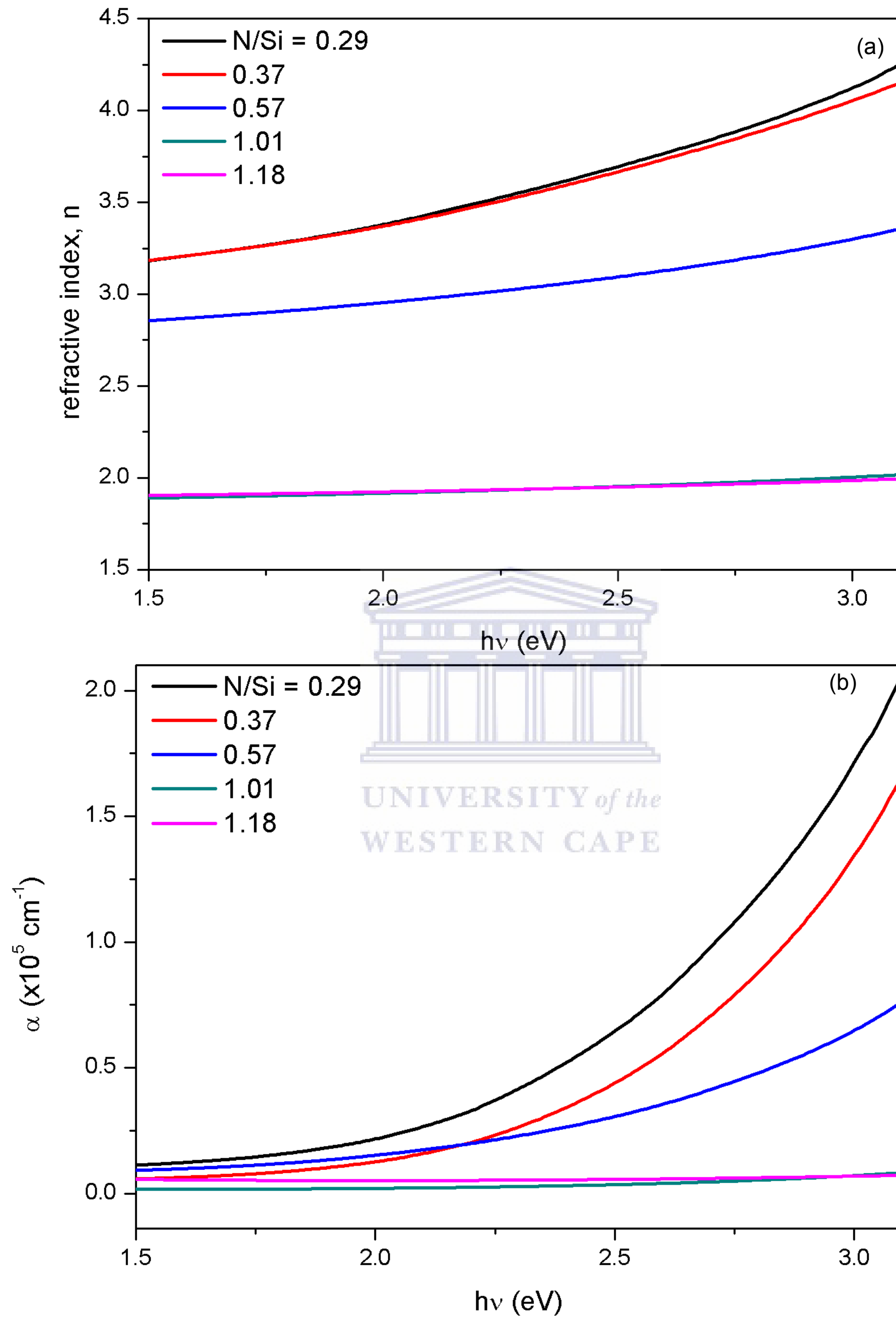

UNIVERSITY of the
WESTERN CAPE

Figure 7.23: Dispersion in the (a) refractive index and (b) absorption coefficient of SiN_x thin films with various N/Si ratios.

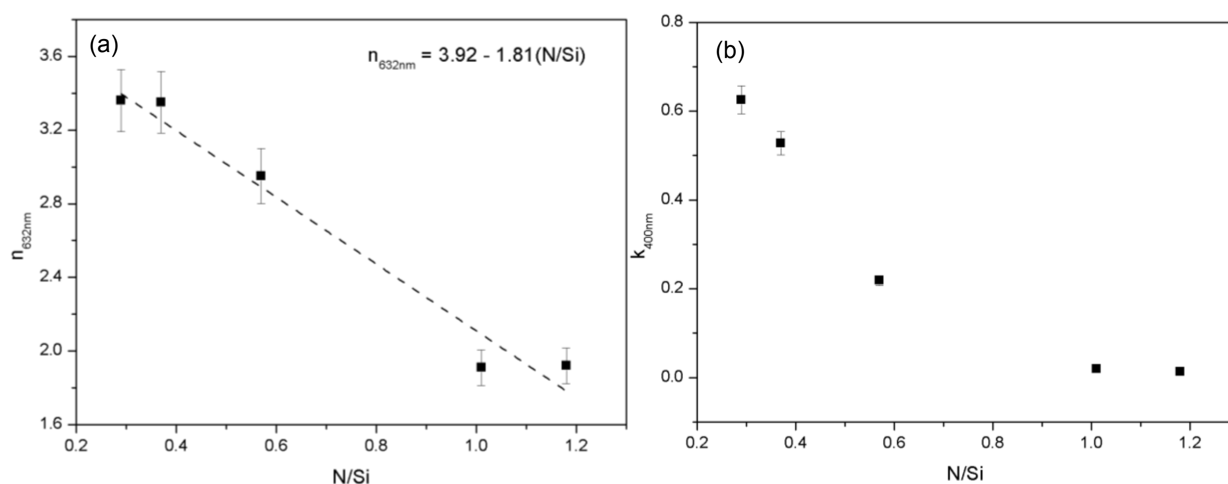

Figure 7.24: (a) Refractive index at 632 nm and (b) extinction coefficient at 400 nm as a function of N/Si.

The refractive index decrease linearly with an increasing N/Si ratio according to:

$$n_{632nm} = 3.92 - 1.81\left(\frac{N}{Si}\right) \qquad (7.6).$$

The extrapolated n_{630nm} value of 3.92 ± 0.21 at N/Si = 0 is close to the value reported for microcrystalline silicon of 3.75 [7.43]. The expected value of n_{632nm} = 1.51 ± 0.24 at N/Si ≈ 1.33 is lower than the value of 1.90 for α-Si_3N_4 and is attributed to the presence of tensile stress observed for SiN_x ($x > 0.57$) thin films in this study.

The enhancing incorporation of N within the film results in the increasing number of the energetically favoured Si-N bonds [7.31] and a reduction in the [Si-Si] bonds. Figure 7.24b shows that a noticeable reduction of k_{400nm} occurs with an increase in the N/Si ratio, which idicate less absorption within the visible wavelenght regions. Figure 7.25 shows the Tauc band gap of the SiN_x layers disclosing that the band gap widens linearly with an increase in N/Si according to:

$$E_{Tauc} = 1.31 + 2.49\left(\frac{N}{Si}\right) \qquad (7.7).$$

The relation expressed in equation (7.7) differs from that reported for the deposition of SiN_x from SiH_4 and NH_3 gas mixtures [7.44]. Nevertheless, the E_{Tauc} values reduces to 1.31 eV at N/Si = 0; corresponding well with the reported value for microcrystalline silicon [7.30] and to 4.63 eV which is approaching 5 eV for Si_3N_4 [7.45].

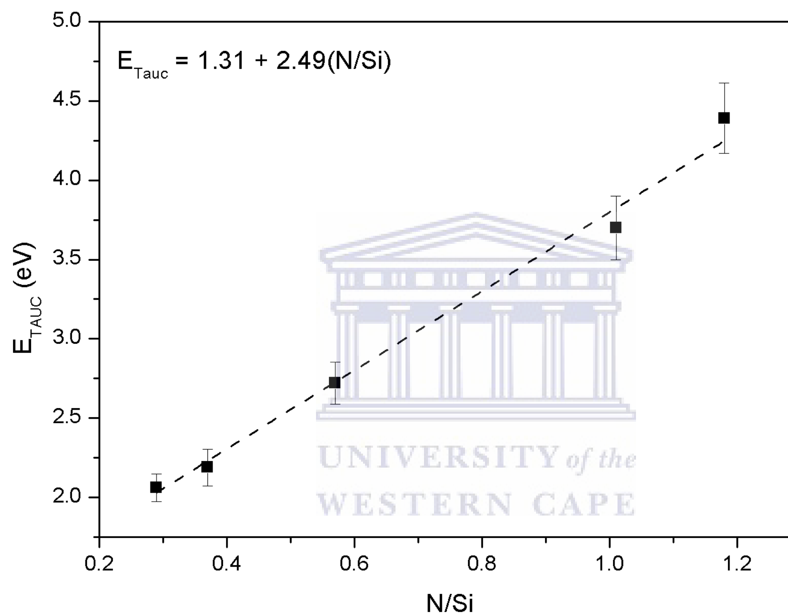

Figure 7.25: Tauc optical band gap as a function of N/Si ratio.

The Tauc optical band gap increased linearly with an enhancing N/Si ratio. Conversely, the refractive index decreased linearly with an increasing N/Si ratio. The behaviour of the optical properties corresponds well to the increasing N and Si-N concentration, regardless of the presence of $Si_xN_yO_z$ interfaces. These interfaces are relatively low in concentration compared to the SiN_x bulk and therefore changes within the chemical composition especially N incorporation into the SiN_x thin films dominate the optical properties.

7.5 CONCLUSION

The chemical composition, bonding densities, stress and optical properties of hydrogenated SiN_x thin films as a function of NH_3 flow rate synthesized by HWCVD have been studied. Independent XPS and EDS analysis corroborate each other on the determination of the N/Si ratio. Nitrogen from the NH_3 gas was effectively incorporated into the film while the hydrogen content decreased with an increasing N/Si ratio. The band gap of the SiN_x thin films increased with an enhancing N/Si ratio. Conversely, the refractive index decreased with an increasing N/Si ratio. Compressive film stress occurred in Si-rich SiN_x thin films which decreases and then changed to tensile stress as the N content increase. Filament degradation and gas phase reactions determined the SiN_x growth rate. The increasing incorporation of N within the SiN_x thin films created defects regardless of the enhancing etching by atomic hydrogen as the NH_3 flow rate increased. Nevertheless, highly transparent, H-containing and low reflection SiN_x layers were fabricated, which is promising for applications as anti-reflective coatings and passivation layers on solar cells.

UNIVERSITY of the WESTERN CAPE

REFERENCES

7.1 V. Verlaan, C. H. M. van der Werf, Z. S. Houweling, I. G. Romijn, A. W. Weeber, H. F. W. Dekkers, H. D. Goldbach, R. E. I. Schropp (2007) Prog. Photovolt: Res. Appl. **15**:563.

7.2 B. Stannowski, J. K. Rath, R. E. I. Schropp (2001) Thin Solid Films **395**:339.

7.3 R.E.I. Schropp, C. H. M. van der Werf, V. Verlaan, J. K. Rath, H. Li (2009) Thin Solid Films **517**:3039.

7.4 N. Park, C. Choi, T. Seong, S. Park (2001) Phys. Rev. Lett. **86**:1355.

7.5 V. Verlaan, A. D. Verkerk, W. M. Arnoldbik, C. H. M. van der Werf, R. Bakker, Z. S. Houweling, I. G. Romijn , D. M. Borsa, A.W. Weeber, S.L. Luxembourg, M. Zeman, H. F. W. Dekkers, R. E. I. Schropp (2009) Thin Solid Films **517**:3499.

7.6 F. Giorgis, F. Giuliani, C. F. Pirri, E. Tresso, C. Summonte, R. Rizzoli, R. Galloni, A. Desalvo, P. Rava(1998) Philos. Mag. B **77**:925.

7.7 V. Verlaan, Z. S. Houweling, C. H. M. van der Werf, I. G. Romijn, A. W. Weeber, H. D. Goldbach, R. E. I. Schropp (2008) Thin Solid Films **516**:533.

7.8 A. H. Mahan, A. C. Dillon, L. M. Gedvilas, D. L. Williamson, J. D. Perkins (2003) J. Appl. Phys. **94**:2360.

7.9 F. Liu, S. Ward, L. Gedvilas, B. Keyes, B. To, Q. Wang, E. Sanchez, S. Wang (2004) J. Appl. Phys. **96**:2973.

7.10 Q. Wang, S. Ward, L. Gedvilas, B. Keyes, E. Sanchez, S. Wang (2004) Appl. Phys. Lett. **84**:338.

7.11 P. Alpium, L. M. Gonçalves, E. S. Marins, T. M. R. Viseu, S. Ferdov, J. E. Bourée (2009) Thin Solid Films **517**:3503.

UNIVERSITY of the WESTERN CAPE

7.12 J. E. Bourée, J. Guillet, C. Grattepain, J. Chaumont (2003) Thin Solid Films **430**:110.

7.13 C.J. Arendse, M.Sc. thesis, University of the Western Cape, Bellville, South Africa (1999).

7.14 N. Maley (1992) Phys. Rev. B **46**:2078.

7.15 M. H. Brodsky, M. Cardona, J. J. Cuomo (1977) Phys. Rev. B **16**:3556.

7.16 G. G. Stoney (1909) Proc. R. Soc. Lond. A **82**:172.

7.17 K. Takimoto, A. Fukuta, Y. Yamamoto, N. Yoshida, T. Itoh, S. Nonomura (2002) J. Non-Cryst. Solids **299-302:**314.

7.18 T. F. G. Muller, C. J. Arendse, S. Halindintwali, D. Knoesen, R. E. I. Schropp (2011) Thin Solid Films **519**:4462.

7.19 E. Zeiler, S. Schwarz, S. M. Rosiwal, R. F. Singer (2002) Mat. Sci. Eng. A-Struct. **A335**:236.

7.20 C. H. M. van der Werf, P. A. T. T. van Veenendaal, M.K. van Veen, A. J. Hardeman, M. Y. S. Rusche, J. K. Rath, R. E. I. Schropp (2003) Thin Solid Films **430**:46.

7.21 I. Langmuir, J. Am. Chem. Soc. (1912) **34**:860.

7.22 E. Bustarret, M. Bensouda, M. C. Habrard, J. C. Bruyère, S. Poulin, S. C. Gujrathi (1988) Phys. Rev. B **38**:8171.

7.23 V. Verlaan, C. H. M. van der Werf, W. M. Arnoldbik, H. D. Goldbach, R. E. I. Schropp (2006) Phys. Rev. B **73**:195333.

7.24 H. Matsumura, A. Masuda, H. Umemoto (2006) Thin Solid Films **501**:58.

7.25 P. Hovington, D. Drouin, R. Gauvin (1996) Scanning **19**:1.

7.26 W. A. Lanford, M. J. Rand (1978) J. Appl. Phys. **49**:2473.

7.27 Z. Yin, F. W. Smith (1990) Phys. Rev. B **42**:3666.

UNIVERSITY of the
WESTERN CAPE

7.28 J. J. Mei, H. Chen, W. Z. Shen, H. F. Dekkers (2006) J. Appl. Phys. **100**:073516.

7.29 C. J. Oliphant, C. J. Arendse, D. Knoesen, T. F. G. Muller, S. Prins, G. Malgas (2011) Thin Solid Films **519**:4437.

7.30 R. E. I. Schropp, Miro Zeman (1998), Amorphous and Microcrystalline Silicon Solar Cells: Modelling, Materials, and Device Technology, Springer.

7.31 F. W. Smith, Z. Yin (1991) J. of Non-Cryst. Solids **137&138**:871.

7.32 Verlaan, Z. S. Houweling, C. H. M. van der Werf, H. D. Goldbach, R. E. I. Schropp (2006) MRS Proceedings 910:0910-A03-03.

7.33 B. Stannowski, J. K. Rath, R. E. I. Schropp (2003) J. Appl. Phys. **93**:2618.

7.34 R. E. I. Schropp, S. Nishizaki, Z. S. Houweling, V. Verlaan, C. H. M. van der Werf, H. Matsumura (2008) Solid State Electron. **52**:427.

7.35 L. V. Mercaldo, E. M. Esposito, P. D. Veneri, G. Fameli, S. Mirabella, G. Nicotra (2010) Appl. Phys. Lett. **97**:153112.

7.36 J. Bandet, B. Despax, M. Caumont (1999) J. Appl. Phys. **85**:7899.

7.37 M. Luysberg, P. Hapke, R. Carius, F. Finger, Philos. Mag. A 75 (1997) 31.

7.38 P. Mishra, K. P. Jain (2001) Phys. Rev. B **64**:073304.

7.39 R. P. Wang, G. Xu, P. Jin (2004) Phys. Rev. B 63:113303.

7.40 H. N. Wanka, M. B. Schubert (1997) MRS Proceedings **467**:651.

7.41 H. Fukuda, M. Yasuda, T. Iwabuchi, S. Ohno (1992) Applied Surface Science **60/61**:359.

7.42 S. Hasegawa, Y. Amano, T. Inokuma, Y. Kurata (1992) J. Appl. Phys. **72**:5676.

7.43 A. Fontcuberta i Morral, P. Roca i Cabarrocas (2001) Thin Solid Films **383**:161.

UNIVERSITY of the WESTERN CAPE

7.44 B. Swatowska, T. Stapinski (2008) Vacuum **82**:942.

7.45 I.V. Afanasyev-Charkin, M. Nastasi (2003) Nucl. Instrum. Meth. B **206**:736.

SUMMARY

During the last few decades, hydrogenated amorphous silicon (a-Si:H) and amorphous silicon nitride (SiN_x) thin films have become vital, cost reductive components suitable for applications in large area electronics such as liquid crystal displays and solar cells. However, the electronic stability and the current plasma based manufacturing process are major challenges in further developing devices based on a-Si:H and SiN_x.

UNIVERSITY of the
WESTERN CAPE

Nanocrystalline silicon (nc-Si:H) has proven to offer more stability and improved electrical properties than a-Si:H by incorporating properties from its crystalline and amorphous constituents. Silicon nitride is a versatile material that found widespread applications as transparent, anti-reflective coatings for multicrystalline silicon (mc-Si) solar cells and as a dielectric in thin film transistors. Both nc-Si:H and SiN_x thin films can be deposited using the hot-wire chemical vapour deposition (HWCVD) technique at rapid growth rates and with no ion bombardment compared to plasma enhanced chemical vapour deposition (PECVD). During HWCVD, process gas mixtures are dissociated, either thermally and/or catalytically, into radicals by a heated filament. The radicals can then react in the gas phase, eventually depositing and growing into a film on a substrate. Nevertheless, the film growth mechanism and filament stability are still major concerns for the HWCVD of nc-Si:H and SiN_x thin films.

This thesis focused on investigating the growth mechanisms of nc-Si:H and SiN_x thin films deposit by the HWCVD technique. In each case, the structural evolution of the filament was investigated. In Chapter 2 the HWCVD system and the characterization tools used in this study are introduced.

In Chapter 3, an investigation was carried out into the degradation of a tantalum (Ta) filament during the HWCVD of nc-Si:H thin films. Electron backscatter diffraction (EBSD) analysis revealed that predominantly Ta-rich Ta-silicides formed at the centre whereas Si-rich Ta-silicides at the cooler ends near the electrical contacts. Solid layers of crystalline silicon were also deposited at the cooler ends. The crystal orientation with respect to the incident electron beam also contributes to the contrast in backscatter electron micrographs of aged filaments. Hardness measurements disclosed that the recrystallized Ta-core was softer but less brittle than the surrounding silicides. Based on the findings we proposed that Si evaporates more at the hotter centre regions, causing the growth of more Ta-rich silicides. At the cooler ends the more Si is incorporated into the filament consequently favouring Si-rich silicides.

Chapter 4 reported on the growth kinetics of nc-Si:H thin films deposited by HWCVD at various hydrogen (H_2) dilutions of silane (SiH_4). Increasing the H_2-dilution resulted in significant ordering within the crystalline volume fraction and enhancing crystallite sizes due to the agglomeration of smaller crystallites. The expanding crystallite Si regions exert pressure on the surrounding a-Si network, causing a reduction in tensile strain as deduced by an increasing wavenumber of the Raman a-Si transverse optic peak.

UNIVERSITY of the
WESTERN CAPE

Monitoring the film thickness as a function of deposition time revealed that surface reactions are determining the growth of before and after the onset of crystallinity. The diffusion of H within the film at regions close to the transition from a-Si:H to nc-Si:H controlled the growth. The optical absorption within the films decreased with an increasing H_2-dilution corresponding to an enhancing crystallinity at the expense of a-Si networks.

In Chapter 5 the effects of the deposition pressure and time on the structural, optical and mechanical properties of nc-Si:H films synthesized by HWCVD were studied. Initially, all the nc-Si:H films are porous and crystallites sizes < 10 nm. All the films experienced an increasing tensile stress with an enhancing deposition pressure. At 20 minutes of deposition the film stress became less tensile, even compressive for deposition pressures ≤ 80 µbar. During this time, the expanding crystallites induced compressive stress on the surround a-Si network. Subsequently, the a-Si became more compact and started to counteract the stresses caused by the growing crystallite, resulting in a reduction in tensile stress, even inducing compressive stress at deposition pressures ≤ 80 µbar. The film refractive index enhanced with an increasing compressive stress and decrease when the films are under tensile stress. Given the observed decrease in crystallite sizes as deduced from the Raman analysis despite the enhancing crystalline volume fractions, the nucleation of small crystallites enlarged the band gap via the quantum confinement effect. At 60 minutes the structural, optical and mechanical properties of the nc-Si:H films are less dependent on the deposition pressure.

UNIVERSITY of the
WESTERN CAPE

In Chapter 6, the degradation of a Ta-filament during the HWCVD of SiN_x films is discussed. EBSD analysis disclosed that the Ta transformed to include a recrystallized Ta-core with Ta-nitrides and Ta-silicides. The nitrides form deeper within the filament bulk than the silicides. A solid silicon nitride layer encapsulated the filament at the cooler ends near the electrical contacts. Cracks and porosity were prevalent throughout the filament. The cracks, porosity and Ta-nitride formation were enhanced at the hotter centre regions, where filament failure eventually occurred.

In Chapter 7 we report on the HWCVD of amorphous SiN_x thin films from a SiH_4 / ammonia (NH_3) / H_2 gas mixture. The total gas flow rates were < 31 sccm with NH_3 flow rates < 3 sccm, a deposition pressure of 150 μbar and filament temperature of ~ 1600 °C. At these low process conditions, we deposited transparent, low reflection amorphous SiN_x layers at growth rates up to 24 nm / min with hydrogen content of ~ 9 at. %, suitable for use as passivating and anti-reflective coatings on solar cells. The addition of H_2 to the gas mixture and the effectiveness of a heated Ta-filament to produce atomic hydrogen ensured an efficient NH_3 dissociation and improved N incorporation within the SiN_x thin films. The enhancing N-content within the SiN_x films resulted in a reduction of the film refractive index and widening of the optical band gap. Nevertheless, the SiN_x film growth rate was influenced by the filament ageing process whereby gaseous precursors were incorporated into the filament during nitridation and silicidation.

WESTERN CAPE

Unfortunately, it was not possible within the time constraint to fabricate devices using the nc-Si:H and SiN_x films deposited by HWCVD. We recommend that future studies should include:

- Thermal annealing studies of SiN_x films
- Coating mc-Si solar cells with HWCVD SiN_x films to test the passivation quality
- Investigate the kinetics underpinning the filament silicidation and nitridation process at different filament temperatures and deposition times

PUBLICATIONS

Publications related to this thesis:

C. J. Oliphant, C. J. Arendse, T. F. G. Muller, W. A. Jordaan, D. Knoesen, *"Degradation of a tantalum filament during the Hot-Wire CVD of silicon nitride thin films"*, submitted to Thin Solid Films.

UNIVERSITY of the
WESTERN CAPE

Clive J. Oliphant, Christopher J. Arendse, Sara N. Prins, Gerald F. Malgas, Dirk Knoesen, *"Structural evolution of a Ta-filament during hot-wire chemical vapour deposition of Silicon investigated by electron backscatter diffraction"*, Journal Of Materials Science, **47**:2405 (2012).

C. J. Oliphant, C. J. Arendse, D. Knoesen, T. F. G. Muller, S. Prins, G. F. Malgas, *"Growth kinetics of nc-Si:H deposited at 200 °C by hot-wire vapour deposition chemical"*, Thin Solid Films, **519**:4437 (2011).

Other Contributions:

C. J. Arendse, N. Towfie, T. F. G. Muller , D. Knoesen, **C. J. Oliphant**, G. F. Malgas, B. A. Julies, *"Silicon thin films by dynamic variation of hydrogen dilution during hot-wire CVD"*, submitted to Thin Solid Films.

T. F. G. Muller, S. Jacobs, C. J. Arendse, G. F. Malgas, **C. J. Oliphant**, D. Knoesen, *"Isochronal annealing of HWCVD amorphous silicon nitride"*, submitted to Thin Solid Films.

A. S. Bolokang, M. J. Phasha, **C. Oliphant**, D. Motaung, *"XRD analysis and microstructure of milled and sintered V, W, C, and Co powders"*, International Journal of Refractory Metals and Hard Materials, **29**:108 (2011).

UNIVERSITY of the
WESTERN CAPE

C. J. Oliphant, C. J. Arendse, G. F. Malgas, D. E. Motaung, T. F. G. Muller, D. Knoesen, "Dual Catalytic Purpose of the Tungsten Filament during the synthesis of single helix carbon microcoils by Hot-wire CVD", Journal of Nanoscience and Nanotechnology, 9:5870 (2009).

V. Verlaan, C.H.M. van der Werf, **C.J. Oliphant**, R. Bakker, Z.S. Houweling, R.E.I. Schropp, *"Effect of ammonia on Ta filaments in the hot wire CVD process"*, Thin Solid Films, 517:3435 (2009).

C. J. Oliphant, C. J. Arendse, G. F. Malgas, D. E. Motaung, T. F. G. Muller, S. Halindintwali, B. A. Julies, D. Knoesen, *"Filament poisoning at typical carbon nanotube deposition conditions by hot-filament CVD",* Journal of Materials Science, 44:2610 (2009).

C. H. M. van der Werf, H. Li, V. Verlaan, **C. J. Oliphant**, R. Bakker, Z. S. Houweling, R. E. I. Schropp, *"Reversibility of silicidation of Ta filaments in HWCVD of thin film silicon",* Thin Solid Films, 517:3431 (2009).

David E. Motaung, Gerald F. Malgas, Christopher J. Arendse, Sipho E. Mavundla, **Clive J. Oliphant** and Dirk Knoesen, *"The influence of thermal annealing on the morphology and structural properties of a conjugated polymer in blends with an organic acceptor material"*, Journal of Materials Science, 44:3192 (2009).

UNIVERSITY of the
WESTERN CAPE

David E. Motaung, Gerald F. Malgas, Christopher J. Arendse, Sipho E. Mavundla, **Clive J. Oliphant** and Dirk Knoesen, *"Thermal-induced changes on the properties of spin-coated P3HT:C60 thin films for solar cell applications"*, Solar Energy Materials & Solar Cells, 93:1674 (2009).

C. J. Arendse, G. F. Malgas, T. F. G. Muller, D. Knoesen, **C. J. Oliphant**, D. E. Motaung, S. Halindintwali and B. W. Mwakikunga, *"Thermally Induced Nano-*

Structural and Optical Changes of nc-SiH deposited by Hot-wire CVD", Nano Research Letters, 4:307 (2009).